

COMPUTATIONALLY EFFICIENT DATA-ENHANCED  
MANIFOLD MODELING OF MULTI-MODAL  
TURBULENT COMBUSTION

CRISTIAN ESTREMER LACEY

A DISSERTATION  
PRESENTED TO THE FACULTY  
OF PRINCETON UNIVERSITY  
IN CANDIDACY FOR THE DEGREE  
OF DOCTOR OF PHILOSOPHY

RECOMMENDED FOR ACCEPTANCE  
BY THE DEPARTMENT OF  
MECHANICAL AND AEROSPACE ENGINEERING  
ADVISER: PROFESSOR MICHAEL E. MUELLER

MAY 2023

© Copyright by Cristian Estremera Lacey, 2023.

All rights reserved.

# Abstract

The design of improved energy conversion devices may be facilitated by Large Eddy Simulation (LES) – a computationally efficient modeling approach for simulating turbulent flows. Brute-force combustion modeling approaches that directly transport up to hundreds or even thousands of chemical species are generally applicable but intractable in simulations of realistic systems. Projecting the high-dimensional thermochemical state onto a reduced-order manifold provides an efficient alternative for modeling the unresolved combustion processes but does not traditionally generalize to the multi-modal combustion regimes present in practical engineering devices, introducing a fundamental modeling trade-off between computational cost and model generality. Though more general, higher-dimensional manifold models capable of breaking this trade-off exist in theory, their implementation is impeded by large computational cost and memory requirements associated with pretabulating the thermochemical state as well as unclosed terms that appear in the manifold equations.

A novel algorithm termed In-Situ Adaptive Manifolds (ISAM) is developed to enable LES implementations of more general, higher-dimensional manifold models by computing manifold solutions ‘on-the-fly’ and reusing them with In-Situ Adaptive Tabulation (ISAT). ISAM is verified and evaluated via LES of two canonical turbulent nonpremixed jet flames and extended to two higher-dimensional manifold models capable of capturing multiple and/or inhomogeneous stream mixing and multi-modal combustion. The computational cost of ISAM rapidly reaches parity with traditional pretabulation approaches independent of the chemical mechanism size and model complexity while requiring up to seven orders of magnitude less memory.

Then, data-based approaches are leveraged to augment physics-based manifold models – namely, to provide closure for unclosed dissipation rates that parameterize the solutions to the manifold equations. The instantaneous dissipation rate profiles in both premixed and multi-modal turbulent combustion are extracted from Direct Numerical Simulation (DNS) databases, and deep neural networks (DNNs) are trained to accurately capture the previously

unconsidered spatiotemporal variation of the profile shapes. Quantitative predictions of flame stabilization, ignition, and pollutant formation are shown to be particularly sensitive to the shape of the dissipation rate profiles. In conjunction with ISAM, the hybrid physics- and data-based models developed in this dissertation represent a critical advancement in multi-modal turbulent combustion simulations – tools essential for developing cleaner, more efficient power generation technology.

## Acknowledgements

Attending graduate school has been an enormously rewarding experience – both from a professional and personal perspective – entirely due to the people that I have met and that have shaped my life over the past five years. Foremost among them is my adviser, Prof. Michael E. Mueller, whose continued support and guidance have been central to both my success as a researcher as well as my well-being as a graduate student. Michael is without a doubt a world-class researcher and lecturer, but more importantly he is an incredibly supportive and compassionate mentor. Despite his many other responsibilities, Michael always makes time for his graduate students, whether it be to answer technical questions, carefully review written documents, or just chat about life. There are a lot of smart people in the world, but in my experience it is *exceedingly* rare to simultaneously be such an exceptionally caring human being. I find it difficult to convey just how grateful I am to have had such an individual as an adviser. I consider Michael not just a mentor whom I greatly admire but also my friend, and I think that is the greatest compliment a student can offer.

I would like to further acknowledge the many other faculty members and external researchers, whose efforts have informed my academic growth. Through their coursework and lectures, Prof. Chung K. Law and Prof. Howard A. Stone have provided me with a strong theoretical foundation in the topics of combustion and fluid mechanics, while also deepening my appreciation for fundamental science. Prof. Sankaran Sundaresan set aside many hours to discuss my research progress, always posing thoughtful questions that proved invaluable, for which I am very thankful. I also deeply appreciate Dr. Jacqueline H. Chen and Dr. Martin Rieth at Sandia National Laboratories for generously donating their time to our collaboration, consistently providing insightful feedback, and supplying a wealth of high-fidelity simulation data – without which much of the work of this dissertation would have been impossible. I would also like to thank my Ph.D. committee members Prof. Luc Deike and Prof. Yiguang Ju, my dissertation readers Prof. Chung K. Law and Prof. Luc

Deike, and my Final Public Oral examiners Prof. Sankaran Sundaresan and Prof. Marcus Hultmark.

This section would be incomplete without recognizing all the wonderful people in the Computational Turbulent Reacting Flow Laboratory (CTRFL) that I have had the privilege to spend my graduate school years with. Thank you to Bruce Perry and Cody Nunno for setting the tone in the lab and the MAE department as a whole when I was first starting out, ensuring both were (and continue to be) warm and inviting places. Alex Novoselov, thank you for playing such a central role in my development as a researcher, relaying all the subtle intricacies of turbulent combustion modeling with clarity and patience. I know I have told you this before, but it genuinely makes me so happy that you have become a professor. The world of academia needs more advisers like you. Kerry Klemmer, thank you for teaching me everything I know about turbulence and crossword puzzles. I am honestly not sure which of the two has been more important to life in the lab. Above all, thank you for being such a good friend and being there for me when I need it most. Jinyoung Lee, you carry yourself with a humility and kindness that I find truly admirable. I greatly enjoyed being your labmate and conference roommate during my time at Princeton. I would also like to say a special thank you to Katie VanderKam, Hannah Williams, Israel Bonilla, Agnes Robang, and honorary CTRFL member Megan Mazzatenta for being such tremendously thoughtful and caring friends to me this past year. You are all so dear to me, and I will greatly miss seeing you in lab every day. There is no group of people I would rather descend into LEGO Town mode with more than you. Katie, thank you for single-handedly keeping crossword time alive. Without you, the rest of us would be struggling with Thursdays as if they were Saturdays. Hannah, I appreciate your selfless willingness to design such beautiful lab graphics, knowing full well we will force you to make them your least favorite color regardless. Izzy, thank you for being the new Cristian. I am happy and proud that the role has been passed to someone as wonderful as you. Agnes, I so deeply appreciate the unmitigated chaos you bring to lab. Truly though, it has been a pleasure to get to know

you, and I am very impressed with all the work you have done. Megan, your callbacks are masterful, and you will never convince me otherwise. Thank you for always making me smile. To the newest members of the CTRFL – Sydney Rzepka, John Boerchers, and Trevor Fush – I am glad I got the chance to get to know you all better over these past few months. The future of the lab is certainly bright. Finally, I would like to thank current and former postdoctoral researchers Giuseppe D’Alessio, Hernando Maldonado Colmán, Esteban Cisneros Garibay, Pavan Prakash Duvvuri, Aditya Aiyer, and Pierre-Yves Taunay for their many helpful discussions and suggestions over the years.

I am also very grateful to the exceptional people that make up my cohort – in particular, thank you to Rory Conlin, Paul Kaneelil, and Amlan Sinha. Rory, thank you for being such a loyal friend and grumpy dungeon master. I always look forward to catching up with you during our lunch and dinner dates, and I hope you know I consider you a very important friend. Paul, I do not see you as often as I would like to these days, but it is always nice to catch up with you when I do. You are such a kind-hearted person. Amlan, I feel the same about you. I should also thank you for introducing me to the Sanchez and ruining an almost twenty-three-year streak of devout pescetarianism. Also, I would be remiss not to mention at least a few of the many wonderful humans that occasionally or consistently grace the atrium lunch table with their presence: Daniel Pardo, Andy Rothstein, Sasha Bodrova, Dan Shaw, Marcel Louis, and Satya Butler. Chatting, coming up with new axes, and playing board games with you all has been such a great time. You all make the MAE department a better place.

I must also thank my family, whose love and support form the foundation for all that I am. Juliet, thank you for being such a wonderful and supportive friend. You are and always will be my best little buddy. You understand me in a way that few people do, and I feel so fortunate to have you as a sibling. I find it deeply reassuring knowing that we will always have each other. Mama, you are the ideal mother and caregiver. You are selfless and warm in a way that makes it seem so easy and obvious, even when I am sure that it is not. You

make me feel profoundly loved, and I am so very grateful to be your son. Papa, thank you for always believing in me. From an early age, you instilled in me the confidence required to face the many academic challenges I have encountered over the years. For that, I am very grateful. I hope that this dissertation makes all of you proud.

I gratefully acknowledge funding provided by the Gordon Y. S. Wu Fellowship in Engineering, Daniel and Florence Guggenheim Foundation Fellowship, and the Charlotte Elizabeth Procter Fellowship through Princeton University. I also acknowledge funding from the U.S. Department of Energy Office of Science Graduate Student Research (SCGSR) fellowship program, the Army Research Office (ARO) Young Investigator Program (YIP) under grant W911NF-17-1-0391, the National Aeronautics and Space Administration (NASA) under grant NNX16AP90A, the University Coalition for Fossil Energy Research through the U.S. Department of Energy's National Energy Technology Laboratory (DE-FE0026825), and the Schmidt DataX Fund at Princeton University made possible through a major gift from the Schmidt Futures Foundation. The work from Sandia National Laboratories was supported by the Exascale Computing Project (ECP), Project Number: 17-SC-20-SC, a collaborative effort of two DOE organizations – the Office of Science and the National Nuclear Security Administration. Sandia National Laboratories is a multimission laboratory managed and operated by National Technology and Engineering Solutions of Sandia, LLC., a wholly owned subsidiary of Honeywell International, Inc., for the U.S. Department of Energy's National Nuclear Security Administration under contract DE-NA-0003525. The simulations presented in this dissertation were performed on computational resources supported by the Oak Ridge Leadership Computing Facility (OLCF), the Princeton Institute for Computational Science and Engineering (PICSciE), and the Office of Information Technology's High Performance Computing Center and Visualization Laboratory at Princeton University.

This dissertation carries T#3442 in the records of the Department of Mechanical and Aerospace Engineering.



To my family and friends

# Contents

Abstract . . . . .	iii
Acknowledgements . . . . .	v
List of Tables . . . . .	xv
List of Figures . . . . .	xvi
<b>1 Introduction</b>	<b>1</b>
1.1 Asymptotic Combustion Modes . . . . .	3
1.2 Simulation of Turbulent Combustion . . . . .	4
1.2.1 Thermochemical State . . . . .	5
1.2.2 Chemical Kinetics Modeling . . . . .	6
1.2.3 Manifold Modeling . . . . .	7
1.2.4 Turbulence Modeling . . . . .	10
1.2.5 Filtered Chemical Source Term Modeling . . . . .	12
1.3 Augmenting Physics-Based Models with Data . . . . .	16
1.4 Contributions and Organization . . . . .	17
<b>2 Governing Equations</b>	<b>21</b>
2.1 Transport Equations . . . . .	21
2.2 Chemical Source Terms . . . . .	25
2.3 Large Eddy Simulation (LES) . . . . .	26
2.3.1 Subfilter Stress Closure . . . . .	27

2.3.2	Subfilter Scalar Flux Closure . . . . .	30
2.3.3	Extension of Manifold Modeling to LES . . . . .	31
2.4	Deep Neural Networks (DNNs) . . . . .	32
2.4.1	DNN Training . . . . .	34
2.4.2	DNN Hyperparameter and Architecture Selection . . . . .	36
<b>3</b>	<b>In-Situ Adaptive Manifolds (ISAM): A Novel Algorithm for Manifold Modeling</b>	<b>38</b>
3.1	Nonpremixed Manifold Model . . . . .	39
3.2	Manifold Modeling Algorithms . . . . .	42
3.2.1	Precomputation, Preconvolution, and Pretabulation (PPP) . . . . .	42
3.2.2	Convolution-on-the-fly (COTF) . . . . .	43
3.2.3	In-Situ Adaptive Manifolds (ISAM) . . . . .	43
3.3	Test Configurations: Turbulent Nonpremixed Jet Flames . . . . .	46
3.3.1	Computational Infrastructure . . . . .	46
3.3.2	Configuration I: Hydrogen Jet Flame . . . . .	46
3.3.3	Configuration II: Sandia Flame D . . . . .	47
3.4	ISAM Verification . . . . .	47
3.4.1	Verification: Hydrogen Jet Flame . . . . .	47
3.4.2	Verification: Sandia Flame D . . . . .	48
3.5	Performance Assessment . . . . .	48
3.6	Numerical ISAT Jacobian . . . . .	51
3.7	Tolerance Sensitivity Analysis . . . . .	53
3.8	Improving ISAM Performance . . . . .	55
3.8.1	MPI Synchronization . . . . .	55
3.8.2	Speeding Up Manifold Calculations . . . . .	58
3.9	Outcomes: ISAM . . . . .	60

<b>4</b>	<b>Extension of ISAM to Multiple and/or Inhomogeneous Inlet Streams</b>	<b>61</b>
4.1	Test Configuration: Sydney Flame . . . . .	61
4.2	Nonpremixed Manifold Model: Modification for an Inhomogeneous Stream .	62
4.3	Sydney Flame: Constrained Dissipation Rate . . . . .	64
4.4	Sydney Flame: Unconstrained Dissipation Rate . . . . .	67
4.5	Outcomes: Sydney Flame . . . . .	69
<b>5</b>	<b>Extension of ISAM to Multi-Modal Combustion</b>	<b>71</b>
5.1	Multi-Modal Manifold Model . . . . .	71
5.2	Test Configuration: Cabra Flame . . . . .	77
5.3	Evaluation of Multi-Modal Model Performance . . . . .	78
5.3.1	Feasibility . . . . .	78
5.3.2	Interpretability . . . . .	79
5.4	Outcomes: Cabra Flame . . . . .	83
<b>6</b>	<b>Data-Based Dissipation Rate Modeling for Premixed Combustion</b>	<b>84</b>
6.1	Premixed Manifold Model . . . . .	84
6.2	DNS Data and Profile Extraction . . . . .	87
6.2.1	DNS Data . . . . .	87
6.2.2	Extraction Methodology . . . . .	88
6.2.3	Evaluating Profile ‘Universality’ . . . . .	89
6.3	Data-Based Modeling Approach . . . . .	92
6.3.1	DNS Filtering and Training Data Generation . . . . .	92
6.3.2	Input Feature Selection . . . . .	93
6.3.3	Network Hyperparameter Selection . . . . .	93
6.4	Results and Discussion . . . . .	94
6.4.1	DNN Model Evaluation . . . . .	94
6.4.2	<i>A Priori</i> Analysis . . . . .	96

6.4.3	Data-Based Variable Importance: Integrated Gradients . . . . .	100
6.4.4	Physics-Based Variable Importance: Conditional Generalized Progress Variable Dissipation Rate Transport Equation . . . . .	105
6.5	Outcomes: Premixed Dissipation Rate Profile Modeling . . . . .	108
<b>7</b>	<b>Data-Based Dissipation Rate Modeling for Multi-Modal Combustion</b>	<b>110</b>
7.1	DNS Dataset Selection . . . . .	111
7.2	Multi-Modal Manifold Model: Modification for Temporally Evolving Flames	112
7.3	Nonlinear Reference Species Definition . . . . .	113
7.4	Dissipation Rate Modeling Approach . . . . .	114
7.5	Filtered Dissipation Rate Modeling . . . . .	115
7.5.1	Algebraic Models: Pierce and Linear Relaxation Models . . . . .	116
7.5.2	Enforcing Physical Constraints in DNN Models . . . . .	117
7.5.3	Training Data Generation . . . . .	118
7.5.4	DNN Model Details . . . . .	118
7.5.5	DNN Model Evaluation . . . . .	119
7.6	Instantaneous Dissipation Rate Profile Modeling . . . . .	122
7.6.1	Algebraic Dissipation Rate Profile Models . . . . .	124
7.6.2	Profile Extraction Methodology . . . . .	125
7.6.3	Profile Regression Methods: PLI and GPR . . . . .	127
7.6.4	<i>A Priori</i> Evaluation of Regression Methods . . . . .	130
7.6.5	Evaluating Profile ‘Universality’ . . . . .	132
7.6.6	Training Data Generation . . . . .	135
7.6.7	DNN Model Details . . . . .	136
7.6.8	DNN Model Evaluation . . . . .	136
7.6.9	<i>A Priori</i> Analysis . . . . .	137
7.7	Outcomes: Multi-Modal Dissipation Rate Modeling . . . . .	144

<b>8</b>	<b>Physics-Based Dimensionality Reduction (PBDR)</b>	<b>146</b>
8.1	Input Feature Dimensionality Reduction . . . . .	147
8.1.1	PCA-Based Dimensionality Reduction . . . . .	147
8.1.2	Physics-Based Dimensionality Reduction (PBDR) . . . . .	149
8.2	DNN Model Details . . . . .	151
8.2.1	DNS Filtering and Training Data Generation . . . . .	151
8.2.2	Input Feature Selection . . . . .	151
8.2.3	Network Hyperparameter Selection . . . . .	154
8.3	DNN Model Evaluation . . . . .	155
8.3.1	ODI versus Algebraic Models . . . . .	155
8.3.2	ODI versus PBDR . . . . .	155
8.3.3	Sensitivity to the Dimensionally-Homogeneous Set . . . . .	159
8.3.4	PBDR versus PCA-FE and PCA-FS . . . . .	161
8.4	Outcomes: Physics-Based Dimensionality Reduction . . . . .	163
<b>9</b>	<b>Conclusions</b>	<b>165</b>
9.1	Opportunities for Future Work . . . . .	170
<b>A</b>	<b>Conditional Progress Variable Dissipation Rate Transport Equation</b>	
	<b>Derivation</b>	<b>174</b>
	<b>Bibliography</b>	<b>177</b>

# List of Tables

6.1	DNS parameters. . . . .	87
7.1	DNS time snapshot parameters. The time snapshot selected in this work is highlighted in light gray. . . . .	113
8.1	Summary of input features used to train each DNN model. . . . .	152
8.2	Summary of training, validation, and testing losses for each DNN model (evaluated based on datasets corresponding to filter stencil sizes of $\Delta_\alpha/h_\alpha = 2, 8, 16$ ). . . . .	154

# List of Figures

1.1	Comparison of traditional turbulent combustion modeling approaches and their associated regimes of applicability. Models further to the left are less computationally expensive and less general, while models further to the right are more computationally expensive and more general. . . . .	15
2.1	Graphical representation of a deep neural network. Figure adapted from Neutelings [84]. . . . .	34
3.1	Time-averaged statistics at $x/D = 22.5$ for the hydrogen jet flame. The vertical dashed line denotes the stoichiometric mixture fraction $Z_{\text{st}} = 0.0285$ . The solid line corresponds to COTF, the dashed line to ISAM, and symbols to experimental measurements with estimated uncertainty [95]. . . . .	48
3.2	Time-averaged statistics at $x/D = 15$ for Sandia Flame D. The vertical dashed line denotes the stoichiometric mixture fraction $Z_{\text{st}} = 0.353$ . The solid line corresponds to COTF, the dashed line to ISAM, and symbols to experimental measurements with estimated uncertainty [99]. . . . .	49
3.3	Baseline computational cost per time step for the hydrogen jet flame and Sandia Flame D. . . . .	50



3.4	Time-averaged statistics at $x/D = 15$ for Sandia Flame D. The vertical dashed line denotes the stoichiometric mixture fraction $Z_{\text{st}} = 0.353$ . The solid red line (—) corresponds to an ISAT Jacobian delta of $10^{-2}$ , the dashed blue line (--) to $10^{-3}$ , the dotted cyan line (...) to $10^{-4}$ , and symbols to experimental measurements with estimated uncertainty [99]. . . . .	52
3.5	Sensitivity of the baseline computational cost per time step with respect to the Jacobian delta $\Delta \ln \chi_{ZZ,\text{ref}}$ for Sandia Flame D. . . . .	52
3.6	Time-averaged statistics at $x/D = 15$ for Sandia Flame D. The vertical dashed line denotes the stoichiometric mixture fraction $Z_{\text{st}} = 0.353$ . The solid red line (—) corresponds to an ISAT relative error tolerance of $10^{-2}$ , the dashed blue line (--) to $10^{-3}$ , the dotted cyan line (...) to $10^{-4}$ , and symbols to experimental measurements with estimated uncertainty [99]. . . . .	54
3.7	Time-averaged statistics at $x/D = 15$ for Sandia Flame D. The vertical dashed line denotes the stoichiometric mixture fraction $Z_{\text{st}} = 0.353$ . The solid red line (—) corresponds to a PDRs relative error tolerance of $10^{-6}$ , the dashed blue line (--) to $10^{-7}$ , the dotted cyan line (...) to $10^{-8}$ , and symbols to experimental measurements with estimated uncertainty [99]. . . . .	54
3.8	Sensitivity of the baseline computational cost per time step to ISAT and PDRs relative error tolerances for Sandia Flame D. . . . .	55
3.9	Computational cost measured as cumulative wall time and time per time step for LES of Sandia Flame D, comparing COTF, ISAM without MPI synchronization, and ISAM with MPI synchronization after every time step. The time per time step versus time steps plot limits the vertical range to visualize the fluctuations in computational cost. . . . .	57

3.10	Computational cost measured as cumulative wall time and baseline cost for LES of Sandia Flame D, comparing COTF, ISAM without MPI synchronization, ISAM with MPI synchronization after every time step, ISAM with constant synchronization, and ISAM with exponential synchronization. . . .	58
3.11	ISAM performance improvements for Sandia Flame D corresponding to vectorizing the manifold solver PDRs (a) and leveraging hybrid MPI/OpenMP parallelization (b). Figures adapted from Bonilla et al. [103]. . . . .	59
4.1	Time-averaged radial statistics for mixture fraction and temperature at $x/D = 10$ for the Sydney flame with $\chi_{ZZ,\text{ref}} = 100 \text{ s}^{-1}$ . . . . .	65
4.2	Nonpremixed manifold model solutions for $F = 0.2$ , $\chi_{ZZ,\text{ref}} = 100 \text{ s}^{-1}$ ; $F = 0.2$ , $\chi_{ZZ,\text{ref}} = 200 \text{ s}^{-1}$ ; and $F = 0.3$ , $\chi_{ZZ,\text{ref}} = 100 \text{ s}^{-1}$ . . . . .	66
4.3	Computational cost measured as cumulative wall time, time per time step, and baseline cost for LES of the Sydney flame with $\chi_{ZZ,\text{ref}} = 100 \text{ s}^{-1}$ , comparing COTF, ISAM with MPI synchronization after every time step, and ISAM with two forms of exponential synchronization. . . . .	67
4.4	Single time snapshot of Sydney flame LES data plotted versus $\chi_{ZZ,\text{ref}}$ and $F$ , colored by the MPI rank in (a) and the filtered mixture fraction in (b). . . .	68
5.1	Baseline computational cost per time step for the Cabra flame. The dashed line (--) denotes that ‘error checking’ is disabled in ISAT after 100 time steps. Figure taken from Novoselov et al. [70]. . . . .	79
5.2	Time-averaged centerline profile of temperature (—). The flame is found to be statistically lifted at $x/D_{\text{jet}} = 37$ , denoted by a dashed line (--). Figure taken from Novoselov et al. [70]. . . . .	80

5.3	Instantaneous centerline snapshots of the three inverse time scales $S_{\dot{m}_\Lambda}$ (—), $S_{\chi_{\Lambda\Lambda}}$ (⋯), and $S_{\chi_{ZZ}}$ (—). Snapshots (a)-(d) are presented in chronological order, each separated by approximately 2 milliseconds in time. Provided insets share the same linear colorbar and display the generalized progress variable source term fields centered around $x/D_{\text{jet}} = 40$ . Figure taken from Novoselov et al. [70]. . . . .	81
5.4	Instantaneous radial snapshot of the three inverse time scales $S_{\dot{m}_\Lambda}$ (—), $S_{\chi_{\Lambda\Lambda}}$ (⋯), and $S_{\chi_{ZZ}}$ (—) is shown on top. The instantaneous radial snapshot of the alignment of the mixture fraction and generalized progress variable gradients is shown on bottom. Both snapshots correspond to that of Fig. 5.3 (a). Figure taken from Novoselov et al. [70]. . . . .	82
6.1	Instantaneous conditional dissipation rate profiles extracted from DNS data for both Karlovitz number cases, normalized by the reference dissipation rate. Solid black lines denote 250 normalized dissipation rate profiles randomly sampled from the extracted profiles for each Karlovitz number case; dotted cyan lines denote the conditional mean of the DNS (averaged over 500,000 samples for each Karlovitz number case); dashed red lines denote the algebraic expression for the stretched model in Eq. 6.7; and dashed blue lines denote the unstretched flat-flame solution in Eq. 6.7, normalized by the dissipation rate at the reference generalized progress variable. . . . .	90
6.2	Maximum value of the normalized dissipation rate profile $g_{\text{max}}$ versus the reference dissipation rate $\chi_{\Lambda\Lambda,\text{ref}}$ colored by $\Lambda_{\text{peak}}$ , the generalized progress variable at which $g_{\text{max}}$ occurs. . . . .	91

6.3	Conditional mean of the normalized dissipation rate profiles for datasets corresponding to $\Delta_\alpha/h_\alpha = 4$ . Black dotted lines denote the mean of the normalized dissipation rate profiles from the DNS data; cyan dot-dot-dashed lines denote the mean of the DNN normalized dissipation rate profile predictions; red dashed lines denote the stretched model from Eq. 6.7; and blue dashed lines denote the unstretched model from Eq. 6.6. Note that black dotted lines nearly exactly coincide with cyan dot-dot-dashed lines. . . . .	95
6.4	Conditional average instantaneous model error for datasets corresponding to $\Delta_\alpha/h_\alpha = 4$ . Black dotted lines denote the average error associated with the mean of the normalized dissipation rate profiles from the DNS data; cyan dot-dashed lines denote the average error in DNN instantaneous normalized dissipation rate profile predictions; red dashed lines denote the average error in the stretched model from Eq. 6.7; and blue dashed lines denote the average error in the unstretched model from Eq. 6.6. . . . .	96
6.5	Manifold solutions corresponding to profiles with $\chi_{\Lambda\Lambda,\text{ref}} = 26,327 \text{ s}^{-1}$ and $\Lambda_{\text{peak}} < 0.5$ in (a)-(c), $\chi_{\Lambda\Lambda,\text{ref}} = 14,514 \text{ s}^{-1}$ and $\Lambda_{\text{peak}} > 0.5$ in (d)-(f), and $\chi_{\Lambda\Lambda,\text{ref}} = 29,197 \text{ s}^{-1}$ and $\Lambda_{\text{peak}} \approx 0.5$ in (g)-(i). Black solid lines, black dotted lines, cyan dot-dashed lines, red dashed lines, and blue dashed lines denote solutions corresponding to instantaneous normalized dissipation rate profiles extracted from DNS data, the mean DNS model, the DNN model, the stretched model, and the unstretched model, respectively. Note that black solid lines nearly exactly coincide with cyan dot-dashed lines. . . . .	97

6.6	Set of integrated gradients $\{IG_{ij}\}_{j=1}^m$ for the filtered strain rate magnitude and generalized progress variable subfilter variance conditionally averaged with respect to the filtered generalized progress variable, where $\Lambda_j$ denotes the generalized progress variable at the discrete value of the normalized dissipation rate profile corresponding to index $j$ and $x_i$ denotes the corresponding input feature. . . . .	102
6.7	Set of integrated gradients $\{IG_{ij}\}_{j=1}^m$ for the principal rates of strain conditionally averaged with respect to the filtered generalized progress variable, where $\Lambda_j$ denotes the generalized progress variable at the discrete value of the normalized dissipation rate profile corresponding to index $j$ and $x_i$ denotes the corresponding input feature. . . . .	103
6.8	Probability density function of the principal rates of strain $\alpha$ and $\gamma$ present in the DNS data. . . . .	103
6.9	Set of integrated gradients $\{IG_{ij}\}_{j=1}^m$ for the filtered generalized progress variable conditionally averaged with respect to the filtered generalized progress variable, where $\Lambda_j$ denotes the generalized progress variable at the discrete value of the normalized dissipation rate profile corresponding to index $j$ and $x_i$ denotes the corresponding input feature, $x_i = \tilde{\Lambda}$ . Integrated gradients associated with the deep neural network trained on all input features are presented in (a), and those of the reduced deep neural network trained without the principal rates of strain or alignments are presented in (b). . . . .	104
6.10	Conditional velocity gradient conditioned on generalized progress variable, colored by $\Delta\Lambda_{\text{peak}} = \Lambda_{\text{peak}} - \Lambda_{\text{ref}}$ . The conditional velocity gradient from the DNS ( $\Delta_\alpha/h_\alpha = 0$ ) is shown in (a), and the resolved conditional velocity gradient from the filtered DNS ( $\Delta_\alpha/h_\alpha = 16$ ) is shown in (b). . . . .	107

7.1	Unconstrained DNN predictions ( $\cdots$ ) of the filtered mixture fraction dissipation rate, filtered cross-dissipation rate, and filtered generalized progress variable dissipation rate, each conditionally averaged on the filtered mixture fraction in (a) or on the filtered generalized progress variable in (b). DNN predictions are compared to conditionally averaged DNS data ( $\circ$ ), conditionally averaged Pierce model predictions ( $--$ ), and conditionally averaged LRM predictions ( $-\cdot-$ ). Conditional averages are reported for withheld testing data with $\Delta_\alpha/h_\alpha = 8$ . . . . .	120
7.2	Constrained DNN predictions ( $\cdots$ ) of the filtered mixture fraction dissipation rate, filtered cross-dissipation rate, and filtered generalized progress variable dissipation rate, each conditionally averaged on the filtered mixture fraction in (a) or on the filtered generalized progress variable in (b). DNN predictions are compared to conditionally averaged DNS data ( $\circ$ ), conditionally averaged Pierce model predictions ( $--$ ), and conditionally averaged LRM predictions ( $-\cdot-$ ). Conditional averages are reported for withheld testing data with $\Delta_\alpha/h_\alpha = 8$ . . . . .	121
7.3	Parity plots for the filtered mixture fraction dissipation rate, filtered cross-dissipation rate, and filtered generalized progress variable dissipation rate, comparing DNN predictions to corresponding filtered DNS data. (a) demonstrates the results of the unconstrained DNN, and (b) demonstrates the results of the constrained DNN, both as two-dimensional histograms shaded on a log-scale according to the number of data samples $N$ at each point. The dashed red line ( $-\cdot-$ ) denotes exact agreement between DNN predictions and the filtered DNS data. Parity plots are reported for withheld testing data with $\Delta_\alpha/h_\alpha = 8$ . . . . .	123

7.4	Mixture fraction dissipation rate, cross-dissipation rate, and generalized progress variable dissipation rate profiles plotted as color contour plots versus mixture fraction and generalized progress variable. (a) shows raw unstructured data extracted from the DNS along a particular representative manifold stream-surface computed from Eq. 7.19; (b) shows the structured data interpolated with piecewise linear interpolation; and (c) shows the structured data interpolated with Gaussian process regression. . . . .	128
7.5	Unfiltered thermochemical profiles computed as solutions to Eq. 5.4, given dissipation rate profiles interpolated with either piecewise linear interpolation (PLI) or Gaussian process regression (GPR). . . . .	130
7.6	Comparison of 90 filtered thermochemical quantities ( $\circ$ ) computed from Eq. 5.15 ( $\Delta_\alpha/h_\alpha = 32$ ), given dissipation rate profiles interpolated with either piecewise linear interpolation (PLI) or Gaussian process regression (GPR) with outlier profiles removed. One-to-one correspondence is denoted by the red dashed line ( $-.$ ) and $\pm 10\%$ error bounds are denoted by the solid red lines ( $-$ ). . . . .	132
7.7	Instantaneous normalized mixture fraction dissipation rate, alignment, and normalized generalized progress variable dissipation rate profiles plotted as color contour plots versus mixture fraction and generalized progress variable. (a) corresponds to instantaneous DNS profiles at a primary location on the DNS grid; (b) corresponds to instantaneous DNS profiles at a secondary location on the DNS grid; (c) corresponds to the ‘universal’ conditional mean of the extracted DNS profiles; and (d) corresponds to the ‘universal’ algebraic models. . . . .	134

7.8	Conditionally averaged instantaneous error profiles plotted as color contour plots versus mixture fraction and generalized progress variable. (a) corresponds to the DNN model; (b) corresponds to the mean DNS model; and (c) corresponds to the algebraic models. . . . .	138
7.9	Instantaneous mixture fraction dissipation rate, cross-dissipation rate, and generalized progress variable dissipation rate profiles plotted as color contour plots versus mixture fraction and generalized progress variable. (a) corresponds to instantaneous DNS profiles; (b) corresponds to instantaneous DNN model predictions; (c) corresponds to the ‘universal’ conditional mean of the extracted DNS profiles; and (d) corresponds to the ‘universal’ algebraic models.	140
7.10	Temperature solutions plotted as color contour plots versus mixture fraction and generalized progress variable. Each subfigure corresponds to the multi-modal manifold solution for a set of dissipation rate profiles determined via a different modeling approach. . . . .	141
7.11	Carbon monoxide mass fraction solutions plotted as color contour plots versus mixture fraction and generalized progress variable. Each subfigure corresponds to the multi-modal manifold solution for a set of dissipation rate profiles determined via a different modeling approach. . . . .	142
7.12	Generalized progress variable source term solutions plotted as color contour plots versus mixture fraction and generalized progress variable. Each subfigure corresponds to the multi-modal manifold solution for a set of dissipation rate profiles determined via a different modeling approach. . . . .	143



8.1	Comparison of instantaneous snapshots of the filtered progress variable dissipation rate fields from filtered DNS data, predictions of a DNN trained on the eight original dimensionally-inhomogeneous features, the Pierce model, and LRM. Isocontours of $\ln(\tilde{\chi}_{\Lambda\Lambda}) = 8$ are denoted by solid black lines ( <b>—</b> ). Snapshots are plotted for the central span-wise plane of the withheld testing data corresponding to $\Delta_\alpha/h_\alpha = 4$ . . . . .	156
8.2	DNN predictions ( <b>...</b> ) of the filtered progress variable dissipation rate conditionally averaged on the filtered progress variable corresponding to a DNN trained on the eight original dimensionally-inhomogeneous features in (a) and (b) and corresponding to a DNN trained on the most correlated five dimensionally-homogeneous features in (c) and (d). DNN predictions are compared to conditionally averaged DNS data ( $\circ$ ), conditionally averaged Pierce model predictions ( <b>-.</b> ), and conditionally averaged LRM predictions ( <b>..</b> ). Conditional averages are reported for withheld testing data with $\Delta_\alpha/h_\alpha = 4$ . . . . .	157
8.3	Parity plots for the filtered progress variable dissipation rate, comparing DNN predictions to corresponding filtered DNS data. (a) and (b) demonstrate the fidelity of a DNN trained on the eight original dimensionally-inhomogeneous features, and (c) and (d) demonstrate the fidelity of a DNN trained on the most correlated five dimensionally-homogeneous features, both as two-dimensional histograms shaded on a log-scale according to the number of data samples $N$ at each point. The dashed red line ( <b>-.</b> ) denotes exact agreement between DNN predictions and the filtered DNS data. Parity plots are reported for withheld testing data with $\Delta_\alpha/h_\alpha = 4$ . . . . .	158

8.4	DNN predictions ( $\dots$ ) of the filtered progress variable dissipation rate conditionally averaged on the filtered progress variable corresponding to a DNN trained on the least correlated five dimensionally-homogeneous features (with division by zero) in (a) and (b) and corresponding to a DNN trained on the least correlated five dimensionally-homogeneous features (without division by zero) in (c) and (d). DNN predictions are compared to conditionally averaged DNS data ( $\circ$ ), conditionally averaged Pierce model predictions ( $-\bullet-$ ), and conditionally averaged LRM predictions ( $-\bullet\bullet-$ ). Conditional averages are reported for withheld testing data with $\Delta_\alpha/h_\alpha = 4$ . . . . .	160
8.5	Parity plots for the filtered progress variable dissipation rate, comparing DNN predictions to corresponding filtered DNS data. (a) and (b) demonstrate the fidelity of a trained on the least correlated five dimensionally-homogeneous features (with division by zero), and (c) and (d) demonstrate the fidelity of a DNN trained on the least correlated five dimensionally-homogeneous features (without division by zero), both as two-dimensional histograms shaded on a log-scale according to the number of data samples $N$ at each point. The dashed red line ( $-\bullet-$ ) denotes exact agreement between DNN predictions and the filtered DNS data. Parity plots are reported for withheld testing data with $\Delta_\alpha/h_\alpha = 4$ . . . . .	161

8.6	Parity plots for the filtered progress variable dissipation rate, comparing DNN predictions to corresponding filtered DNS data. (a) and (b) demonstrate the fidelity of a DNN trained on the five extracted PCA-scores, and (c) and (d) demonstrate the fidelity of a DNN trained on the five features selected via the algorithm of Krzanowski [131], both as two-dimensional histograms shaded on a log-scale according to the number of data samples $N$ at each point. The dashed red line (--) denotes exact agreement between DNN predictions and the filtered DNS data. Parity plots are reported for withheld testing data with $\Delta_\alpha/h_\alpha = 4$ . . . . .	162
-----	--	-----

# Chapter 1

## Introduction

Harnessing fire stands among our most profound achievements – providing our early ancestors with warmth and light in the cold and dark. Yet, as humanity has evolved, so too has our relationship with fire. Today, combustion is the dominant source of energy conversion for transportation and electricity generation [1]. The chemical energy stored in the bonds of predominantly hydrocarbon fuels, such as petroleum and natural gas, is released as heat and converted to useful work via energy conversion devices. Unfortunately, the combustion of hydrocarbon fuels necessarily produces carbon dioxide ( $\text{CO}_2$ ) as a byproduct, a greenhouse gas responsible for climate change and the persistent increase in global temperatures [1, 2]. Hydrocarbon combustion also often produces trace amounts of pollutants such as carbon monoxide ( $\text{CO}$ ), nitrogen oxides ( $\text{NO}_x$ ), and solid carbon particulates known as soot, all of which negatively impact human health and the environment [1, 3, 4].

Despite the obvious drawbacks associated with burning fossil fuels, combustion remains the only feasible power source for applications such as commercial aviation [5]. Renewable energy sources such as wind and solar are promising alternatives for electricity generation under certain circumstances but suffer from intermittency and are limited to particular geographical regions that possess the weather conditions appropriate for deployment. Though advancements in battery storage and expansion of power transmission networks could offer

a firmer pathway forward for large-scale renewable energy adoption, such development is likely still many years away [6]. In fact, the United States projects that fossil fuel combustion will retain a central role in energy generation for *at least* the next several decades [7]. It is therefore critical that combustion phenomena be further studied to facilitate the design of combustion systems that are higher performing, more reliable, and more efficient yet still cost-effective within the context of evolving net-zero-emissions fuels such as biofuels, electrofuels, hydrogen ( $\text{H}_2$ ), and ammonia ( $\text{NH}_3$ ). Computational simulations possess the capacity to significantly expedite the design and development of improved power generation technology by providing engineers with performance predictions without the time and financial burden associated with iterative physical prototyping.

Computational combustion simulations are applicable over a large range of flow and combustion conditions, but focusing on regimes most relevant to the operation of realistic engineering devices allows for simplification of modeling approaches. For instance, depending on the relative balance of inertial and viscous effects, characterized by the Reynolds number  $Re$ , a flow may be either laminar or turbulent. At high Reynolds number, the inertia of fluid elements dominates over stabilizing viscous effects, leading to highly chaotic vortical motions and significantly enhanced mixing. Virtually all practical engineering devices leverage this enhanced mixing to promote chemical reaction, so energy conversion devices operate at highly turbulent flow conditions.

Fluid flows are also categorized based on the relative magnitude of the flow velocity and the speed of sound, characterized by the Mach number  $Ma$ . At large Mach number ( $Ma > 1$ ), the flow is supersonic and shocks occur. At intermediate Mach number ( $0.3 < Ma < 1$ ), the flow is subsonic and acoustic waves travel at finite velocities. At low Mach number ( $Ma < 0.3$ ), the flow is again subsonic but can be treated in the limiting case of zero Mach number for which acoustic information has an infinite propagation speed and is no longer resolved in a simulation. Accurately resolving acoustic waves with a compressible flow solver is particularly important for the prediction of thermoacoustic instabilities, even at low Mach

number [8]. However, for low Mach number cases where thermoacoustic instabilities are not expected to manifest, a low Mach number assumption is appropriate. Traditional energy conversion devices, such as internal combustion engines or gas turbines, often avoid high Mach number conditions and the ensuing damage from high pressure shock waves. Many practical devices instead operate at low Mach number. This work is therefore focused on flows most relevant to real-world energy generation applications – low Mach number, turbulent, reacting flows. Computational modeling of these types of flows is impeded by the high-dimensionality of thermochemical state space as well as the wide range of length and time scales relevant to turbulence and combustion, many of which cannot be efficiently resolved in simulations of realistic systems. The remainder of this chapter discusses these modeling challenges in additional detail before laying out objectives to overcome them, dictating the structure of this dissertation.

## 1.1 Asymptotic Combustion Modes

Turbulent combustion modeling efforts are further complicated by the existence of three different asymptotic behaviors or ‘modes’ that combustion exhibits based on the local relative importance of chemical reaction and transport. Two of these modes are flames – thin regions in physical space where both chemical reaction and transport are tightly-coupled – and are further subdivided based on the initial distribution of fuel and oxidizer. The three combustion modes are delineated according to the following:

- *Homogeneous Autoignition*: Occurs where only chemical reaction is present in the limit of zero transport (that is, all spatial gradients are zero). This corresponds to a homogeneous premixture of fuel and oxidizer that reacts uniformly to produce heat and product species.
- *Nonpremixed Combustion*: The particular class of flames for which the fuel and oxidizer are initially separated in physical space. Since chemical reactions require mixing of fuel

and oxidizer on a molecular scale for collisions to occur, turbulent nonpremixed flames are often predominantly controlled by turbulent mixing [9].

- *Premixed Combustion:* Flames that instead burn as a reacting front, propagating into an unburned premixture of fuel and oxidizer and leaving behind a burned mixture of high-temperature product species. Important quantities of interest in premixed combustion, such as the flame thickness  $\delta_F$  and laminar flame speed  $s_L$ , are often highly sensitive to the chemistry model and thermochemical conditions [10].

Practical systems operate in combustion regimes that are inherently multi-modal – they cannot be characterized by any of the single asymptotic limits alone, whether it be homogeneous autoignition, nonpremixed, or premixed combustion. Furthermore, emerging combustion technologies often involve additional complexities including multiple inlet streams, such as oxidizer, fuel, and exhaust gas recirculation (EGR) [11]; inhomogeneous inlet streams, such as those with partially premixed fuel vapor from vaporizing liquid fuel sprays; and staged combustion, as in rich-quench-lean (RQL) gas turbine combustors [12] or multi-injection diesel engines [13]. Current computationally efficient modeling approaches face significant obstacles in multi-modal combustion regimes and require further generalization to handle these additional complexities.

## 1.2 Simulation of Turbulent Combustion

The goal of computationally simulating turbulent combustion is often to aid in the development of practical engineering devices by predicting thermochemical quantities of interest, such as temperature and pollutant concentrations, across a range of design conditions. However, simulating these quantities of interest at a reasonable computational cost poses a considerable modeling challenge.

### 1.2.1 Thermochemical State

The set of all possible thermochemical quantities of interest – including enthalpy, entropy, internal energy, density, and so on – is referred to as the thermochemical state and can be represented mathematically according to

$$\phi \equiv \{h, s, e, \rho, \dots, T, P\} , \quad (1.1)$$

where  $h$  is the specific enthalpy,  $s$  is the specific entropy,  $e$  is the specific internal energy,  $\rho$  is the density,  $T$  is the temperature, and  $P$  is the pressure. The entire thermochemical state of a *single-component* ideal gas can be reconstructed from any two intensive properties. This can be expressed mathematically according to

$$\phi = \phi(T, P) , \quad (1.2)$$

where temperature and pressure are used as examples, though any two intensive properties would be appropriate.

This concept is generalized for a *multi-component* ideal gas composed of many reacting chemical species (i.e. flows relevant to combustion simulations) by introducing an additional dependence on the local chemical composition, comprising a set of species mass fractions  $\{Y_k\}_{k=1}^n$  with  $n$  denoting the total number of chemical species. Each species mass fraction  $Y_k$  is defined as the fraction of the total mass attributed to chemical species  $k$ . With this modification, the dependence of the thermochemical state for a *multi-component* ideal gas is instead expressed as

$$\phi = \phi(Y_k, \dots, Y_n, T, P) . \quad (1.3)$$

The additional dependence of the thermochemical state on the composition introduces considerable additional computational cost in combustion simulations, as the number of chemical species can be  $\mathcal{O}(10^2)$  to  $\mathcal{O}(10^3)$  for realistic transportation fuels [14], and each chemical



species must be accounted for by solving a corresponding transport equation, unless modeled otherwise. These governing transport equations constitute partial differential equations describing the spatiotemporal evolution of thermochemical scalars and are outlined in detail in Chapter 2.

### 1.2.2 Chemical Kinetics Modeling

The global single-step reaction that describes the conversion of fuel and oxidizer to heat and product species ( $\text{C}_a\text{H}_b + [a + \frac{b}{4}] \text{O}_2 \rightarrow a\text{CO}_2 + \frac{b}{2}\text{H}_2\text{O}$ , for complete combustion of a general hydrocarbon fuel) actually occurs on a molecular scale as a complicated network of elementary reactions between reactants, products, and intermediate chemical species. An *ideal* detailed chemical kinetic model, called a chemical mechanism, would account for every single possible intermediate chemical species and reaction. However, a fuel that involves  $\mathcal{O}(10^3)$  chemical species would possess *at least*  $\mathcal{O}(10^5)$  possible two-body reactions – an overwhelming number without even considering the possibility of the same two chemical species reacting to form different products or the existence of activated internal energy states and three-body reactions – yet the vast majority of these reactions are not important to the dynamics of the chemistry due to very long relative time scales. Instead of accounting for every possible elementary reaction, only reactions and chemical species that impact important thermochemical quantities are included in chemical mechanisms. These simplified chemical mechanisms are referred to as skeletal chemical mechanisms (described in more detail in Chapter 2). Skeletal chemical mechanisms with minimal reduction of species and reactions are often referred to as detailed chemical mechanisms, though it is worth noting that all chemical mechanisms involve some degree of simplification.

One method of approaching the challenge posed by the high-dimensionality of the thermochemical state involves reducing the number of transported chemical species. This reduction can be accomplished by introducing additional simplifying assumptions that further reduce the number of reactions and intermediate chemical species involved in skeletal chemical mech-

anisms, forming reduced skeletal mechanisms that approximate the predictions of important thermochemical quantities of interest produced by larger skeletal mechanisms. Simplifying approaches such as Computational Singular Perturbation (CSP) [15] and Directed Relation Graphs (DRG) [16, 17] can reduce the number of transported species for large hydrocarbon fuels to  $\mathcal{O}(10^1)$ , though transporting even that many species remains computationally expensive. Moreover, this reduction comes at a cost – reduced skeletal mechanisms are only applicable over a narrow range of thermochemical conditions, including temperature, pressure, and fuel/oxidizer composition. Further reduction of skeletal mechanisms introduces additional assumptions and narrower thermochemical ranges of applicability. Recent efforts to instead dynamically select the appropriate reduced skeletal mechanism based on the local thermochemical conditions have enabled the replacement of a single reduced skeletal mechanism with several heavily reduced skeletal mechanisms, decreasing the number of transported species [18]. However, generating additional reduced skeletal mechanisms is often a laborious process that requires hand-tuning [19], introducing additional complexities and motivating the development of alternative model reduction approaches.

### 1.2.3 Manifold Modeling

Rather than directly solving a transport equation for every relevant chemical species in a simulation, the dimensionality of the unresolved combustion processes can be significantly reduced by using a reduced-order manifold. This approach characterizes the underlying combustion process with far fewer variables by projecting the high-dimensional thermochemical state space onto a low-dimensional space of manifold variables. Mathematically, the thermochemical state  $\phi$  can be reparameterized in terms of a general space of manifold variables  $\Omega$  according to

$$\begin{aligned} \phi(\mathbf{x}, t) &= \phi(Y_k[\mathbf{x}, t], \dots, Y_n[\mathbf{x}, t], T[\mathbf{x}, t], P) \\ &\quad \downarrow \mathcal{M} \\ \phi(\mathbf{x}, t) &\approx \phi_{\mathcal{M}}(\Omega_1[\mathbf{x}, t], \dots, \Omega_m[\mathbf{x}, t]) \ , \end{aligned} \tag{1.4}$$

where  $\mathcal{M}$  denotes the transformation to manifold variable space,  $\phi_{\mathcal{M}}$  denotes the manifold mapping, and  $m \ll n$ . This approach is considerably more computationally efficient since evaluating the thermochemical state only requires that  $m$  manifold variables be transported in a flow solver, compared to  $n$  chemical species and an energy variable.

The relevant space of manifold variables  $\Omega$  is selected differently depending on the particular manifold model. Data-based manifold models involve selecting the manifold variables via principal components analysis (PCA) and transporting the principal components (PCs) instead of the species mass fractions [20, 21, 22, 23]. Nonlinear alternatives to PCA have also been explored, including isometric mapping and multivariate adaptive spline regression, though these approaches are more challenging to implement in an LES [24, 25]. Physics-based manifold models instead select the set of manifold variables based on physical reasoning specific to the combustion problem at hand. The remainder of this work focuses on physics-based manifold approaches as they possess a reduced dependence on data.

One method of defining the manifold mapping  $\phi_{\mathcal{M}}$  is through differential equations for the thermochemical state in terms of the manifold variables, hereafter referred to as *manifold equations*. The independent variables in these manifold equations will be referred to as *manifold coordinates* (typically a mixture fraction  $Z$  and/or a progress variable  $\Lambda$ ), while additional coefficients that appear in the manifold equations will be referred to as *manifold parameters* (typically dissipation rates  $\chi_{\psi\omega}$  in terms of general manifold coordinates  $\psi$  and  $\omega$ ). In turbulent combustion simulations, transport equations are evolved or algebraic relationships are evaluated for the manifold variables, and the thermochemical state is determined from solutions to the manifold equations. As commonly implemented, solutions to the manifold equations are precomputed and pretabulated against the manifold variables.

Physics-based manifolds are typically constructed by making *a priori* assumptions about the nature of the combustion processes, namely that they occur in the limit of a single asymptotic mode of combustion, either nonpremixed combustion, premixed combustion, or homogeneous autoignition. The steady flamelet model [26] is a notable example of a single-

mode manifold model applicable to nonpremixed combustion and is discussed in more detail in Chapter 3. Extensions of the steady flamelet model to nonpremixed combustion with extinction and reignition include the unsteady flamelet model [27] and the Flamelet/Progress Variable (FPV) approach [28]. Examples of single-mode manifold models applicable to premixed combustion include Flamelet Generated Manifolds (FGM) [29] and Flamelet Progression of Intrinsically low-dimensional manifolds (FPI) [30], both of which involve approximating the flame structure of a three-dimensional turbulent premixed flame with the solution to a component problem of a laminar premixed freely-propagating flat flame.

Though physics-based manifold models have traditionally been developed for two-stream, isobaric, adiabatic, single-mode combustion, theoretical physics-based manifold models applicable to more complex combustion physics already exist, including: multiple and/or inhomogeneous stream mixing [31, 32, 33], pressure variation [34], heat losses [35, 36], and multi-modal combustion [37, 38]. However, these more general manifold models possess higher-dimensional manifolds, posing a challenge to conventional approaches that rely on precomputation and pretabulation of the manifold solutions. Not only are higher-dimensional manifold solutions more computationally expensive to obtain, but the manifold solutions also span a higher-dimensional space, meaning far more memory is required to store a precomputed thermochemical database even though many of these solutions are never ultimately needed in a simulation. Some efforts have focused on using either parallel computing [39, 40] or alternative data structures [41, 42] to at least partially mitigate the memory requirement issue, but these approaches still rely on precomputation of a large number of potentially unneeded manifold solutions. Until recently, additional manifold solutions and memory requirements rendered more general, higher-dimensional manifold models intractable for simulations of practical systems. However, a new algorithm for manifold modeling called In-Situ Adaptive Manifolds (ISAM) [43] overcomes these obstacles by computing solutions to the manifold equations as the simulation proceeds and storing the thermochemical state for later reuse with In-Situ Adaptive Tabulation (ISAT) [44].

This dissertation is preoccupied in particular with multi-modal turbulent combustion modeling. There are two broad classes of manifold modeling approaches for multi-modal combustion: mode-switching approaches and nonlinear approaches. Mode-switching approaches model multi-modal behavior as a linear combination of single-mode model predictions, though they often suffer due to the highly nonlinear nature of turbulent combustion physics [45, 46]. Nonlinear approaches aim to model the nonlinear coupling between combustion modes directly, often by projecting the dependence of the thermochemical state onto both a mixture fraction and a progress variable [37, 38, 47]. However, until recently, application of these two-dimensional manifold equations has been limited to “representative” manifolds, for which only a few or even a single thermochemical state is used at all points in space and time in a flow solver domain [47, 48, 49] – an approximation that is not appropriate in general. The model proposed by Mueller [38] allows for the thermochemical state to be uniquely defined at all points in space and time, providing considerable additional generality. Therefore, a considerable portion of the work outlined in this thesis is concerned with enabling and further developing this modeling approach.

### 1.2.4 Turbulence Modeling

In addition to the wide range of length and time scales relevant to combustion, turbulence introduces additional length and time scales spanning from the largest energy-containing scales (integral length scale  $l_0$ , often set by the configuration geometry) down to the smallest scales at which the kinetic energy of the turbulent motions is dissipated as heat due to viscosity (Kolmogorov length scale  $\eta$ ). The most theoretically straightforward approach to simulating turbulent flows is called Direct Numerical Simulation (DNS) and involves directly resolving all length and time scales of the turbulent structures with an appropriately fine computational grid. However, the range of turbulent length scales relevant to a particular flow increases with increasing Reynolds number according to  $Re^{3/4}$ , meaning larger Reynolds number flows possess smaller vortical structures to be resolved (for a fixed integral length

scale) and require a larger number of computational grid points. Additionally, the simulation time step is restricted by the Courant-Friedrichs-Lewy (CFL) number, so that the overall computational cost of DNS scales with  $Re^3$ . Current DNS of turbulent reacting flows are limited to  $Re \approx \mathcal{O}(10^4)$  [50, 51], though realistic engineering devices often operate at  $Re \approx \mathcal{O}(10^4) - \mathcal{O}(10^8)$  [52]. DNS therefore requires an improvement to computational hardware of as much as a factor of *one trillion* before it offers a feasible approach for simulating the fully resolved thermochemical state  $\phi$  in all real-world devices. In the meantime, DNS remains a largely academic tool, providing both fundamental physical insights and rich sources of data invaluable for model development.

Rather than resolving all turbulent length and time scales with a very fine computational grid, it is more common in industry applications to instead simulate flow domains with a coarser computational grid and model the unresolved length scales with coarse-grained approaches such as Reynolds-Averaged Navier-Stokes (RANS) or Large Eddy Simulation (LES). RANS is the more computationally efficient approach and involves averaging over an ensemble of flow realizations along a statistically stationary coordinate (physical space, time, or multiple simulations). Applying this averaging operation to the governing transport equations yields unclosed turbulent transport terms that impact the mean flow, such as the Reynolds stress and the turbulent scalar flux. In RANS, these quantities are *modeled at all scales*, even the largest anisotropic scales at which the turbulent behavior is highly configuration-dependent. As a result, the predictive capabilities of even the most ubiquitous RANS models, such as the  $k - \epsilon$  and  $k - \omega$  models [53], often depend on error cancellation in even canonical flows [54].

As opposed to an ensemble average, LES involves spatial filtering of the governing transport equations, resulting in predictions for the filtered thermochemical state  $\overline{\phi}$ . In density-varying flows, density-weighted (Favre) filtering is more convenient and is typically denoted by  $\tilde{\phi}$ . Unlike RANS, in LES the transported filtered quantities can be interpreted as the resolved part of corresponding DNS fields. Unclosed turbulent transport terms in LES are

instead referred to as the subfilter stress and subfilter scalar flux, representing the contribution of the unresolved subfilter scales on the resolved velocity and scalar fields, respectively. LES involves *resolving the large scales* and *modeling the small scales*, formulating models for the unclosed turbulent transport terms based on the hypothesis of scale similarity within the inertial subrange – a range of length scales between the integral and Kolmogorov length scales in which turbulence is isotropic and independent of configuration-specific length scales and the molecular viscosity. In configurations that possess an inertial subrange, the scale similarity hypothesis can be correctly applied with an appropriately chosen grid resolution. Though computational grids for LES incur a higher computational cost than RANS, LES is considerably more accurate than RANS while also remaining significantly less computationally expensive than DNS. LES also resolves time-dependent dynamic information that would otherwise be lost in RANS and is critically important to unsteady combustion devices. For these reasons, the remainder of the work in this dissertation will be presented in the context of LES, though the ideas could easily be extended to RANS with minimal modification.

### 1.2.5 Filtered Chemical Source Term Modeling

In addition to the subfilter turbulent transport terms already mentioned, LES of reacting flows also requires the closure of filtered variables  $\tilde{\varphi}$  with known nonlinear functional dependence on the thermochemical state  $\phi$ , such that  $\varphi(\phi)$ . These variables include the filtered chemical source terms  $\overline{\dot{m}_k}$  that appear in transport equations for filtered reactive scalars (discussed in more detail in Chapter 2) as well as the filtered density  $\bar{\rho}$  and filtered molecular diffusivities  $\tilde{D}_{\phi_k}$ . In particular, appropriately modeling the chemical source terms is a considerable challenge, as they encode the complex coupling of turbulence and chemical reaction on the unresolved subfilter scales. Naive first-order closure approaches that presume  $\widetilde{\varphi(\phi)} \approx \varphi(\tilde{\phi})$  are inaccurate even at small filter sizes. This is due to the fact that the thermochemical state can vary appreciably on the subfilter scale in regions around a flame,

and chemical source terms are generally especially sensitive to the thermochemical state in highly nonlinear combustion reactions.

A common approach for providing closure for this special class of filtered variables  $\tilde{\varphi}$  is via a subfilter probability density function (PDF)  $\tilde{P}$  that accounts for the variation of the thermochemical state  $\phi$  on the subfilter scale. An estimate of  $\tilde{\phi}$  can be formed as a local average of  $\phi$ , weighted by how often it takes a particular value at the unresolved scale. In the most general case, this local average comprises a convolution in thermochemical state space given by

$$\tilde{\phi} = \int \phi \tilde{P}(\phi) d\phi. \quad (1.5)$$

These PDF-based approaches are classified by the method used to attain PDF closure. Modeling the PDF in Eq. 1.5 with an algebraic expression would be exceedingly difficult due to the high dimensionality of the thermochemical state, so it is often directly transported in physical space, time, and thermochemical state space. This particular modeling approach constitutes the transported PDF (TPDF) model [55], a general method for modeling turbulent combustion that is unfortunately burdened by large computational cost and difficulties associated with modeling unresolved mixing using only local information [56].

Alternatively, when the thermochemical state is projected onto a low-dimensional manifold, Eq. 1.5 is modified according to

$$\tilde{\phi} = \int \phi(\Omega) \tilde{P}(\Omega) d\Omega. \quad (1.6)$$

Since  $\Omega$  represents a low-dimensional manifold space, providing algebraic closure for the PDF  $\tilde{P}(\Omega)$  becomes feasible [57, 58]. In this sense, projecting the thermochemical state onto a low-dimensional manifold not only reduces the computational cost associated with transporting many chemical species, but also makes the PDF easier to model. These low-dimensional manifold approaches are further subclassified based on the method used to obtain the unfiltered thermochemical state  $\phi(\Omega)$ . The first subclass constitutes a *non-equilibrium manifold*



*model* that involves conditioning the thermochemical state on one or more manifold variables. Note that the term ‘non-equilibrium’ in this context does not refer to thermodynamic non-equilibrium but rather indicates that the thermochemical state *conditioned on a particular choice of phase space variable or variables* depends on history effects encoded in non-negligible spatial and temporal partial derivatives. Non-equilibrium manifold models constitute a particular class of *presumed* subfilter PDF approaches including the Conditional Moment Closure (CMC) approach for nonpremixed combustion [59] and its extension to premixed combustion [60]. A generalization of the CMC concept to higher-dimensional manifolds, the Multiple Mapping Conditioning (MMC) approach [61, 62] also involves projecting the thermochemical state onto a low-dimensional manifold. However, MMC instead involves explicitly transporting the subfilter PDF, placing it somewhere between the TPDF and CMC approaches. Both CMC and MMC involve solving costly transport equations for conditional quantities in physical space, time, and phase space, though MMC involves a similar Lagrangian particle approach as the TPDF model. Even though MMC can theoretically overcome the single-mode assumptions of CMC by conditioning on multiple variables, such an approach would require appreciable computational cost for practical applications.

*Equilibrium manifold models* (such as the steady flamelet model [26]) constitute a second subclass of presumed subfilter PDF model that involves further reducing computational cost by computing the unfiltered thermochemical state  $\phi(\Omega)$  as the solution to a simpler set of equilibrium manifold equations rather than a set of non-equilibrium manifold equations. In contrast, the equilibrium manifold equations presume that the thermochemical state *conditioned on a particular choice of phase space variable or variables* instantaneously ‘equilibrates’ to the local flow conditions and is independent of history effects – an assumption that is appropriate when the time scales associated with changes in the manifold parameters are large relative to relevant chemical time scales. The focus of this work is directed toward equilibrium manifold modeling approaches, which are far more computationally efficient than TPDF, CMC, and MMC approaches, but are traditionally constrained by single-mode man-

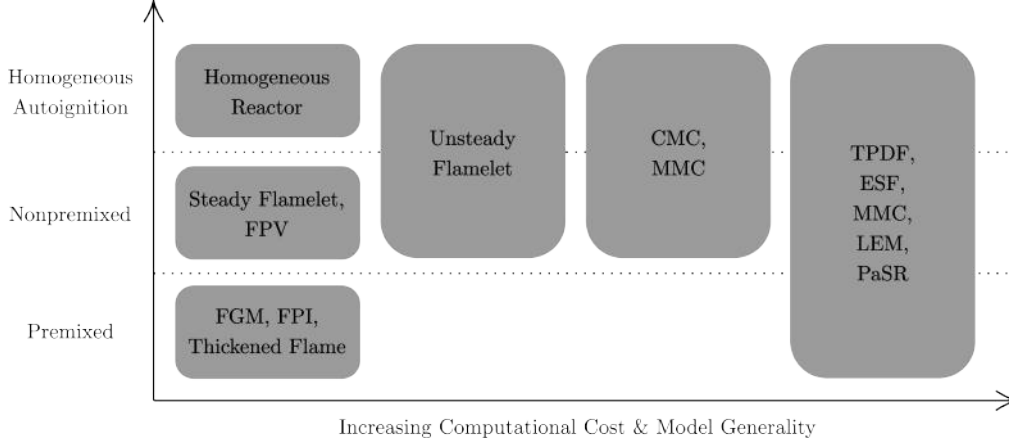


Figure 1.1: Comparison of traditional turbulent combustion modeling approaches and their associated regimes of applicability. Models further to the left are less computationally expensive and less general, while models further to the right are more computationally expensive and more general.

ifold assumptions. Extending these approaches beyond single-mode manifold models offers a pathway forward for formulating a turbulent combustion model that offers both the computational efficiency of a presumed subfilter PDF manifold model and the generality of the TPDF approach.

Additional turbulent combustion modeling approaches that provide subfilter closure include the Linear Eddy Model (LEM) [63] and partially stirred reactor (PaSR) model [64, 65]. Though these approaches circumvent directly modeling a PDF, they still share many of the shortcomings of TPDF models. The Eulerian Stochastic Fields (ESF) model [66] offers a modified implementation of the TPDF approach but also faces similar challenges. Alternatively, thickened flame models [67] seek to forego providing subfilter closure entirely by artificially thickening flames up to a length scale resolvable by the computational grid, without modifying the flame speed. The result is a modeling approach applicable only to premixed combustion that fundamentally cannot produce accurate flame structure predictions, an important model capability for simulation of pollutant formation. The traditional turbulent combustion models discussed in this chapter are summarized in Fig. 1.1.

### 1.3 Augmenting Physics-Based Models with Data

Consider a physics-based manifold model for which the unfiltered thermochemical state is modeled according to

$$\phi \approx \phi_{\mathcal{M}}(\Omega[\mathbf{x}, t]) , \quad (1.7)$$

where the manifold variables may in general vary on resolved space and time scales. Thermochemical information is lost when the manifold parameters are modeled as a function of the manifold coordinates – a necessary step to provide closure for the manifold equations. This idea can be expressed mathematically according to

$$\phi \approx \phi_{\mathcal{M}}(\Omega_c, \Omega_p[\Omega_c; \mathbf{x}, t]) , \quad (1.8)$$

where  $\Omega_c$  is the space of  $m_c$  manifold coordinates and  $\Omega_p$  is the space of  $m_p$  manifold parameters, with  $m = m_c + m_p$ . In coarse-grained simulations such as LES, models for the manifold parameters in terms of the manifold coordinates encode the unresolved physical coupling of combustion and turbulence and are critical for accurate prediction of the thermochemical state. Though several physics-based manifold parameter models already exist, they are limited to the single-modes of nonpremixed [68] or premixed combustion [37]. Moreover, existing physics-based manifold parameter models are implicitly developed to capture the manifold parameter dependence on the manifold coordinates in a conditionally averaged sense rather than the localized, instantaneous dependence. Additional efforts are needed to account for the spatiotemporal variation of manifold parameter closure in single-mode manifold models as well as to provide manifold parameter closure in the context of multi-modal combustion, for which physics-based manifold parameter models have yet to be validated for turbulent configurations [69].

For cases in which the fundamental physics are either unknown or too complex to compute directly (i.e. turbulent combustion), physics-based modeling is often eschewed in favor of data-based modeling in which large data sets are leveraged to instead ‘learn’ auxiliary

relationships via a trained machine learning model. However, data-based models suffer from several significant shortcomings. Data-based models often discard known physics and are typically unaware of physical constraints. Since training data is finite, data-based models must be generalizable beyond the training data, but, without these physical constraints, data-based models can lead to erroneous predictions when applied in regimes outside the training data. For these reasons, directly modeling the thermochemical state via a data-based approach does not guarantee the correct reconstruction of thermodynamic limits.

Rather than directly modeling the thermochemical state, it is more reasonable to adopt an indirect approach, only using data to provide manifold parameter closure. Such an approach leverages the physical constraints already embedded into physics-based manifold models, reducing the information needed to be ‘learned’ from data, increasing the model generalizability, and guaranteeing that thermodynamic limits are satisfied. This modeling approach is referred to as a *hybrid* physics- and data-based modeling approach, and will be leveraged for a simple single-mode manifold model for premixed combustion as well as to provide model closure for the multi-modal manifold model [38].

## 1.4 Contributions and Organization

The overall objective of this dissertation is to break the long-standing trade-off between computational efficiency and model generality in existing computational models of turbulent combustion. This overall objective is loosely divided into three sub-objectives:

- *Sub-Objective 1*: Develop a new computational algorithm that enables more general, higher-dimensional (but traditionally intractable) manifold models and test the performance of the algorithm on a simple single-mode model.
- *Sub-Objective 2*: Extend the algorithm to more general models (i.e. multiple and/or inhomogeneous inlet streams, multi-modal combustion).

- *Sub-Objective 3*: Provide instantaneous manifold parameter closure for the multi-modal manifold equations with a hybrid data-based and physics-based approach.

The work encompassed by this dissertation comprises the following chapters and corresponding articles and presentations. Chapter 2 offers an exception, presenting the three-dimensional governing transport equations for turbulent combustion and extending the equations to LES.

In Chapter 3, a novel algorithm for manifold modeling of turbulent combustion called In-Situ Adaptive Manifolds (ISAM) is developed to enable more general, higher-dimensional manifold models capable of capturing multi-physics behavior present in complex turbulent reacting flows. The performance of ISAM is evaluated relative to traditional pretabulation approaches via LES of turbulent nonpremixed flames and a one-dimensional manifold model. [C. E. Lacey, A. G. Novoselov, M. E. Mueller, In-Situ Adaptive Manifolds: Enabling computationally efficient simulations of complex turbulent reacting flows, *Proceedings of the Combustion Institute* **38** (2021) 2673-2680] [43]

In Chapter 4, performance improvements made to the ISAM approach are discussed, and the method is extended to a configuration with multiple and/or inhomogeneous inlet streams. In particular, the sensitivity of the thermochemical state to different ISAM input parameters is assessed. [C. E. Lacey, M. E. Mueller, Large Eddy Simulations of turbulent flames with multiple and/or inhomogeneous inlets using In-Situ Adaptive Manifolds, *12th U.S. National Combustion Meeting*, College Station, TX, May 24-26, 2021]

In Chapter 5, the ISAM approach is leveraged to enable a more general manifold model applicable to multi-modal turbulent combustion, which would otherwise be intractable using traditional pretabulation approaches. A turbulent, lifted flame configuration is simulated in LES, and the feasibility and interpretability of the multi-modal manifold modeling approach are evaluated. [A. G. Novoselov, C. E. Lacey, B. A. Perry, M. E. Mueller, Large Eddy Simulation of a turbulent lifted flame using multi-modal manifold-based models: Feasibility and interpretability, *Proceedings of the Combustion Institute* **38** (2021) 2581-2588] [70]

(Note: Contribution to this work included the development and implementation of the ISAM approach for the multi-modal manifold model and aiding in the analysis of LES results.)

In Chapter 6, a physics-based manifold model applicable to turbulent premixed combustion is augmented with data, and the instantaneous conditional progress variable dissipation rate profiles are modeled using a deep neural network. The data-based model is evaluated *a priori* via solutions to one-dimensional premixed manifold equations in progress variable, demonstrating an improvement over traditional models based on the conditional mean profiles. A variable importance study is conducted via both data-based and physics-based approaches. [C. E. Lacey, S. Sundaresan, M. E. Mueller, Data-based instantaneous conditional progress variable dissipation rate modeling for turbulent premixed combustion, *Combustion and Flame* (2023) submitted] [71]

In Chapter 7, a physics-based manifold model applicable to turbulent multi-modal combustion is augmented with data, providing model closure for the three scalar dissipation rates that parameterize the solutions to the manifold equations. First, closure for the filtered dissipation rates is achieved via deep neural networks, the predictive performance of which is compared to algebraic models. Multiple regression methods are investigated for generating structured training labels corresponding to the instantaneous shape of the dissipation rate and alignment profiles from unstructured data, and data-based models for the dissipation rates are evaluated *a priori* via solutions to two-dimensional multi-modal manifold equations in mixture fraction and generalized progress variable. [C. E. Lacey, M. Rieth, J. H. Chen, M. E. Mueller, Deep learning model for the instantaneous dissipation rate profiles in multi-modal turbulent combustion, *13th U.S. National Combustion Meeting*, College Station, TX, March 19-22, 2023]

In Chapter 8, a systematic approach for input feature selection during deep neural network training is developed based on the Buckingham Pi Theorem, using the filtered progress variable dissipation rate as a test quantity of interest. The performance of a deep neural network trained with a set of dimensional input features is compared to one trained with

fewer dimensionally-homogeneous input features. The physics-based dimensionality reduction approach is then compared to linear PCA-based approaches for the same number of input features. [C. E. Lacey, G. D'Alessio, S. Sundaresan, M. E. Mueller, Physics-based dimensionality reduction and deep learning model for the progress variable dissipation rate in turbulent premixed combustion, *18th International Conference on Numerical Combustion*, San Diego, CA, May 8-11, 2022]

In Chapter 9, overall conclusions are presented, and suggestions and directions for future work are discussed.

# Chapter 2

## Governing Equations

Before presenting the novel contributions of this dissertation, it is useful to first establish a clear mathematical description of the equations governing turbulent combustion simulations as well as the fundamentals of data-based modeling. This chapter describes the governing transport equations fundamental to low Mach number reacting flows and their extension to coarse-grained simulations such as LES. The manifold equations derived in Chapter 3, Chapter 5, and Chapter 6 are derived from these governing transport equations, and the details of LES closure models presented here are leveraged throughout Chapter 3, Chapter 4, and Chapter 5. This chapter concludes with a brief overview of the data-based modeling approaches leveraged in this dissertation.

### 2.1 Transport Equations

Directly computing the thermochemical state  $\phi$  in a turbulent combustion DNS requires explicitly solving the three-dimensional governing transport equations for mass, momentum, temperature (or another energy variable), and species, in conjunction with an equation of state. For low Mach number flows ( $Ma < 0.3$ ), the pressure can be expanded in terms of thermodynamic (zeroth-order), hydrodynamic (first-order), and higher-order pressures, using  $\epsilon = Ma^2$  as a small expansion parameter [10]. Applying the same expansion procedure



to the governing equations and canceling higher-order terms yields the governing transport equations for a multi-component reacting flow at low Mach number given by

$$\frac{\partial \rho}{\partial t} + \frac{\partial \rho u_j}{\partial x_j} = 0, \quad (2.1)$$

$$\frac{\partial \rho u_i}{\partial t} + \frac{\partial \rho u_j u_i}{\partial x_j} = -\frac{\partial p_1}{\partial x_i} + \frac{\partial \tau_{ij}}{\partial x_j} + \rho g_i, \quad (2.2)$$

$$\begin{aligned} \frac{\partial \rho T}{\partial t} + \frac{\partial \rho u_j T}{\partial x_j} = & \frac{1}{c_p} \frac{\partial}{\partial x_j} \left( \lambda \frac{\partial T}{\partial x_j} \right) - \sum_k \frac{c_{p,k}}{c_p} \rho Y_k V_{k,j} \frac{\partial T}{\partial x_j} \\ & - \sum_k \frac{h_k}{c_p} \dot{m}_k + \frac{1}{c_p} \frac{dp_0}{dt} + \frac{\dot{Q}}{c_p}, \end{aligned} \quad (2.3)$$

$$\frac{\partial \rho Y_k}{\partial t} + \frac{\partial \rho u_j Y_k}{\partial x_j} = -\frac{\partial}{\partial x_j} (\rho Y_k V_{k,j}) + \dot{m}_k, \quad (2.4)$$

$$p_0 = \rho \hat{R} T \sum_k \frac{Y_k}{W_k}, \quad (2.5)$$

where  $u_i$  is the velocity component in the direction  $i$ ,  $\dot{m}_k$  is the chemical source term of chemical species  $k$ ,  $p_0$  is the thermodynamic pressure,  $p_1$  is the hydrodynamic pressure,  $\tau_{ij}$  is the viscous stress tensor,  $\dot{Q}$  is a volumetric heat loss,  $\lambda$  is the mixture thermal conductivity,  $c_p$  is the mixture specific heat,  $c_{p,k}$  is the specific heat of chemical species  $k$ ,  $V_{k,j}$  is the diffusion velocity of species  $k$ ,  $W_k$  is the molar mass of species  $k$ , and  $\hat{R}$  is the universal gas constant. The thermodynamic pressure  $p_0$  is constant in physical space, while the hydrodynamic pressure  $p_1$  varies spatially to enforce mass conservation via the solution of a pressure Poisson equation. Equations 2.1 - 2.5 are referred to as the continuity equation, momentum transport equation, temperature transport equation, species transport equation for species  $k$ , and equation of state for a multi-component ideal gas, respectively.

The last two terms in Eq. 2.3 can be neglected for isobaric, adiabatic flows. Presuming the absence of body-forces and second-order effects, the species diffusion velocities in Eq.

2.3 and Eq. 2.4 can be simplified according to the Curtiss-Hirschfelder approximation [72]:

$$V_{k,j} = -\frac{1}{X_k} D_k \frac{\partial X_k}{\partial x_j} + V_{c,j} , \quad (2.6)$$

where  $X_k$  is the mole fraction of species  $k$ ,  $D_k$  is the molecular diffusivity of species  $k$ , and  $V_{c,j}$  is a correction velocity that ensures mass conservation, defined according to

$$V_{c,j} = \sum_{k=1}^{N_s} \frac{Y_k}{X_k} D_k \frac{\partial X_k}{\partial x_j} , \quad (2.7)$$

where  $N_s$  is the number of chemical species (for brevity,  $\sum_{k=1}^{N_s}$  is written as  $\sum_k$  in transport equations). Molecular transport coefficients are often negligibly small relative to turbulent transport coefficients in large Reynolds number flows. For these predominant cases, it is appropriate to assume that temperature and every chemical species have equal molecular diffusivities such that  $\frac{\lambda}{\rho c_p} = D_k \equiv D$  [73, 74]. This is referred to as the unity effective Lewis number approximation (since  $Le_k \equiv \frac{\lambda}{\rho c_p D_k}$ ), and simplifies the expression for the species diffusion velocities to  $V_{k,j} = -D \frac{1}{Y_k} \frac{\partial Y_k}{\partial x_j}$ . Plugging this simplified expression into the transport equations for the temperature and species mass fractions in physical space and time yields

$$\frac{\partial \rho T}{\partial t} + \frac{\partial \rho u_j T}{\partial x_j} = \frac{\partial}{\partial x_j} \left( \frac{\lambda}{c_p} \frac{\partial T}{\partial x_j} \right) + \frac{\lambda}{c_p^2} \frac{\partial c_p}{\partial x_j} \frac{\partial T}{\partial x_j} + \sum_k \frac{c_{p,k}}{c_p} \rho D \frac{\partial Y_k}{\partial x_j} \frac{\partial T}{\partial x_j} - \sum_k \frac{h_k}{c_p} \dot{m}_k , \quad (2.8)$$

$$\frac{\partial \rho Y_k}{\partial t} + \frac{\partial \rho u_j Y_k}{\partial x_j} = \frac{\partial}{\partial x_j} \left( \rho D \frac{\partial Y_k}{\partial x_j} \right) + \dot{m}_k . \quad (2.9)$$

These simplified temperature and species transport equations constitute the starting point for deriving unity effective Lewis number manifold equations for use in LES where the unity effective Lewis number approximation is typically appropriate.

Even at large Reynolds numbers, the unity effective Lewis number approximation does not necessarily hold in low Karlovitz number ( $Ka \equiv \frac{\delta_F^2}{\eta^2}$ ) turbulent premixed flames in which

the flame length scale  $\delta_F$  is small relative to the Kolmogorov length scale  $\eta$ . Under these particular conditions, turbulent eddies are too large to penetrate the flame structure. Therefore, molecular transport becomes non-negligible relative to turbulent transport, and differential molecular diffusion is no longer suppressed by the indiscriminate action of turbulent mixing. In the presence of appreciable differential diffusion effects, flame curvature sometimes produces super-adiabatic flame regions and localized flame extinction where the relative transport of heat and radical species leads to an amplification or suppression of chemical reaction, respectively. Previous work has shown that molecular transport can still play an important role for combustion of highly diffusive fuels such as hydrogen and weakly diffusive fuels such as *n*-heptane up to a higher Karlovitz number threshold [75, 76]. Though the unity effective Lewis number approximation is not universally appropriate, it is applicable to the configurations presented in this dissertation. Note that the algorithm and modeling efforts detailed in this dissertation are developed independent of the unity effective Lewis number approximation, so they may easily be extended to non-unity Lewis number manifold equation formulations [38].

For a Newtonian fluid, the viscous stress tensor  $\tau_{ij}$  in Eq. 2.2 is modeled linearly with respect to the symmetric part of the velocity gradient. In variable-density flows, it is consistent with the low Mach number approximation to invoke Stokes' hypothesis [77] ( $\mu'' \frac{\partial u_k}{\partial x_k} \delta_{ij} = 0$ , where  $\mu''$  is the mixture bulk viscosity), simplifying the constitutive relationship for the viscous stress tensor to

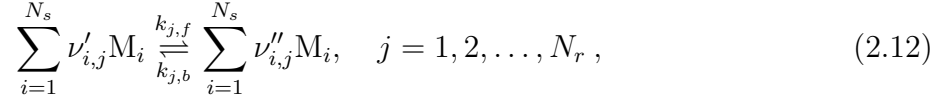
$$\tau_{ij} = 2\rho\nu \left( S_{ij} - \frac{1}{3} S_{kk} \delta_{ij} \right), \quad (2.10)$$

where  $\nu$  is the mixture kinematic viscosity (related to the mixture dynamic viscosity  $\mu$  according to  $\nu = \frac{\mu}{\rho}$ ),  $\delta_{ij}$  is the Kronecker delta, and  $S_{ij}$  is the strain rate tensor given by

$$S_{ij} = \frac{1}{2} \left( \frac{\partial u_i}{\partial x_j} + \frac{\partial u_j}{\partial x_i} \right). \quad (2.11)$$

## 2.2 Chemical Source Terms

Closure of Eq. 2.8 and Eq. 2.9 depends on evaluation of the chemical source terms  $\dot{m}_k$ , which are obtained via a chemical mechanism – a simplified model of dominant elementary reactions between important chemical species. The complex network of  $N_r$  elementary reactions between  $N_s$  chemical species in a chemical mechanism can be represented in general by



where  $M_i$  is the chemical formula of species  $i$ ,  $\nu'_{i,j}$  and  $\nu''_{i,j}$  are the forward and backward molar stoichiometric coefficients of species  $i$  in reaction  $j$ , and  $k_{j,f}$  and  $k_{j,b}$  are the forward and backward reaction rate coefficients of reaction  $j$ . The law of mass action provides an expression for the net reaction rate  $\dot{\omega}_j$  of reaction  $j$ , accounting for the simultaneous progression of both the forward and backward reactions:

$$\dot{\omega}_j = k_{j,f} \prod_{i=1}^{N_s} \left( \frac{\rho Y_i}{W_i} \right)^{\nu'_{i,j}} - k_{j,b} \prod_{i=1}^{N_s} \left( \frac{\rho Y_i}{W_i} \right)^{\nu''_{i,j}}. \quad (2.13)$$

The net production of species  $k$  across all reactions is then determined as the sum of the contributions from each reaction according to

$$\dot{m}_k = W_k \sum_{j=1}^{N_r} [(\nu''_{k,j} - \nu'_{k,j}) \dot{\omega}_j]. \quad (2.14)$$

Combining Eq. 2.13 and Eq. 2.14 yields the final expression for the chemical source terms in the temperature and chemical species transport equations:

$$\dot{m}_k = W_k \sum_{j=1}^{N_r} \left[ (\nu''_{k,j} - \nu'_{k,j}) \left( k_{j,f} \prod_{i=1}^{N_s} \left( \frac{\rho Y_i}{W_i} \right)^{\nu'_{i,j}} - k_{j,b} \prod_{i=1}^{N_s} \left( \frac{\rho Y_i}{W_i} \right)^{\nu''_{i,j}} \right) \right]. \quad (2.15)$$

Closure of the forward reaction rate coefficients  $k_{j,f}$  is generally attained according to the modified Arrhenius form given by

$$k_{j,f} = A_{j,f} T^{B_{j,f}} \exp\left(-\frac{E_{a_{j,f}}}{\hat{R}T}\right), \quad (2.16)$$

where  $A_{j,f}$  is the pre-exponential factor,  $B_{j,f}$  is the temperature exponent, and  $E_{a_{j,f}}$  is the activation energy corresponding to the forward reaction  $j$ , all of which are empirically obtained and provided to the mechanism. The backward reaction rate coefficients  $k_{j,b}$  are often indirectly closed via the equilibrium constants  $K_{c_j} = \frac{k_{j,f}}{k_{j,b}}$ .

## 2.3 Large Eddy Simulation (LES)

The LES in this dissertation were conducted via a grid-filtered approach, leveraging coarsened grids to implicitly filter the governing transport equations rather than with an explicit secondary filtering operation applied to a finer grid. This filtering operation is represented for a general scalar  $\psi$  by

$$\bar{\psi}(\mathbf{x}, t) = \int \psi(\mathbf{x} - \mathbf{r}, t) G(\mathbf{r}, \mathbf{x}) d\mathbf{r}, \quad (2.17)$$

where  $G$  is the filter kernel representing the effect of using a coarsened grid and  $\mathbf{r}$  is a spatial variable of integration. The dependence of the filter kernel on space allows for nonuniform grids in which the degree of coarsening relative to the smallest physical length scales varies spatially. Even in these cases, the filter kernel is presumed to vary slowly in space relative to the filtered quantities so that the filtering operation commutes with spatial gradients. This is a reasonable assumption for grids with moderate degrees of stretching. Since turbulent combustion deals with density-varying flows, the density-weighted filtering operation defined by  $\tilde{\psi} \equiv \overline{\frac{\rho\psi}{\rho}}$  is preferred to the filtering operation of Eq. 2.17.

### 2.3.1 Subfilter Stress Closure

The momentum equation corresponding to LES is obtained by filtering Eq. 2.2, yielding

$$\frac{\partial \bar{\rho} \tilde{u}_i}{\partial t} + \frac{\partial \bar{\rho} \tilde{u}_j \tilde{u}_i}{\partial x_j} = -\frac{\partial \bar{p}_2}{\partial x_i} + \frac{\partial \bar{\tau}_{ij}}{\partial x_j} - \frac{\partial}{\partial x_j} \underbrace{(\bar{\rho} \tilde{u}_j \tilde{u}_i - \bar{\rho} \tilde{u}_j \tilde{u}_i)}_{\tau_{ij}^{\text{sfs}}} + \bar{\rho} g_i, \quad (2.18)$$

where  $\tau_{ij}^{\text{sfs}}$  denotes the subfilter stress responsible for turbulent transport of momentum. The filtered shear stress  $\bar{\tau}_{ij}$  is closed by filtering Eq. 2.10:

$$\bar{\tau}_{ij} = 2\bar{\rho}\tilde{\nu} \left( \tilde{S}_{ij} - \frac{1}{3}\tilde{S}_{kk}\delta_{ij} \right), \quad (2.19)$$

where it has been implicitly assumed that the subfilter correlation between molecular viscosity and the strain rate is negligible. This is a good approximation for large Reynolds number flows in which molecular transport is eclipsed by turbulent transport. The deviatoric part of the subfilter stress is modeled via the Boussinesq hypothesis – the assumption that turbulent transport of momentum behaves in the same way as molecular transport of momentum, predominantly acting in the opposite direction of filtered velocity gradients according to

$$\tau_{ij}^{\text{sfs}} - \frac{1}{3}\tau_{kk}^{\text{sfs}}\delta_{ij} = -2\bar{\rho}\nu_t \left( \tilde{S}_{ij} - \frac{1}{3}\tilde{S}_{kk}\delta_{ij} \right), \quad (2.20)$$

where  $\nu_t$  is the subfilter turbulent kinematic viscosity (sometimes denoted by  $\nu_{\text{sfs}}$ ). Closure of turbulent transport coefficients is traditionally achieved via the Prandtl mixing length model [78], an approach that presumes direct proportionality of turbulent transport coefficients with the product of a pair of characteristic length and velocity scales. The Smagorinsky model [79] is effectively an extension of the Prandtl mixing length model to LES, in which the characteristic length scale is selected as the local filter size  $\Delta$  and a characteristic time scale is selected (in lieu of a characteristic velocity scale) as the local scaled filtered strain rate

magnitude  $|\tilde{\mathcal{S}}| \equiv (2\tilde{S}_{ij}\tilde{S}_{ij})^{1/2}$  such that

$$\nu_t = C_s \Delta^2 |\tilde{\mathcal{S}}|, \quad (2.21)$$

where  $C_s$  is a coefficient of proportionality that remains to be determined. The constant Smagorinsky model assigns a single value to  $C_s$ , typically estimated to be  $0.17^2$  based on a sharp spectral filter [80]. One downside of the constant Smagorinsky model formulation is that  $\nu_t$  is positive by construction, prohibiting energy transfer from small to large scales (backscatter).

Alternatively, the coefficient of proportionality  $C_s$  can be permitted to be negative as well as vary in physical space and time. The dynamic Smagorinsky model [81] closes  $C_s$  based on the assumption of scale similarity applied only to the smallest length scales resolved in an LES. The smallest length scales are discerned from the large scales via an explicit test filtering operation applied to the original LES fields, resulting in a filter scale corresponding to the grid resolution  $\Delta$  and a filter scale corresponding to the test filtering operation  $\tilde{\Delta}$ . For density-varying flows, there are four relevant filtering operations including the grid filter  $(\overline{\cdot})$ , the density-weighted grid filter  $(\widetilde{\cdot})$ , the test filter  $(\tilde{\cdot})$ , and the density-weighted test filter  $(\tilde{\cdot})$ . In addition to the subfilter stress  $\tau_{ij}^{\text{sfs}}$ , an unclosed residual stress is defined corresponding to the double-filtering operation:

$$T_{ij} = \widetilde{\widehat{\rho u_j u_i}} - \widetilde{\widehat{\rho}} \widetilde{\widehat{u_j}} \widetilde{\widehat{u_i}}. \quad (2.22)$$

Though the first term is unclosed, this double-filtered residual stress  $T_{ij}$  is used to define the resolved stress  $\mathcal{L}_{ij}$  – the residual stress corresponding to the turbulent motions with length scales between the test filter length scale  $\tilde{\Delta}$  and the original LES grid filter scale  $\Delta$

– according to

$$\begin{aligned}\mathcal{L}_{ij} &\equiv T_{ij} - \widetilde{\tau_{ij}^{\text{sfs}}} \\ &= \widetilde{\widetilde{\rho} \widetilde{u_j} \widetilde{u_i}} - \widetilde{\widetilde{\rho} \widetilde{u_j} \widetilde{u_i}}.\end{aligned}\tag{2.23}$$

This resolved stress is closed. The scale similarity hypothesis is expected to hold in the range of length scales between the test filter length scale and the original LES grid filter scale since these length scales lie in the inertial subrange (with an appropriately chosen grid resolution). Therefore, the resolved stress can be related to the Smagorinsky model, allowing  $C_s$  to be dynamically computed to enforce consistency with the scale similarity hypothesis. The Boussinesq hypothesis applies to the deviatoric part of the resolved stress, which is given in terms of the deviatoric parts of the double-filtered residual stress and the test-filtered subfilter stress according to

$$\mathcal{L}_{ij}^{\text{d}} = T_{ij}^{\text{d}} - \widetilde{\tau_{ij}^{\text{d}}},\tag{2.24}$$

where  $\tau_{ij}^{\text{d}}$  is the deviatoric part of the subfilter stress in Eq. 2.20. The deviatoric part of the resolved stress  $\mathcal{L}_{ij}^{\text{d}}$  can be modeled by substituting the Smagorinsky model into each term in Eq. 2.24, with corresponding length and time scales:

$$\mathcal{L}_{ij}^{\text{S}} = C_s \underbrace{2\widetilde{\rho} \left[ \Delta^2 \left( \widetilde{|\widetilde{\mathcal{S}}| \widetilde{\mathcal{S}}_{ij}} - \frac{1}{3} \widetilde{|\widetilde{\mathcal{S}}| \widetilde{\mathcal{S}}_{kk} \delta_{ij}} \right) - \widetilde{\Delta}^2 \left( \widehat{|\widetilde{\mathcal{S}}| \widetilde{\mathcal{S}}_{ij}} - \frac{1}{3} \widehat{|\widetilde{\mathcal{S}}| \widetilde{\mathcal{S}}_{kk} \delta_{ij}} \right) \right]}_{M_{ij}},\tag{2.25}$$

where  $\mathcal{L}_{ij}^{\text{S}}$  is the Smagorinsky model for the deviatoric part of the resolved stress. Though  $M_{ij}$  is closed, setting  $\mathcal{L}_{ij}^{\text{d}} = \mathcal{L}_{ij}^{\text{S}}$  results in an overdetermined system of equations. Therefore,  $C_s$  is instead computed as the least-squares solution [82]:

$$C_s = \frac{M_{ij} \mathcal{L}_{ij}}{M_{kl} M_{kl}}.\tag{2.26}$$



### 2.3.2 Subfilter Scalar Flux Closure

The filtered transport equation for a general reactive scalar  $\psi$  is obtained by filtering, for instance, Eq. 2.9, yielding

$$\frac{\partial \bar{\rho} \tilde{\psi}}{\partial t} + \frac{\partial \bar{\rho} \tilde{u}_j \tilde{\psi}}{\partial x_j} = \frac{\partial}{\partial x_j} \left( \bar{\rho} \tilde{D}_\psi \frac{\partial \tilde{\psi}}{\partial x_j} \right) - \frac{\partial}{\partial x_j} \underbrace{(\bar{\rho} \tilde{u}_j \tilde{\psi} - \bar{\rho} \tilde{u}_j \tilde{\psi})}_{f_j^{\text{sfs}}} + \bar{m}_\psi, \quad (2.27)$$

where an equivalent approximation is leveraged for the molecular transport term as is in Eq. 2.19, that is

$$\widetilde{\bar{\rho} D_\psi \frac{\partial \psi}{\partial x_j}} \approx \bar{\rho} \tilde{D}_\psi \frac{\partial \tilde{\psi}}{\partial x_j}. \quad (2.28)$$

Closure of the subfilter flux  $f_j^{\text{sfs}}$  is attained via the gradient diffusion hypothesis, a generalization of the Boussinesq hypothesis for a general scalar  $\psi$ :

$$f_j^{\text{sfs}} = -\bar{\rho} D_t \frac{\partial \tilde{\psi}}{\partial x_j}, \quad (2.29)$$

where  $D_t$  is the subfilter turbulent diffusivity (sometimes denoted by  $D_{\text{sfs}}$ ) and can be obtained through the subfilter turbulent viscosity  $\nu_t$  via a constant turbulent Schmidt number  $Sc_t = \nu_t / D_t$  or by adopting a dynamic approach via a Smagorinsky-like procedure. The latter approach yields

$$\underbrace{\widetilde{\bar{\rho} \tilde{u}_j \tilde{\psi}} - \bar{\rho} \tilde{u}_j \tilde{\psi}}_{\mathcal{F}_j} = C'_s \bar{\rho} \underbrace{\left( \Delta^2 |\tilde{\mathcal{S}}| \frac{\partial \tilde{\psi}}{\partial x_j} - \tilde{\Delta}^2 |\tilde{\mathcal{S}}| \frac{\partial \tilde{\psi}}{\partial x_j} \right)}_{\mathcal{N}_j}, \quad (2.30)$$

where  $C'_s$  is also computed as a least-squares solution:

$$C'_s = \frac{\mathcal{N}_j \mathcal{F}_j}{\mathcal{N}_k \mathcal{N}_k}. \quad (2.31)$$

Note that while Eq. 2.27 can be used to directly transport the components of the thermochemical state (chemical species and temperature), the only scalars explicitly transported in the LES presented in this dissertation are the manifold coordinate moments described by Eq. 2.33. The transport equation for the subfilter scalar variance  $\psi_v$  of a general reactive scalar  $\psi$  is given by

$$\begin{aligned} \frac{\partial \bar{\rho} \psi_v}{\partial t} + \frac{\partial \bar{\rho} \tilde{u}_j \psi_v}{\partial x_j} = \frac{\partial}{\partial x_j} \left[ \bar{\rho} \left( \tilde{D} + D_t \right) \frac{\partial \psi_v}{\partial x_j} \right] - \bar{\rho} \left[ \tilde{\chi}_{\psi\psi} - 2 \left( \tilde{D} + D_t \right) \frac{\partial \tilde{\psi}}{\partial x_j} \frac{\partial \tilde{\psi}}{\partial x_j} \right] \\ + 2 \left( \overline{\psi \dot{m}_\psi} - \tilde{\psi} \overline{\dot{m}_\psi} \right) , \end{aligned} \quad (2.32)$$

where the gradient diffusion hypothesis has been leveraged to provide closure for the subfilter scalar flux.

### 2.3.3 Extension of Manifold Modeling to LES

Equation 1.8 requires modification for the filtered thermochemical state  $\tilde{\phi}$  in the context of LES. The unfiltered thermochemical state  $\phi$  depends on manifold coordinates  $\mathbf{\Omega}_c$  and manifold parameters  $\mathbf{\Omega}_p$  that exist as phase space variables on the subfilter scales. However, the filtered thermochemical state depends on both the unfiltered thermochemical state and additional manifold coordinate moments through the convolution operation against the presumed subfilter PDF, as demonstrated by Eq. 1.6. The space of manifold variables in LES must therefore be expanded according to

$$\tilde{\phi} \approx \tilde{\phi}_{\mathcal{M}}(\mathbf{\Omega}_c, \mathbf{\Omega}_p[\mathbf{\Omega}_c; \mathbf{x}, t], \mathbf{\Omega}_q[\mathbf{x}, t]) , \quad (2.33)$$

where  $\mathbf{\Omega}_q$  denotes the space of additional manifold coordinate moments, usually limited to first- and second-order moments. The manifold coordinate moments may be modeled algebraically or transported explicitly. The latter approach is more accurate and is adopted for the remainder of this work. Equations 2.27 and 2.32 represent the transport equations

for the first- and second-order manifold coordinate moments of a general reactive scalar  $\psi$ , respectively.

## 2.4 Deep Neural Networks (DNNs)

The latter half of this dissertation is primarily concerned with providing closure for  $\Omega_p[\Omega_c; \mathbf{x}, t]$ . In general, the relationship between manifold coordinates and manifold parameters is unknown and can be highly nonlinear. A natural candidate for modeling these functional relationships is therefore a deep neural network (DNN) – a nonlinear universal function approximator capable of estimating continuous functions over a bounded or closed domain [83]. The following describes the basics of supervised deep learning in the context of regression, as this will be the core application of DNNs in this work.

Given a general functional relationship between input variables  $\mathbf{x} \in \mathbb{R}^{n_x}$  and output variables  $\mathbf{y} \in \mathbb{R}^{n_y}$  according to  $\mathbf{y} = f(\mathbf{x})$ , a deep neural network approximates the function  $f$  in terms of the input variables by taking linear combinations of the inputs, applying a nonlinear function to those combinations, taking a linear combination of these intermediate results, and then successively repeating this process. For a simple DNN with a single set of intermediate quantities, the DNN prediction of the outputs can be represented by

$$\mathbf{y}_{\text{DNN}} = \sigma^{(2)} \left( \mathbf{W}^{(2)} \underbrace{\sigma^{(1)} (\mathbf{W}^{(1)} \mathbf{x} + \mathbf{b}^{(1)})}_{\mathbf{a}^{(1)}} + \mathbf{b}^{(2)} \right), \quad (2.34)$$

where  $\mathbf{W}^{(1)}$  and  $\mathbf{W}^{(2)}$  are weight matrices that store the coefficients of the linear combinations of inputs and intermediate quantities,  $\mathbf{a}^{(1)}$  is a vector of intermediate quantities,  $\mathbf{b}^{(1)}$  and  $\mathbf{b}^{(2)}$  are bias vectors that introduce constant offsets, and  $\sigma^{(1)}$  and  $\sigma^{(2)}$  are called activation functions and are typically chosen to be nonlinear functions applied elementwise. Note that a linear activation function is used for the outermost activation function  $\sigma^{(2)}$  in the regression problems of this work, though sigmoid or softmax functions are common in classification

problems. For a linear activation function  $\sigma^{(2)}$ , the activation function  $\sigma^{(1)}$  defines a nonlinear basis for approximating  $f$ . If both  $\sigma^{(2)}$  and  $\sigma^{(1)}$  are linear activation functions, then Eq. 2.34 reduces to a linear estimator of  $f$  (linear regression), since

$$\mathbf{y}_{\text{DNN}} = \underbrace{\mathbf{W}^{(2)}\mathbf{W}^{(1)}}_{\mathbf{W}^*} \mathbf{x} + \underbrace{\mathbf{W}^{(2)}\mathbf{b}^{(1)} + \mathbf{b}^{(2)}}_{\mathbf{b}^*}. \quad (2.35)$$

Equation 2.34 represents the prediction of  $f$  for a *single hidden layer* neural network. This network can be interpreted to have a total of three layers: an input layer for the input variables  $\mathbf{x}$ , a single hidden layer for the intermediate variables  $\mathbf{a}^{(1)}$ , and an output layer for the output variables  $\mathbf{y}$ . Figure 2.1 depicts a graphical representation of a *deep* neural network possessing multiple (three) hidden layers and outputs predicted according to

$$\mathbf{y}_{\text{DNN}} = \sigma^{(4)} \left( \mathbf{W}^{(4)} \sigma^{(3)} \left( \mathbf{W}^{(3)} \sigma^{(2)} \left( \underbrace{\mathbf{W}^{(2)} \sigma^{(1)} \left( \underbrace{\mathbf{W}^{(1)} \mathbf{x} + \mathbf{b}^{(1)}}_{\mathbf{a}^{(1)}} \right) + \mathbf{b}^{(2)}}_{\mathbf{a}^{(2)}} \right) + \mathbf{b}^{(3)} \right) + \mathbf{b}^{(4)} \right) \right), \quad (2.36)$$

which can be extended to an arbitrary finite number of hidden layers. Each element of each vector takes a single scalar value, defining a node in the network of Fig. 2.1. The entries of the weight matrices are represented by lines connecting these nodes. The number of nodes in each layer  $n_N$  and the number of hidden layers  $n_L$  together define the architecture of a deep neural network. This architecture in turn sets the total number of trainable parameters and the complexity of the function  $f$  the DNN is capable of approximating – deeper and wider networks generally have a greater capacity for modeling complexity.

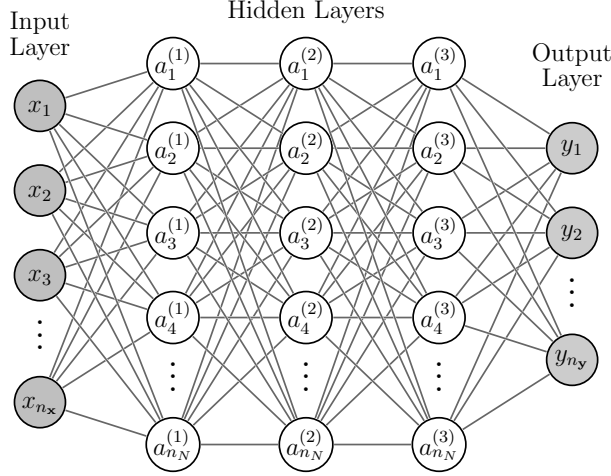


Figure 2.1: Graphical representation of a deep neural network. Figure adapted from Neutelings [84].

### 2.4.1 DNN Training

The sets of weights and biases  $\{(\mathbf{W}^{(k)}, \mathbf{b}^{(k)})\}_{k=1}^{(n_L+1)}$  are determined through a process called DNN training, leveraging  $d$  samples of known input and output variables comprising a training dataset  $\{(\mathbf{x}_i, \mathbf{y}_i)\}_{i=1}^d$ . In the context of DNN training, samples of known input variables are referred to as *features* and known output variables are referred to as *labels*. DNN weights and biases are tuned to minimize a metric for error, represented by a loss (or cost) function. An example loss function for the mean square error is given by

$$\mathcal{L}(\mathbf{W}^{(1)}, \dots, \mathbf{W}^{(n_L+1)}, \mathbf{b}^{(1)}, \dots, \mathbf{b}^{(n_L+1)}) = \frac{1}{d} \sum_{i=1}^d (\mathbf{y}_i - \mathbf{y}_{\text{DNN},i})^\top (\mathbf{y}_i - \mathbf{y}_{\text{DNN},i}). \quad (2.37)$$

To improve the predictive accuracy of the DNN, the value of the loss function can be decreased via gradient descent – the simplest form of which iteratively updates the weights and biases  $\{(\mathbf{W}^{(k)}, \mathbf{b}^{(k)})\}_{k=1}^{(n_L+1)}$  according to

$$W_{ij}^{(k)'} = W_{ij}^{(k)} - \gamma \frac{\partial \mathcal{L}}{\partial W_{ij}^{(k)}}, \quad (2.38)$$

$$b_i^{(k)'} = b_i^{(k)} - \gamma \frac{\partial \mathcal{L}}{\partial b_i^{(k)}} , \quad (2.39)$$

where  $W_{ij}^{(k)'}$  and  $b_i^{(k)'}$  are the updated weights and biases for layer  $k$ , and  $\gamma$  is the learning rate. More sophisticated modifications of gradient descent adaptively determine learning rates for each trainable parameter and provide a sense of ‘inertia’ to avoid high loss local extrema, though the principal concept in these approaches is the same. The gradients of the loss function with respect to the weights and biases could be computed with finite-differences, however this would require at least two forward passes through the DNN for each trainable parameter. Instead, the gradients are evaluated via automatic differentiation according to the current iteration of weights and biases. This approach is referred to as back propagation and effectively amounts to successive applications of the chain rule. To illustrate the gradients computed via back propagation, attention is directed once more to the single hidden layer DNN of Eq. 2.34 for simplicity. The gradients for the trainable parameters in this DNN are given by

$$\frac{\partial \mathcal{L}}{\partial W_{ij}^{(2)}} = \frac{\partial \mathcal{L}}{\partial a_i^{(2)}} \frac{\partial a_i^{(2)}}{\partial W_{ij}^{(2)}} , \quad (2.40)$$

$$\frac{\partial \mathcal{L}}{\partial b_i^{(2)}} = \frac{\partial \mathcal{L}}{\partial a_i^{(2)}} \frac{\partial a_i^{(2)}}{\partial b_i^{(2)}} , \quad (2.41)$$

$$\frac{\partial \mathcal{L}}{\partial W_{ij}^{(1)}} = \sum_{l=1}^{n_y} \frac{\partial \mathcal{L}}{\partial a_l^{(2)}} \frac{\partial a_l^{(2)}}{\partial a_i^{(1)}} \frac{\partial a_i^{(1)}}{\partial W_{ij}^{(1)}} , \quad (2.42)$$

$$\frac{\partial \mathcal{L}}{\partial b_i^{(1)}} = \sum_{l=1}^{n_y} \frac{\partial \mathcal{L}}{\partial a_l^{(2)}} \frac{\partial a_l^{(2)}}{\partial a_i^{(1)}} \frac{\partial a_i^{(1)}}{\partial b_i^{(1)}} , \quad (2.43)$$

where derivatives of the activation functions can be analytically computed for each iteration of weights and biases.

The loss function in Eq. 2.37 is computed over the entire training dataset – a process which ensures a fairly stable definition of the gradient but at the cost of considerable memory

overhead. Furthermore, introducing a degree of stochasticity in the gradient has been found to decrease instances in which the algorithm gets trapped in high loss local extrema [85]. For these reasons, the loss function is often approximated over a small subset of the data called a mini-batch, and the number of training samples used in each mini-batch is referred to as the batch size. The entire dataset is typically fed through the gradient descent algorithm in several successive passes, where each full pass of the entire dataset is referred to as an epoch. Training often continues over many epochs until the validation loss (the loss associated with a separate dataset called a validation dataset) begins to overtake the training loss. Beyond this point, DNNs are deemed to overfit to the training data, often resulting in poor predictive performance when applied to new datasets. An important limitation of DNNs is that they typically do not extrapolate well beyond the data used for training. DNNs that exhibit a high degree of generalizability, providing reliable predictions across a broad range of physical regimes, must therefore be trained on large quantities of data spanning these regimes of interest.

### 2.4.2 DNN Hyperparameter and Architecture Selection

Network *hyperparameters* are DNN parameters that are typically set prior to training and fixed while tuning the weights and biases of a particular model. Hyperparameters include quantities such as the learning rate and batch size, among others. The DNN architecture, set by the number of neurons per layer and total number of layers, must also be selected *a priori* while ensuring that the degrees of freedom needed to model the complexity of a particular functional relationship are provided without introducing too many degrees of freedom and encouraging overfitting. Manually exploring the state space of possible network architectures to identify an appropriate architecture that strikes this balance for a given problem is cumbersome and time-consuming. Neural architecture search (NAS) algorithms seek to streamline this process by automating the selection of the network architecture [86, 87]. The DNN models throughout this dissertation have been predominantly trained

with a novel NAS algorithm that selects the number of neurons per layer and total number of layers by iteratively training DNN models with architectures identified via a notion of power law convergence of the validation loss with respect to the network architecture [71].



# Chapter 3

## In-Situ Adaptive Manifolds (ISAM): A Novel Algorithm for Manifold Modeling

This chapter addresses *Sub-Objective 1*, outlining the development of a new computational algorithm that enables more general, higher-dimensional manifold modeling approaches. As manifold dimensionality increases, not all manifold solutions are required over the course of a simulation, rendering precomputation of unneeded solutions wasted effort. More importantly, storing these unneeded solutions is a tremendous waste of limited memory resources. In this chapter, rather than using precomputed and pretabulated manifold solutions, a far more efficient and sensible approach is developed in which manifold calculations are performed ‘on-the-fly’ and adaptively tabulated using In-Situ Adaptive Tabulation (ISAT) [44]. This approach, termed In-Situ Adaptive Manifolds (ISAM) [43], enables more complex and general manifold models that have never before been practical for implementation in LES. This chapter focuses on ISAM applied to nonpremixed combustion, leveraging the steady flamelet model as a vehicle to evaluate the implementation and computational overhead of ISAM in LES with variation in chemical mechanism sizes. ISAM is further extended to more complex

turbulent combustion LES with multiple and/or inhomogeneous inlet streams and multi-modal combustion in Chapter 4 and Chapter 5, respectively.

### 3.1 Nonpremixed Manifold Model

For the case of adiabatic, nonpremixed combustion with two inlets (fuel and oxidizer), the thermochemical state can be expressed in terms of the mixture fraction  $Z$  and the mixture fraction dissipation rate  $\chi_{ZZ}$  (to be defined later). This formulation involves defining the local mixture fraction  $Z$ , which is zero in the oxidizer stream and unity in the fuel stream, as a conserved scalar with unity Lewis number [88] according to its transport equation:

$$\frac{\partial \rho Z}{\partial t} + \frac{\partial \rho u_j Z}{\partial x_j} = \frac{\partial}{\partial x_j} \left( \rho D \frac{\partial Z}{\partial x_j} \right), \quad (3.1)$$

where  $\rho$  is the density,  $u_j$  is the velocity, and  $D$  is the molecular diffusivity (implicitly assumed to be the same for all scalars via the unity Lewis number assumption).

Equations 2.8 and 2.9 can then be transformed into mixture fraction space by replacing derivatives with respect to physical space and time via the chain rule:

$$\frac{\partial}{\partial t} = \frac{\partial Z}{\partial t} \frac{d}{dZ} \quad \text{and} \quad \frac{\partial}{\partial x_j} = \frac{\partial Z}{\partial x_j} \frac{d}{dZ}. \quad (3.2)$$

Assuming unity effective Lewis numbers [73], this transformation results in the nonpremixed manifold equations (referred to as the steady flamelet equations) for the temperature and species mass fractions [26]:

$$0 = \frac{\rho c_p \chi_{ZZ}}{2} \frac{d^2 T}{dZ^2} + \frac{\rho \chi_{ZZ}}{2} \frac{dc_p}{dZ} \frac{dT}{dZ} + \frac{\rho \chi_{ZZ}}{2} \sum_k c_{p,k} \frac{dY_k}{dZ} \frac{dT}{dZ} - \sum_k h_k \dot{m}_k, \quad (3.3)$$

$$0 = \frac{\rho \chi_{ZZ}}{2} \frac{d^2 Y_k}{dZ^2} + \dot{m}_k, \quad (3.4)$$

where  $\dot{m}_k$  is the chemical source term and  $\chi_{ZZ} \equiv 2D_Z \nabla Z \cdot \nabla Z$  is the mixture fraction dissipation rate. With this model, the unfiltered thermochemical state  $\phi$  is expressed as a function of the mixture fraction and the mixture fraction dissipation rate:

$$\phi(\mathbf{x}, t) \approx \phi_{\mathcal{M}}(Z[\mathbf{x}, t], \chi_{ZZ}[\mathbf{x}, t]) . \quad (3.5)$$

That is, for the nonpremixed manifold model, there is a single manifold coordinate  $\Omega_c = \{Z\}$  and a single manifold parameter  $\Omega_p = \{\chi_{ZZ}\}$ .

To close Eq. 3.3 and Eq. 3.4, the spatial dependence of the mixture fraction dissipation rate must instead be modeled as a function of the mixture fraction – the independent variable in the nonpremixed manifold equations. The presumed dependence of the dissipation rate on the mixture fraction is often obtained from an analytical solution for the dissipation rate in a counterflow flame [68]:

$$\chi_{ZZ}(Z) = \chi_{ZZ,\text{ref}} \frac{\exp\left(-2\left[\text{erfc}^{-1}(2Z)\right]^2\right)}{\exp\left(-2\left[\text{erfc}^{-1}(2Z_{\text{ref}})\right]^2\right)} . \quad (3.6)$$

The characteristic reference value for the dissipation rate  $\chi_{ZZ,\text{ref}}$  is evaluated at the stoichiometric mixture fraction  $Z_{\text{st}}$ .

As discussed in Chapter 2.1, LES is concerned with the filtered thermochemical state, which can be obtained through convolution of the manifold against a presumed subfilter PDF for the manifold variables, in this case, the mixture fraction:

$$\tilde{\phi} = \int \phi(Z; \chi_{ZZ,\text{ref}}) \tilde{P}(Z; \tilde{Z}, Z_v) dZ . \quad (3.7)$$

The density-weighted subfilter PDF of the mixture fraction  $\tilde{P}(Z; \tilde{Z}, Z_v)$  is presumed to be a beta distribution [58], parameterized by the filtered mixture fraction  $\tilde{Z}$  and its corresponding

subfilter variance  $Z_v \equiv \widetilde{Z}^2 - \tilde{Z}^2$  according to

$$\beta(Z; \tilde{Z}, Z_v) \equiv \frac{\Gamma(\alpha + \beta)}{\Gamma(\alpha)\Gamma(\beta)} Z^{\alpha-1} (1 - Z)^{\beta-1}, \quad (3.8)$$

where

$$\alpha = \tilde{Z} \gamma, \quad (3.9)$$

$$\beta = (1 - \tilde{Z}) \gamma, \quad (3.10)$$

$$\gamma = \frac{\tilde{Z}(1 - \tilde{Z})}{Z_v} - 1 \geq 0. \quad (3.11)$$

The manifold coordinate moments for the nonpremixed manifold model are therefore given by  $\mathbf{\Omega}_q = \{\tilde{Z}, Z_v\}$ , and are obtained from their corresponding transport equations:

$$\frac{\partial \bar{\rho} \tilde{Z}}{\partial t} + \frac{\partial \bar{\rho} \tilde{u}_j \tilde{Z}}{\partial x_j} = \frac{\partial}{\partial x_j} \left[ \bar{\rho} (\tilde{D} + D_t) \frac{\partial \tilde{Z}}{\partial x_j} \right], \quad (3.12)$$

$$\frac{\partial \bar{\rho} Z_v}{\partial t} + \frac{\partial \bar{\rho} \tilde{u}_j Z_v}{\partial x_j} = \frac{\partial}{\partial x_j} \left[ \bar{\rho} (\tilde{D} + D_t) \frac{\partial Z_v}{\partial x_j} \right] - \bar{\rho} \left[ \tilde{\chi}_{ZZ} - 2 (\tilde{D} + D_t) \frac{\partial \tilde{Z}}{\partial x_j} \frac{\partial \tilde{Z}}{\partial x_j} \right]. \quad (3.13)$$

The filtered mixture fraction dissipation rate  $\tilde{\chi}_{ZZ}$  can be obtained from the gradient of the filtered mixture fraction and the subfilter mixture fraction variance [89] according to

$$\tilde{\chi}_{ZZ} \equiv \widetilde{2D \frac{\partial Z}{\partial x_j} \frac{\partial Z}{\partial x_j}} \approx 2\tilde{D} \frac{\partial \tilde{Z}}{\partial x_j} \frac{\partial \tilde{Z}}{\partial x_j} + C_{\chi_{ZZ}} \frac{\nu_t}{\Delta^2} (\widetilde{Z^2} - \tilde{Z}^2). \quad (3.14)$$

The reference mixture fraction dissipation rate can be obtained by deconvoluting the filtered mixture fraction dissipation rate ( $\phi = \chi_{ZZ}(Z)$  in Eq. 3.7) combined with the presumed dependence of the dissipation rate on the mixture fraction (Eq. 5.13):

$$\chi_{ZZ,\text{ref}} = \frac{\tilde{\chi}_{ZZ}}{\int \frac{f(Z)}{f(Z_{\text{ref}})} \tilde{P}(Z; \tilde{Z}, Z_v) dZ}, \quad (3.15)$$

where  $f(Z) \equiv \exp\left(-2\left[\operatorname{erfc}^{-1}(2Z)\right]^2\right)$ . Pulling  $\chi_{ZZ,\text{ref}}$  out of the integral in Eq. 3.7 implicitly presumes there is no subfilter variation of the reference dissipation rate. As a result, the filtered thermochemical state in LES can be expressed in terms of either the filtered mixture fraction dissipation rate or the reference mixture fraction dissipation rate:

$$\begin{aligned}\tilde{\phi}(\mathbf{x}, t) &\approx \tilde{\phi}_{\mathcal{M}}\left(\tilde{Z}[\mathbf{x}, t], Z_v[\mathbf{x}, t], \tilde{\chi}_{ZZ}[\mathbf{x}, t]\right) \\ &\approx \tilde{\phi}_{\mathcal{M}}\left(\tilde{Z}[\mathbf{x}, t], Z_v[\mathbf{x}, t], \chi_{ZZ,\text{ref}}[\mathbf{x}, t]\right) .\end{aligned}\tag{3.16}$$

## 3.2 Manifold Modeling Algorithms

Two operations are required to obtain the filtered thermochemical state in Eq. 3.16: computation of the solutions of the manifold equations (Eq. 3.4) and convolution of the manifold solutions against the presumed subfilter PDF of the mixture fraction (Eq. 3.7). Different software implementations are possible depending on when these operations occur.

### 3.2.1 Precomputation, Preconvolution, and Pretabulation (PPP)

In the conventional implementation, the solutions to the manifold equations are computed, convoluted against the presumed subfilter PDF, and tabulated before the LES. For the steady flamelet model, the precomputed, preconvoluted, and pretabulated (PPP) database  $\mathcal{T}_{\text{PPP}}$  depends on the filtered mixture fraction, subfilter mixture fraction variance, and reference dissipation rate (or filtered dissipation rate):

$$\mathcal{T}_{\text{PPP}} : \tilde{\phi} = \tilde{\phi}\left(\tilde{Z}, Z_v, \chi_{ZZ,\text{ref}}\right) .\tag{3.17}$$

For this relatively simple combustion model, computation and storage of this database is not difficult, requiring up to several minutes of computational time and hundreds of MB of memory, depending on the size of the chemical mechanism considered and the number of thermochemical variables stored in the database. However, as manifold dimensionality

increases for more complex models, the computational cost and storage requirements quickly become impractical.

### 3.2.2 Convolution-on-the-fly (COTF)

In an effort to reduce the dimensionality of the precomputed table for more complex models with additional manifold coordinates, Perry and Mueller [90] implemented a strategy in which only the manifold solutions were precomputed and pretabulated. Convolution against the presumed subfilter PDF was conducted on-the-fly during the LES – that is, convolution-on-the-fly (COTF). In the case of the steady flamelet model, the dimensionality of the precomputed database  $\mathcal{T}_{\text{COTF}}$  is reduced and depends only on the mixture fraction and the reference mixture fraction dissipation rate:

$$\mathcal{T}_{\text{COTF}} : \phi = \phi(Z, \chi_{ZZ, \text{ref}}) . \quad (3.18)$$

Of course, the trade-off is that one must perform the convolution operation on-the-fly, but Perry and Mueller [90] demonstrated that this could potentially be more computationally efficient than retrieving the filtered thermochemical state from higher-dimensional tables in addition to enabling more complex subfilter PDF models with several (co-)variances that would dramatically increase the dimensionality of a preconvoluted database.

### 3.2.3 In-Situ Adaptive Manifolds (ISAM)

Even with COTF, the problem of precomputing and storing unaccessed manifold states still remains. Only a small portion of the manifold space may actually be sampled over the course of an LES, and the time and memory used to compute the potentially large number of unaccessed states of the manifold could be reclaimed by solving the manifold equations as the simulation proceeds. However, unlike with convolution against the presumed subfilter PDF, which is implemented simply as a scalar product, the solution of the manifold equations,

even the steady flamelet equations, is computationally non-trivial. Therefore, rather than repeatedly solving the same set of manifold equations on-the-fly as is done in the in-situ flamelet-generated manifolds (IFM) approach by Lodier et al. [91], solutions to the manifold equations must be saved and reused subsequently in the LES. Efficient reuse is accomplished by storing and retrieving manifold solutions using In-Situ Adaptive Tabulation (ISAT) [44].

## Overview of ISAT

ISAT relies on a binary tree data structure that is adaptively constructed as the database is queried. Consider a generic input-output  $\mathbf{y}(\mathbf{x})$ , where both the inputs and outputs can be vectors. Each leaf of the tree is associated with a particular value of the input  $\mathbf{x}^0$  and an “ellipsoid of accuracy” within which a local linear approximation to the output satisfies a user-specified error tolerance (combination of a relative and an absolute tolerance). With each query to the ISAT database with input  $\mathbf{x}^q$ , the binary tree is traversed to locate a nearby  $\mathbf{x}^0$  and determine whether the query point is located within the corresponding ellipsoid of accuracy. Typically, one of three outcomes is possible:

1. *Retrieval*: If the query point is within the ellipsoid of accuracy, return the local linear approximation to the output:

$$\mathbf{y}(\mathbf{x}^q) \approx \mathbf{y}(\mathbf{x}^0) + \mathbf{J}^0(\mathbf{x}^q - \mathbf{x}^0) , \quad (3.19)$$

where  $\mathbf{J}^0$  is the Jacobian matrix at  $\mathbf{x}^0$ .

2. *Growth*: If the query point is not within the ellipsoid of accuracy, explicitly evaluate the output. If the resulting difference between the explicit evaluation and the local linear approximation is less than the user-specified error tolerance, then expand the ellipsoid of accuracy to include the query point.
3. *Addition*: If the query point is not within the ellipsoid of accuracy, explicitly evaluate the output. If the resulting difference between the direct evaluation and the local linear

approximation is greater than the user-specified error tolerance, then add a new leaf corresponding to the query point  $\mathbf{x}^q$ .

## ISAT Implementation with the Steady Flamelet Model

With the steady flamelet model, the lone input  $\mathbf{x}$  to the ISAT database is the reference scalar dissipation rate  $\chi_{ZZ,\text{ref}}$ . The discrete solutions to Eq. 3.4 for every thermochemical quantity of interest  $\phi_k(Z_j; \chi_{ZZ,\text{ref}})$ , where  $\phi_k$  is each thermochemical quantity of interest and  $Z_j$  are the discrete points in mixture fraction space, are aggregated as the output  $\mathbf{y}$ . Over the course of the LES, at each grid point at each time step, the reference dissipation rate is computed and input to ISAT. For each thermochemical quantity of interest, the outputs from ISAT, which are discrete functions of the mixture fraction, are convoluted against the presumed subfilter PDF of the mixture fraction. The weights are precomputed and pretabulated as in the COTF algorithm [90]. The ultimate output is the filtered thermochemical state which is updated in the LES code. However, only the unfiltered thermochemical state is stored in ISAT.

The initial ISAM implementation uses a separate ISAT table for each MPI process. The tables are not synchronized at any point during the simulation, meaning that thermochemical states previously computed by one MPI process and needed by another are inaccessible, requiring some redundant computation. Additionally, domain decomposition across MPI processes is static and uniform in terms of the grid points per MPI process. Ideally, the domain would be decomposed such that approximately a uniform number of manifold solutions are computed on each MPI process for more efficient load-balancing. Synchronizing ISAT tables across MPI processes and introducing dynamic load-balancing could therefore both improve ISAM performance, and this initial implementation could be viewed as a ‘worst-case’ scenario in terms of computational overhead. Support for synchronization of ISAT tables across MPI processes is introduced and evaluated at the end of this chapter.



## 3.3 Test Configurations: Turbulent Nonpremixed Jet Flames

### 3.3.1 Computational Infrastructure

To test the newly-developed ISAM approach, two canonical turbulent nonpremixed jet flames were simulated using NGA – a structured, finite-difference, low Mach number flow solver [92, 93]. For LES, all subfilter transport terms are closed with dynamic Smagorinsky-like models [81], with the exception discussed below. The one-dimensional manifold equations given by Eq. 3.4 are solved using the PDRs code [38, 94]. To ensure convergence, PDRs starts with the thermodynamic equilibrium profile and evolves the manifold equations in pseudo-time to provide an initial guess for a Newton solver. An analytical PDRs Jacobian matrix has also been implemented for the manifold equations, which converges more smoothly than a numerical PDRs Jacobian matrix and further ensures solver convergence. The ISAT Jacobian matrix  $\mathbf{J}^0$  is set to zero in the initial ISAM implementation, effectively enforcing a local constant approximation. Use of a numerical ISAT Jacobian is also explored upon further refinement of the ISAM approach.

### 3.3.2 Configuration I: Hydrogen Jet Flame

The first configuration is a turbulent nonpremixed hydrogen simple jet flame with a Reynolds number of 10,000 [95, 96, 97]. Only pure hydrogen, undiluted by helium, is considered in this work. The flame was simulated in cylindrical coordinates using a stretched grid with  $256 \times 144 \times 64$  grid points along the axial, radial, and circumferential directions, respectively. A uniform inlet velocity profile was imposed for the coflow, and the central jet inflow velocity profile was generated from a separate simulation of fully-developed turbulent pipe flow. The chemical mechanism for hydrogen combustion [98] consists of 9 species. The relative and absolute error tolerances in ISAT are set to  $10^{-3}$  and  $10^{-9}$ , respectively. For this flame,

statistics were computed using a constant Smagorinsky constant of 0.12 and a constant turbulent Schmidt number of 0.7. However, timings are shown with the dynamic models for comparison with the other flame configuration.

### 3.3.3 Configuration II: Sandia Flame D

The second configuration is Sandia Flame D, a turbulent piloted partially premixed methane/air jet flame with a Reynolds number of 22,400 [99]. The flame was simulated in cylindrical coordinates using a stretched grid with  $256 \times 144 \times 64$  grid points along the axial, radial, and circumferential directions, respectively. Uniform inlet velocity profiles were imposed for the coflow and pilot, and the central jet inflow velocity profile was generated from a separate simulation of fully-developed turbulent pipe flow. The mechanism for methane combustion, GRI-3.0 [100], consists of 35 species with the nitrogen chemistry removed. The relative and absolute error tolerances in ISAT are also set to  $10^{-3}$  and  $10^{-9}$ , respectively.

## 3.4 ISAM Verification

The COTF approach is compared to ISAM in order to verify the implementation of the latter, and the two approaches are compared to experimental measurements. The relative computational performance of ISAM is then assessed for both test configurations.

### 3.4.1 Verification: Hydrogen Jet Flame

Figure 3.1 compares spatial statistics for the mixture fraction and conditional statistics for the temperature and the water mass fraction. The results with the COTF approach and with ISAM are in good agreement, verifying the ISAM implementation. Both approaches are in good agreement with the experimental measurements for mixture fraction, temperature, and the water mass fraction.

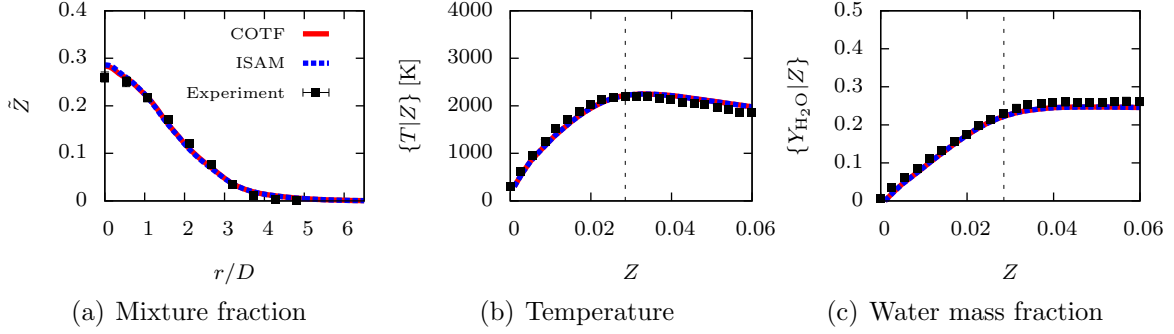


Figure 3.1: Time-averaged statistics at  $x/D = 22.5$  for the hydrogen jet flame. The vertical dashed line denotes the stoichiometric mixture fraction  $Z_{\text{st}} = 0.0285$ . The solid line corresponds to COTF, the dashed line to ISAM, and symbols to experimental measurements with estimated uncertainty [95].

### 3.4.2 Verification: Sandia Flame D

Figure 3.2 compares spatial statistics for the mixture fraction and conditional statistics for the temperature and carbon dioxide mass fraction. As for the hydrogen flame, COTF and ISAM are in good agreement, verifying the ISAM implementation for hydrocarbon chemistry. Compared to the experimental measurements, the only major discrepancy is the temperature on the rich side of the flame, but this is consistent with previous studies using the same combustion model, which attributed the error to slight overpredictions of heat release due to the partial premixing of the methane with air [101].

## 3.5 Performance Assessment

The performance of the initial implementation of ISAM is evaluated by comparing the baseline time elapsed per time step as each simulation proceeds. In the initial ISAM implementation, the cost per time step in ISAM fluctuates up to a factor of seven in the worst cases, depending on the number of ISAT retrieves versus additions during a particular time step. The baseline cost is defined as the “minimum” cost for a time step in which most ISAT evaluations are simply retrieves. In other words, this cost indicates the overhead of traversing

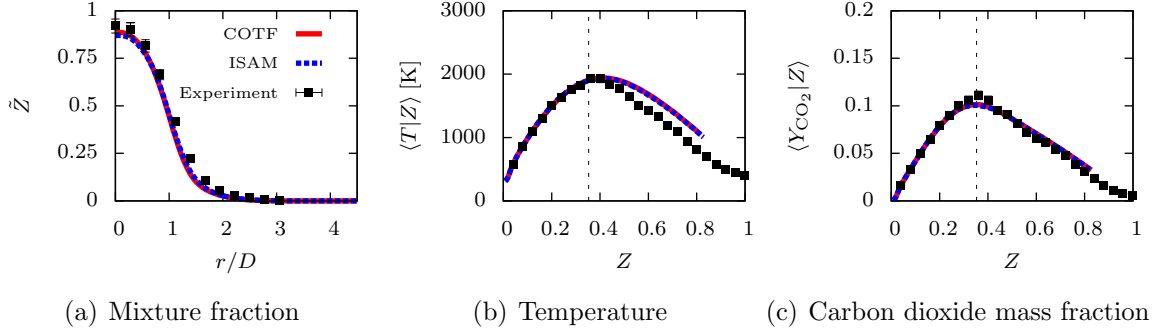


Figure 3.2: Time-averaged statistics at  $x/D = 15$  for Sandia Flame D. The vertical dashed line denotes the stoichiometric mixture fraction  $Z_{st} = 0.353$ . The solid line corresponds to COTF, the dashed line to ISAM, and symbols to experimental measurements with estimated uncertainty [99].

the binary tree constructed by ISAT. This baseline cost becomes increasingly regular as the simulation progresses and the relative number of retrieves versus additions increases. Addition of MPI synchronization of the ISAT tables (see Sec. 3.8) and dynamic load-balancing would reduce the number of manifold solutions required to be computed by each processor and effectively reduce the fluctuations to zero after an initial transient.

Figure 3.3 (a) demonstrates how the baseline cost of ISAM evolves for the hydrogen jet flame. As one might expect, the cost of the first step is relatively expensive as the ISAT tables are populated from scratch. However, the cost is only a few minutes and does not require that the manifold solutions be precomputed, preconvoluted, and pretabulated as in the conventional approach, which typically takes far longer than a few minutes (often several hours, depending on the database resolution). The cost sharply declines over the first ten time steps and rapidly reaches a plateau of 6.4 s after approximately 100 – 1000 time steps. Remarkably, the additional baseline cost incurred by ISAM is no more than that of convolution-on-the-fly, implying that traversing the binary tree comes at a nearly negligible cost for the hydrogen jet flame case.

Figure 3.3 (b) shows that the cost of COTF is actually less than that of PPP for the Sandia Flame D simulation, also observed by Perry and Mueller [90]. Overhead from convolution

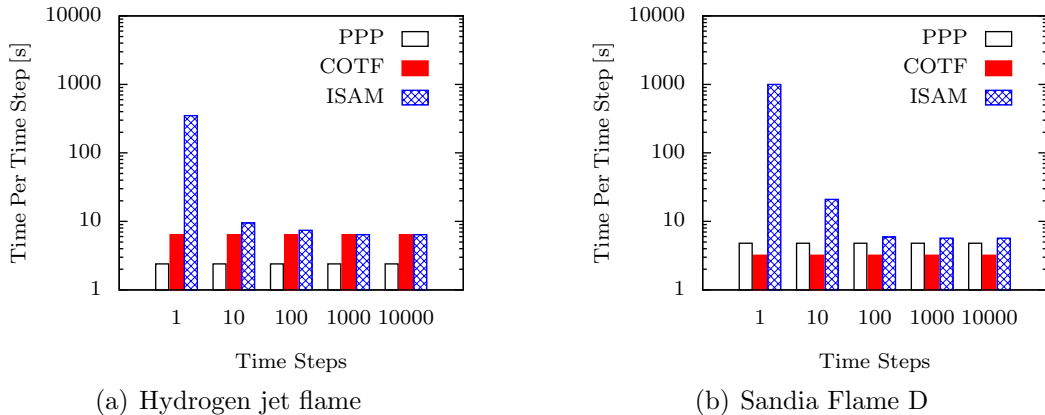


Figure 3.3: Baseline computational cost per time step for the hydrogen jet flame and Sandia Flame D.

can be lower than additional lookup costs from larger tables. Simply stated, as the database grows, memory management with larger tables in PPP can become limiting compared to the relatively cheap floating point operations of convolution against the subfilter PDF in COTF. The figure also illustrates a similar trend in the baseline cost as the hydrogen jet flame, though the initial cost of populating the ISAT tables is greater due to the greater number of species in the methane chemical mechanism. However, the cost of the first time step is measured in minutes, which is far less than the typical time taken for construction of a conventional PPP database (again often several hours, depending on the database resolution). The cost of ISAM reduces rapidly, leveling off at 5.7 s, only marginally more than PPP. The number of points per MPI process is the same as for the hydrogen flame, demonstrating that the computational overhead of ISAM at steady-state does not depend on the size of the chemical mechanism. Therefore, ISAM is feasible even for larger chemical mechanisms.

Additionally, while the computational cost of ISAM and PPP are comparable, the ISAM database size in memory is over 100 times smaller than that of PPP. Though database size is not a limiting factor for the steady flamelet model, this already considerable memory savings will only increase with more complex manifold-based models. While the computational overhead will increase with increased manifold dimensionality and model complexity, ISAT

has been used with explicit chemistry exceeding 150 species (see, e.g., Ref. [102]), so even extremely complex manifold-based models should not introduce significant computational overhead. In addition, aside from the first few time steps in which the manifold solutions are computed to populate the ISAT tables, no significant overhead is incurred for larger chemical mechanisms.

### 3.6 Numerical ISAT Jacobian

As a further refinement of the ISAM approach, the ISAT Jacobian matrix  $\mathbf{J}^0$  is computed numerically via a forward difference as a central difference would require an additional manifold equation solution and higher computational cost. To provide improved load-balancing of manifold solutions across MPI processes, the natural logarithm of the reference mixture fraction dissipation rate is passed as the input to ISAT rather than the reference mixture fraction dissipation rate itself since the mixture fraction dissipation rate varies most appreciably in small regions of physical space around the flame. The ISAT Jacobian matrix is therefore computed according to

$$\left. \frac{\partial \phi_k(Z_j; \ln \chi_{ZZ,\text{ref}})}{\partial \ln \chi_{ZZ,\text{ref}}} \right|_{\ln \chi_{ZZ,\text{ref}}^0} \approx \frac{\phi_k(Z_j; \ln \chi_{ZZ,\text{ref}}^0 + \Delta \ln \chi_{ZZ,\text{ref}}) - \phi_k(Z_j; \ln \chi_{ZZ,\text{ref}}^0)}{\Delta \ln \chi_{ZZ,\text{ref}}}, \quad (3.20)$$

where  $\ln \chi_{ZZ,\text{ref}}^0$  is the tabulated point in the ISAT input space and  $\Delta \ln \chi_{ZZ,\text{ref}}$  is the step size taken in the ISAT input space, referred to as the Jacobian delta for brevity. The impact of the choice of Jacobian delta on model accuracy and ISAM performance is evaluated via LES of Sandia Flame D.

Figure 3.4 demonstrates that the time-averaged and conditional statistics are relatively insensitive to the size of the Jacobian delta unless the selected Jacobian delta is too small relative to the PDRs relative error tolerance  $\varepsilon_{\text{rel,PDRs}} = 10^{-6}$ . In this situation, the numerical approximation to the ISAT Jacobian effectively amounts to the derivative of numerical noise

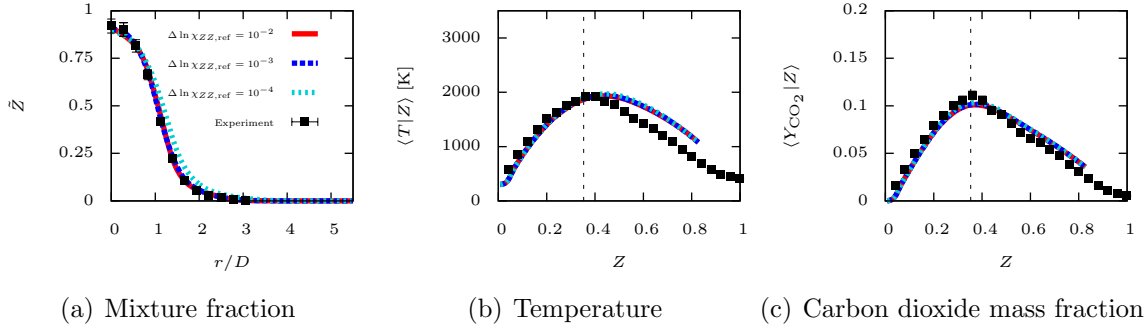


Figure 3.4: Time-averaged statistics at  $x/D = 15$  for Sandia Flame D. The vertical dashed line denotes the stoichiometric mixture fraction  $Z_{\text{st}} = 0.353$ . The solid red line (—) corresponds to an ISAT Jacobian delta of  $10^{-2}$ , the dashed blue line (- -) to  $10^{-3}$ , the dotted cyan line (···) to  $10^{-4}$ , and symbols to experimental measurements with estimated uncertainty [99].

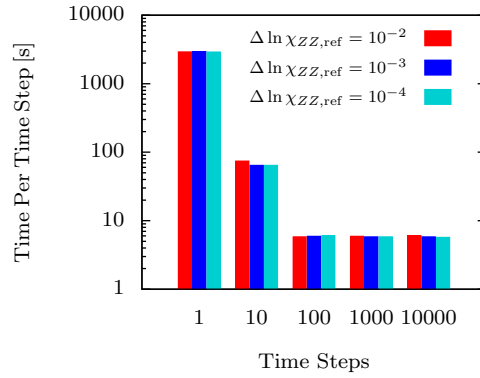


Figure 3.5: Sensitivity of the baseline computational cost per time step with respect to the Jacobian delta  $\Delta \ln \chi_{ZZ,\text{ref}}$  for Sandia Flame D.

and causes error to increase. To avoid this issue, the Jacobian delta should be selected such that its square is greater than or equal to the PDRs relative error tolerance:

$$(\Delta \ln \chi_{ZZ,\text{ref}})^2 \geq \varepsilon_{\text{rel,PDRs}} . \quad (3.21)$$

Figure 3.5 demonstrates that the choice of Jacobian delta has a negligible influence on ISAM performance, though introducing the numerical ISAT Jacobian does incur a greater transient computational cost relative to the performance observed in Fig. 3.3 (b) due to the

additional manifold solutions required by the forward difference. However, the performance is evaluated using the same ISAT and PDRs relative error tolerances used by the initial ISAM implementation in which the ISAT Jacobian matrix was neglected. The ISAT tolerances necessary when using a first-order extrapolation for the unfiltered thermochemical state (with a numerical ISAT Jacobian matrix) are expected to be larger relative to using a zeroth-order extrapolation for the unfiltered thermochemical state (no numerical ISAT Jacobian matrix).

### 3.7 Tolerance Sensitivity Analysis

To ensure error tolerances are appropriately selected with the addition of a numerical ISAT Jacobian, a sensitivity analysis is conducted for the ISAT relative error tolerance  $\epsilon_{\text{rel,ISAT}}$  and PDRs relative error tolerance  $\epsilon_{\text{rel,PDRs}}$  (the absolute error tolerances are set to extremely small values). The impact of the choice of ISAT and PDRs relative error tolerances on model accuracy and ISAM performance is again evaluated via LES of Sandia Flame D. Figure 3.6 demonstrates that the time-averaged Sandia Flame D statistics are insensitive to loosening or tightening the ISAT relative error tolerance, and that a larger ISAT relative error tolerance is allowable after the introduction of the numerical Jacobian. Figure 3.7 demonstrates a similar insensitivity of the time-averaged statistics to the PDRs relative error tolerance.

Figure 3.8 (a) demonstrates that the initial transient cost of constructing the ISAT databases increases by nearly an order of magnitude with a two order of magnitude decrease in the ISAT relative error tolerance. Though introducing a numerical ISAT Jacobian increases the cost associated with an ISAT relative error tolerance of  $10^{-3}$ , it simultaneously enables use of a less computationally costly ISAT relative error tolerance of  $10^{-2}$ , returning the transient cost to the levels observed in Fig. 3.3 (b). As the ISAT tables are saturated with manifold solutions, the steady-state computational cost approaches the negligible overhead cost associated with traversing the binary trees. Therefore, the net effect of adding the



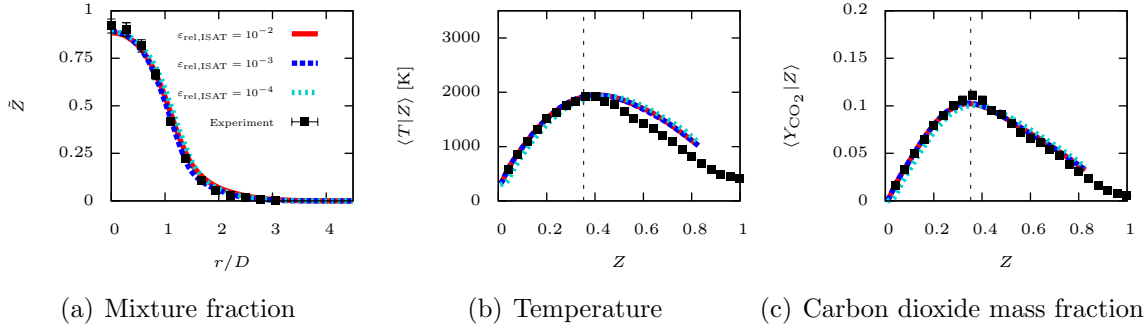


Figure 3.6: Time-averaged statistics at  $x/D = 15$  for Sandia Flame D. The vertical dashed line denotes the stoichiometric mixture fraction  $Z_{\text{st}} = 0.353$ . The solid red line (—) corresponds to an ISAT relative error tolerance of  $10^{-2}$ , the dashed blue line (--) to  $10^{-3}$ , the dotted cyan line (...) to  $10^{-4}$ , and symbols to experimental measurements with estimated uncertainty [99].

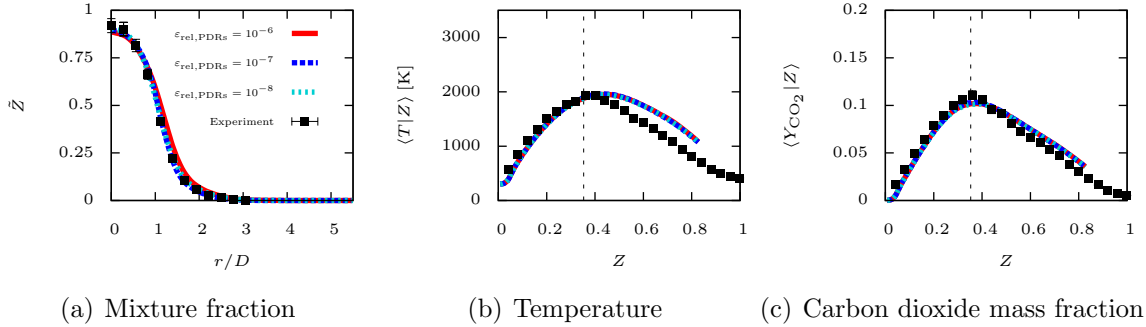


Figure 3.7: Time-averaged statistics at  $x/D = 15$  for Sandia Flame D. The vertical dashed line denotes the stoichiometric mixture fraction  $Z_{\text{st}} = 0.353$ . The solid red line (—) corresponds to a PDRs relative error tolerance of  $10^{-6}$ , the dashed blue line (--) to  $10^{-7}$ , the dotted cyan line (...) to  $10^{-8}$ , and symbols to experimental measurements with estimated uncertainty [99].

numerical ISAT Jacobian is to provide the ISAM approach additional numerical stability without any associated detriment to computational cost.

Figure 3.8 (b) demonstrates that the initial transient cost of constructing the ISAT databases increases only slightly as the PDRs relative error tolerance is tightened. Consequently, the PDRs relative error tolerance should be selected in tandem with the Jacobian delta, prioritizing the satisfaction of Eq. 3.21.

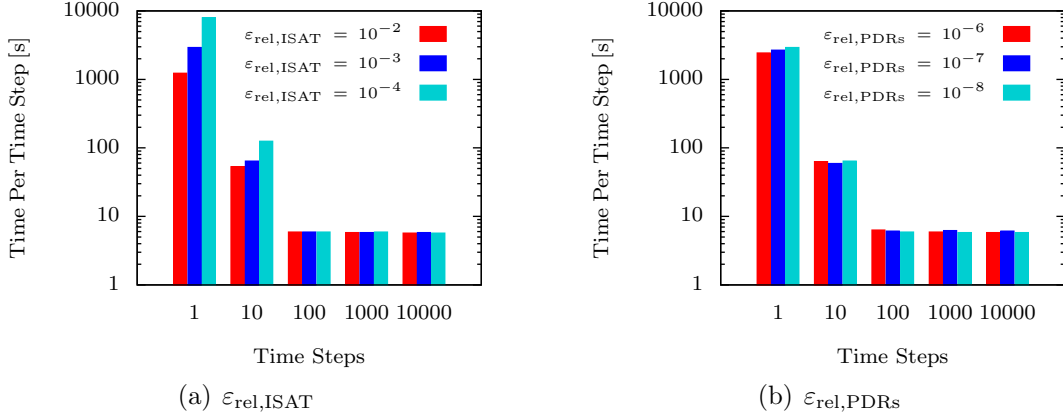


Figure 3.8: Sensitivity of the baseline computational cost per time step to ISAT and PDRs relative error tolerances for Sandia Flame D.

## 3.8 Improving ISAM Performance

Introducing further reductions of the computational cost of ISAM will allow it to be extended to increasingly high-dimensional manifold models capable of describing even more complex physics. The most expensive part of ISAM is associated with the *transient cost* of populating the ISAT tables with manifold solutions. Reduction of the overall ISAM cost can therefore be achieved from two directions: first, by populating the ISAT tables more quickly to attain the *steady-state cost* faster (MPI synchronization in ISAT), or second, by directly speeding up the manifold solver (PDRs) to reduce the initial *transient cost* (vectorization of the manifold solver and hybrid MPI/OpenMP parallelization).

### 3.8.1 MPI Synchronization

As previously stated, the initial ISAM implementation utilizes a separate ISAT database for each MPI process [43], each of which is completely isolated from one another. As a result, manifold calculations already performed by one MPI process are inaccessible to other processes, leading to redundant manifold calculations and a larger initial computational cost to construct the ISAT database. Even for a simple one-dimensional model, a single manifold

calculation costs more than a single LES time step. Therefore, it is critical to reduce the number of redundant manifold calculations and rapidly saturate the state space, ensuring that all subsequent queries to the ISAT database result in database *retrieves* rather than new database *additions* to reduce the number of manifold calculations to zero.

To reduce the computational cost of constructing the ISAT database, software infrastructure has been added that enables the synchronization of ISAT databases across MPI processes. Each time an ISAT database query results in an *addition* or a *growth*, the information stored in the newly-added leaf of the binary tree data structure is also stored in a buffer corresponding to the MPI process on which the query occurs. After a user-specified interval, each MPI process cycles through the buffers, copying the contents into its respective ISAT database. This process involves blocking communication to transfer the contents of each buffer to all MPI processes, so, for simulations that are not perfectly load-balanced, the initial cost will increase as processes wait for synchronization. This effect introduces a trade-off between computational cost incurred due to redundant manifold calculations and the consequence of imperfect load-balancing with blocking communication. Clearly, the synchronization interval and strategy is important to minimize the net effect of these issues and so the computational cost of constructing the ISAT database.

Multiple ISAM synchronization strategies are investigated and compared to COTF. First, ISAT databases are synchronized after each time step. To further reduce the number of redundant manifold calculations, the ISAT databases may also be synchronized multiple times during the first time step. If this additional synchronization is performed every  $x$  grid points (with  $x$  held constant), then it is termed *constant* synchronization. If the synchronization is performed every  $x$  grid points (with  $x$  increasing exponentially), then it is termed *exponential* synchronization. Multiple exponential forms of varying “aggressiveness” (meaning how much they deviate from a constant) are utilized. As a control, these strategies are compared to the performance of ISAM without any synchronization strategy in place.

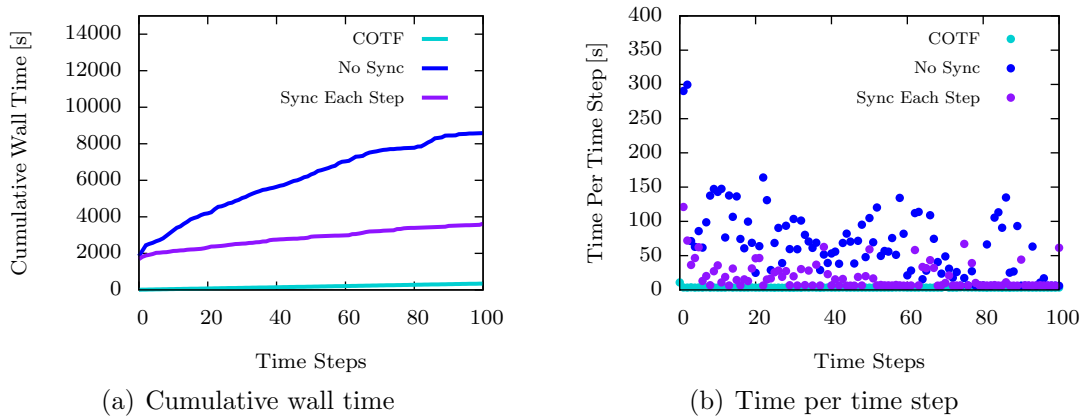


Figure 3.9: Computational cost measured as cumulative wall time and time per time step for LES of Sandia Flame D, comparing COTF, ISAM without MPI synchronization, and ISAM with MPI synchronization after every time step. The time per time step versus time steps plot limits the vertical range to visualize the fluctuations in computational cost.

Figure 3.9 compares the computational cost of simulating Sandia Flame D with COTF versus with ISAM, both without MPI synchronization and with synchronization implemented after every time step. The initial computational cost of ISAM observed during the first few time steps is due to the need to construct the thermochemical database. However, once this database is constructed, the cost of ISAM rapidly approaches the same steady-state cost as COTF. The jumps in the cumulative wall time observed at around the second and eighty-fifth time steps without synchronization are due to additional manifold calculations that have already been performed on other processors. The steady-state cost is unchanged with synchronization but is achieved much more rapidly after only about 10 time steps, versus 100 time steps without synchronization. As a result, synchronization halves the cumulative cost after 100 time steps. MPI synchronization is clearly very important to reduce the initial cost by quickly approaching the steady-state cost.

Figure 3.10 compares the computational cost of simulating Sandia Flame D with COTF versus with ISAM, now with additional synchronization strategies. When evaluating the computational cost of ISAM, it is important to consider both the cost of the first time step (during which the majority of the database is constructed) as well as the steady-state cost.

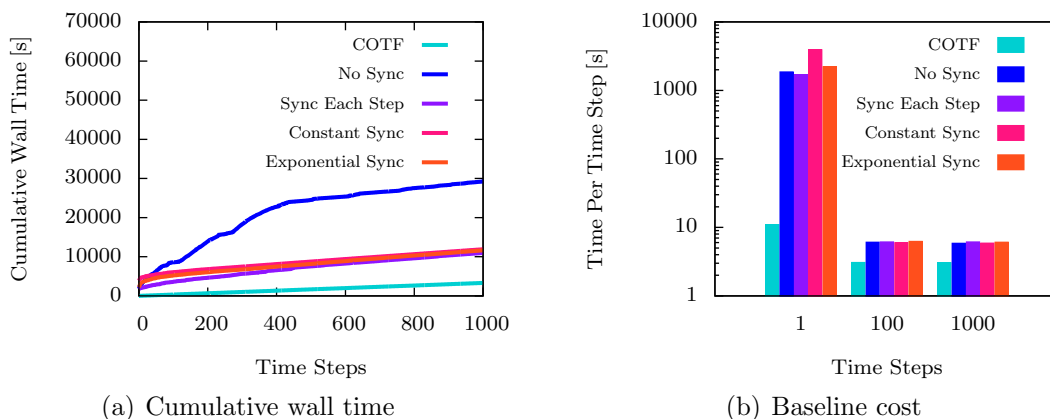


Figure 3.10: Computational cost measured as cumulative wall time and baseline cost for LES of Sandia Flame D, comparing COTF, ISAM without MPI synchronization, ISAM with MPI synchronization after every time step, ISAM with constant synchronization, and ISAM with exponential synchronization.

After 100 time steps, all MPI synchronization strategies yield the same steady-state cost as for with no synchronization strategy, which is to be expected since redundant manifold calculations are no longer performed once the steady-state cost has been reached. It is also clear that constant synchronization nearly doubles the cost of the first time step, as it adds too much communication blocking compared to exponential synchronization. The constant synchronization strategy is therefore discarded moving forward. For a simple one-dimensional manifold model, there is no significant benefit to additional exponential synchronization during the first time step over just synchronizing the ISAT databases at the end of each time step. However, synchronization during the first time step may become important depending on the input to ISAT and should be further investigated in the context of higher-dimensional manifold models.

### 3.8.2 Speeding Up Manifold Calculations

The computational cost of ISAM can also be further reduced by directly speeding up the calculation of manifold solutions. Vectorizing hotspots in the manifold solver PDRs – namely evaluation of the chemical source terms – yields a PDRs cost reduction of 35% ( $1.5\times$  speed-

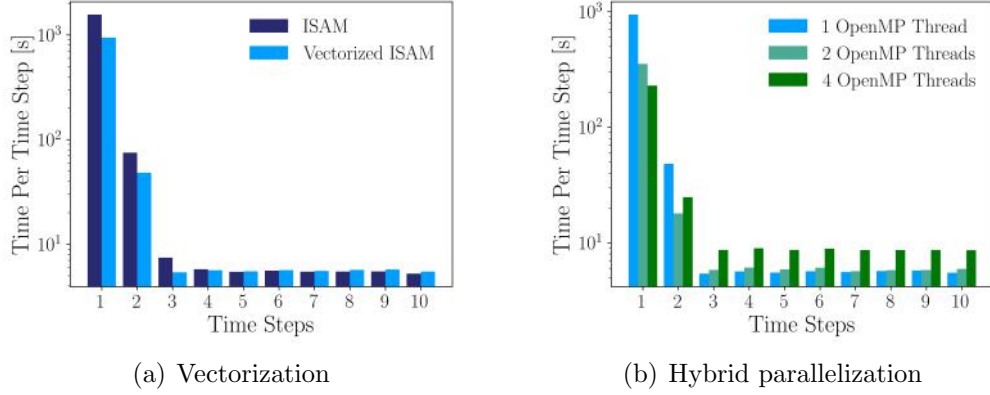


Figure 3.11: ISAM performance improvements for Sandia Flame D corresponding to vectorizing the manifold solver PDRs (a) and leveraging hybrid MPI/OpenMP parallelization (b). Figures adapted from Bonilla et al. [103].

up) [103]. Figure 3.11 (a) demonstrates that this translates to an equivalent speed-up in the transient cost of ISAM. Furthermore, redundant manifold solutions computed in the interval between MPI synchronization events can be mitigated with a reduction in the number of MPI processes. Leveraging the hybrid MPI/OpenMP parallelization built into the flow solver NGA, additional threads are freed up for use by the manifold solver PDRs when reducing the number of MPI processes for the same number of CPU cores. Figure 3.11 (b) demonstrates that the combined benefit of faster multithreaded manifold calculations and reduced manifold calculation redundancy considerably reduces the transient cost of ISAM a further 60% ( $2.5\times$  speed-up) when using 2 OpenMP threads and 80 MPI processes over 1 OpenMP thread and 160 MPI processes [103]. Using more than 2 OpenMP threads introduces additional steady-state cost due to imperfect NGA parallelization efficiency and single-threading in ISAT. The overall ISAM performance improvement with both vectorization of PDRs and hybrid MPI/OpenMP parallelization of NGA is therefore a transient cost reduction of nearly 75% ( $4\times$  speed-up) compared to the initial ISAM implementation.

### 3.9 Outcomes: ISAM

A new software implementation that integrates manifold-based modeling approaches and on-the-fly adaptive tabulation has been developed to address problems with existing methods involving pretabulation, which traditionally limit manifold model complexity. This approach, termed In-Situ Adaptive Manifolds (ISAM), was applied with the steady flamelet model to simulate two turbulent nonpremixed jet flames using both hydrogen and methane as fuels. Statistics demonstrated good agreement between ISAM and the conventional approach, verifying the ISAM implementation. The baseline cost of ISAM was shown to be comparable to that of previous pretabulation approaches after 100 – 1000 time steps (further reduced to only 10 time steps with MPI synchronization) for both hydrogen and methane chemical mechanisms, demonstrating the minimal overhead incurred by traversing binary trees and the insensitivity of the cost to the size of the chemical mechanism. Furthermore, introduction of a numerical ISAT Jacobian provided better numerical stability without incurring additional computational cost, synchronization of ISAT databases across MPI processes reduced the initial cost through quick convergence to the steady-state cost, and ongoing efforts to reduce the cost of manifold calculations yielded almost a further  $4\times$  speed-up over the initial ISAM implementation. Though this demonstration of ISAM has proved very promising, the test configurations simulated so far have admittedly been limited to the relatively simple nonpremixed manifold model. The ISAM approach will now be extended to the more complex manifold models it was developed to enable in the first place – combustion with multiple and/or inhomogeneous inlet streams and multi-modal combustion.

# Chapter 4

## Extension of ISAM to Multiple and/or Inhomogeneous Inlet Streams

This chapter presents work toward extending the ISAM approach to more general manifold models as per *Sub-Objective 2*, specifically to a case with inhomogeneous stream mixing. The nonpremixed manifold model is utilized again, this time with modified boundary conditions [33], resulting in additional inputs to ISAT. LES in these configurations are still tractable using pretabulation and serve as a more complex performance benchmark for ISAM. Strategies for synchronizing the ISAT databases across MPI processes are further investigated in the context of a higher-dimensional ISAT input space for which the computational cost of constructing ISAT databases is higher. The performance of ISAM and the sensitivity of output quantities of interest to the model-specific ISAT inputs is evaluated for a turbulent piloted jet flame representative of inhomogeneous, three-stream mixing.

### 4.1 Test Configuration: Sydney Flame

To evaluate the performance of the ISAM approach for a higher-dimensional manifold model, LES of a turbulent nonpremixed jet flame with three-stream mixing was performed. The configuration was initially developed at the University of Sydney [104, 105, 106] and consists



of a modified methane/air piloted burner assembly with an inhomogeneous central “fuel” stream composed of fuel and air (that inhomogeneously mix within the burner), pilot, and coflow air. Among the several experimental configurations available, the inhomogeneous case with a recess distance of 75 mm, a bulk jet velocity of 57 m/s, and a Reynolds number of 26,800 was selected for simulation. The piloted burner with inhomogeneous inlet conditions (from here on referred to as the Sydney flame) was simulated in cylindrical coordinates using a stretched grid with  $256 \times 128 \times 64$  grid points along the axial, radial, and circumferential directions, respectively. The inhomogeneous fuel stream inlet conditions for the Sydney flame were generated from a separate simulation of fully-developed, non-reacting, turbulent mixing [33]. The chemical mechanism for methane combustion, GRI-3.0 [100], was utilized and consists of 35 species with the nitrogen chemistry removed. The LES were performed using NGA [92, 93]. All subfilter transport terms were again closed with dynamic Smagorinsky-like models [81]. The one-dimensional manifold equations given by Eq. 3.3 and Eq. 3.4 were solved using the PDRs code [38, 94]. The relative error tolerances in ISAT and PDRs were set to  $10^{-3}$  and  $10^{-6}$ , respectively.

## 4.2 Nonpremixed Manifold Model: Modification for an Inhomogeneous Stream

The Sydney flame is an example of adiabatic nonpremixed combustion with an inhomogeneous fuel stream (that is, resulting from the partial mixing of two other streams) and a homogeneous oxidizer stream. For this case, two mixture fractions (both defined as conserved scalars) can be used to distinguish mixing between the inhomogeneous central stream and coflow air  $Z$  from mixing between fuel and any air  $Z^*$ . For combustion controlled by mixing between the inhomogeneous central “fuel” stream and coflow air, the manifold equations remain unchanged, and the fuel side boundary conditions are modified [33]. A fuel premixing fraction,  $F$ , is defined according to  $F = Z^*/Z$ , and corresponds to the fuel

fraction in the mixture originating from the inhomogeneous central stream. The fuel side boundary conditions are then modified according to

$$Y_i(B^1) = FY_i(B^{1,F}) + (1 - F)Y_i(B^{1,O}) = Y_i(F), \quad (4.1)$$

$$h(B^1) = Fh(B^{1,F}) + (1 - F)h(B^{1,O}) = h(F), \quad (4.2)$$

where  $h$  is the mixture specific enthalpy,  $B^1$  is the  $Z = 1$  boundary condition for the inhomogeneous central stream formed by the partial premixing of a fuel-containing stream  $B^{1,F}$ , and an air-containing stream  $B^{1,O}$ .

For adiabatic nonpremixed combustion with an inhomogeneous fuel stream and homogeneous oxidizer stream, the manifold solutions (in general) additionally depend on the fuel premixing fraction:

$$\tilde{\phi} = \iint \phi(Z, F) \tilde{P}(Z, F; \tilde{Z}, Z_v, \tilde{F}, F_v, \Sigma_{ZF}) dZ dF, \quad (4.3)$$

where  $\Sigma_{ZF} \equiv \widetilde{ZF} - \tilde{Z}\tilde{F}$  is the subfilter covariance of the mixture fraction and fuel premixing fraction. Perry et al. [33] found that presuming that the fuel premixing fraction does not vary on the subfilter scale is a reasonable assumption for the Sydney flame. With this assumption, the joint density-weighted subfilter PDF of the mixture fraction and fuel premixing fraction is replaced with a beta-delta distribution in mixture fraction and fuel premixing fraction:

$$\tilde{P}(Z, F; \tilde{Z}, Z_v, \tilde{F}, F_v, \Sigma_{ZF}) = \beta(Z; \tilde{Z}, Z_v) \delta(F - \tilde{F}), \quad (4.4)$$

which, when substituted into Eq. 4.3, yields

$$\tilde{\phi} = \int \phi(Z; \chi_{ZZ,\text{ref}}, \tilde{F}) \beta(Z; \tilde{Z}, Z_v) dZ. \quad (4.5)$$

The local reference dissipation rate is again computed from the filtered dissipation rate by inverting Eq. 4.5 when  $\phi = \chi_{ZZ}$ . Though the manifold equations, manifold coordinate, and manifold coordinate moments remain unchanged compared to the nonpremixed manifold model so that  $\mathbf{\Omega}_c = \{Z\}$  and  $\mathbf{\Omega}_q = \{\tilde{Z}, Z_v\}$ , this modification for inhomogeneous streams introduces an additional manifold parameter so that  $\mathbf{\Omega}_p = \{\chi_{ZZ}, \tilde{F}\}$ . The local density-weighted filtered fuel premixing fraction is obtained from  $\tilde{F} = \tilde{Z}^*/\tilde{Z}$ , assuming no subfilter correlation between the two mixture fractions, where the mixture fraction  $\tilde{Z}^*$  is obtained from a separate transport equation:

$$\frac{\partial \bar{\rho} \tilde{Z}^*}{\partial t} + \frac{\partial \bar{\rho} \tilde{u}_j \tilde{Z}^*}{\partial x_j} = \frac{\partial}{\partial x_j} \left[ \bar{\rho} (\tilde{D} + D_t) \frac{\partial \tilde{Z}^*}{\partial x_j} \right]. \quad (4.6)$$

Since the fuel premixing fraction is presumed not to vary on the subfilter scale,  $\tilde{F}$  is replaced with  $F$  from here on, in the interest of notational clarity.

For combustion with an inhomogeneous central “fuel” stream, the inputs to the ISAT database are both the reference scalar dissipation rate  $\chi_{ZZ,\text{ref}}$  and the fuel premixing fraction  $F$  such that the output stores the discrete solutions  $\phi_k(Z_j; \chi_{ZZ,\text{ref}}, F)$ . Convolution against the presumed subfilter PDF occurs in the same way as for homogeneous, two-stream cases, as described by Eq. 4.5.

### 4.3 Sydney Flame: Constrained Dissipation Rate

For a simple one-dimensional case with homogeneous, two-stream mixing, no significant benefit was observed when using additional exponential synchronization during the first time step over just synchronizing the ISAT databases at the end of each time step. However, synchronization during the first time step becomes important depending on the input to ISAT.

The Sydney flame was first simulated holding  $\chi_{ZZ,\text{ref}}$  constant at  $100 \text{ s}^{-1}$  and allowing  $F$  to vary freely in order to maintain the same number of inputs to ISAT as for Sandia Flame

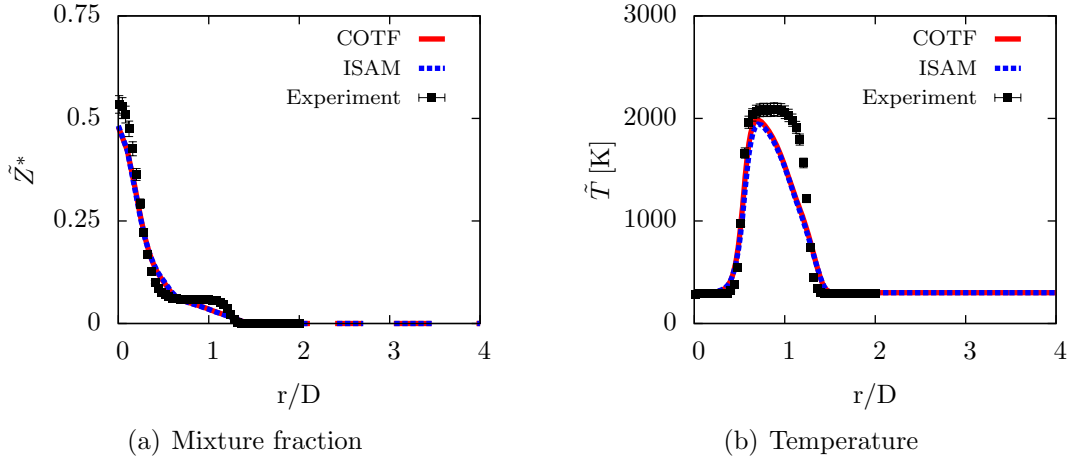


Figure 4.1: Time-averaged radial statistics for mixture fraction and temperature at  $x/D = 10$  for the Sydney flame with  $\chi_{ZZ,\text{ref}} = 100 \text{ s}^{-1}$ .

D (a single variable), isolating the impact of the particular choice of ISAT input variable. Figure 4.1 compares time-averaged radial statistics generated with COTF and ISAM to experimental measurements at 10 diameters downstream. Agreement with the experimental measurements is not expected to be perfect when the dissipation rate is constrained to a single value or when the nonpremixed manifold model is utilized in this upstream region where predominantly premixed combustion behavior dominates. However, more importantly, the statistics generated with the COTF and ISAM approaches agree with one another, as should be the case for two software implementations of the same modeling approach.

For the inhomogeneous Sydney flame, the transient cost associated with the first time step increases by almost an order of magnitude over Sandia Flame D. This increased transient computational cost can be attributed to a higher sensitivity of the manifold solutions to  $F$  than  $\chi_{ZZ,\text{ref}}$ . Figure 4.2 shows three examples of nonpremixed manifold solutions, two with the same  $F$  value and different  $\chi_{ZZ,\text{ref}}$  values and a third with a different  $F$  value. Since the value of the stoichiometric mixture fraction changes with  $F$ , a small change in  $F$  causes a more dramatic change in the profile than a change in  $\chi_{ZZ,\text{ref}}$ . As a result, ISAM databases require more leaves in the binary trees for  $F$ , since more manifold calculations are needed to

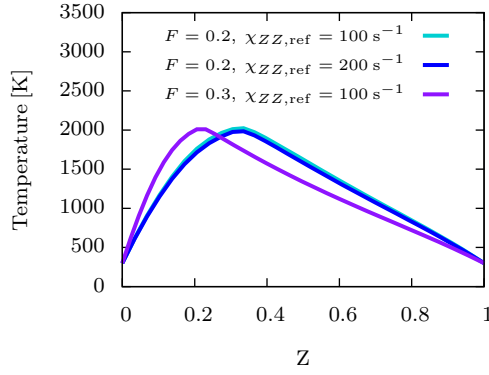


Figure 4.2: Nonpremixed manifold model solutions for  $F = 0.2$ ,  $\chi_{ZZ,\text{ref}} = 100 \text{ s}^{-1}$ ;  $F = 0.2$ ,  $\chi_{ZZ,\text{ref}} = 200 \text{ s}^{-1}$ ; and  $F = 0.3$ ,  $\chi_{ZZ,\text{ref}} = 100 \text{ s}^{-1}$ .

span the accessed state space. This is equivalent to a higher resolution requirement for  $F$  in a precomputed database.

Figure 4.3 compares the computational cost of simulating the Sydney flame with COTF versus with ISAM, synchronizing every time step as well as with two different forms of exponential synchronization. The observed trends demonstrate that, unlike for the case of Sandia Flame D, the synchronization strategy is critical to reducing the transient computational cost for the Sydney flame. Adopting an exponential synchronization strategy over synchronizing every time step yields more than a factor of four speed-up after the first time step. However, the specific exponential form is not as important, changing the cost of the first time step by less than fifty percent. Note also that though the transient cost is higher for the Sydney flame compared to Sandia Flame D, the steady-state cost remains the same order of magnitude at only around 10 seconds after 100 time steps. This observed increase in the steady-state cost is attributed to the larger binary trees required to store the unfiltered thermochemical state with a higher resolution in state space, for larger binary trees take longer to traverse.

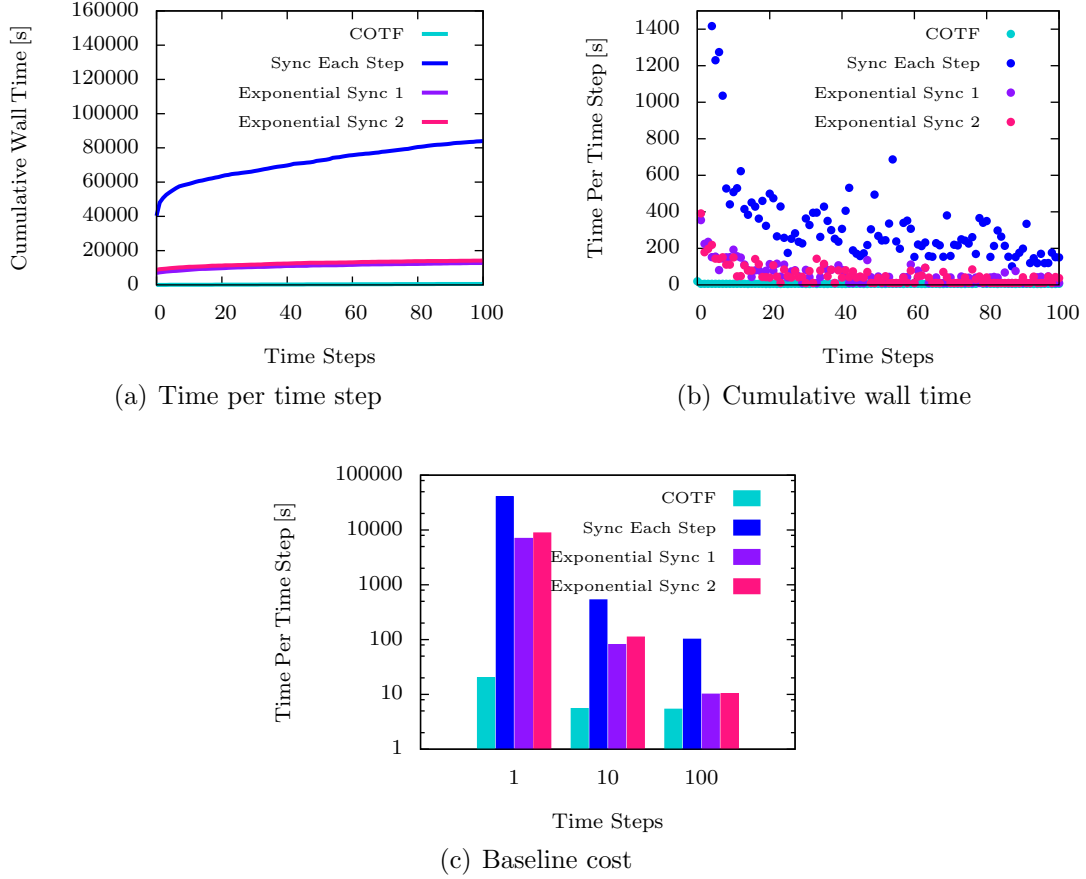


Figure 4.3: Computational cost measured as cumulative wall time, time per time step, and baseline cost for LES of the Sydney flame with  $\chi_{ZZ,\text{ref}} = 100 \text{ s}^{-1}$ , comparing COTF, ISAM with MPI synchronization after every time step, and ISAM with two forms of exponential synchronization.

## 4.4 Sydney Flame: Unconstrained Dissipation Rate

The single-value constraint on the reference mixture fraction dissipation rate is now removed, allowing both the reference mixture fraction dissipation rate and the fuel premixing fraction to vary freely. Figure 4.4 clearly demonstrates that only a portion of state space is realized in the LES, even when the reference mixture fraction dissipation rate is unconstrained. Since there is no way to know which points in this state space will be accessed in an LES *a priori*, pretabulation approaches such as COTF require the thermochemical database be precomputed and pretabulated, spanning the entire state space. Based on the sensitivity

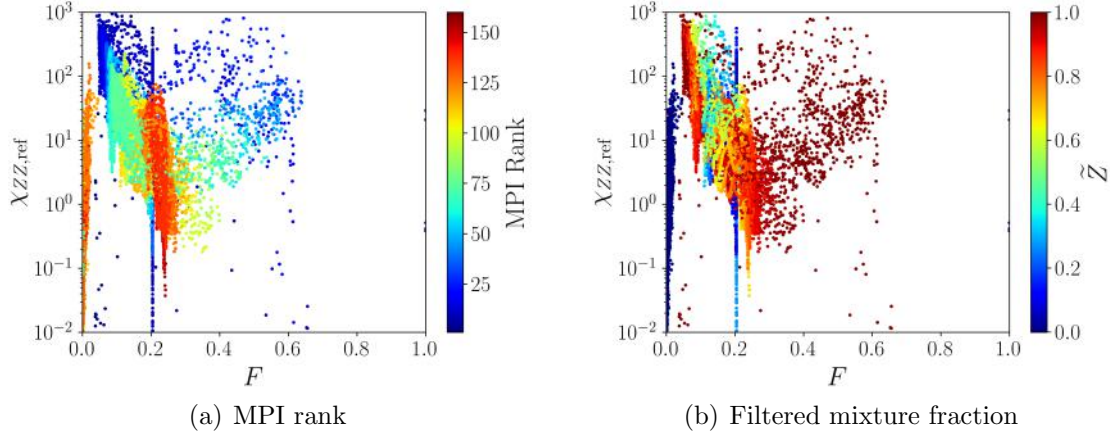


Figure 4.4: Single time snapshot of Sydney flame LES data plotted versus  $\chi_{ZZ,ref}$  and  $F$ , colored by the MPI rank in (a) and the filtered mixture fraction in (b).

demonstrated by Fig. 4.2, the thermochemical database for COTF is likely considerably under-resolved in the fuel premixing fraction and the mixture fraction grid. Assuming a more appropriate resolution of  $100 \times 1000$  points in  $\chi_{ZZ,ref}$  and  $F$ , respectively, a precomputed thermochemical database for COTF would take an estimated 833 hours to generate (in serial with 30 seconds per manifold calculation) and would occupy around 1 GB of memory. Despite the extremely high computational cost associated with pretabulation, many of the computed solutions would never be accessed over the course of an LES and are therefore wasted effort. To reduce cost, it is far more reasonable to construct the database on-the-fly with an approach such as ISAM.

Constructing the thermochemical database with ISAM ‘on-the-fly’ (without the improvements of Bonilla et al. [103] outlined in Sec. 3.8.2) only requires around 50 MB per ISAT table and is more than an order of magnitude faster than using pretabulation – though it is still quite slow due to blocking communication. Comparing the cost of the first time step between multiple forms of exponential synchronization demonstrates that the specific exponential form can impact the transient cost by over 30%. Using an aggressive exponential synchronization strategy (more frequent MPI synchronization at the beginning of the time step) yields a first time step cost of 49.1 hours, while instead adopting a less aggressive

exponential synchronization strategy yields 36.8 hours (less frequent MPI synchronization at the beginning of the time step). The cost of the first time step is therefore highly sensitive to the form of the exponential synchronization strategy for the Sydney flame, unlike Sandia D. This trend is observed due to the higher sensitivity to blocking communication in the Sydney flame as the number of required manifold calculations during the first time step increases – a combined effect of the higher-dimensionality of the ISAT state space and the higher-resolution requirement for the fuel premixing fraction. Including the ISAM performance improvements described in Sec. 3.8.2 mitigates the issue of blocking communication substantially, resulting in an additional order of magnitude ISAM speed-up in the first time step for the Sydney flame (around 4 hours compared to the 833 hours required by COTF).

Figure 4.4 (a) demonstrates considerable overlap in state space across ISAT tables associated with different MPI processes, highlighting the importance of frequent (but not too frequent) MPI synchronization during the first time step. Ideally, there would be little-to-no overlap in state space and MPI synchronization could be used more infrequently, further reducing the problem associated with blocking communication. A more sophisticated MPI synchronization strategy would take this into account, discretizing ISAT tables in state space as opposed to physical space (as in the work of Han et al. [102]) and dynamically consolidating and synchronizing the least accessed regions in state space. Such an approach would prove more challenging to implement from a software engineering point of view, but would allow for more infrequent MPI synchronization and better load-balancing. Figure 4.4 (b) shows that the large cluster of points located near zero fuel premixing fraction is present due to dividing by zero mixture fraction in the coflow regions of the domain.

## 4.5 Outcomes: Sydney Flame

In this chapter, ISAM was extended to a case with an inhomogeneous fuel stream using the nonpremixed manifold model and variable boundary conditions. Two inputs to ISAT



are required in this situation: the fuel premixing fraction  $F$  and the reference scalar dissipation rate  $\chi_{ZZ,\text{ref}}$ . Additional computational cost was incurred when changing the ISAT input variable to  $F$  due to the increased sensitivity of the manifold solutions to this parameter. However, this additional cost was shown to be mitigated substantially by synchronizing the ISAT databases across MPI processes combined with the ISAM performance improvements described in 3.8.2. Comparing multiple synchronization strategies revealed that exponential synchronization, in particular, has the potential to considerably reduce the cost of constructing ISAT databases for higher-dimensional, more general models moving forward. Most importantly, constructing a thermochemical database with ISAM was shown to incur a computational cost over two orders of magnitude less than that of pretabulation, while simultaneously requiring two orders of magnitude less memory than pretabulation. Though the thermochemical database memory requirement for COTF remains feasible for the configuration presented in this chapter, manifold models requiring even a single additional mixture fraction would be entirely untenable with pretabulation.

# Chapter 5

## Extension of ISAM to Multi-Modal Combustion

This chapter further addresses *Sub-Objective 2*, extending the ISAM approach to a manifold model applicable to multi-modal combustion. Unlike the inhomogeneous stream configuration of the previous chapter, the extension presented in this chapter involves both an increase in the dimensionality of the ISAT input space *and* an increase in the dimensionality of the manifold equations themselves, rendering pretabulation intractable and presenting a more demanding test of the ISAM approach. The details of the multi-modal manifold model are outlined in detail and employed to perform an LES of a multi-modal turbulent lifted hydrogen jet flame. The multi-modal manifold modeling approach is evaluated based on computational feasibility with ISAM as well as the interpretability of the model predictions.

### 5.1 Multi-Modal Manifold Model

Adiabatic, isobaric, two-stream, multi-modal combustion can be described with two-dimensional manifold equations in terms of the mixture fraction  $Z$  (defined in the same way as for nonpremixed combustion according to Eq. 3.1) and a generalized progress variable  $\Lambda$ , which takes a value of zero in an unburned gas mixture and unity at thermodynamic

equilibrium. Unlike the mixture fraction, the generalized progress variable  $\Lambda$  is ‘generated’ by chemical reactions, so it is not a conserved scalar. The generalized progress variable transport equation with unity effective Lewis number must therefore be modified according to

$$\frac{\partial \rho \Lambda}{\partial t} + \frac{\partial \rho u_j \Lambda}{\partial x_j} = \frac{\partial}{\partial x_j} \left( \rho D \frac{\partial \Lambda}{\partial x_j} \right) + \dot{m}_\Lambda, \quad (5.1)$$

where  $\dot{m}_\Lambda$  is the generalized progress variable source term, defined shortly.

A coordinate transformation into manifold variable space is defined, replacing derivatives in physical space and time via the chain rule:

$$\frac{\partial}{\partial t} = \frac{\partial Z}{\partial t} \frac{\partial}{\partial Z} + \frac{\partial \Lambda}{\partial t} \frac{\partial}{\partial \Lambda} \quad \text{and} \quad \frac{\partial}{\partial x_j} = \frac{\partial Z}{\partial x_j} \frac{\partial}{\partial Z} + \frac{\partial \Lambda}{\partial x_j} \frac{\partial}{\partial \Lambda}. \quad (5.2)$$

Assuming unity effective Lewis numbers, the temperature and species mass fraction transport equations in Eq. 2.8 and Eq. 2.9 are transformed into mixture fraction and generalized progress variable space, resulting in the multi-modal manifold equations [38]:

$$\begin{aligned} \frac{\partial T}{\partial \Lambda} \dot{m}_\Lambda &= \frac{\rho \chi_{ZZ}}{2} \frac{\partial^2 T}{\partial Z^2} + \rho \chi_{Z\Lambda} \frac{\partial^2 T}{\partial Z \partial \Lambda} + \frac{\rho \chi_{\Lambda\Lambda}}{2} \frac{\partial^2 T}{\partial \Lambda^2} - \frac{1}{c_p} \sum_k h_k \dot{m}_k \\ &+ \frac{1}{c_p} \left[ \frac{\rho \chi_{ZZ}}{2} \frac{\partial T}{\partial Z} \frac{\partial c_p}{\partial Z} + \frac{\rho \chi_{Z\Lambda}}{2} \left( \frac{\partial T}{\partial Z} \frac{\partial c_p}{\partial \Lambda} + \frac{\partial T}{\partial \Lambda} \frac{\partial c_p}{\partial Z} \right) + \frac{\rho \chi_{\Lambda\Lambda}}{2} \frac{\partial T}{\partial \Lambda} \frac{\partial c_p}{\partial \Lambda} \right] \\ &+ \sum_k \frac{c_{p,k}}{c_p} \left[ \frac{\rho \chi_{ZZ}}{2} \frac{\partial T}{\partial Z} \frac{\partial Y_k}{\partial Z} + \frac{\rho \chi_{Z\Lambda}}{2} \left( \frac{\partial T}{\partial Z} \frac{\partial Y_k}{\partial \Lambda} + \frac{\partial T}{\partial \Lambda} \frac{\partial Y_k}{\partial Z} \right) + \frac{\rho \chi_{\Lambda\Lambda}}{2} \frac{\partial T}{\partial \Lambda} \frac{\partial Y_k}{\partial \Lambda} \right], \end{aligned} \quad (5.3)$$

$$\frac{\partial Y_k}{\partial \Lambda} \dot{m}_\Lambda = \frac{\rho \chi_{ZZ}}{2} \frac{\partial^2 Y_k}{\partial Z^2} + \rho \chi_{Z\Lambda} \frac{\partial^2 Y_k}{\partial Z \partial \Lambda} + \frac{\rho \chi_{\Lambda\Lambda}}{2} \frac{\partial^2 Y_k}{\partial \Lambda^2} + \dot{m}_k, \quad (5.4)$$

where the generalized progress variable source term  $\dot{m}_\Lambda$  is defined using the solution to Eq. 5.4 for a reference species  $Y_R$  according to

$$\dot{m}_\Lambda \equiv \left[ \frac{1}{\partial Y_k / \partial \Lambda} \left( \frac{\rho \chi_{ZZ}}{2} \frac{\partial^2 Y_k}{\partial Z^2} + \rho \chi_{Z\Lambda} \frac{\partial^2 Y_k}{\partial Z \partial \Lambda} + \frac{\rho \chi_{\Lambda\Lambda}}{2} \frac{\partial^2 Y_k}{\partial \Lambda^2} + \dot{m}_k \right) \right]_R. \quad (5.5)$$

The marked advantage of this ‘generalized’ progress variable definition is that it does not require the reference species to be a linear combination of chemical species as is typically necessary. A nonlinear reference species definition is explored further by Novoselov et al. [69] as well as in Sec. 7.3. The work in this chapter leverages a linear reference species definition according to

$$Y_R(Z, \Lambda) = (1 - \Lambda)Y_{R,u}(Z) + \Lambda Y_{R,b}(Z) , \quad (5.6)$$

where  $Y_{R,u}$  and  $Y_{R,b}$  are the water mass fractions in the burned and unburned mixtures, respectively.

The additional parameters  $\chi_{ZZ}$ ,  $\chi_{Z\Lambda}$ , and  $\chi_{\Lambda\Lambda}$  in the multi-modal manifold equations are the mixture fraction dissipation rate, cross-dissipation rate, and generalized progress variable dissipation rate, respectively. Each of these dissipation rates represents an additional manifold parameter defined according to the general expression  $\chi_{\psi\omega} = 2D\nabla\psi \cdot \nabla\omega$ . The unfiltered thermochemical state is therefore expressed as a function of the mixture fraction, the generalized progress variable, and the three dissipation rates:

$$\phi(\mathbf{x}, t) \approx \phi_{\mathcal{M}}(Z[\mathbf{x}, t], \Lambda[\mathbf{x}, t], \chi_{ZZ}[\mathbf{x}, t], \chi_{Z\Lambda}[\mathbf{x}, t], \chi_{\Lambda\Lambda}[\mathbf{x}, t]) , \quad (5.7)$$

with two manifold coordinates  $\boldsymbol{\Omega}_c = \{Z, \Lambda\}$  and three manifold parameters  $\boldsymbol{\Omega}_p = \{\chi_{ZZ}, \chi_{Z\Lambda}, \chi_{\Lambda\Lambda}\}$ .

These three dissipation rates  $\chi_{\psi\omega}$  are fundamentally important to the multi-modal manifold model, for they encode the information about the underlying combustion process [70]. Each single-mode manifold model can be recovered from the multi-modal manifold equations in the asymptotic limits of zero dissipation rates. In homogeneous autoignition, the spatial gradients of mixture fraction and generalized progress variable are both zero so that  $\chi_{ZZ} = \chi_{Z\Lambda} = \chi_{\Lambda\Lambda} = 0$ , reducing the multi-modal manifold equations for temperature and

species mass fractions to

$$\frac{dT}{d\Lambda}\dot{m}_\Lambda = -\frac{1}{c_p} \sum_k h_k \dot{m}_k, \quad (5.8)$$

$$\frac{dY_k}{d\Lambda}\dot{m}_\Lambda = \dot{m}_k. \quad (5.9)$$

In premixed combustion, the spatial gradient of the mixture fraction is zero so that  $\chi_{ZZ} = \chi_{Z\Lambda} = 0, \chi_{\Lambda\Lambda} \neq 0$ , reducing the multi-modal manifold equations for temperature and species mass fractions to the premixed manifold equations later derived in Eq. 6.2 and Eq. 6.3. With an appropriate choice of reference species (discussed in more detail in Sec. 7.3), the spatial gradient of the generalized progress variable is zero in nonpremixed combustion so that  $\chi_{ZZ} \neq 0, \chi_{Z\Lambda} = \chi_{\Lambda\Lambda} = 0$ , reducing the multi-modal manifold equations for temperature and species mass fractions to the unsteady nonpremixed manifold equations (a generalization of the steady flamelet equations in Eq. 3.3 and Eq. 3.4):

$$c_p \frac{\partial T}{\partial \Lambda} \dot{m}_\Lambda = \frac{\rho c_p \chi_{ZZ}}{2} \frac{\partial^2 T}{\partial Z^2} + \frac{\rho \chi_{ZZ}}{2} \frac{\partial c_p}{\partial Z} \frac{\partial T}{\partial Z} + \frac{\rho \chi_{ZZ}}{2} \sum_k c_{p,k} \frac{\partial Y_k}{\partial Z} \frac{\partial T}{\partial Z} - \sum_k h_k \dot{m}_k, \quad (5.10)$$

$$\frac{\partial Y_k}{\partial \Lambda} \dot{m}_\Lambda = \frac{\rho \chi_{ZZ}}{2} \frac{\partial^2 Y_k}{\partial Z^2} + \dot{m}_k, \quad (5.11)$$

where the generalized progress variable source term introduces a pseudo time-like term reminiscent of the unsteady flamelet equations [27]. In this way, the simpler single-mode combustion models are built into the multi-modal manifold equations as asymptotic limits. Furthermore, the combustion modes intermediate to these asymptotic limits are nonlinear couplings of the single-mode models – a coupling which is embedded in the three dissipation rates  $\chi_{\psi\omega}$ .

To close the multi-modal manifold equations, the dependence of the dissipation rates on spatial gradients must instead be modeled as a function of the independent variables in Eq. 5.4 – namely, the mixture fraction and generalized progress variable. Typical algebraic models for dissipation rate profiles are developed for a single mode of combustion and often

with simplifying, ad hoc assumptions [68]. Often, the shape of the dissipation profiles are presumed to be ‘universal’ – that is, independent of space and time – and scaled by a reference value of the dissipation rate  $\chi_{\psi\omega,\text{ref}} \equiv \chi_{\psi\omega}(\psi_{\text{ref}}, \omega_{\text{ref}})$  or scaled alignment for the cross-dissipation rate. A novel modeling approach for the three dissipation rates that appear in the multi-modal manifold equations is discussed further in Chapter 7. In this chapter, the cross-dissipation rate is neglected entirely, enforcing  $\chi_{Z\Lambda}(Z, \Lambda) = 0$  per the work of Sitte and Mastorakos [47]. The mixture fraction dissipation rate is modeled presuming no dependence on the generalized progress variable, in the same way as for nonpremixed combustion:

$$\chi_{ZZ}(Z) = \chi_{ZZ,\text{ref}} \frac{f(Z)}{f(Z_{\text{ref}})}, \quad (5.12)$$

where

$$f(\psi) \equiv \exp\left(-2\left[\text{erfc}^{-1}(2\psi)\right]^2\right). \quad (5.13)$$

The generalized progress variable dissipation rate is modeled to possess the general shape as Eq. 5.13 while varying in both mixture fraction and generalized progress variable and possessing a peak value at the reference values [37, 69] given by

$$\chi_{\Lambda\Lambda}(Z, \Lambda) = \chi_{\Lambda\Lambda,\text{ref}} \frac{f(\Lambda)}{f(\Lambda_{\text{ref}})} \exp\left[-2\left(\text{erfc}^{-1}\left(\frac{2Z(1 - Z_{\text{ref}})}{(1 - Z)Z_{\text{ref}} + Z(1 - Z_{\text{ref}})}\right)\right)^2\right], \quad (5.14)$$

where  $Z_{\text{ref}} = Z_{\text{st}}$  and  $\Lambda_{\text{ref}} = 0.5$ .

In LES, the density-weighted filtered thermochemical state  $\tilde{\phi}$  is again obtained through convolution of the manifold solutions against a presumed subfilter PDF in terms of the manifold variables. The subfilter variation of the reference dissipation rates is typically neglected in LES. For adiabatic, isobaric, two-stream combustion:

$$\tilde{\phi} = \iint \phi(Z, \Lambda; \chi_{ZZ,\text{ref}}, \chi_{Z\Lambda,\text{ref}}, \chi_{\Lambda\Lambda,\text{ref}}) \tilde{P}(Z, \Lambda; \tilde{Z}, Z_v, \tilde{\Lambda}, \Lambda_v) dZ d\Lambda, \quad (5.15)$$

where the subfilter covariance of the mixture fraction and generalized progress variable  $\Sigma_{Z\Lambda} \equiv \widetilde{Z\Lambda} - \widetilde{Z}\widetilde{\Lambda}$  is neglected and presumed to be zero. Consistent with this approximation, the density-weighted subfilter PDF of the mixture fraction and generalized progress variable is taken to be the product of two independent distributions, each further presumed to be a beta distribution so that  $\widetilde{P}(Z, \Lambda; \widetilde{Z}, Z_v, \widetilde{\Lambda}, \Lambda_v) = \beta(Z; \widetilde{Z}, Z_v)\beta(\Lambda; \widetilde{\Lambda}, \Lambda_v)$ . The density-weighted subfilter PDF is parameterized by the filtered mixture fraction  $\widetilde{Z}$ , the filtered generalized progress variable  $\widetilde{\Lambda}$ , and their corresponding subfilter variances  $Z_v$  and  $\Lambda_v$ , all of which are obtained from transport equations. The manifold coordinate moments for the multi-modal manifold model (as implemented, neglecting the covariance) are therefore  $\mathbf{\Omega}_q = \{\widetilde{Z}, Z_v, \widetilde{\Lambda}, \Lambda_v\}$ . The transport equations for the filtered mixture fraction and mixture fraction subfilter variance are given by Eq. 3.12 and Eq. 3.13. Since the generalized progress variable is not a conserved scalar, the transport equations for its corresponding moments are slightly modified according to

$$\frac{\partial \bar{\rho}\widetilde{\Lambda}}{\partial t} + \frac{\partial \bar{\rho}\widetilde{u}_j\widetilde{\Lambda}}{\partial x_j} = \frac{\partial}{\partial x_j} \left[ \bar{\rho} \left( \widetilde{D} + D_t \right) \frac{\partial \widetilde{\Lambda}}{\partial x_j} \right] + \bar{m}_\Lambda, \quad (5.16)$$

$$\begin{aligned} \frac{\partial \bar{\rho}\Lambda_v}{\partial t} + \frac{\partial \bar{\rho}\widetilde{u}_j\Lambda_v}{\partial x_j} = & \frac{\partial}{\partial x_j} \left[ \bar{\rho} \left( \widetilde{D} + D_t \right) \frac{\partial \Lambda_v}{\partial x_j} \right] - \bar{\rho} \left[ \widetilde{\chi}_{\Lambda\Lambda} - 2 \left( \widetilde{D} + D_t \right) \frac{\partial \widetilde{\Lambda}}{\partial x_j} \frac{\partial \widetilde{\Lambda}}{\partial x_j} \right] \\ & + 2 \left( \overline{\Lambda\dot{m}_\Lambda} - \widetilde{\Lambda}\bar{m}_\Lambda \right), \end{aligned} \quad (5.17)$$

where the subfilter scalar flux has been closed by applying the gradient diffusion hypothesis. The filtered generalized progress variable source term  $\bar{m}_\Lambda$  is obtained with Eq. 5.15 according to

$$\bar{m}_\Lambda = \bar{\rho} \iint \frac{\dot{m}_\Lambda}{\rho}(Z, \Lambda; \chi_{ZZ,\text{ref}}, \chi_{Z\Lambda,\text{ref}}, \chi_{\Lambda\Lambda,\text{ref}}) \widetilde{P}(Z, \Lambda; \widetilde{Z}, Z_v, \widetilde{\Lambda}, \Lambda_v) dZ d\Lambda. \quad (5.18)$$

The filtered generalized progress variable dissipation rate  $\widetilde{\chi}_{\Lambda\Lambda}$  is closed similarly to the mixture fraction dissipation rate in Eq. 3.14 [89]:

$$\widetilde{\chi}_{\Lambda\Lambda} \equiv \widetilde{2D \frac{\partial \Lambda}{\partial x_j} \frac{\partial \Lambda}{\partial x_j}} \approx 2\widetilde{D} \frac{\partial \widetilde{\Lambda}}{\partial x_j} \frac{\partial \widetilde{\Lambda}}{\partial x_j} + C_{\chi_{\Lambda\Lambda}} \frac{\nu_t}{\Delta^2} \left( \widetilde{\Lambda^2} - \widetilde{\Lambda}^2 \right). \quad (5.19)$$

The local reference dissipation rates  $\chi_{\psi\omega,\text{ref}}$  can be computed from corresponding filtered dissipation rates  $\tilde{\chi}_{\psi\omega}$  by inverting Eq. 5.15 when  $\phi = \chi_{\psi\omega}$ , presuming there is no appreciable subfilter variation in the reference dissipation rates.

Neglecting the cross-dissipation rate, the multi-modal manifold model requires both the mixture fraction reference scalar dissipation rate  $\chi_{ZZ,\text{ref}}$  and the generalized progress variable reference scalar dissipation rate  $\chi_{\Lambda\Lambda,\text{ref}}$  as inputs to the ISAT database. The ISAT databases also store the outputs comprising the discrete solutions  $\phi_k(Z_i, \Lambda_j; \chi_{ZZ,\text{ref}}, \chi_{\Lambda\Lambda,\text{ref}})$  to the multi-modal manifold equations, where  $Z_i$  are the discrete points in mixture fraction space and  $\Lambda_j$  are the discrete points in generalized progress variable space. Convolution against the presumed subfilter PDF occurs in the same way as for the nonpremixed manifold model but extended for an additional dimension.

## 5.2 Test Configuration: Cabra Flame

The configuration selected to evaluate the multi-modal manifold model with ISAM is a lifted hydrogen jet flame with a vitiated coflow stream, based on the experimental Cabra burner [107, 108]. The Cabra flame possesses a central diluted hydrogen jet (74%  $\text{N}_2$ , by volume) with a velocity  $V_{\text{jet}}$  of 107 m/s and a temperature  $T_{\text{jet}}$  of 305 K. The coflow is composed of vitiated product species (corresponding to an equivalence ratio of 0.25) with a velocity  $V_{\text{coflow}}$  of 3.5 m/s and a temperature  $T_{\text{coflow}}$  of 1,045 K. The flame is generally agreed to be stabilized by autoignition, possessing a trailing nonpremixed flame downstream of the lift-off location. However, the particular lift-off height observed in experiments has been shown to vary considerably with small variations in coflow conditions [109]. The Cabra flame is therefore only used to qualitatively validate the multi-modal manifold model by investigating its ability to predict the same stabilization mechanism and general behavior rather than expecting quantitative agreement with the experimental lift-off height.



LES of the Cabra flame was performed using the structured, finite-difference, low Mach number flow solver NGA [92, 93]. Subfilter transport terms were again closed with dynamic Smagorinsky-like models [81], a third-order WENO scheme was used to discretize the convective terms in scalar equations [110], and the two-dimensional multi-modal manifold equations given by Eq. 5.3 and Eq. 5.4 were solved using PDRs [94]. The stretched manifold solution grid in mixture fraction and generalized progress variable space possessed  $16 \times 16$  grid points, respectively – sufficient resolution for a qualitative assessment of the predictive capabilities of the multi-modal manifold model. The physical space LES grid possessed  $256 \times 144 \times 64$  grid points along the axial, radial, and circumferential directions, respectively. The relative error tolerances in ISAT and PDRs were set to  $10^{-1}$  and  $10^{-6}$ , respectively. Note that the LES was performed without a numerical ISAT Jacobian or the performance improvements described in Sec. 3.8.

## 5.3 Evaluation of Multi-Modal Model Performance

### 5.3.1 Feasibility

The performance of the multi-modal model with ISAM is first evaluated by considering computational cost and required memory. Figure 5.1 demonstrates that the transient cost of the multi-modal model is more expensive than the nonpremixed manifold model, but less expensive than the nonpremixed manifold model modified for an inhomogeneous central stream (note that ‘error checking’ is an ISAT feature that was used to provide simulation stability before the addition of the numerical ISAT Jacobian). Even without the performance improvements of Sec. 3.8, the first time step takes around one hour. This relatively large computational cost quickly levels off after only 100 - 1000 time steps, as was observed for the nonpremixed manifold model. A filtered thermochemical database for use with the PPP approach with a conservative estimate of 100 points in each  $\chi_{ZZ,\text{ref}}$ ,  $\chi_{\Lambda\Lambda,\text{ref}}$ ,  $\tilde{Z}$ ,  $Z_v$ ,  $\tilde{\Lambda}$ , and  $\Lambda_v$  would take around 100 hours to generate and occupy around 500 TB of memory. In contrast,

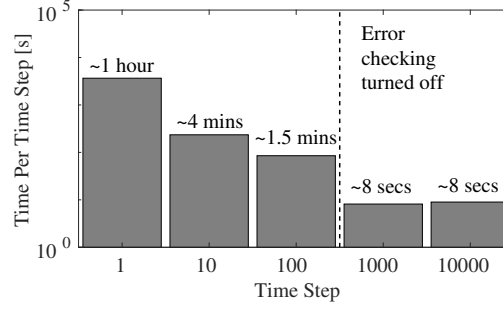


Figure 5.1: Baseline computational cost per time step for the Cabra flame. The dashed line (--) denotes that ‘error checking’ is disabled in ISAT after 100 time steps. Figure taken from Novoselov et al. [70].

the ISAT tables generated for the multi-modal model with ISAM take a couple of hours to populate and are each only around 50 MB. The ISAM approach therefore involves two orders of magnitude less computational overhead compared to PPP and seven orders of magnitude less memory.

Most importantly, Fig. 5.1 also shows that the final steady-state cost is only around 8 seconds per time step, approximately the same cost as the nonpremixed manifold model with or without the modification for an inhomogeneous central stream. This result provides further evidence that the overhead associated with traversing binary trees in ISAT is negligible, suggesting that the ISAM approach can practically be extended to even more complex manifold models that simultaneously account for multi-modal combustion as well as additional complex combustion phenomena such as pressure variation, heat losses, and multiple and/or inhomogeneous inlet streams.

### 5.3.2 Interpretability

Figure 5.2 shows the time-averaged centerline statistics for temperature in the Cabra flame as predicted by the LES, demonstrating that the flame is statistically lifted at a downstream axial location of around  $x/D_{\text{jet}} = 37$ . Though this result lies on the high-end of experimentally observed lift-off heights, the high sensitivity of the lift-off height to the burner conditions

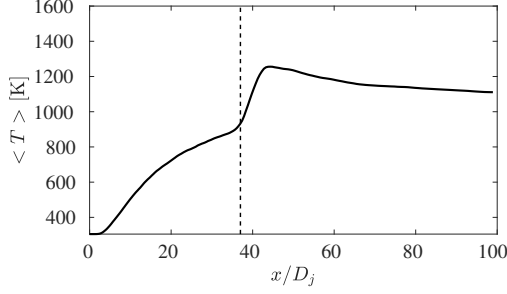


Figure 5.2: Time-averaged centerline profile of temperature (—). The flame is found to be statistically lifted at  $x/D_{\text{jet}} = 37$ , denoted by a dashed line (- -). Figure taken from Novoselov et al. [70].

implies only qualitative agreement with experiments should be expected. Regardless, the objective of this evaluation is not to quantitatively match the lift-off height but to predict the same qualitative flame behavior, as previously discussed. To assess the qualitative flame behavior predicted by the multi-modal manifold model, three inverse timescales are defined:

$$S_{\dot{m}_\Lambda} \equiv \bar{m}_\Lambda / \bar{\rho} \tilde{\Lambda}, \quad (5.20)$$

$$S_{\chi_{ZZ}} \equiv \tilde{\chi}_{ZZ} / \tilde{Z}^2, \quad (5.21)$$

$$S_{\chi_{\Lambda\Lambda}} \equiv \tilde{\chi}_{\Lambda\Lambda} / \tilde{\Lambda}^2. \quad (5.22)$$

As discussed in Sec. 5.1, homogeneous autoignition exists in the limit that all three dissipation rates are zero, corresponding to a situation where  $S_{\dot{m}_\Lambda}$  dominates relative to  $S_{\chi_{ZZ}}$  and  $S_{\chi_{\Lambda\Lambda}}$ . Premixed combustion occurs in the limit of zero mixture fraction dissipation rate and cross-dissipation rate, corresponding to a situation where  $S_{\chi_{\Lambda\Lambda}}$  dominates relative to  $S_{\dot{m}_\Lambda}$  and  $S_{\chi_{ZZ}}$ . With a linear choice of reference species, nonpremixed combustion occurs where  $S_{\chi_{ZZ}}$  is large relative to  $S_{\dot{m}_\Lambda}$ .  $S_{\chi_{\Lambda\Lambda}}$  can also be expected to be appreciable since gradients of generalized progress variable are only zero in nonpremixed combustion with a nonlinear choice of reference species (see Sec. 7.3).

Figure 5.2 presents these inverse time scales plotted on a semi-log plot for four instantaneous centerline snapshots of the Cabra flame LES. These four snapshots demonstrate that

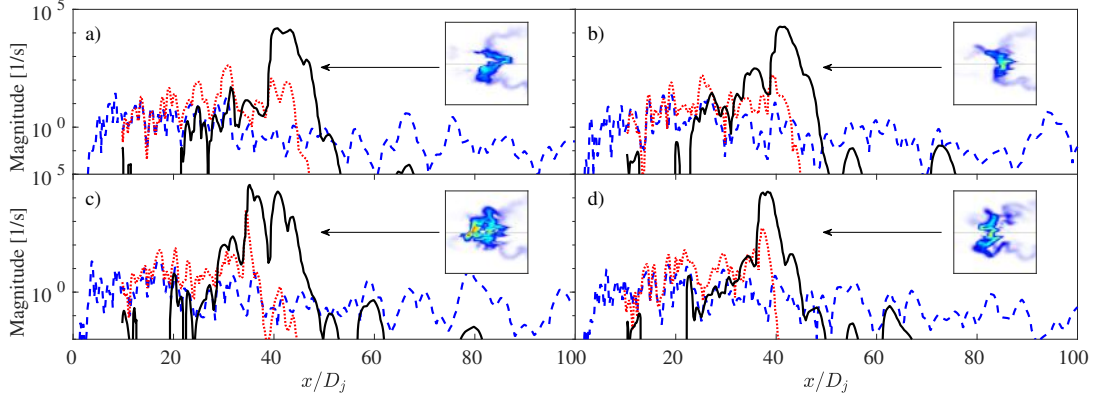


Figure 5.3: Instantaneous centerline snapshots of the three inverse time scales  $S_{\dot{m}_\Lambda}$  ( $\text{—}$ ),  $S_{\chi_{\Lambda\Lambda}}$  ( $\cdots$ ), and  $S_{\chi_{ZZ}}$  ( $-\cdot-$ ). Snapshots (a)-(d) are presented in chronological order, each separated by approximately 2 milliseconds in time. Provided insets share the same linear colorbar and display the generalized progress variable source term fields centered around  $x/D_{\text{jet}} = 40$ . Figure taken from Novoselov et al. [70].

the same qualitative behavior is exhibited at all time, but the following discussion focuses on Fig. 5.2 (a) for illustrative purposes. Starting upstream at  $x/D_{\text{jet}} < 10$ , the dominant term is  $S_{\chi_{ZZ}}$ . Since the temperature is low in this region, the multi-modal manifold model indicates that nonreactive mixing is dominant upstream. Further downstream where  $10 < x/D_{\text{jet}} < 37$ ,  $S_{\chi_{\Lambda\Lambda}}$  grows and eventually dominates over  $S_{\dot{m}_\Lambda}$  and  $S_{\chi_{ZZ}}$ , indicating the activation of generalized progress variable transport. At  $37 < x/D_{\text{jet}} < 50$ ,  $S_{\dot{m}_\Lambda}$  is by far the largest term, suggesting that ignition occurs. Since this location is where the flame is predicted to be statistically lifted in Fig. 5.2, the multi-modal model predicts that the Cabra flame is kinetically stabilized. Finally, even further downstream where  $x/D_{\text{jet}} > 50$ ,  $S_{\chi_{ZZ}}$  begins to dominate again, indicating a nonpremixed flame trails behind the lift-off location. In this way, the multi-modal manifold model predicts the correct modal behavior of the Cabra flame (kinetically stabilized with a trailing nonpremixed flame) as an output of the model, whereas traditional single-mode manifold models have always required the combustion mode be an input to the model.

To further investigate the mechanism triggering ignition, focus is returned to the region where  $10 < x/D_{\text{jet}} < 37$ . Figure 5.4 shows an instantaneous radial snapshot of the three

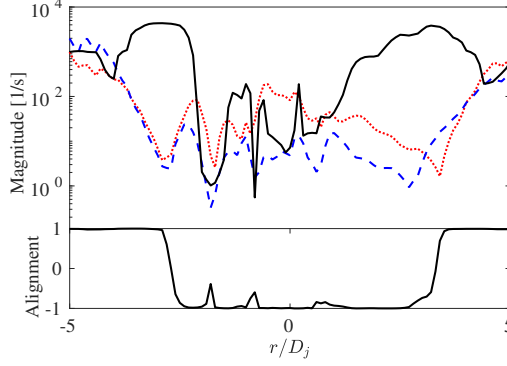


Figure 5.4: Instantaneous radial snapshot of the three inverse time scales  $S_{\dot{m}_\Lambda}$  ( $\text{—}$ ),  $S_{\chi_{\Lambda\Lambda}}$  ( $\cdots$ ), and  $S_{\chi_{ZZ}}$  ( $\text{-- --}$ ) is shown on top. The instantaneous radial snapshot of the alignment of the mixture fraction and generalized progress variable gradients is shown on bottom. Both snapshots correspond to that of Fig. 5.3 (a). Figure taken from Novoselov et al. [70].

inverse timescales at  $x/D_{\text{jet}} = 25$ . The dominance of  $S_{\dot{m}_\Lambda}$  away from the centerline and the importance of  $S_{\chi_{\Lambda\Lambda}}$  between the two peaks of  $S_{\dot{m}_\Lambda}$  indicates that radicals are formed at the most reactive mixture fraction and carried to the centerline via reactive transport. The alignment of the mixture fraction and generalized progress variable gradients can be defined as the cosine of the angle between them according to

$$\Theta \equiv \frac{\nabla Z \cdot \nabla \Lambda}{|\nabla Z| |\nabla \Lambda|}, \quad (5.23)$$

where  $\Theta = 1$  corresponds to perfect alignment of the gradients,  $\Theta = -1$  corresponds to anti-alignment of the gradients, and  $\Theta = 0$  corresponds to perpendicular gradients. Considering the alignment changes sign across the peaks of  $S_{\dot{m}_\Lambda}$ , progress variable transport occurs along gradients of the mixture fraction. This observation implies that the cross-dissipation may in fact be important to quantitative predictions of multi-modal combustion and should likely not be neglected.

## 5.4 Outcomes: Cabra Flame

This chapter extended the ISAM approach to a manifold model applicable to multi-modal combustion. The performance of the multi-modal manifold model was evaluated via LES of the Cabra flame – a turbulent lifted hydrogen jet flame that exhibits multi-modal behavior. The computational cost of ISAM was shown to be feasible, with a transient cost of only a couple of hours and a rapid plateau after only 100 time steps to a steady-state cost comparable to that of the nonpremixed manifold model. Implementation of the performance improvements in Sec. 3.8 would offer further reduction of the transient cost. Even with the initial ISAM implementation, two orders of magnitude reduction in computational cost and seven orders of magnitude reduction in the memory requirement was attained relative to the PPP approach. The multi-modal manifold model also successfully predicted the qualitative behavior of the Cabra flame (kinetically stabilized with a trailing nonpremixed flame) – the first time a manifold model has demonstrated the ability to produce the combustion mode as a model output rather than a model input.

# Chapter 6

## Data-Based Dissipation Rate Modeling for Premixed Combustion

Up to this point, the development of the ISAM algorithm and its extension to more general, higher-dimensional manifold models has been presented. This chapter marks a shift in objective. The remainder of this dissertation instead focuses on leveraging data to address *Sub-Objective 3* – constructing instantaneous manifold parameter (dissipation rate) models for manifold modeling of turbulent combustion. The ultimate goal is to close the dissipation rate profiles in the multi-modal manifold equations given by Eq. 5.3 and Eq. 5.4 via a data-based approach. As an initial step toward achieving this goal, this chapter sets out to first use a deep neural network to model the instantaneous dissipation rates profiles in a simple one-dimensional manifold model applicable to premixed combustion.

### 6.1 Premixed Manifold Model

For the case of adiabatic, premixed combustion, the thermochemical state is parameterized in terms of the generalized progress variable  $\Lambda$  and the generalized progress variable dissipation rate  $\chi_{\Lambda\Lambda} \equiv 2D_{\Lambda}\nabla\Lambda\cdot\nabla\Lambda$ . The generalized progress variable is again defined to take a value of

zero in an unburned premixture of fuel and oxidizer and unity at thermodynamic equilibrium. The transport equation for the generalized progress variable is given by Eq. 5.1.

A coordinate transformation that replaces the independent variables in Eq. 2.8 and Eq. 2.9 from physical coordinates and time to generalized progress variable is defined by

$$\frac{\partial}{\partial t} = \frac{\partial \Lambda}{\partial t} \frac{d}{d\Lambda} \quad \text{and} \quad \frac{\partial}{\partial x_j} = \frac{\partial \Lambda}{\partial x_j} \frac{d}{d\Lambda}, \quad (6.1)$$

and, when applied to the temperature and species mass fraction transport equations, yields the one-dimensional premixed manifold equations for the temperature and species mass fractions with unity effective Lewis numbers:

$$c_p \frac{dT}{d\Lambda} \dot{m}_\Lambda = \frac{\rho c_p \chi_{\Lambda\Lambda}}{2} \frac{d^2 T}{d\Lambda^2} + \frac{\rho \chi_{\Lambda\Lambda}}{2} \frac{dc_p}{d\Lambda} \frac{dT}{d\Lambda} + \frac{\rho \chi_{\Lambda\Lambda}}{2} \sum_k c_{p,k} \frac{dY_k}{d\Lambda} \frac{dT}{d\Lambda} - \sum_k h_k \dot{m}_k, \quad (6.2)$$

$$\frac{dY_k}{d\Lambda} \dot{m}_\Lambda = \frac{\rho \chi_{\Lambda\Lambda}}{2} \frac{d^2 Y_k}{d\Lambda^2} + \dot{m}_k. \quad (6.3)$$

Alternatively, Eq. 6.2 and Eq. 6.3 may be obtained from the multi-modal manifold equations in the asymptotic limit of premixed combustion. According to the premixed manifold model, the unfiltered thermochemical state  $\phi$  is therefore expressed as a function of the generalized progress variable and the generalized progress variable dissipation rate:

$$\phi(\mathbf{x}, t) \approx \phi_{\mathcal{M}}(\Lambda[\mathbf{x}, t], \chi_{\Lambda\Lambda}[\mathbf{x}, t]), \quad (6.4)$$

with a single manifold coordinate  $\Omega_c = \{\Lambda\}$  and a single manifold parameter  $\Omega_p = \{\chi_{\Lambda\Lambda}\}$ .

To close the one-dimensional premixed manifold equations, a presumed dependence of the dissipation rate on the generalized progress variable is required – that is, the conditional generalized progress variable dissipation rate. This conditional generalized progress variable dissipation rate is typically expressed as some presumed profile  $f(\Lambda)$  scaled by a reference



value  $\chi_{\Lambda\Lambda,\text{ref}}$ :

$$\chi_{\Lambda\Lambda}(\Lambda) = \chi_{\Lambda\Lambda,\text{ref}} \frac{f(\Lambda)}{f(\Lambda_{\text{ref}})} \equiv \chi_{\Lambda\Lambda,\text{ref}} g(\Lambda), \quad (6.5)$$

where the characteristic reference value for the dissipation rate  $\chi_{\Lambda\Lambda,\text{ref}}$  is evaluated at the reference generalized progress variable  $\Lambda_{\text{ref}}$ . The profile  $g(\Lambda)$ , discussed in further detail in Sec. 6.2.3, includes the scaling factor at the reference generalized progress variable. The conditional generalized progress variable dissipation rate can be modeled based on the *unstretched* solution to freely-propagating premixed flat flames [37]:

$$g_u(\Lambda) = \frac{\chi_{\Lambda\Lambda}^u(\Lambda)}{\chi_{\Lambda\Lambda}^u(\Lambda_{\text{ref}})}, \quad (6.6)$$

or based on an analytical solution for the dissipation rate in a *stretched* counterflow flame [68], which assumes constant  $\rho^2 D$ :

$$g_s(\Lambda) = \frac{\exp\left(-2\left[\text{erfc}^{-1}(2\Lambda)\right]^2\right)}{\exp\left(-2\left[\text{erfc}^{-1}(2\Lambda_{\text{ref}})\right]^2\right)}, \quad (6.7)$$

where  $u$  and  $s$  denote unstretched and stretched solutions, respectively. Both models implicitly assume that the conditional dissipation rate profiles are ‘universal,’ meaning their shapes do not vary with the local flow conditions. The conditional dissipation rate profiles are only scaled by the local value of  $\chi_{\Lambda\Lambda,\text{ref}}$  in LES or RANS. Previous work that investigated the instantaneous conditional dissipation rate (formulated based on mixture fraction rather than generalized progress variable) for nonpremixed combustion in spray flames demonstrated appreciable variation in the observed profile shape with respect to flow parameters, yet the shape was accurately modeled via a data-based approach [111]. The first objective of this chapter is to determine whether the assumption of spatiotemporal ‘universality’ is valid for turbulent premixed combustion by extracting the instantaneous conditional generalized progress variable dissipation rate profiles from DNS data of turbulent premixed jet flames at varying Karlovitz numbers.

## 6.2 DNS Data and Profile Extraction

### 6.2.1 DNS Data

Two DNS databases of turbulent premixed planar jet flames [112, 113] have been leveraged to evaluate the spatial and temporal non-uniformity of the instantaneous conditional dissipation rate. Both configurations consist of a turbulent central jet of a stoichiometric hydrogen-air premixture (diluted with 20% nitrogen by volume), a laminar coflow of equilibrium products, and a jet Reynolds number of 5000 defined by  $Re_0 \equiv U_0 H_0 / \nu$  where  $\nu$ ,  $U_0$ , and  $H_0$  are the kinematic viscosity, velocity, and height of the central jet, respectively. The two databases correspond to a low (Case K1) and high (Case K2) Karlovitz number. Case K1 is dominated by chemistry effects due to a longer Kolmogorov time scale relative to the flame time scale, while Case K2 is dominated by turbulence effects due to an increased turbulence intensity and a shorter Kolmogorov time scale. Relevant simulation parameters at  $x/H_0 = 3$  are summarized in Table 6.1.

A low Mach number, finite-difference solver with a structured, non-uniform grid in Cartesian coordinates [92, 93] was used to solve the transport equations for mass, momentum, temperature, and species mass fractions, along with the ideal gas equation of state. The chemical mechanism for hydrogen combustion consisted of nine species [98] with constant, non-unity Lewis numbers [74].

Table 6.1: DNS parameters.

Case	K1	K2
$Ka_{\tilde{\Lambda}=0.5}$	3.7	54.0
$Da_{\tilde{\Lambda}=0.5}$	0.60	0.05
$U_0$ (m/s)	23.4	93.4
$H_0$ (mm)	4.32	1.08
$Re_0$	5000	
$s_L$ (m/s)	1.195	
$\delta_F$ (mm)	0.435	

### 6.2.2 Extraction Methodology

Instantaneous conditional generalized progress variable dissipation rate profiles  $\chi_{\Lambda\Lambda}(\Lambda)$  have been extracted from the DNS databases by tracing out paths aligned with the local generalized progress variable gradient (hereafter referred to as generalized progress variable streamlines) and defining  $\chi_{\Lambda\Lambda}(\Lambda)$  as the dependence of  $\chi_{\Lambda\Lambda}$  on  $\Lambda$  along these generalized progress variable streamlines. The generalized progress variable  $\Lambda$  is defined according to

$$\Lambda = \frac{Y_{\text{H}_2\text{O}} - Y_{\text{H}_2\text{O},\text{u}}}{Y_{\text{H}_2\text{O},\text{b}} - Y_{\text{H}_2\text{O},\text{u}}} , \quad (6.8)$$

where  $Y_{\text{H}_2\text{O},\text{b}}$  and  $Y_{\text{H}_2\text{O},\text{u}}$  are the water mass fractions in the burned and unburned mixtures, respectively.

Generalized progress variable streamlines are identified using the procedure described by Chan et al. [114]. Starting from each grid point  $\mathbf{x}_0$ , the subsequent point in physical space  $\mathbf{x}_{t+1}$  that lies on the generalized progress variable streamline passing through  $\mathbf{x}_t$  is determined using a constant step size in generalized progress variable space. Using the chain rule,  $\mathbf{x}_{t+1}$  can be estimated in terms of the current location  $\mathbf{x}_t$  and the local generalized progress variable gradient:

$$\mathbf{x}_{t+1} = \mathbf{x}_t + \left. \frac{\nabla \Lambda}{|\nabla \Lambda|^2} \right|_{\mathbf{x}_t} d\Lambda . \quad (6.9)$$

Equation 6.9 is iterated upon with  $d\Lambda = d\Lambda_{\text{step}}$  until the generalized progress variable increases to  $\Lambda = 1$ , within a threshold of 0.05, and then repeated with  $d\Lambda = -d\Lambda_{\text{step}}$  until the generalized progress variable decreases to  $\Lambda = 0$ , within the same threshold. This approach adapts the step size in physical space so as to take smaller steps where the generalized progress variable gradient is steep and larger steps where the generalized progress variable gradient is shallow. The constant generalized progress variable step size  $d\Lambda_{\text{step}}$  is taken as  $10^{-2}$ , and the extracted instantaneous conditional generalized progress variable dissipation rates are insensitive to further refinement of  $d\Lambda_{\text{step}}$ . In this way, an instantaneous conditional generalized progress variable dissipation rate profile is extracted for each point on the grid,

corresponding to the starting point  $\mathbf{x}_0$ . Each instantaneous conditional generalized progress variable dissipation rate profile is then interpolated onto a one-dimensional uniform grid in generalized progress variable space with 32 points to reduce the memory requirement of the data.

### 6.2.3 Evaluating Profile ‘Universality’

In practice, the shape of the instantaneous conditional dissipation rates are presumed ‘universal’ and scaled by assuming a constant  $\chi_{\Lambda\Lambda,\text{ref}}$  in a grid cell determined by the local value of the density-weighted filtered dissipation rate  $\tilde{\chi}_{\Lambda\Lambda}$ . The focus of this chapter is the shape of the instantaneous conditional dissipation rate profiles rather than the magnitude, so the profiles are normalized by the corresponding value at  $\Lambda_{\text{ref}}$ , yielding the normalized dissipation rate profiles:

$$g(\Lambda) \equiv \frac{f(\Lambda)}{f(\Lambda_{\text{ref}})} = \frac{\chi_{\Lambda\Lambda}(\Lambda)}{\chi_{\Lambda\Lambda,\text{ref}}}, \quad (6.10)$$

where  $g(\Lambda)$  is unity at  $\Lambda_{\text{ref}} = 0.5$  by construction.

Figure 6.1 shows the normalized dissipation rate profiles extracted from the DNS data of each Karlovitz number case compared against the ‘universal’ models from Eq. 6.6 and Eq. 6.7. For the low Karlovitz number case (Case K1), there is some minor observable variation in the instantaneous normalized dissipation rate profiles. However, for the most part, this ‘universal’ approximation – and the unstretched model, in particular – appears to be appropriate at low Karlovitz number. This is physically reasonable since combustion is approximately ‘universal’ in generalized progress variable space and dominates turbulent mixing at low Karlovitz number [115]. As the Karlovitz number increases, the turbulence dictates mixing and the conditional dissipation rate, and the flow is less correlated with the generalized progress variable [115, 116, 117]. The high Karlovitz number case (Case K2) is consistent with this trend, demonstrating a much stronger variation in the instantaneous normalized dissipation rate profiles.

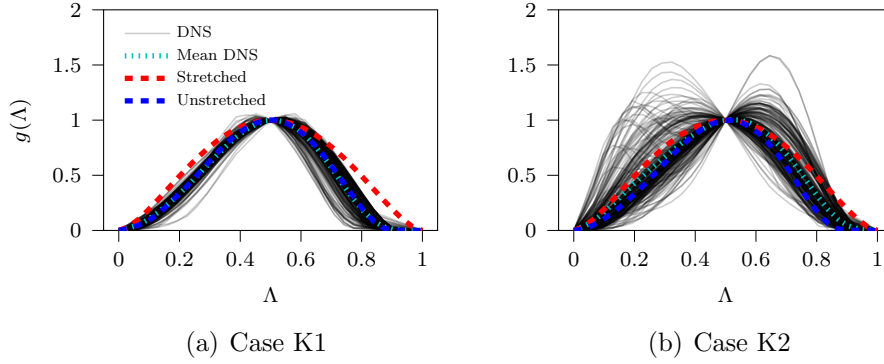


Figure 6.1: Instantaneous conditional dissipation rate profiles extracted from DNS data for both Karlovitz number cases, normalized by the reference dissipation rate. Solid black lines denote 250 normalized dissipation rate profiles randomly sampled from the extracted profiles for each Karlovitz number case; dotted cyan lines denote the conditional mean of the DNS (averaged over 500,000 samples for each Karlovitz number case); dashed red lines denote the algebraic expression for the stretched model in Eq. 6.7; and dashed blue lines denote the unstretched flat-flame solution in Eq. 6.7, normalized by the dissipation rate at the reference generalized progress variable.

The instantaneous normalized dissipation rate profiles are also compared to the conditional mean averaged over 500,000 samples from each Karlovitz number case, representing a best-case scenario ‘universal’ model. The conditional mean in Case K1 demonstrates a larger deviation from the stretched profile, though the conditional mean profiles for both Case K1 and Case K2 are narrower than the stretched profile. The unstretched model reconstructs the conditional mean in Case K1 due to the dominance of chemistry over turbulent strain at low Karlovitz number. Case K2 demonstrates that as the Karlovitz number increases and turbulent strain effects become more important relative to the chemistry, the stretched model becomes a better representation of the conditional mean, and the unstretched model begins to deviate, as expected. The consequence of accurately reconstructing the conditional mean is explored further later on.

Figure 6.2 demonstrates the variation in the instantaneous normalized dissipation rate profiles for Case K2 by tracking the maximum value of each extracted normalized dissipation rate profile  $g_{\max}$ . Due to the way the profiles are normalized, left or right-shifted profiles

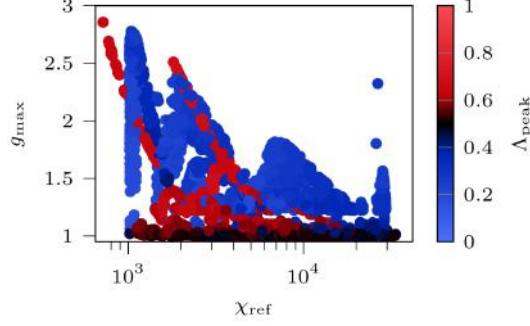


Figure 6.2: Maximum value of the normalized dissipation rate profile  $g_{\max}$  versus the reference dissipation rate  $\chi_{\Lambda\Lambda,\text{ref}}$  colored by  $\Lambda_{\text{peak}}$ , the generalized progress variable at which  $g_{\max}$  occurs.

will possess larger values of  $g_{\max}$ , indicating more variation in the normalized dissipation rate profile. Therefore, the observed decrease in the range of  $g_{\max}$  indicates a decreased variation in the normalized dissipation rate profile with increasing reference dissipation rate  $\chi_{\Lambda\Lambda,\text{ref}}$ . As this variation decreases,  $\Lambda_{\text{peak}}$  (the location in generalized progress variable space at which  $g_{\max}$  occurs) tends toward  $\Lambda_{\text{ref}}$ . The observed decrease in profile variation with increasing  $\chi_{\Lambda\Lambda,\text{ref}}$  is likely a result of decreasing length scales in the generalized progress variable that are affected by smaller turbulence scales. These smaller turbulent scales are weaker, imparting less influence on the profile shape.

Evidently, instantaneous normalized dissipation rate profiles can deviate appreciably from the conditional mean. In this chapter, the instantaneous normalized dissipation rate profiles are modeled and compared to models for the mean normalized dissipation rate profiles. These mean models include the unstretched flame solution in Eq. 6.6, the algebraic expression for a stretched flame in Eq. 6.7, as well as the conditional average of the instantaneous normalized dissipation rate profiles extracted from the DNS data (hereafter referred to as the unstretched, stretched, and mean DNS models, respectively).

## 6.3 Data-Based Modeling Approach

Modeling the instantaneous normalized dissipation rate profile via a physics-based approach remains elusive and is discussed in more detail later. In this chapter, the instantaneous normalized dissipation rate profile is instead modeled via a data-based approach with a deep neural network (DNN) – a tool that has proved successful in modeling the filtered dissipation rate in turbulent premixed combustion [118]. The resulting DNN is then investigated to glean insight into the feasibility of developing a tractable physics-based model by identifying the most important input features.

### 6.3.1 DNS Filtering and Training Data Generation

To emulate data from a coarse-grained simulation such as LES, each quantity  $\phi$  is filtered with varying filter stencil sizes  $\Delta_\alpha/h_\alpha = 2, 4, 8, 16$  where  $\Delta_\alpha$  and  $h_\alpha$  are the filter size and grid spacing in the direction  $\alpha$ , respectively. Each filter stencil size corresponds to a filter stencil volume  $V_{\text{stencil}}$  with  $(\Delta_\alpha/h_\alpha + 1)^3$  grid points. A clipped Gaussian filter is applied to the stencil volume surrounding each grid point:

$$\bar{\phi}(\mathbf{x}) = \sum_{V_{\text{stencil}}} \phi(\mathbf{x} - \mathbf{x}') G(\mathbf{x}'; \mathbf{\Delta}) d\mathbf{x}'. \quad (6.11)$$

The filter  $G(\mathbf{x}'; \mathbf{\Delta})$  is an inhomogeneous tensor-product Gaussian filter characterized by the filter size  $\mathbf{\Delta}$ . Note that, since the grid in the DNS is not the same in all three coordinate directions, the filter is also not the same in each of the three coordinate directions but is consistent with the aspect ratio of the DNS grid. Density-weighted filtered quantities are determined according to  $\tilde{\phi} \equiv \overline{\rho\phi}/\bar{\rho}$ .

A total of eight datasets are generated by filtering snapshots of the DNS data, four cases for each Karlovitz number case corresponding to  $\Delta_\alpha/h_\alpha = 2, 4, 8, 16$ . Each dataset contains five hundred thousand samples randomly sampled from the filtered data. The six datasets corresponding to  $\Delta_\alpha/h_\alpha = 2, 8, 16$  for both Karlovitz number cases are aggregated into a

single dataset with three million samples, 15% and 20% of which is set aside for validation and testing, respectively. The remaining two datasets corresponding to  $\Delta_\alpha/h_\alpha = 4$  are withheld for additional testing of the generalizability of the final trained DNN.

### 6.3.2 Input Feature Selection

The following input features were selected for training: the filtered generalized progress variable  $\tilde{\Lambda}$ , the generalized progress variable subfilter variance  $\Lambda_v$ , the magnitude of the filtered generalized progress variable gradient  $|\nabla\tilde{\Lambda}|$ , the filtered generalized progress variable dissipation rate  $\tilde{\chi}_{\Lambda\Lambda}$ , the Frobenius norm of the filtered strain rate  $|\tilde{S}|$ , the filtered generalized progress variable diffusivity  $\tilde{D}_\Lambda$ , the filtered density  $\bar{\rho}$ , the filtered generalized progress variable source term  $\bar{m}_\Lambda$ , and the local filter size  $\Delta_L \equiv V_{\text{stencil}}^{1/3}$ . The eigenvalues of the filtered strain rate  $\alpha, \beta, \gamma$  (principal rates of strain) as well as the alignment of their corresponding eigenvectors with the local generalized progress variable gradient ( $e_\alpha \cdot \nabla\tilde{\Lambda}/|\nabla\tilde{\Lambda}|$ ,  $e_\beta \cdot \nabla\tilde{\Lambda}/|\nabla\tilde{\Lambda}|$ ,  $e_\gamma \cdot \nabla\tilde{\Lambda}/|\nabla\tilde{\Lambda}|$ ) have been incorporated as additional input features as per Yellapantula et al. [118], though a significant change in prediction accuracy was not observed.

### 6.3.3 Network Hyperparameter Selection

In this chapter, the instantaneous normalized dissipation rate profiles are modeled with a fully-connected, feed-forward DNN, with each of 32 outputs corresponding to one of 32 points comprising each discretized generalized progress variable dissipation rate profile. The Adam optimizer [119] extends stochastic gradient descent by determining individual adaptive learning rates for each trainable network parameter and was utilized with a learning rate of  $10^{-3}$ . The mean absolute error was selected as the loss function. A leaky rectified linear unit was selected as the activation function with a negative slope coefficient of 0.1. Neural network training was implemented with the Python library `TensorFlow` and the `Keras` API.

An iterative algorithm was employed to determine the network architecture. Beginning with an initial neural network with a single hidden layer of 32 fully-connected nodes, each



model was trained over 100 epochs in batch sizes of 512 samples. Subsequent network architectures were chosen based on the evaluated validation loss of trained networks and a presumed power law convergence of the loss with respect to network parameters to satisfy a user-specified threshold on the validation loss. The number of hidden layers as well as the number of fully-connected nodes per layer were iteratively increased until the validation loss converged with respect to the network architecture or satisfied a threshold of  $10^{-2}$ . The final DNN possesses 8 hidden layers with 36 fully-connected nodes per layer and a total of 11,084 trainable parameters (available for download from public data repositories<sup>1,2</sup>).

## 6.4 Results and Discussion

### 6.4.1 DNN Model Evaluation

The mean absolute errors of the final DNN evaluated on the training, validation, and testing data are 0.03593, 0.03591, and 0.03587, respectively, indicating that it does not suffer from overfitting. As an additional test of the generalizability of the DNN, it is evaluated on the two datasets corresponding to  $\Delta_\alpha/h_\alpha = 4$ .

Figure 6.3 shows the conditional mean of the normalized dissipation rate profiles extracted from the additional test data compared to the mean of the DNN predictions and the stretched and unstretched models. The mean DNN prediction clearly demonstrates excellent agreement with the conditional mean of the normalized dissipation rate profiles, suggesting that opting to model the instantaneous variation of the normalized dissipation rate profile with a DNN also guarantees a faithful reconstruction of the mean without introducing a bias. Both models demonstrate a deviation from the stretched model in the mean sense, and this difference is more significant in Case K1 than in Case K2 since combustion plays a more significant role in the turbulence dynamics in Case K1. The unstretched model also success-

---

<sup>1</sup>GitHub: <https://github.com/cristianlacey/data-based-dissipation-rates>

<sup>2</sup>GitLab: <http://ctrfl-internal.princeton.edu/clacey/data-based-dissipation-rates>

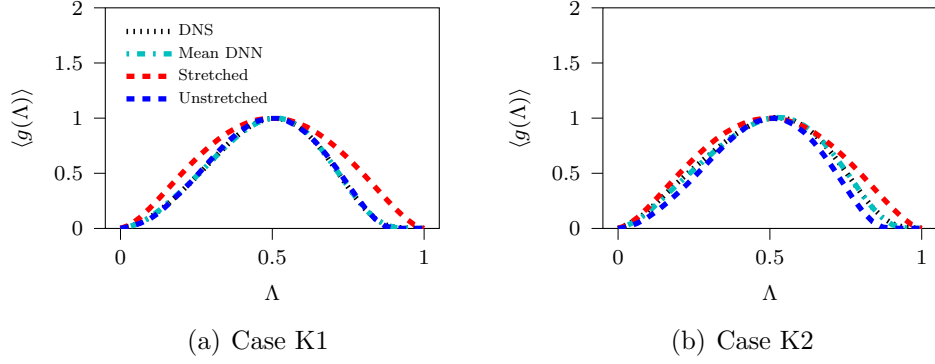


Figure 6.3: Conditional mean of the normalized dissipation rate profiles for datasets corresponding to  $\Delta_\alpha/h_\alpha = 4$ . Black dotted lines denote the mean of the normalized dissipation rate profiles from the DNS data; cyan dot-dot-dashed lines denote the mean of the DNN normalized dissipation rate profile predictions; red dashed lines denote the stretched model from Eq. 6.7; and blue dashed lines denote the unstretched model from Eq. 6.6. Note that black dotted lines nearly exactly coincide with cyan dot-dot-dashed lines.

fully reconstructs the mean in Case K1, suggesting the Karlovitz number is low enough for chemistry effects to dominate, as in a laminar flame. As expected, this trend begins to break down in Case K2, as the Karlovitz number increases.

To quantify the predictive advantage of modeling the instantaneous normalized dissipation rate profiles using a DNN over other ‘universal’ conditional mean models, an *instantaneous* model error is defined as

$$\epsilon_{\text{model}}(\Lambda) = \left| g_{\text{model}}(\Lambda) - g_{\text{DNS}}(\Lambda) \right|, \quad (6.12)$$

which is then conditionally averaged over the data for each model. To quantify the effect of the deviation in the mean DNS data from the ‘universal’ models on the averaged instantaneous error, it is also important to look at the performance of the mean DNS model.

Figure 6.4 demonstrates a lower average instantaneous error using the unstretched, mean DNS, and DNN models as compared to the stretched model. For Case K1, the unstretched model and mean DNS model predict the instantaneous normalized dissipation rate profiles relatively well, which is due to the lower observed variance of the normalized dissipation rate

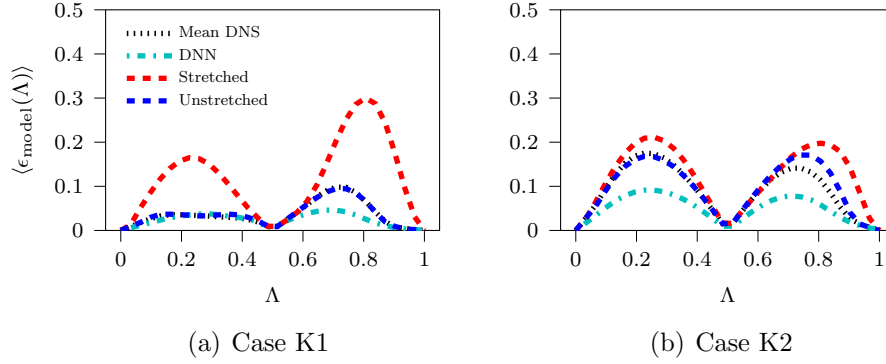


Figure 6.4: Conditional average instantaneous model error for datasets corresponding to  $\Delta_\alpha/h_\alpha = 4$ . Black dotted lines denote the average error associated with the mean of the normalized dissipation rate profiles from the DNS data; cyan dot-dashed lines denote the average error in DNN instantaneous normalized dissipation rate profile predictions; red dashed lines denote the average error in the stretched model from Eq. 6.7; and blue dashed lines denote the average error in the unstretched model from Eq. 6.6.

profiles about the mean in the low Karlovitz number case. In Case K2, the unstretched model and mean DNS model perform only marginally better than the stretched model, which is the worst performer at both Karlovitz numbers. However, for Case K2, there is a pronounced advantage in adopting an instantaneous modeling approach with a DNN over using even the mean DNS model, for the DNN can capture the larger variance in normalized dissipation rate profiles at high Karlovitz number.

### 6.4.2 *A Priori* Analysis

To quantify the effect of consideration of the instantaneous normalized dissipation rate profile on thermochemical quantities of interest, the normalized dissipation rate profiles predicted by each modeling approach are used to solve the one-dimensional premixed manifold equations in Eq. 6.3, the solutions to which are computed using the PDRs code [38, 94]. Attention is focused on Case K2 where the large variance in the normalized dissipation rate profiles lends the DNN modeling approach a marked advantage. Equation 6.3 considers unity effective Lewis numbers, for differential diffusion effects are expected to be of reduced importance in

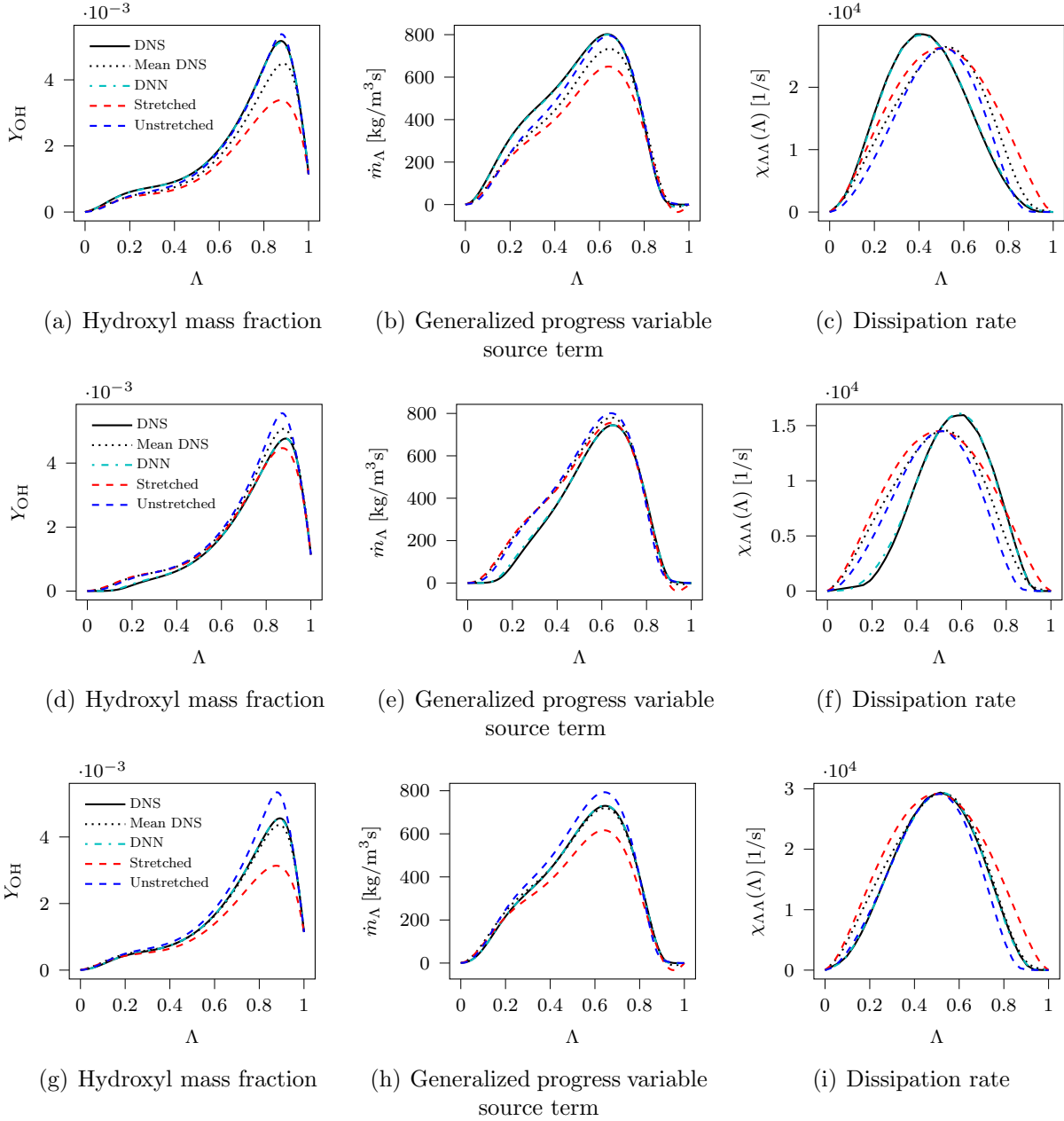


Figure 6.5: Manifold solutions corresponding to profiles with  $\chi_{\Lambda\Lambda, \text{ref}} = 26, 327 \text{ s}^{-1}$  and  $\Lambda_{\text{peak}} < 0.5$  in (a)-(c),  $\chi_{\Lambda\Lambda, \text{ref}} = 14, 514 \text{ s}^{-1}$  and  $\Lambda_{\text{peak}} > 0.5$  in (d)-(f), and  $\chi_{\Lambda\Lambda, \text{ref}} = 29, 197 \text{ s}^{-1}$  and  $\Lambda_{\text{peak}} \approx 0.5$  in (g)-(i). Black solid lines, black dotted lines, cyan dot-dashed lines, red dashed lines, and blue dashed lines denote solutions corresponding to instantaneous normalized dissipation rate profiles extracted from DNS data, the mean DNS model, the DNN model, the stretched model, and the unstretched model, respectively. Note that black solid lines nearly exactly coincide with cyan dot-dashed lines.

Case K2 [120]. Regardless, evaluating the sensitivity of the instantaneous thermochemical state to the particular conditional generalized progress variable dissipation rate profile model only requires comparison to a baseline thermochemical state. Three instantaneous profiles are examined as examples of varying values of  $\Lambda_{\text{peak}}$  ( $> 0.5$ ,  $< 0.5$ ,  $\approx 0.5$ ) with reference dissipation rates ( $\chi_{\Lambda\Lambda,\text{ref}} = 14,514 \text{ s}^{-1}$ ;  $26,327 \text{ s}^{-1}$ ;  $29,197 \text{ s}^{-1}$ , respectively).

Figure 6.5 (a)-(c) shows the hydroxyl mass fraction and generalized progress variable source term profiles corresponding to an instantaneous normalized dissipation rate profile with a leftward shift compared to the ‘universal’ models, which is predicted very well by the DNN. The stretched model underpredicts the hydroxyl mass fraction by as much as 40% at high generalized progress variable, while the DNN exactly matches that of the instantaneous normalized dissipation rate profile from the DNS. The mean DNS model outperforms the stretched model but still suffers from underprediction. Generalized progress variable source term predictions deviate more significantly from the instantaneous normalized dissipation rate profile from the DNS, while the DNN produces the same results. Prediction of the magnitude of the peak generalized progress variable source term is critical to accurately predicting flame propagation rates.

Figure 6.5 (d)-(f) again demonstrates the hydroxyl mass fraction and generalized progress variable source term profiles for each normalized dissipation rate model. The instantaneous normalized dissipation rate profile extracted from the DNS now demonstrates a rightward shift in generalized progress variable space relative to the ‘universal’ model predictions, which is again predicted with excellent accuracy by the DNN. Radicals such as the hydroxyl mass fraction are considerably over and underpredicted by the ‘universal’ models at the peak value, particularly in comparison to the agreement between the DNS and DNN. Furthermore, predictions of the generalized progress variable source term deviate significantly at low generalized progress variable, while the DNN produces the same results as the instantaneous normalized dissipation rate profile from the DNS. Predictions of reactivity at low generalized progress variable would be exceptionally important for predicting ignition phe-

nomena, so consideration of the instantaneous dissipation rate profile is likely very important for predicting ignition in addition to flame speed.

In Fig. 6.5 (g)-(i), the instantaneous normalized dissipation rate profile extracted from the DNS is approximately centered in generalized progress variable space, just as the ‘universal’ model predictions. Though there is still a significant deviation in the hydroxyl mass fraction and generalized progress variable source term predicted by the stretched model and unstretched model versus the instantaneous normalized dissipation rate profile from the DNS, the mean DNS model, as well as the DNN, both produce excellent predictions. However, the stretched model and unstretched model still underpredict and overpredict the peak reactivity, respectively. This is reasonable, as neither model perfectly reconstructs the conditional mean dissipation rate profile of the DNS in Case K2.

When the instantaneous normalized dissipation rate profiles are shifted in generalized progress variable space, adopting a modeling approach that captures not just the mean but also the instantaneous profiles is important for the accurate prediction of radical species, ignition, and flame propagation speeds. In these cases, a DNN produces excellent predictions. Replacing the ‘universal’ models with the DNN model for the instantaneous normalized dissipation rate profiles in an LES, of course, would require parameterizing the manifold solutions in terms of all relevant DNN input features. With previous implementations of manifold modeling that involve pretabulating manifold solutions spanning the entire parameter space, this would be intractable. However, with the new manifold modeling implementation of In-Situ Adaptive Manifolds (ISAM) developed by Lacey et al. [43], manifold solutions with many more input quantities can now be computed on-the-fly in a far more memory-efficient and computationally-tractable way. Integration of the DNN model with ISAM and *a posteriori* validation in LES is left for future work.

### 6.4.3 Data-Based Variable Importance: Integrated Gradients

To determine which input features are responsible for the shifting in the instantaneous normalized dissipation rate profiles observed at high Karlovitz number, a variable importance study was conducted utilizing the method of integrated gradients [121]. The integrated gradients method involves computing a sensitivity metric for each of  $m$  output quantities of interest relative to each of  $n$  input features. Each metric is obtained by integrating a component of the output Jacobian with respect to the input features along a straight line in the input feature space from a specified baseline location to the location in input feature space corresponding to the evaluated Jacobian. This operation is defined according to

$$IG_{ij} = (x_i - x'_i) \int_0^1 \frac{\partial F_j(\mathbf{x}' + \xi(\mathbf{x} - \mathbf{x}'))}{\partial x_i} d\xi, \quad (6.13)$$

where  $IG_{ij}$  is the integrated gradient of output  $F_j$  with respect to input feature  $x_i$ ,  $\mathbf{x}$  is the location in input feature space at which the integrated gradients are evaluated,  $\mathbf{x}'$  is the baseline location in input feature space, and  $\xi$  is a dummy variable of integration. Note that the prefactor  $(x_i - x'_i)$  in Eq. 6.13 appears as a result of changing the variable of integration from  $\mathbf{x}$  to  $\xi$ , and each set of integrated gradients  $\{IG_{ij}\}_{i=1}^n$  have the same physical dimensions as the corresponding output  $F_j$ . In this chapter, the  $m$  output features are the dimensionless, discretized values of the normalized dissipation rate profile predicted by the DNN. As such, the integrated gradients are also all dimensionless.

Given the present choice of activation function, the integrated gradients also satisfy the following property:

$$\sum_{i=1}^n IG_{ij} = F_j(\mathbf{x}) - F_j(\mathbf{x}'). \quad (6.14)$$

By carefully selecting a baseline  $\mathbf{x}'$  such that  $\mathbf{F}(\mathbf{x}')$  is the conditional mean of the normalized dissipation rate profiles, each set of integrated gradients  $\{IG_{ij}\}_{j=1}^m$  can be interpreted

as the linear contribution of input feature  $x_i$  to the deviation of the normalized dissipation rate profile relative to its conditional mean profile. For a given set of integrated gradients  $\{IG_{ij}\}_{j=1}^m$ , positive integrated gradients for  $j$  values corresponding to  $\Lambda > \Lambda_{\text{ref}}$  and negative integrated gradients for  $j$  values corresponding to  $\Lambda < \Lambda_{\text{ref}}$  indicate that input feature  $x_i$  contributes to a rightward shift in the normalized dissipation rate profile. Likewise, negative integrated gradients for  $j$  values corresponding to  $\Lambda > \Lambda_{\text{ref}}$  and positive integrated gradients for  $j$  values corresponding to  $\Lambda < \Lambda_{\text{ref}}$  indicate that input feature  $x_i$  contributes to a leftward shift in the normalized dissipation rate profile. All positive or all negative integrated gradients in a set  $\{IG_{ij}\}_{j=1}^m$  indicate a positive or negative vertical translation due to input feature  $x_i$ , respectively – but, due to the use of normalized profiles, such situations are not observed.

The integrated gradients are computed for a uniform random sampling of 4,000 points from the high Karlovitz number dataset, Case K2. To more easily visualize and interpret the role of each input variable in shifting the normalized dissipation rate profiles, each set of integrated gradients  $\{IG_{ij}\}_{j=1}^m$  is conditioned on the filtered generalized progress variable  $\langle IG_{ij} | \tilde{\Lambda} \rangle$  and plotted with respect to the filtered generalized progress variable  $\tilde{\Lambda}$ . The magnitude of the conditional integrated gradients is 50 to 100 times smaller for the alignments of the principal rates of strain with the generalized progress variable gradient, generalized progress variable source term, filter size, filtered generalized progress variable dissipation rate, and generalized progress variable gradient magnitude compared to that of the most important input features, so analysis of these input features is neglected.

Figure 6.6 demonstrates that the set of conditionally averaged integrated gradients corresponding to the filtered strain rate magnitude and the generalized progress variable subfilter variance are large and lead to left- and right-shifting, respectively. However, the filtered strain rate magnitude and generalized progress variable subfilter variance are positively correlated, implying that the net effect of the opposite shifting tendency cancels out. A similar trend is observed in the sensitivity to the density and diffusivity: the conditionally averaged



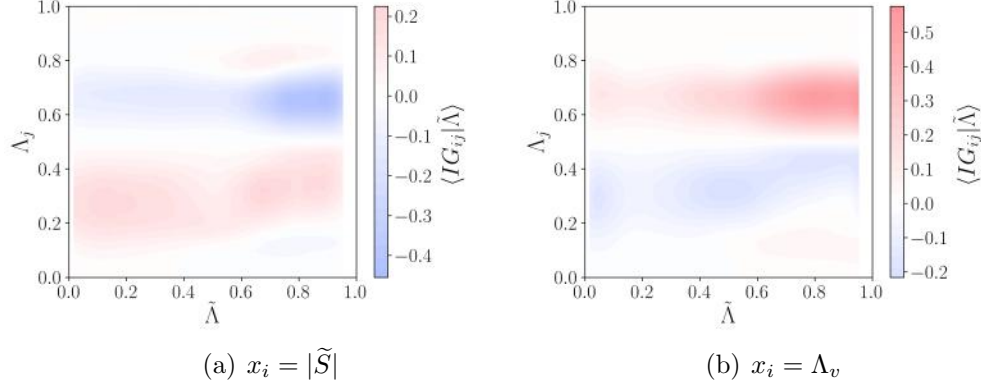


Figure 6.6: Set of integrated gradients  $\{IG_{ij}\}_{j=1}^m$  for the filtered strain rate magnitude and generalized progress variable subfilter variance conditionally averaged with respect to the filtered generalized progress variable, where  $\Lambda_j$  denotes the generalized progress variable at the discrete value of the normalized dissipation rate profile corresponding to index  $j$  and  $x_i$  denotes the corresponding input feature.

integrated gradients for these input features exhibit the same qualitative shifting behavior. The strong negative correlation between density and diffusivity implies that the net effect of these two input features again cancels.

Figure 6.7 demonstrates the set of conditionally averaged integrated gradients corresponding to the three principal rates of strain  $\alpha$ ,  $\beta$ , and  $\gamma$ , in ascending order. Figure 6.7 (b) shows that  $\beta$  tends to contribute a minor left-shift in the profile throughout the high Karlovitz number dataset. Figure 6.7 (a) and (c) show that increasing  $\alpha$  and  $\gamma$  contributes to a large right- and left-shift, respectively. The PDF of  $\alpha$  and  $\gamma$  in Fig. 6.8 shows that the two variables are highly negatively correlated, implying that the overall shifting attributed to the principal rates of strain is additive and does not cancel. To further evaluate the importance of the principal rates of strain, a separate reduced DNN model is retrained with the same input features as the baseline network except without  $\alpha, \beta, \gamma, e_\alpha \cdot \nabla \tilde{\Lambda} / |\nabla \tilde{\Lambda}|, e_\beta \cdot \nabla \tilde{\Lambda} / |\nabla \tilde{\Lambda}|, e_\gamma \cdot \nabla \tilde{\Lambda} / |\nabla \tilde{\Lambda}|$ . Repeating the integrated gradient analysis for this reduced DNN demonstrates the same qualitative dependence on the remaining input features, but with increased sensitivity to the dominant features. The reduced DNN also yields equivalent testing error and average instantaneous error, seeming to contradict the analysis of the integrated gradients corresponding

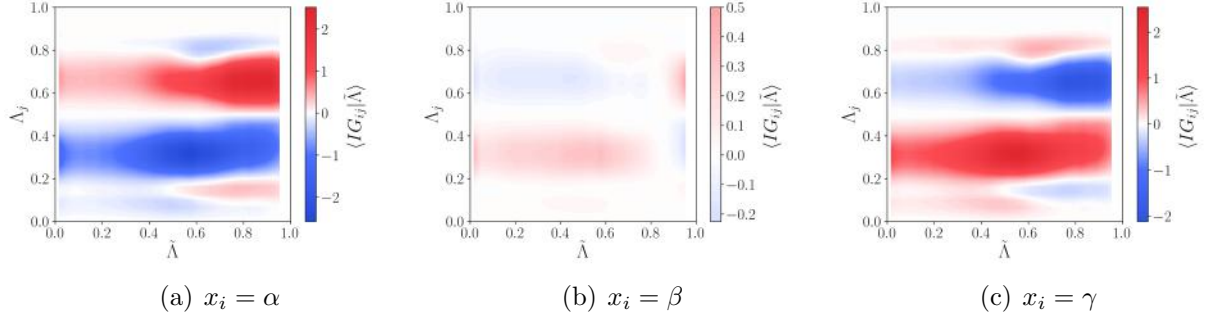


Figure 6.7: Set of integrated gradients  $\{IG_{ij}\}_{j=1}^m$  for the principal rates of strain conditionally averaged with respect to the filtered generalized progress variable, where  $\Lambda_j$  denotes the generalized progress variable at the discrete value of the normalized dissipation rate profile corresponding to index  $j$  and  $x_i$  denotes the corresponding input feature.

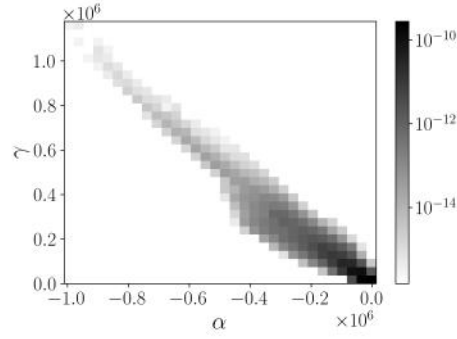


Figure 6.8: Probability density function of the principal rates of strain  $\alpha$  and  $\gamma$  present in the DNS data.

to the original DNN and suggesting that the principal rates of strain and their alignments are not critical model quantities. Instead, the observed sensitivity of the integrated gradients to the principal rates of strain could simply be attributed to a separate physical quantity that happens to be correlated with both  $\alpha$  and  $\gamma$ .

Returning to the integrated gradient analysis for the original DNN, Fig. 6.9 (a) demonstrates that the largest conditionally averaged integrated gradients correspond to the filtered generalized progress variable. However, the resulting shifting direction appears to change across the mean flame - an inconsistent result considering that a given extracted profile can only be either shifted left or right and always spans the range of generalized progress

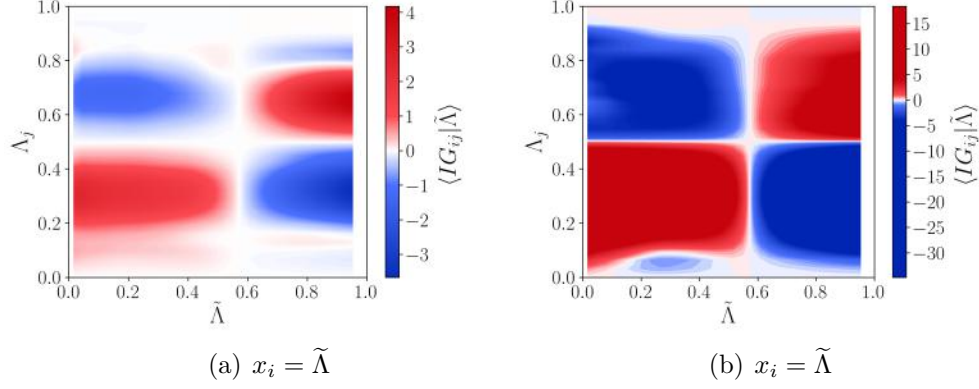


Figure 6.9: Set of integrated gradients  $\{IG_{ij}\}_{j=1}^m$  for the filtered generalized progress variable conditionally averaged with respect to the filtered generalized progress variable, where  $\Lambda_j$  denotes the generalized progress variable at the discrete value of the normalized dissipation rate profile corresponding to index  $j$  and  $x_i$  denotes the corresponding input feature,  $x_i = \tilde{\Lambda}$ . Integrated gradients associated with the deep neural network trained on all input features are presented in (a), and those of the reduced deep neural network trained without the principal rates of strain or alignments are presented in (b).

variables by construction. The considerable sensitivity observed with respect to the filtered generalized progress variable can therefore be interpreted as the neural network learning a relationship for the output as a function of inputs that are only correlated with the underlying variable or variables that truly characterize the fundamental physical relationship with the output, rather than actually learning the physically correct model itself. This interpretation is further supported by the filtered generalized progress variable integrated gradients corresponding to the reduced DNN shown in Fig. 6.9 (b). Though the reduced DNN integrated gradients display the same qualitative shifting direction flip in filtered generalized progress variable space, the magnitude of the integrated gradients is an order of magnitude larger for the reduced DNN than for the baseline DNN – indicative of an increasing reliance on correlations with the filtered generalized progress variable as the number of input training features is further reduced. This evidence suggests that the large sensitivity of the DNN predictions to the filtered generalized progress variable reflects that the chosen set of input training features is missing one or more physical quantities that are fundamentally important

to the shifting of the normalized dissipation rate profiles.

#### 6.4.4 Physics-Based Variable Importance: Conditional Generalized Progress Variable Dissipation Rate Transport Equation

The input features selected to train the DNN were initially chosen in part because they are accessible in an LES or RANS simulation. Unclosed quantities were not initially considered. To better elucidate the mechanism driving the shifting of the normalized dissipation rate profiles, this constraint is loosened. The transport equation for the conditionally filtered (or conditionally averaged) generalized progress variable dissipation rate is derived in A, and the dominant terms are identified, whether they are closed or unclosed in a coarse-grained simulation. The density-weighted conditional filtering operation for a quantity  $\phi$  is defined according to  $\widetilde{\phi}_{,\lambda} = \overline{\rho\phi\psi} / \overline{\rho\psi}$ , where  $\psi = \delta(\lambda - \Lambda)$  is the fine-grained subfilter probability density function (PDF),  $\delta$  is the delta function, and  $\lambda$  is the phase space (sample-space) variable for  $\Lambda$ . The conditional generalized progress variable dissipation rate transport equation is given by

$$\begin{aligned}
& \underbrace{\frac{\partial}{\partial t} (\bar{\rho} \tilde{P} \widetilde{\chi_{\Lambda\Lambda}}_{,\lambda})}_{\text{T1}} + \underbrace{\frac{\partial}{\partial x_j} (\bar{\rho} \tilde{P} \widetilde{u_{j,\lambda} \chi_{\Lambda\Lambda}}_{,\lambda})}_{\text{T2}} + \underbrace{\frac{\partial}{\partial \lambda} (\bar{P} \widetilde{\dot{m}_{\Lambda,\lambda} \chi_{\Lambda\Lambda}}_{,\lambda})}_{\text{T3}} = \\
& \underbrace{-\frac{\partial}{\partial x_j} [\bar{\rho} \tilde{P} (\widetilde{u_j \chi_{\Lambda\Lambda}}_{,\lambda} - \widetilde{u_{j,\lambda} \chi_{\Lambda\Lambda}}_{,\lambda})]}_{\text{T4}} - \underbrace{\frac{\partial}{\partial \lambda} [\bar{P} (\widetilde{\dot{m}_{\Lambda} \chi_{\Lambda\Lambda}}_{,\lambda} - \widetilde{\dot{m}_{\Lambda,\lambda} \chi_{\Lambda\Lambda}}_{,\lambda})]}_{\text{T5}} \\
& + \underbrace{\bar{P} \frac{\partial}{\partial x_j} \left( \rho D \frac{\partial \chi_{\Lambda\Lambda}}{\partial x_j} \right)_{,\lambda}}_{\text{T6}} - \underbrace{4\bar{\rho} \tilde{P} D^2 \left[ \frac{\partial}{\partial x_j} \left( \frac{\partial \Lambda}{\partial x_j} \right) \right]^2_{,\lambda}}_{\text{T7}} - \underbrace{4\bar{\rho} \tilde{P} D \frac{\partial \Lambda}{\partial x_i} S_{ij} \frac{\partial \Lambda}{\partial x_j} _{,\lambda}}_{\text{T8}} \\
& + \underbrace{2\bar{\rho} \tilde{P} \widetilde{\chi_{\Lambda\Lambda} \frac{\partial u_j}{\partial x_j}}_{,\lambda}}_{\text{T9}} + \underbrace{4\bar{P} D \frac{\partial \Lambda}{\partial x_j} \frac{\partial \dot{m}_{\Lambda}}{\partial x_j} _{,\lambda}}_{\text{T10}} - \underbrace{\frac{\partial^2}{\partial x_j \partial \lambda} \left( \bar{\rho} \tilde{P} D \widetilde{\chi_{\Lambda\Lambda} \frac{\partial \Lambda}{\partial x_j}}_{,\lambda} \right)}_{\text{T11}} \\
& + \underbrace{\frac{\partial}{\partial \lambda} \left( \bar{\rho} \tilde{P} D \widetilde{\chi_{\Lambda\Lambda} \frac{\partial \Lambda}{\partial x_j}}_{,\lambda} \right)}_{\text{T12}} - \underbrace{\frac{\partial^2}{\partial \lambda^2} \left( \frac{1}{2} \bar{\rho} \tilde{P} \widetilde{\chi_{\Lambda\Lambda} \chi_{\Lambda\Lambda}}_{,\lambda} \right)}_{\text{T13}}.
\end{aligned} \tag{6.15}$$

The three terms on the left-hand side of Eq. 6.15 correspond to: unsteadiness (T1), advection in physical space (T2), and advection in generalized progress variable space due to the generalized progress variable source term (T3). The ten terms on the right-hand side of Eq. 6.15 correspond to: conditional turbulent transport in physical space (T4), conditional turbulent transport in phase space due to the generalized progress variable source term (T5), conditional molecular transport in physical space (T6), conditional dissipation (T7), conditional generalized progress variable gradient and strain rate alignment source (T8), conditional dilatation (T9), conditional generation due to chemical reactions (T10), conditional physical and phase space transport (T11, T12), and phase space diffusion (T13). In the large Karlovitz number limit, the chemical time scales are long compared to the turbulence time scales, implying the terms T5, T9, and T10 can be neglected. Further noting that terms T6, T7, T11, T12, and T13 are all second-order diffusion-like terms (scaling with  $D^2$ ), these terms are negligible at elevated Reynolds number. Therefore, the dominant right-hand-side terms in Eq. 6.15 are terms T4 and T8, and term T4 can simply be closed with a gradient diffusion model. However, term T8 depends on the conditional velocity gradient aligned with the generalized progress variable gradient, implying that the conditional generalized progress variable dissipation rate – and hence the shifting of the normalized dissipation rate profile – fundamentally depends on the conditional velocity gradient aligned with the generalized progress variable gradient (from here on referred to as the conditional velocity gradient for brevity).

Figure 6.10 shows the conditional velocity gradient conditioned on the generalized progress variable, colored by  $\Delta\Lambda_{\text{peak}} = \Lambda_{\text{peak}} - \Lambda_{\text{ref}}$ . Figure 6.10 (a) demonstrates that the unfiltered conditional velocity gradient directly extracted from the DNS data  $\frac{\partial u_{\nabla\Lambda}}{\partial x_{\nabla\Lambda} \text{ DNS}} \approx \frac{\Delta(u \cdot \nabla\Lambda)}{\Delta\Lambda}$  is positively correlated with  $\Delta\Lambda_{\text{peak}}$ , as expected from Eq. 6.15. Some deviations in this trend are observed at small and large generalized progress variables where the dissipation rate is small and less important. Based on this observation, a simple approach for modeling the conditional velocity gradient – and thereby modeling

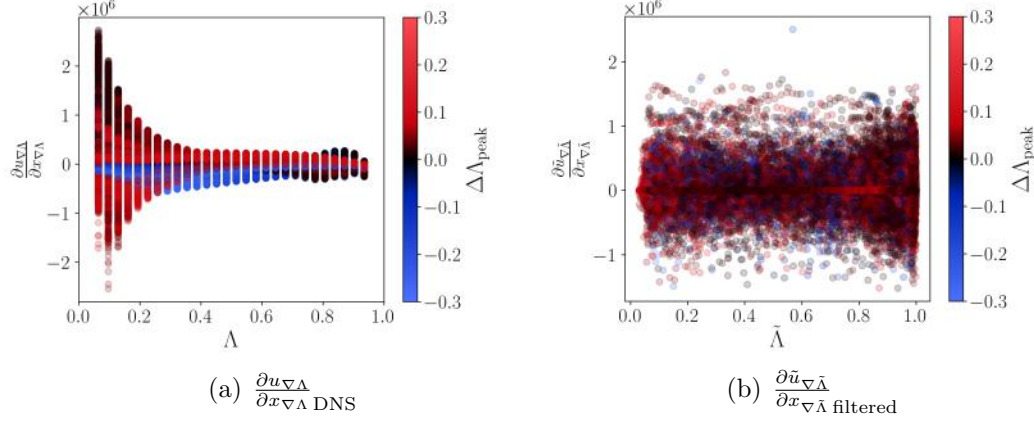


Figure 6.10: Conditional velocity gradient conditioned on generalized progress variable, colored by  $\Delta \Lambda_{\text{peak}} = \Lambda_{\text{peak}} - \Lambda_{\text{ref}}$ . The conditional velocity gradient from the DNS ( $\Delta_{\alpha}/h_{\alpha} = 0$ ) is shown in (a), and the resolved conditional velocity gradient from the filtered DNS ( $\Delta_{\alpha}/h_{\alpha} = 16$ ) is shown in (b).

the normalized dissipation rate shifting – would seemingly be to use the filtered velocity and generalized progress variable fields to define a resolved conditional velocity gradient  $\frac{\partial \tilde{u}_{\nabla \tilde{\Lambda}}}{\partial x_{\nabla \tilde{\Lambda}}} \approx \frac{\Delta(\tilde{u} \cdot \nabla \tilde{\Lambda})}{\Delta \tilde{\Lambda}}$ . However, Fig. 6.10 (b) demonstrates that this resolved conditional velocity gradient no longer correlates with  $\Delta \Lambda_{\text{peak}}$ , implying that the unresolved contribution to the conditional velocity gradient is of fundamental importance. Though the conditional velocity gradient can be obtained, such a physics-based approach would involve solving additional conditional velocity transport equations that evolve in time as well as physical space and phase space, introducing considerable additional computational cost [115]. It may be possible to model the conditional velocity gradient via a dynamic approach at elevated Karlovitz number, though this approach would not be appropriate at low Karlovitz number where dilatation due to combustion influences the turbulence and introduces additional complexity for a physics-based approach. The present data-based DNN model does not include the conditional velocity as an input and instead projects this dependence largely onto the filtered generalized progress variable. Though this approach is highly correlative, it enables the modeling of phenomena that are simply too complicated for physics-based models. Thus, the dependence of the normalized dissipation rate shifting on the conditional

velocity gradient serves as further support for the utility of a data-based modeling approach for the instantaneous normalized dissipation rates in turbulent premixed combustion.

## 6.5 Outcomes: Premixed Dissipation Rate Profile Modeling

This chapter leveraged DNS data of a turbulent premixed hydrogen jet flame to extract the instantaneous dependence of the generalized progress variable dissipation rate on the generalized progress variable. Considerable variation has been observed in the extracted instantaneous normalized dissipation rate profiles at high Karlovitz number. This variation was shown to be modeled with excellent agreement using a DNN – far better than the typical stretched or unstretched models or even the conditional mean of the profiles extracted from the DNS data. Manifold solutions of radical species and the generalized progress variable source term demonstrate that ‘universal’ models for the conditional generalized progress variable dissipation rate often poorly reconstruct aspects of the local instantaneous thermochemical state, both at low generalized progress variable and near peak values. Studying the relative importance of the input features used for DNN training revealed that the DNN learned the output relationship in terms of inputs that are correlated with the conditional velocity gradient aligned with the generalized progress variable gradient, the fundamental quantity that determines the observed instantaneous shifting of the normalized dissipation rate profiles. The resolved conditional velocity gradient aligned with the filtered generalized progress variable gradient was shown not to correlate with the profile shifting for large filter stencil sizes. To accurately predict both ignition and flame propagation, particularly at high Karlovitz number, the spatial and temporal variation of the instantaneous conditional dissipation rate profiles must be correctly modeled and included in manifold-based combustion models. Despite difficulties associated with modeling the instantaneous conditional dissipation rate profiles in a physics-based manner, data-based approaches offer the ability

to provide closure indirectly by learning correlations with the conditional velocity gradient aligned with the generalized progress variable gradient.



# Chapter 7

## Data-Based Dissipation Rate Modeling for Multi-Modal Combustion

This chapter continues with *Sub-Objective 3*, extending the data-based approach of Chapter 6 to the multi-modal manifold model outlined in Sec. 5.1. The aim of this work is to provide closure for the three unclosed dissipation rates that encode the mode of combustion in the multi-modal manifold equations – both for the filtered dissipation rates as well as the instantaneous normalized dissipation rate profiles. DNS data of a temporally evolving *n*-dodecane/air jet at low-temperature diesel conditions [122] is leveraged to generate features and labels for neural network training. The first part of this chapter is concerned with providing closure for the filtered dissipation rates with a DNN, particularly in a way that enforces inherent physical constraints (positivity of the mixture fraction and generalized progress variable dissipation rates and an alignment  $\Theta \equiv \frac{\nabla Z \cdot \nabla \Lambda}{|\nabla Z||\nabla \Lambda|} \equiv \frac{\chi_{ZZ\Lambda}}{(\chi_{ZZ}\chi_{\Lambda\Lambda})^{1/2}}$  between one and negative one). A DNN model for the filtered dissipation rates is evaluated with and without physical constraints and compared to traditional algebraic models. The second part of this chapter is concerned with providing closure for the instantaneous normalized

dissipation rate profiles. Two regression methods – piecewise linear interpolation (PLI) and Gaussian process regression (GPR) – are leveraged to obtain structured training labels for the instantaneous normalized dissipation rate profiles from incomplete unstructured data, and the sensitivity of the thermochemical state to the regression method is evaluated. A DNN is then trained to predict the instantaneous dissipation rate profiles as a function of coarse-grained data and is evaluated *a priori* relative to ad hoc algebraic models. This chapter provides model closure for the multi-modal manifold equations, resulting in a hybrid physics- and data-derived model applicable to multi-modal combustion.

## 7.1 DNS Dataset Selection

The ideal configuration selected for DNN training is general and exhibits multi-modal combustion as well as low- and high-temperature ignition regimes. The dataset selected for this work is therefore the DNS database generated with S3D-Legion [123] by Borghesi et al. [122] of an autoigniting turbulent *n*-dodecane jet flame representative of low-temperature diesel ignition (referred to as the Borghesi flame from here on). The Borghesi flame exhibits low- and high-temperature ignition, premixed combustion of rich/lean branches of edge flames, and regions of nonpremixed combustion. This temporally evolving flame is periodic in the streamwise and spanwise directions and possesses a jet Reynolds number of 7,063 and a turbulent Reynolds number of 950. The fuel is *n*-dodecane at  $T_F = 450$  K, and the oxidizer is diluted air ( $X_{O_2} = 0.15$  and  $X_{N_2} = 0.85$ ) at  $T_O = 960$  K. The jet velocity and coflow velocity are  $U_{\text{jet}} = 21$  m/s and  $U_{\text{coflow}} = 0.5$  m/s, respectively. The DNS was conducted on a computational grid with approximately 3 billion nodes, at an operating pressure of 25 bar, and leveraging a 35-species reduced *n*-dodecane mechanism.

Six time snapshots of the DNS data are identified as representative of each combustion mode and low- and high-temperature ignition regimes based on the relative contribution of each combustion mode to the heat release rate at each point in time [122]. The time

snapshots selected from the simulation data are summarized in Table 7.1. The dimensionless simulation times  $t^*$  provided are nondimensionalized by the high-temperature ignition delay time  $\tau_{\text{ID,HT}} = 0.325$  ms and include an offset of 0.28 ms for the initial duration that reaction was disabled in the DNS. The work presented in this chapter focuses only on the data from the time snapshot corresponding to  $t = 0.84$  ms, though modeling efforts should be extended to all snapshots in future work if the models are to be expected to truly generalize to multi-modal combustion.

## 7.2 Multi-Modal Manifold Model: Modification for Temporally Evolving Flames

The DNS mixture fraction  $\zeta$  evolves in space and time according to the transport equation:

$$\frac{\partial \rho \zeta}{\partial t} + \frac{\partial \rho u_j \zeta}{\partial x_j} = \frac{\partial}{\partial x_j} \left( \rho D_\zeta \frac{\partial \zeta}{\partial x_j} \right), \quad (7.1)$$

where  $D_\zeta$  is the DNS mixture fraction diffusivity. Since the Borghesi flame is a temporally evolving jet flame, the fuel continuously mixes without replenishment, and the maximum DNS mixture fraction  $\zeta_{\text{max}}$  continuously decreases in time. This poses a problem, for the DNS mixture fraction dissipation rate  $\chi_{\zeta\zeta}$  and DNS cross-dissipation rate  $\chi_{\zeta\Lambda}$  go to zero at  $\zeta = \zeta_{\text{max}}$  (when the gradient of the DNS mixture fraction  $\zeta$  goes to zero) rather than at  $\zeta = 1$ , as it should for the mixture fraction  $Z$  from Eq. 5.4. For this reason, the mixture fraction  $Z$  is not equivalent to  $\zeta$ . Instead, the two mixture fractions are related by a scaling factor, so that  $Z \equiv \zeta/\zeta_{\text{max}}$ . The fuel-side boundary conditions for the mixture fraction  $Z$  must then be modified according to the known fuel-side boundary conditions for the DNS mixture fraction  $\zeta$ , analogous to the expressions from Eq. 4.1 and Eq. 4.2:

$$Y_i(B^{Z=1}) = \zeta_{\text{max}} Y_i(B^{\zeta=1}) + (1 - \zeta_{\text{max}}) Y_i(B^{\zeta=0}) = Y_i(\zeta_{\text{max}}), \quad (7.2)$$

$$h(B^{Z=1}) = \zeta_{\max} h(B^{\zeta=1}) + (1 - \zeta_{\max}) h(B^{\zeta=0}) = h(\zeta_{\max}). \quad (7.3)$$

Modifying the boundary conditions in this way implicitly presumes that the fuel is first diluted with oxidizer via inert mixing prior to reaction – an assumption that will be revisited in future work when considering all the time snapshots in the DNS dataset. The values of the maximum DNS mixture fraction  $\zeta_{\max}$  at each time snapshot are summarized in Table 7.1.

Table 7.1: DNS time snapshot parameters. The time snapshot selected in this work is highlighted in light gray.

$t^*$	$t$ [ms]	$\zeta_{\max}$
0.468	0.432	0.275
0.570	0.465	0.258
0.840	0.553	0.213
1.080	0.631	0.205
1.510	0.771	0.185
1.723	0.840	0.180

### 7.3 Nonlinear Reference Species Definition

To recover the nonpremixed manifold equations of Eq. 5.11 from the multi-modal manifold equations of Eq. 5.4 in the limit of nonpremixed combustion, the generalized progress variable must be defined in such a way as to ensure that the gradients of the generalized progress variable vanish in nonpremixed flames. This is accomplished by defining the generalized progress variable  $\Lambda$  in terms of a nonlinear reference species [38, 69] according to

$$\Lambda = \frac{Y_{\text{R}}^{\text{NP}}(Z_{\text{ref}}) - Y_{\text{R},u}(Z_{\text{ref}})}{Y_{\text{R},b}(Z_{\text{ref}}) - Y_{\text{R},u}(Z_{\text{ref}})}, \quad (7.4)$$

where  $Y_{\text{R},b}$  and  $Y_{\text{R},u}$  are the reference species mass fractions in the burned and unburned mixtures, respectively.  $Y_{\text{R}}^{\text{NP}}$  is the reference species mass fraction profile corresponding to a one-dimensional nonpremixed manifold solution per Eq. 3.4 that coincides with the local

values of the mixture fraction and reference species mass fraction.  $Z_{\text{ref}}$  is the reference mixture fraction (in this work, taken at stoichiometric conditions).

To determine the generalized progress variable fields from the DNS data, sets of one-dimensional solutions to the nonpremixed manifold equations (Eq. 3.3 and Eq. 3.4) are first computed over a range of reference mixture fraction dissipation rates spanning an s-curve [10]. Equation 5.5 requires that the reference species  $Y_{\text{R}}$  be strictly monotonic so that the partial derivative of the reference species with respect to the generalized progress variable  $\frac{\partial Y_{\text{R}}}{\partial \Lambda}$  be strictly positive at all mixture fractions. The generalized progress variable source term is otherwise undefined where  $\frac{\partial Y_{\text{R}}}{\partial \Lambda} = 0$ , corresponding to a location where one-dimensional nonpremixed manifold solutions with different reference mixture fraction dissipation rates intersect. In this way, the nonlinear generalized progress variable definition is essentially a nonlinear normalization of the reference mixture fraction dissipation rate, subject to this reference species monotonicity constraint.

In this work, the reference species (satisfying this monotonicity constraint) is selected as  $Y_{\text{R}} \equiv Y_{\text{H}_2} + Y_{\text{H}_2\text{O}} + Y_{\text{CO}} + Y_{\text{CO}_2}$ , all species important in the high-temperature ignition regime of the chosen time snapshot. Extending this reference species definition to earlier time snapshots may require additional consideration of  $Y_{\text{CH}_2\text{O}}$ , an important intermediate species in low-temperature ignition.

## 7.4 Dissipation Rate Modeling Approach

The multi-modal manifold equations are closed by modeling the dependence of the three dissipation rates on the mixture fraction and generalized progress variable. These three dissipation rate profiles can each be represented by the product of a *magnitude* and profile *shape* according to

$$\chi_{ZZ}(Z, \Lambda) = \chi_{ZZ, \text{ref}} \hat{f}(Z, \Lambda; Z_{\text{ref}}, \Lambda_{\text{ref}}) , \quad (7.5)$$

$$\chi_{Z\Lambda}(Z, \Lambda) = \chi_{Z\Lambda, \text{ref}} \hat{g}(Z, \Lambda; Z_{\text{ref}}, \Lambda_{\text{ref}}) , \quad (7.6)$$

$$\chi_{\Lambda\Lambda}(Z, \Lambda) = \chi_{\Lambda\Lambda, \text{ref}} \hat{h}(Z, \Lambda; Z_{\text{ref}}, \Lambda_{\text{ref}}) , \quad (7.7)$$

where the magnitude of each dissipation rate profile is embedded in the reference dissipation rates  $\chi_{ZZ, \text{ref}}$ ,  $\chi_{Z\Lambda, \text{ref}}$ , and  $\chi_{\Lambda\Lambda, \text{ref}}$ , and the shape of each dissipation rate profile is embedded in the instantaneous normalized dissipation rate profiles  $\hat{f}$ ,  $\hat{g}$ , and  $\hat{h}$ . Isolating the dissipation rate magnitude from the profile shape enables each to be modeled separately, and in turn allows each model to be assessed individually. The present work begins with providing closure for the magnitude of the dissipation rate profiles.

## 7.5 Filtered Dissipation Rate Modeling

The filtered dissipation rates  $\tilde{\chi}_{\psi\omega}$  are important model quantities in LES implementations of the multi-modal manifold model. The reference dissipation rates  $\chi_{\psi\omega, \text{ref}}$ , which parameterize the manifold solutions, fundamentally depend on the model for the filtered dissipation rates through the numerator of the deconvolution operations:

$$\chi_{ZZ, \text{ref}} = \frac{\tilde{\chi}_{ZZ}}{\iint \hat{f}(Z, \Lambda; Z_{\text{ref}}, \Lambda_{\text{ref}}) \tilde{P}(Z, \Lambda; \tilde{Z}, Z_v, \tilde{\Lambda}, \Lambda_v) dZ d\Lambda} , \quad (7.8)$$

$$\chi_{Z\Lambda, \text{ref}} = \frac{\tilde{\chi}_{Z\Lambda}}{\iint \hat{g}(Z, \Lambda; Z_{\text{ref}}, \Lambda_{\text{ref}}) \tilde{P}(Z, \Lambda; \tilde{Z}, Z_v, \tilde{\Lambda}, \Lambda_v) dZ d\Lambda} , \quad (7.9)$$

$$\chi_{\Lambda\Lambda, \text{ref}} = \frac{\tilde{\chi}_{\Lambda\Lambda}}{\iint \hat{h}(Z, \Lambda; Z_{\text{ref}}, \Lambda_{\text{ref}}) \tilde{P}(Z, \Lambda; \tilde{Z}, Z_v, \tilde{\Lambda}, \Lambda_v) dZ d\Lambda} , \quad (7.10)$$

where  $\hat{f}$ ,  $\hat{g}$ , and  $\hat{h}$  are discussed in more detail in the latter half of this chapter. The three filtered dissipation rates also appear in the mixture fraction and generalized progress variable subfilter variance and subfilter covariance transport equations, so appropriate closure models are needed.

### 7.5.1 Algebraic Models: Pierce and Linear Relaxation Models

Algebraic models for the filtered dissipation rates have traditionally been formulated for passive scalars (that is, the mixture fraction). Yet, in the interest of simplicity, such algebraic models are often extended to reactive scalars (that is, progress variables). Two such algebraic models are presented here and used as benchmarks for evaluating data-based models for the filtered dissipation rates.

#### Pierce Model

Originally formulated for the mixture fraction by Pierce and Moin [124], the filtered dissipation rate is modeled assuming the production and dissipation of the scalar subfilter variance are equal. In the interest of brevity, the generalization of this concept to general scalars  $\psi$  and  $\omega$  will be referred to as the Pierce model, which is given by

$$\tilde{\chi}_{\psi\omega} \equiv \widetilde{2D \frac{\partial\psi}{\partial x_j} \frac{\partial\omega}{\partial x_j}} \approx 2 \left( \tilde{D} + D_t \right) \frac{\partial\tilde{\psi}}{\partial x_j} \frac{\partial\tilde{\omega}}{\partial x_j}. \quad (7.11)$$

Note that the assumption of equal scalar subfilter variance production and dissipation poses a couple of problems. The first issue is that this assumption is not necessarily appropriate for reactive scalars, particularly at low Karlovitz number where turbulent strain effects no longer overwhelm dilatation. The second issue is that this assumption discounts the use of the Pierce model in the mixture fraction subfilter variance equation, for doing so would result in the mixture fraction subfilter variance incorrectly evolving as a passive scalar.

#### Linear Relaxation Model (LRM)

An alternative approach for modeling the filtered dissipation rates is via a linear relaxation model (LRM) [89]. This involves closing the filtered dissipation rates by assuming the subfilter contribution is proportional to the scalar subfilter variance scaled by a turbulent

timescale according to

$$\widetilde{\chi}_{\psi\omega} \equiv \widetilde{2D \frac{\partial \psi}{\partial x_j} \frac{\partial \omega}{\partial x_j}} \approx 2\widetilde{D} \frac{\partial \widetilde{\psi}}{\partial x_j} \frac{\partial \widetilde{\omega}}{\partial x_j} + C_{\chi_{\psi\omega}} \frac{\nu_t}{\Delta^2} (\widetilde{\psi\omega} - \widetilde{\psi}\widetilde{\omega}) , \quad (7.12)$$

where  $C_{\chi_{\Lambda\Lambda}} = 20$  [125]. Since this approach no longer presumes equal scalar subfilter variance production and dissipation, the LRM is appropriate for closing the mixture fraction subfilter variance transport equation. However, the LRM is still only developed with passive scalars in mind, lending an advantage to data-based approaches that do not rely on this assumption.

## 7.5.2 Enforcing Physical Constraints in DNN Models

To address the issues associated with existing algebraic models for the filtered dissipation rates, a fully-connected, feed-forward, deep neural network capable of simultaneously predicting  $\widetilde{\chi}_{ZZ}$ ,  $\frac{\widetilde{\chi}_{Z\Lambda}}{(\widetilde{\chi}_{ZZ}\widetilde{\chi}_{\Lambda\Lambda})^{1/2}}$ , and  $\widetilde{\chi}_{\Lambda\Lambda}$  is trained. Note that  $\frac{\widetilde{\chi}_{Z\Lambda}}{(\widetilde{\chi}_{ZZ}\widetilde{\chi}_{\Lambda\Lambda})^{1/2}}$  is referred to as the *pseudo-filtered alignment* due to its resemblance to the alignment of the mixture fraction and generalized progress variable gradients defined in Eq. 5.23. Though this pseudo-filtered alignment is not exactly equivalent to  $\widetilde{\Theta}$ , it possesses the same bounds – that is, the pseudo-filtered alignment must also lie between positive one and negative one. In a similar vein, the mixture fraction and generalized progress variable dissipation rates must both be positive, by construction.

Two DNN models are trained for the filtered dissipation rates. The first (unconstrained) DNN is trained to predict the quantities  $\widetilde{\chi}_{ZZ}$ ,  $\frac{\widetilde{\chi}_{Z\Lambda}}{(\widetilde{\chi}_{ZZ}\widetilde{\chi}_{\Lambda\Lambda})^{1/2}}$ , and  $\widetilde{\chi}_{\Lambda\Lambda}$  directly. The second (constrained) DNN instead enforces the alignment and positivity constraints by mapping the filtered dissipation rates to the entire real line via appropriately chosen functions. This is accomplished by instead training to predict the quantities  $\ln(\widetilde{\chi}_{ZZ})$ ,  $\tanh^{-1}\left(\frac{\widetilde{\chi}_{Z\Lambda}}{(\widetilde{\chi}_{ZZ}\widetilde{\chi}_{\Lambda\Lambda})^{1/2}}\right)$ , and  $\ln(\widetilde{\chi}_{\Lambda\Lambda})$  and inverting the DNN outputs to recover the filtered dissipation rates. The resulting predictions are guaranteed to satisfy the alignment and positivity constraints.



### 7.5.3 Training Data Generation

The DNN training features are generated to emulate LES data in much the same way as described in Sec. 6.3.1. Each quantity of interest  $\phi$  is computed by filtering the DNS data with varying filter stencil sizes  $\Delta_\alpha/h_\alpha = 2, 4, 8, 16, 32$  where  $\Delta_\alpha$  and  $h_\alpha$  are the filter size and grid spacing in the direction  $\alpha$ , respectively. The filter stencil volume is defined in the same way such that  $V_{\text{stencil}}$  has  $(\Delta_\alpha/h_\alpha + 1)^3$  grid points. A clipped top-hat filter is applied to the stencil volume surrounding each grid point:

$$\bar{\phi}(\mathbf{x}) = \sum_{V_{\text{stencil}}} \phi(\mathbf{x} - \mathbf{x}') G(\mathbf{x}'; \Delta) d\mathbf{x}' . \quad (7.13)$$

The filter  $G(\mathbf{x}'; \Delta)$  is now an inhomogeneous tensor-product top-hat filter characterized by the filter size  $\Delta$ . Density-weighted filtered quantities are once again determined according to  $\tilde{\phi} \equiv \overline{\rho\phi}/\bar{\rho}$ .

A total of five datasets are generated by filtering a single time snapshot of the DNS data ( $t = 0.84$  ms) corresponding to  $\Delta_\alpha/h_\alpha = 2, 4, 8, 16, 32$ . Each dataset contains 30,000 samples randomly sampled from the filtered data. The four datasets corresponding to  $\Delta_\alpha/h_\alpha = 2, 4, 16, 32$  are aggregated into a single dataset with 120,000 samples, 15% and 20% of which is set aside for validation and testing, respectively. The remaining dataset corresponding to  $\Delta_\alpha/h_\alpha = 8$  is withheld for additional testing of the final trained DNNs.

### 7.5.4 DNN Model Details

#### Input Feature Selection

The following input features were selected for training: the filtered mixture fraction  $\tilde{Z}$ , the mixture fraction subfilter variance  $Z_v$ , the magnitude of the filtered mixture fraction gradient  $|\nabla \tilde{Z}|$ , the filtered generalized progress variable  $\tilde{\Lambda}$ , the generalized progress variable subfilter variance  $\Lambda_v$ , the magnitude of the filtered generalized progress variable gradient  $|\nabla \tilde{\Lambda}|$ , the

mixture fraction and generalized progress variable subfilter covariance  $\Sigma_{Z\Lambda}$ , the resolved alignment  $\frac{\nabla \tilde{Z} \cdot \nabla \tilde{\Lambda}}{|\nabla \tilde{Z}| |\nabla \tilde{\Lambda}|}$ , the Frobenius norm of the filtered strain rate  $|\tilde{S}|$ , the filtered molecular diffusivity  $\tilde{D}_\Lambda$ , the filtered density  $\bar{\rho}$ , the filtered reference species source term  $\overline{m}_R$ , and the local filter size  $\Delta_L \equiv V_{\text{stencil}}^{1/3}$ .

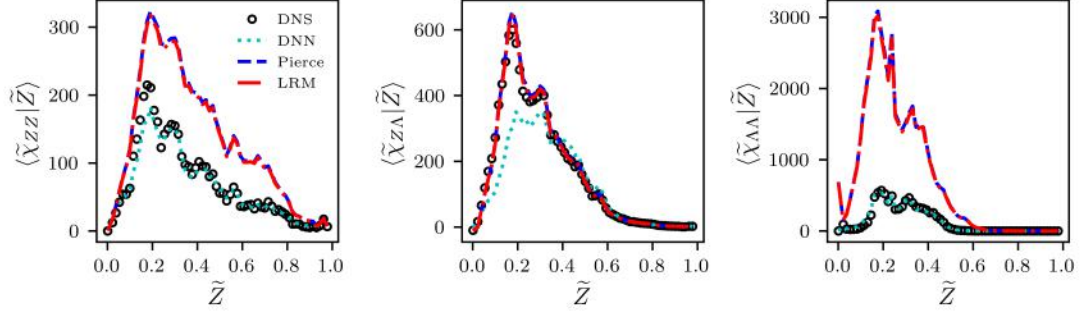
## Network Hyperparameter Selection

The filtered dissipation rates were modeled with two fully-connected, feed-forward DNNs – one with and one without physical constraints enforced on the model predictions. Adam [119] was once again selected as the optimizer, with a learning rate of  $10^{-3}$ . The mean absolute error was chosen as the loss function, and a leaky rectified linear unit with a negative slope coefficient of 0.1 was selected as the activation function. Neural network training was implemented with the Python library **TensorFlow** and the **Keras** API.

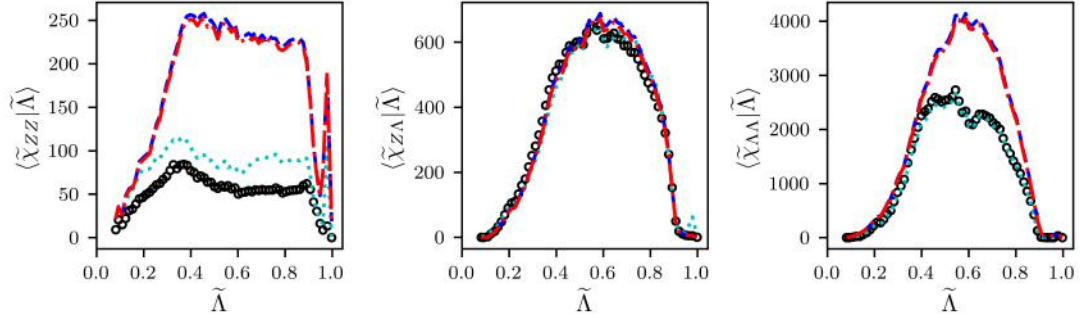
Network architectures were determined using the same iterative algorithm deployed in Sec. 6.3.3. The final unconstrained DNN possesses 14 hidden layers with 32 fully-connected nodes per layer and a total of 14,275 trainable parameters (training, validation, and testing losses are 13.7, 13.7, and 13.8, respectively). The final constrained DNN possesses 15 hidden layers with 35 fully-connected nodes per layer and a total of 18,238 trainable parameters (training, validation, and testing losses are 0.58, 0.54, and 0.55, respectively).

### 7.5.5 DNN Model Evaluation

Figure 7.1 shows the conditional averages of the filtered mixture fraction dissipation rate, filtered cross-dissipation rate, and filtered generalized progress variable dissipation rate predictions generated by the unconstrained DNN with the withheld testing dataset corresponding to  $\Delta_\alpha/h_\alpha = 8$ . The unconstrained DNN demonstrates an improvement over the Pierce and LRM approaches, particularly for the filtered generalized progress variable dissipation rate. This is reasonable, for the Pierce and LRM approaches are derived for a passive scalar, and the generalized progress variable possesses a source term. The success of the unconstrained



(a) Filtered dissipation rates conditionally averaged against filtered mixture fraction

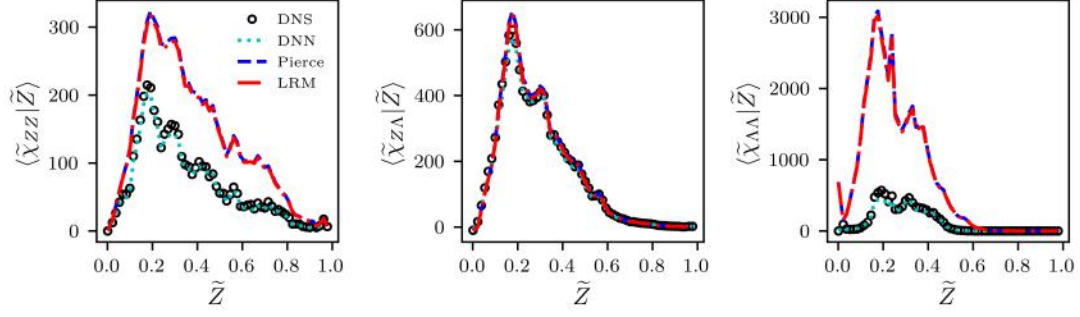


(b) Filtered dissipation rates conditionally averaged against filtered generalized progress variable

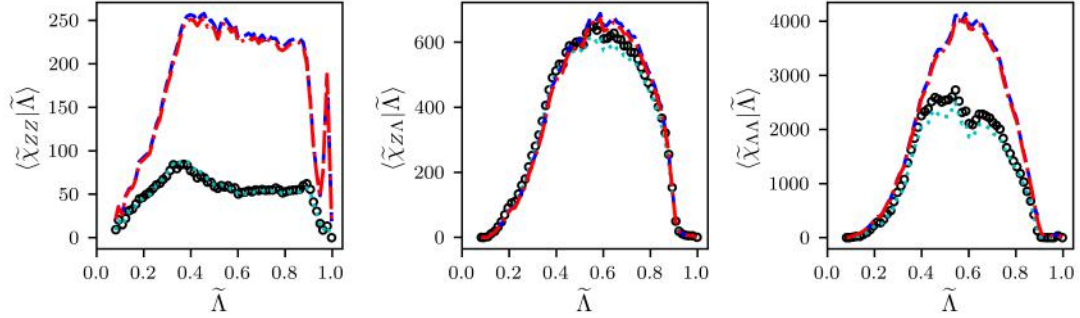
Figure 7.1: Unconstrained DNN predictions ( $\cdots$ ) of the filtered mixture fraction dissipation rate, filtered cross-dissipation rate, and filtered generalized progress variable dissipation rate, each conditionally averaged on the filtered mixture fraction in (a) or on the filtered generalized progress variable in (b). DNN predictions are compared to conditionally averaged DNS data ( $\circ$ ), conditionally averaged Pierce model predictions ( $-\cdot-$ ), and conditionally averaged LRM predictions ( $-\cdot-$ ). Conditional averages are reported for withheld testing data with  $\Delta_\alpha/h_\alpha = 8$ .

DNN is undermined by an overprediction of the filtered mixture fraction dissipation rate when conditioned on the filtered generalized progress variable and an underprediction of the filtered cross-dissipation rate when conditioned on the filtered mixture fraction. Note that the error observed in the filtered cross-dissipation rate predictions results from the compounded effects of the error in the filtered mixture fraction dissipation rate predictions as well as the error in the pseudo-filtered alignment predictions.

Figure 7.2 demonstrates the effect of enforcing physical alignment and positivity constraints on the predictive capability of the DNN model. The constrained DNN exhibits



(a) Filtered dissipation rates conditionally averaged against filtered mixture fraction



(b) Filtered dissipation rates conditionally averaged against filtered generalized progress variable

Figure 7.2: Constrained DNN predictions ( $\cdots$ ) of the filtered mixture fraction dissipation rate, filtered cross-dissipation rate, and filtered generalized progress variable dissipation rate, each conditionally averaged on the filtered mixture fraction in (a) or on the filtered generalized progress variable in (b). DNN predictions are compared to conditionally averaged DNS data ( $\circ$ ), conditionally averaged Pierce model predictions ( $-\cdot-$ ), and conditionally averaged LRM predictions ( $-\cdot\cdot$ ). Conditional averages are reported for withheld testing data with  $\Delta_\alpha/h_\alpha = 8$ .

considerable improvement in the filtered mixture fraction dissipation rate predictions as well as the pseudo-filtered alignment, so that the filtered mixture fraction dissipation rate predictions and the filtered cross-dissipation rate predictions generated by the constrained DNN match nearly exactly with that of the conditionally averaged DNS data, without an appreciable change in the filtered generalized progress variable dissipation rate predictions. Both the Pierce and LRM approaches also accurately reconstruct the filtered cross-dissipation rate in the conditionally averaged sense. However, it is also important to consider the variance in the predictive capability of each modeling approach, in addition to the conditional means.

Figure 7.3 demonstrates the variance in the predictive capabilities of the two DNN models via two-dimensional histograms of model predictions versus filtered DNS data. Figure 7.3 (a) shows that the unconstrained DNN both underpredicts the filtered mixture fraction dissipation rate and often significantly overpredicts or underpredicts the filtered cross-dissipation rate, despite reasonable agreement with conditionally averaged DNS data – that is, the agreement of conditionally averaged predictions with conditionally averaged DNS data does not guarantee accurate instantaneous predictions. Figure 7.3 (b) shows that the constrained DNN possesses a smaller predictive variance corresponding to the filtered mixture fraction dissipation rate and the filtered cross-dissipation rate, indicating more accurate instantaneous predictions of these quantities. The constrained DNN also exhibits a similar predictive variance corresponding to the filtered generalized progress variable dissipation rate as compared to the unconstrained DNN, indicating that enforcing physical constraints on model output quantities of interest either increases or does not have a meaningful effect on model predictive capability. Moving forward, physical constraints are therefore enforced wherever it is possible to do so.

## 7.6 Instantaneous Dissipation Rate Profile Modeling

The remainder of this chapter returns to the challenge of closing Eq. 7.8 to Eq. 7.10, shifting focus from the filtered dissipation rates in the numerators of these expressions to the instantaneous normalized dissipation rate profiles  $\hat{f}$ ,  $\hat{g}$ , and  $\hat{h}$  in the denominators.

Chapter 6 described the one-dimensional instantaneous normalized dissipation rate profiles in the context of the premixed manifold model. The instantaneous normalized dissipation rate profiles of this chapter similarly capture the instantaneous variation in the shape of the dissipation rate profiles with respect to the manifold coordinates, though the dependence of  $\hat{f}$ ,  $\hat{g}$ , and  $\hat{h}$  on the mixture fraction and generalized progress variable introduces additional complexities regarding training data extraction.

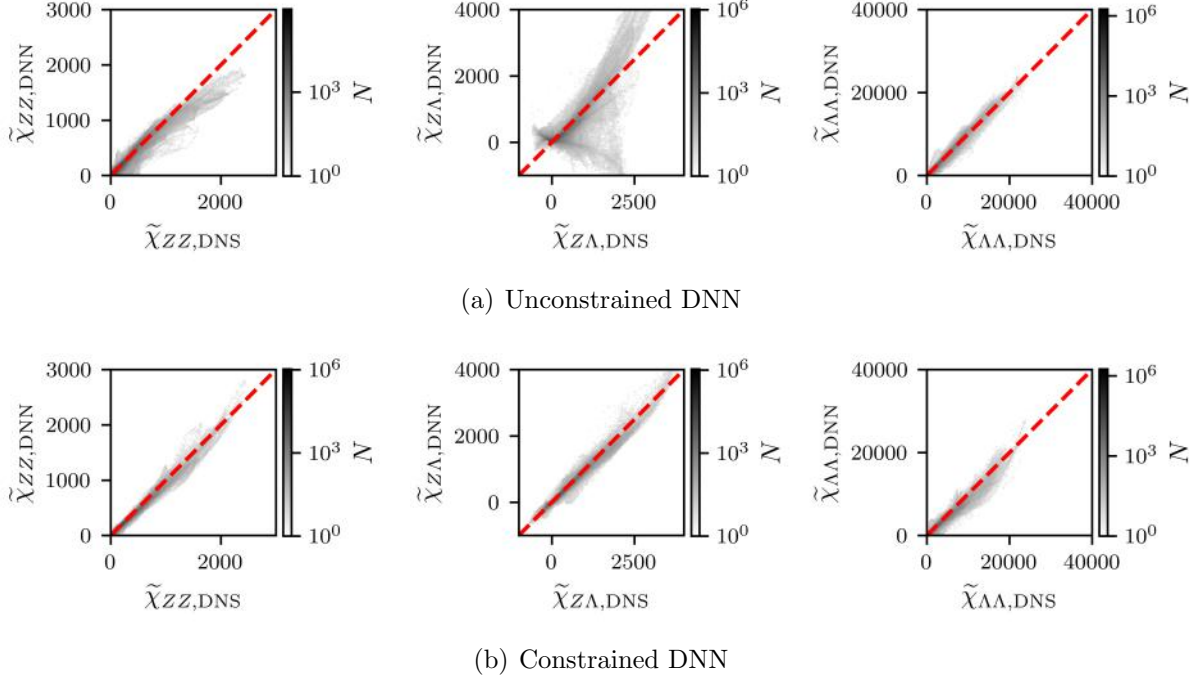


Figure 7.3: Parity plots for the filtered mixture fraction dissipation rate, filtered cross-dissipation rate, and filtered generalized progress variable dissipation rate, comparing DNN predictions to corresponding filtered DNS data. (a) demonstrates the results of the unconstrained DNN, and (b) demonstrates the results of the constrained DNN, both as two-dimensional histograms shaded on a log-scale according to the number of data samples  $N$  at each point. The dashed red line (--) denotes exact agreement between DNN predictions and the filtered DNS data. Parity plots are reported for withheld testing data with  $\Delta_\alpha/h_\alpha = 8$ .

Typical algebraic models for dissipation rate profiles are presumed to be ‘universal’ and are developed for a single mode of combustion – often with simplifying, ad hoc assumptions [68]. Previous work modeling dissipation rates and their instantaneous profiles via a data-based approach has demonstrated considerable success for both premixed and nonpremixed combustion [71, 111, 118]. The current chapter aims to leverage a similar data-based modeling approach to provide closure for the three instantaneous dissipation rate profiles in Eq. 7.5 to Eq. 7.7.

### 7.6.1 Algebraic Dissipation Rate Profile Models

Algebraic models for the mixture fraction dissipation rate profile [68] and generalized progress variable dissipation rate profile [37, 69] are described in Sec. 5.1 and reproduced here in their normalized forms according to

$$\hat{f}_a(Z; Z_{\text{ref}}, \Lambda_{\text{ref}}) = \frac{\exp\left(-2\left[\text{erfc}^{-1}(2Z)\right]^2\right)}{\exp\left(-2\left[\text{erfc}^{-1}(2Z_{\text{ref}})\right]^2\right)}, \quad (7.14)$$

$$\begin{aligned} \hat{h}_a(Z, \Lambda; Z_{\text{ref}}, \Lambda_{\text{ref}}) = \exp\left[-2\left(\text{erfc}^{-1}\left(\frac{2Z(1-Z_{\text{ref}})}{(1-Z)Z_{\text{ref}} + Z(1-Z_{\text{ref}})}\right)\right)^2\right] \\ \times \frac{\exp\left(-2\left[\text{erfc}^{-1}(2\Lambda)\right]^2\right)}{\exp\left(-2\left[\text{erfc}^{-1}(2\Lambda_{\text{ref}})\right]^2\right)}, \end{aligned} \quad (7.15)$$

where the subscript ‘a’ denotes that these expressions each correspond to an algebraic model, and both of these models enforce unity at the reference mixture fraction and reference generalized progress variable.

Since the cross-dissipation was neglected in Chapter 5, an algebraic model for the cross-dissipation rate profile has not yet been introduced. However, recent work by Novoselov et al. [69] involved indirectly developing such an algebraic model for the cross-dissipation rate profile by directly modeling the alignment according to

$$\Theta_a = c_{\Theta} \tanh\left(\frac{2(Z_{\text{ref}} - Z)}{Z_{\text{ref}}(1 - Z_{\text{ref}})}\right), \quad (7.16)$$

where  $c_{\Theta}$  is a constant scaling factor that varies in space and time in the same way as the reference dissipation rates. This algebraic alignment model accounts for front-supported (suppressed) combustion when  $-1 \leq c_{\Theta} < 0$ , back-supported (promoted) combustion when  $0 < c_{\Theta} \leq 1$ , and unaligned scenarios when  $c_{\Theta} = 0$ .

The alignment scaling factor  $c_\Theta$  could be computed at each location in physical space and time in an LES (presuming no subfilter variation) according to

$$c_\Theta = \frac{\tilde{\chi}_{Z\Lambda}}{\iint \tanh\left(\frac{2(Z_{\text{ref}}-Z)}{Z_{\text{ref}}(1-Z_{\text{ref}})}\right) \left(\chi_{ZZa}(Z) \chi_{\Lambda\Lambda a}(Z, \Lambda)\right)^{1/2} \tilde{P}(Z, \Lambda; \tilde{Z}, Z_v, \tilde{\Lambda}, \Lambda_v) dZ d\Lambda}, \quad (7.17)$$

where  $\chi_{ZZa}(Z, \Lambda)$  and  $\chi_{\Lambda\Lambda a}(Z, \Lambda)$  are evaluated with the algebraic models in Eq. 7.14 and Eq. 7.15. However, this approach depends on the presumed form of the subfilter PDF – a quantity that is not well-modeled in the context of multi-modal combustion. Instead, the local alignment scaling factor  $c_\Theta$  is defined as the value which minimizes the mean square error of  $\Theta_a$  relative to the local DNS alignment profile  $\Theta_{\text{DNS}}$ .

Since  $\Theta_a$  is zero at the reference mixture fraction, it is more convenient to directly compute the corresponding instantaneous cross-dissipation rate profile according to

$$\chi_{Z\Lambda a}(Z, \Lambda) = \Theta_a(Z) \left(\chi_{ZZa}(Z) \chi_{\Lambda\Lambda a}(Z, \Lambda)\right)^{1/2}, \quad (7.18)$$

rather than computing the instantaneous normalized cross-dissipation rate profile  $\hat{g}$  in Eq. 7.6.

Note that all of these algebraic models are ‘universal,’ meaning they are fundamentally incapable of capturing the instantaneous variation of the shape of the dissipation rate profiles and alignment profiles. The consequences of this implicit assumption are evaluated later on.

### 7.6.2 Profile Extraction Methodology

Instantaneous normalized dissipation rate and alignment profiles  $\hat{f}(Z, \Lambda)$ ,  $\Theta(Z, \Lambda)$ , and  $\hat{h}(Z, \Lambda)$  have been extracted from the DNS dataset by tracing out surfaces in physical space that are aligned with the local mixture fraction gradient and local generalized progress variable gradient (hereafter referred to as manifold stream-surfaces), a generalization of the approach described in Sec. 6.2.2 for two-dimensional manifolds. The normalized dissipation



rate profiles are defined as the dependence of  $\chi_{ZZ}$  and  $\chi_{\Lambda\Lambda}$  on  $Z$  and  $\Lambda$  along these manifold stream-surfaces, normalized by each respective reference dissipation rate. The alignment profiles are reconstructed from the dependence of  $\chi_{ZZ}$ ,  $\chi_{Z\Lambda}$ , and  $\chi_{\Lambda\Lambda}$  on  $Z$  and  $\Lambda$  along the manifold stream-surfaces.

Manifold stream-surfaces are composed of physical space paths that are everywhere parallel to the local mixture fraction gradient or generalized progress variable gradient (mixture fraction or generalized progress variable streamlines, respectively). Manifold coordinate streamlines are identified using a similar procedure as described by Chan et al. [114]. Each set of extracted instantaneous normalized dissipation rate profiles corresponds to a starting location on the DNS grid  $\mathbf{x}_0$ . Initially,  $\mathbf{x}_t = \mathbf{x}_0$  and the subsequent point in physical space  $\mathbf{x}_{t+1}$  on the manifold coordinate streamline passing through  $\mathbf{x}_t$  is computed with a constant step size in manifold coordinate space.  $\mathbf{x}_{t+1}$  is then approximated in terms of the current location in physical space  $\mathbf{x}_t$  and the local manifold coordinate gradient via the chain rule:

$$\mathbf{x}_{t+1} = \mathbf{x}_t + \frac{\nabla\psi}{|\nabla\psi|^2} \bigg|_{\mathbf{x}_t} d\psi, \quad (7.19)$$

where  $\psi$  represents either mixture fraction or generalized progress variable. Equation 7.19 is first iterated upon with  $d\psi = d\psi_{\text{step}}$  and  $\psi = Z$  until the mixture fraction increases to  $\psi = 1$ , within a threshold of 0.05, and then repeated with  $d\psi = -d\psi_{\text{step}}$  until the mixture fraction decreases to  $\psi = 0$ , within the same threshold. The step size in physical space is therefore adapted dynamically, taking a smaller value where the mixture fraction gradient is steep and a larger value where the mixture fraction gradient is shallow. The constant mixture fraction step size  $d\psi_{\text{step}}$  is set to  $10^{-2}$ , for further refinement of  $d\psi_{\text{step}}$  does not result in appreciable changes to the extracted instantaneous normalized dissipation rate profiles. Once the mixture fraction streamline is extracted, the same procedure is repeated with  $\psi = \Lambda$ , seeding from locations along the extracted mixture fraction streamline. The three dissipation rates are then computed at every point along the extracted manifold stream-surface and divided by

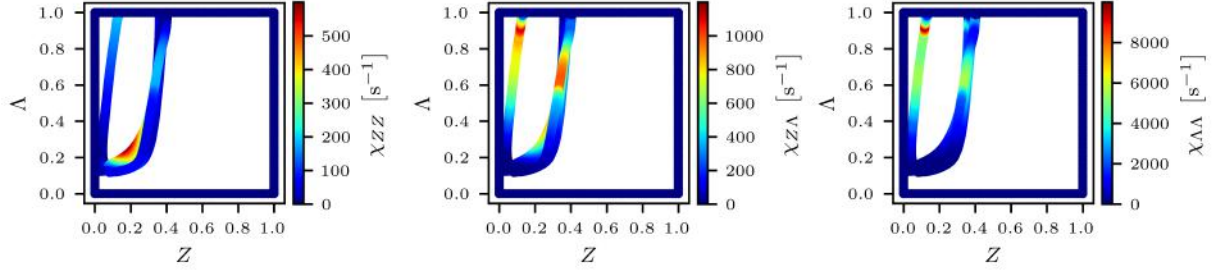
the corresponding reference dissipation rates. Each instantaneous conditional dissipation rate profile is then interpolated onto a two-dimensional uniform grid in mixture fraction and generalized progress variable space with  $64 \times 64$  points.

### 7.6.3 Profile Regression Methods: PLI and GPR

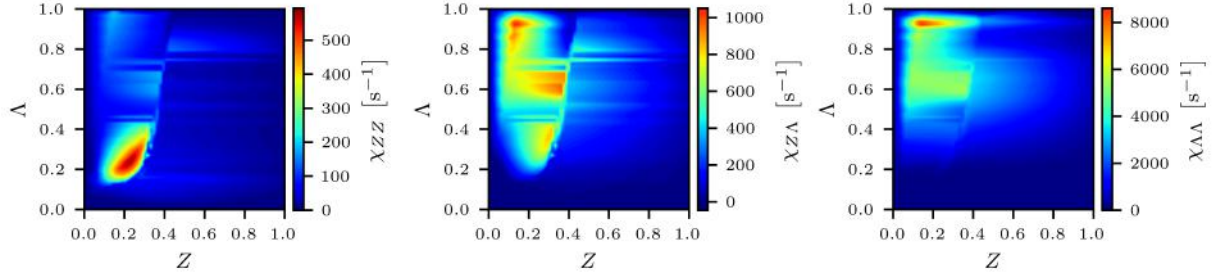
The parameterization of the instantaneous dissipation rate profiles with respect to the manifold coordinates extracted along manifold stream-surfaces is found to often only access a subregion of manifold coordinate space. This is demonstrated by Fig. 7.4 (a), which shows the dissipation rates from a manifold stream-surface corresponding to a representative point on the DNS grid, plotted with respect to the manifold coordinates. Regions of large mixture fraction are unaccessed by the extracted manifold stream-surface since not all mixture fraction and generalized progress variable pairs manifest in the selected time snapshot, introducing an ambiguity in defining the dissipation rates in these unaccessed regions of manifold coordinate space. The training labels for the DNN will be the instantaneous conditional dissipation rate profiles discretized onto a fixed, *structured* manifold coordinate grid, so the dissipation rates must be interpolated in these unaccessed regions. Two different regression methods were investigated, including piecewise linear interpolation (PLI) and Gaussian process regression (GPR). Here  $\mathbf{x}$  represents a point in the two-dimensional manifold coordinate space on the unstructured grid,  $f(\mathbf{x})$  represents a dissipation rate on the unstructured grid,  $\mathbf{x}^*$  represents a point on the structured manifold grid, and  $f^*(\mathbf{x}^*)$  represents a dissipation rate interpolant on the structured grid.

PLI simply involves generating a triangulation for a given unstructured grid and computing the linear barycentric interpolation [126] at each point  $\mathbf{x}^*$  according to

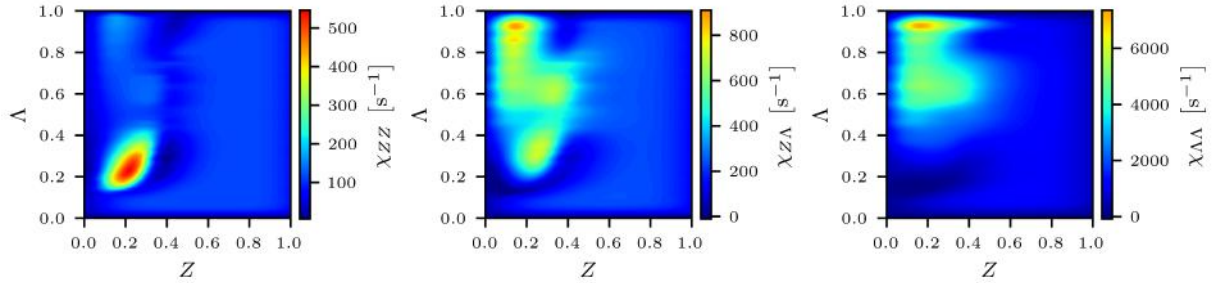
$$f^*(\mathbf{x}^*) = \sum_{i=1}^3 \alpha_i f(\mathbf{x}_i) , \quad (7.20)$$



(a) Unstructured extracted data



(b) Piecewise linear interpolation



(c) Gaussian process regression

Figure 7.4: Mixture fraction dissipation rate, cross-dissipation rate, and generalized progress variable dissipation rate profiles plotted as color contour plots versus mixture fraction and generalized progress variable. (a) shows raw unstructured data extracted from the DNS along a particular representative manifold stream-surface computed from Eq. 7.19; (b) shows the structured data interpolated with piecewise linear interpolation; and (c) shows the structured data interpolated with Gaussian process regression.

where  $\mathbf{x}_i$  are the coordinates of the three nearest-neighbors of point  $\mathbf{x}^*$ , and  $\alpha_i$  are the barycentric coordinates of  $\mathbf{x}^*$  satisfying  $\mathbf{x}^* = \sum_{i=1}^3 \alpha_i \mathbf{x}_i$ .

GPR is a nonlinear regression method that seeks to estimate an unknown quantity of interest  $\mathbf{f}^* = [f^*(\mathbf{x}_1^*), \dots, f^*(\mathbf{x}_s^*)]^\top \in \mathbb{R}^s$  at a set of  $s$  new input coordinates  $\mathbf{X}^* = [\mathbf{x}_1^*, \dots, \mathbf{x}_s^*] \in$

$\mathbb{R}^{n \times s}$  given  $u$  input coordinates  $\mathbf{X} = [\mathbf{x}_1, \dots, \mathbf{x}_u] \in \mathbb{R}^{n \times u}$  and the values of the quantity of interest corresponding to those coordinates  $\mathbf{f} = [f(\mathbf{x}_1), \dots, f(\mathbf{x}_u)]^\top \in \mathbb{R}^u$ , where  $\mathbf{x}_i, \mathbf{x}_i^* \in \mathbb{R}^n$  [127]. The joint distribution of the known and unknown quantity of interest is presumed to be Gaussian with zero mean, covariance matrices obtained from kernelized input data, and independent, identically distributed Gaussian noise such that

$$\begin{bmatrix} \mathbf{f} \\ \mathbf{f}^* \end{bmatrix} \sim \mathcal{N} \left( \begin{bmatrix} \mathbf{0} \\ \mathbf{0} \end{bmatrix}, \begin{bmatrix} \mathbf{K} + \sigma^2 \mathbf{I} & \mathbf{K}^* \\ \mathbf{K}^{*\top} & \mathbf{K}^{**} \end{bmatrix} \right), \quad (7.21)$$

where  $K$  is the selected kernel function,  $\mathbf{K} = K(\mathbf{X}, \mathbf{X})$ ,  $\mathbf{K}^* = K(\mathbf{X}, \mathbf{X}^*)$ , and  $\mathbf{K}^{**} = K(\mathbf{X}^*, \mathbf{X}^*)$ ,  $\sigma$  is the measurement noise level, and  $\mathbf{I}$  is the identity matrix. An expression for the posterior (conditional) distribution is then derived given known data according to

$$\mathbf{f}^* | \mathbf{f}, \mathbf{X}, \mathbf{X}^* \sim \mathcal{N} \left( \underbrace{\mathbf{K}^{*\top} (\mathbf{K} + \sigma^2 \mathbf{I})^{-1} \mathbf{f}}_{\bar{\mathbf{f}}^*}, \mathbf{K}^{**} - \mathbf{K}^{*\top} (\mathbf{K} + \sigma^2 \mathbf{I})^{-1} \mathbf{K}^* \right). \quad (7.22)$$

The quantity of interest at the points  $\mathbf{X}^*$  can then be estimated as the expectation over this distribution  $\bar{\mathbf{f}}^*$ . GPR was implemented via the Python library `scikit-learn` [128], and several kernel functions were investigated, including the radial basis function, Matérn, and rational quadratic kernels, all with and without considering measurement noise. The Matérn kernel was identified as the best compromise between regression cost and quality.

Figure 7.4 (b) and (c) show the three instantaneous conditional dissipation rate profiles predicted using PLI and GPR, respectively. The PLI approach produces discontinuities in the gradient, while the GPR predictions produce comparatively smoother profiles. The differences in the predicted dissipation rates between the two regression methods can be as large as 10%, so the impact of these differences on the thermochemical state must be investigated in more detail.

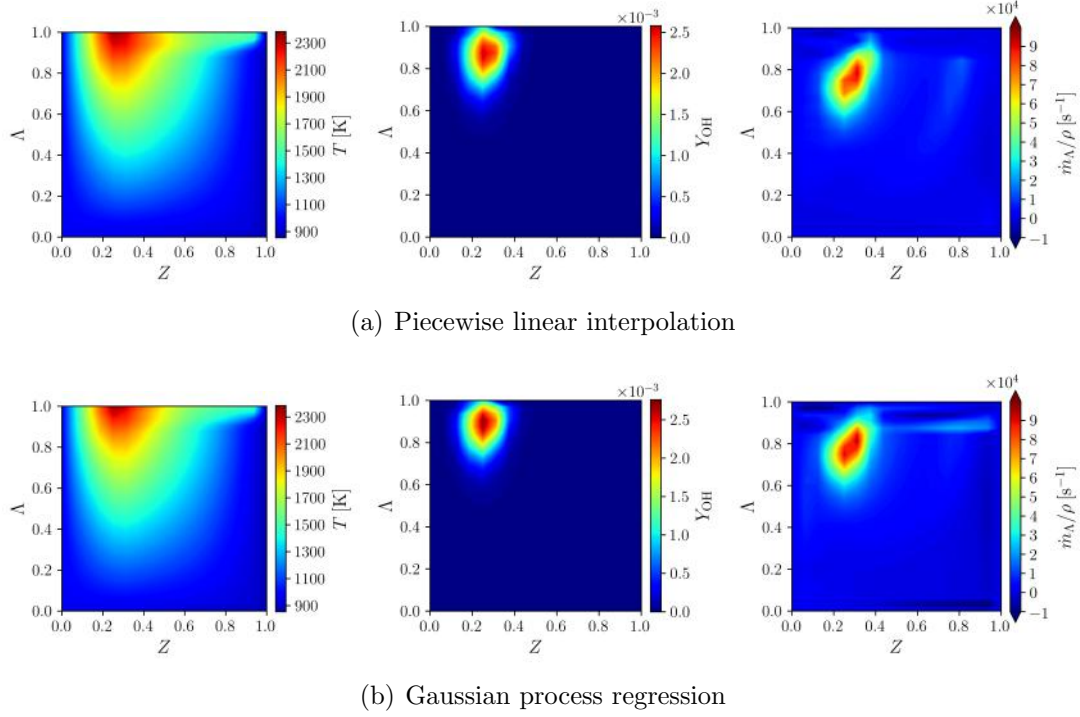


Figure 7.5: Unfiltered thermochemical profiles computed as solutions to Eq. 5.4, given dissipation rate profiles interpolated with either piecewise linear interpolation (PLI) or Gaussian process regression (GPR).

#### 7.6.4 *A Priori* Evaluation of Regression Methods

The sensitivity of the thermochemical state to the regression method used to generate the three instantaneous conditional dissipation rate profiles is explored by comparing the solutions to the two-dimensional multi-modal manifold equations (given by Eq. 5.4) for relevant quantities of interest. The multi-modal manifold equations are solved using the PDRs code [38, 94].

Figure 7.5 compares unfiltered thermochemical solution profiles generated for a single point on the DNS grid, corresponding to the three instantaneous conditional dissipation rate profiles interpolated with both PLI and GPR. While quantities such as temperature are largely unaffected, differences of up to 10% are observed in intermediate species as well as the generalized progress variable source term. Even small differences in the source term could be important for ignition and flame propagation. However, this is only a single point

on the DNS grid and may not be representative of the sensitivity of the thermochemical state elsewhere in dissipation rate space. This analysis should be extended to evaluate the sensitivity of the regression method over a sample of profiles simultaneously. Furthermore, in a coarse-grained simulation such as LES, thermochemical quantities of interest are filtered – it is, therefore, reasonable to compare the filtered thermochemical quantities of interest generated with the two different regression methods.

The filtered thermochemical state is computed for 90 sample points on the DNS grid. At each DNS grid point, the corresponding sets of instantaneous conditional dissipation rate profiles are input to Eq. 5.4, the solutions to which are computed. Equation 5.15 is evaluated numerically for each sample, where  $\phi$  is the unfiltered multi-modal manifold equation solution for a thermochemical quantity of interest (corresponding to a particular regression method), and the PDF  $\tilde{P}$  is parameterized by the locally filtered values of mixture fraction and generalized progress variable and their respective variances corresponding to the particular sample. The analysis is performed for the largest filter stencil size of  $\Delta_\alpha/h_\alpha = 32$ , for which the largest portion of manifold coordinate space is important to the filtered thermochemical state.

Figure 7.6 compares the filtered thermochemical state resulting from the two regression methods. As was the case for the unfiltered case, the temperature is again largely unaffected, and intermediate species such as carbon monoxide and formaldehyde radicals demonstrate relative insensitivity to the dissipation rate regression method (around 10%). Though a variation in the progress variable source term of up to 10% is also observed, this is for the worst-case-scenario at the largest filter stencil size, and errors introduced due to turbulence models and other combustion closure models would dominate at these coarser grid resolutions. Since the two regression methods produce solutions that are at least quantitatively similar, it is logical to select the approach that tends to yield faster manifold calculations. Due to the fact that the profiles produced with GPR are smoother than those produced by PLI, the manifold equation solver tends to converge more quickly using GPR profiles

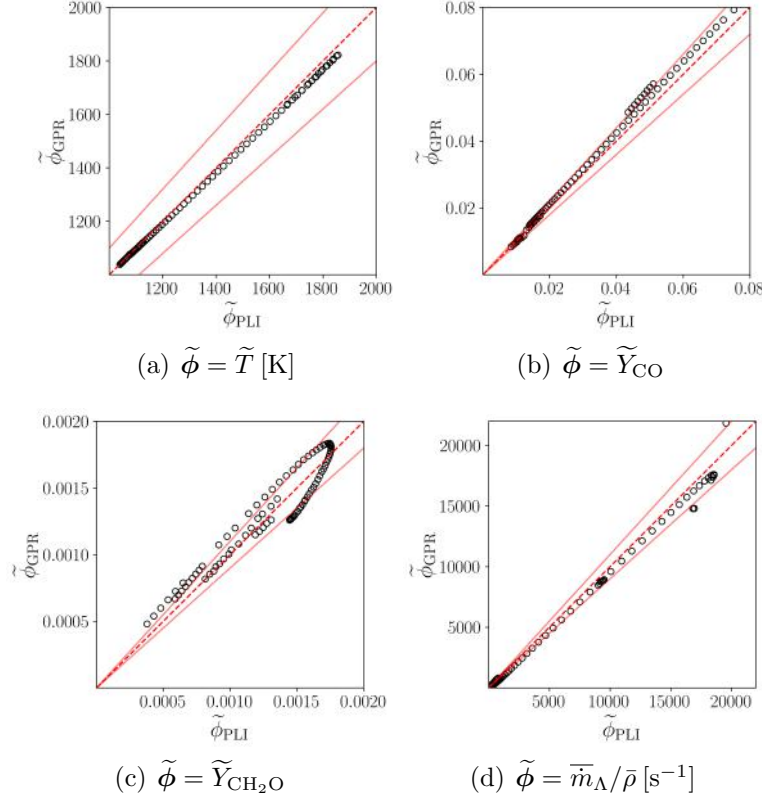


Figure 7.6: Comparison of 90 filtered thermochemical quantities ( $\circ$ ) computed from Eq. 5.15 ( $\Delta_{\alpha}/h_{\alpha} = 32$ ), given dissipation rate profiles interpolated with either piecewise linear interpolation (PLI) or Gaussian process regression (GPR) with outlier profiles removed. One-to-one correspondence is denoted by the red dashed line (--) and  $\pm 10\%$  error bounds are denoted by the solid red lines (—).

than with PLI. As such, GPR offers the best compromise between regression cost and manifold solution cost between the two regression methods and is therefore used to generate the structured training labels.

### 7.6.5 Evaluating Profile ‘Universality’

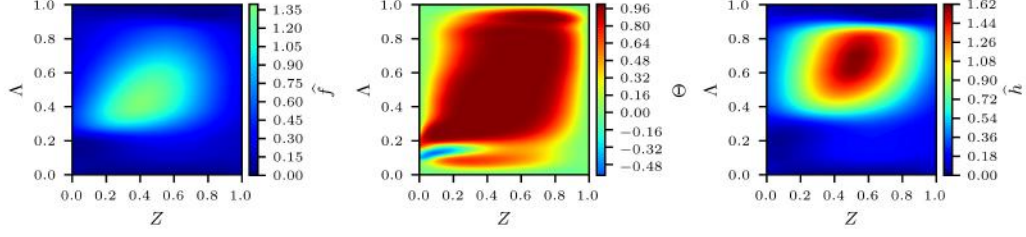
Having selected GPR as the method to generate structured training labels, the instantaneous normalized dissipation rate and alignment profiles are extracted at different locations on the DNS grid corresponding to the time snapshot at  $t = 0.84$  ms, allowing the algebraic model assumption of spatiotemporal profile ‘universality’ to be evaluated. Figure 7.7 (a) and (b)

show instantaneous profiles extracted at two different representative points on the DNS grid. These two sets of instantaneous normalized dissipation rate and alignment profiles are completely different, even qualitatively. The peak values of the instantaneous normalized dissipation rate profiles are as different as 50%, and the locations of the peak values occur in different locations in manifold coordinate space. Even more significant is the qualitative difference in the structure of the alignment profiles – the location in manifold coordinate space where the alignment profiles become negative is completely different in the two locations on the DNS grid. These considerable qualitative and quantitative differences illustrate that the instantaneous normalized dissipation rate and alignment profiles are most certainly not ‘universal’ in space and time, despite the implicit presence of this assumption in traditional algebraic models.

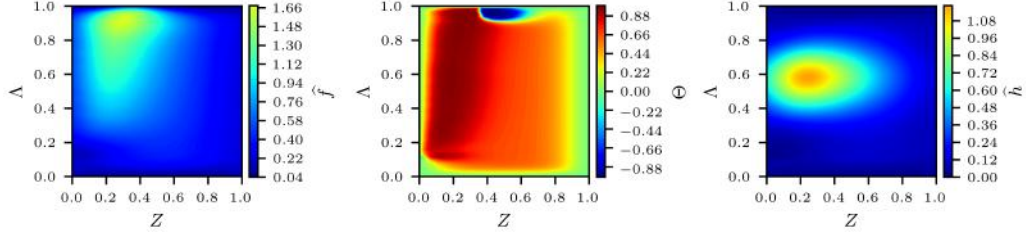
Figure 7.7 (d) illustrates the instantaneous normalized dissipation rate and alignment profiles corresponding to the algebraic models discussed in Sec. 7.6.1. Since Eq. 7.16 requires a value for  $c_\Theta$ , which may change in space and time on the LES grid, a best-case value for  $c_\Theta$  was computed to minimize the mean square error between the algebraic alignment profile and the DNS profile ( $c_\Theta = -0.471$ ) rather than computing  $c_\Theta$  according to Eq. 7.17. Even in this ideal scenario, the algebraic alignment model is qualitatively very different from either of the alignment profiles extracted from the DNS. The algebraic model for the instantaneous normalized generalized progress variable dissipation rate profile is qualitatively similar but misses the peak value by as much as 60%. The algebraic model assumption that the instantaneous normalized mixture fraction dissipation rate profile is independent of the generalized progress variable is also clearly inaccurate.

At the very least, the algebraic models should be expected to represent the conditional average of the instantaneous normalized dissipation rate and alignment profiles extracted from the DNS dataset. Figure 7.7 (c) presents these conditional averages, computed as  $\langle \hat{f}(Z, \Lambda) \rangle$ ,  $\langle \Theta(Z, \Lambda) \rangle$ , and  $\langle \hat{h}(Z, \Lambda) \rangle$ . Though defining the ‘universal’ mean DNS alignment model according to  $c_\Theta \langle \frac{\Theta(Z, \Lambda)}{c_\Theta} \rangle$  (where the outer  $c_\Theta$  is the instantaneous local value) would

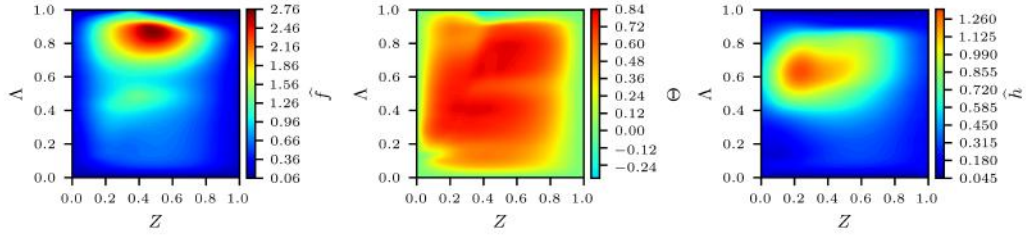




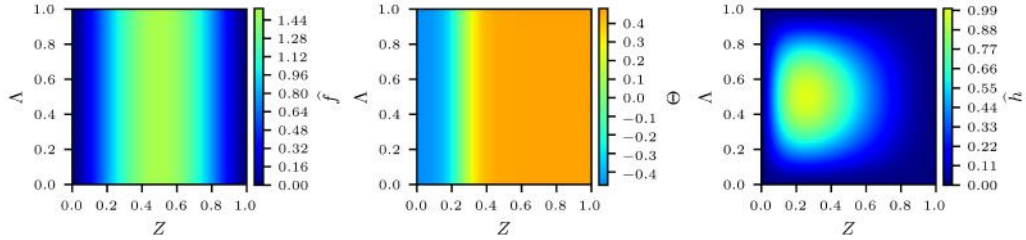
(a) Instantaneous DNS profiles (primary)



(b) Instantaneous DNS profiles (secondary)



(c) Mean normalized DNS model



(d) Algebraic models

Figure 7.7: Instantaneous normalized mixture fraction dissipation rate, alignment, and normalized generalized progress variable dissipation rate profiles plotted as color contour plots versus mixture fraction and generalized progress variable. (a) corresponds to instantaneous DNS profiles at a primary location on the DNS grid; (b) corresponds to instantaneous DNS profiles at a secondary location on the DNS grid; (c) corresponds to the ‘universal’ conditional mean of the extracted DNS profiles; and (d) corresponds to the ‘universal’ algebraic models.

be more consistent with the algebraic alignment model by ensuring that only the ‘universal’ part of the alignment is conditionally averaged, this definition does not enforce physical constraints on the alignment, so  $\langle \Theta(Z, \Lambda) \rangle$  is preferred. This figure demonstrates that not only do the algebraic models not capture the instantaneous spatiotemporal variation in the normalized dissipation rate and alignment profiles, they do not even capture the conditional average (except for the algebraic instantaneous normalized generalized progress variable dissipation rate profile, which is at least qualitatively similar to the conditional average of the DNS profiles). An instantaneous model capable of capturing this observed spatiotemporal variation in the instantaneous normalized dissipation rate and alignment profiles is sought via a data-based approach.

### 7.6.6 Training Data Generation

The DNN training features are generated by emulating data from LES, as described in the first part of this chapter. The same inhomogeneous top-hat filter and filter stencil sizes  $\Delta_\alpha/h_\alpha$  are applied to generate filtered datasets. As previously alluded to, the training labels now comprise the instantaneous normalized dissipation rate profiles  $\hat{f}(Z, \Lambda)$  and  $\hat{h}(Z, \Lambda)$  as well as the instantaneous alignment profile  $\Theta(Z, \Lambda)$ , all discretized on a structured  $64 \times 64$  point grid in manifold coordinate space. Physical constraints are enforced on the alignment by mapping the training labels to  $\hat{f}(Z, \Lambda)$ ,  $\hat{h}(Z, \Lambda)$ , and  $\tanh^{-1}(\Theta(Z, \Lambda))$  before training. A total of 55,000 profiles are generated from the DNS dataset for each filter stencil size ( $\Delta_\alpha/h_\alpha = 2, 4, 16, 32$ ), forming a single aggregated training dataset with a total of 220,000 samples. 15% of this training dataset is set aside for validation, and 20% is used for testing. A dataset with 55,000 samples corresponding to  $\Delta_\alpha/h_\alpha = 8$  is withheld for additional testing of the final trained DNN.

## 7.6.7 DNN Model Details

### Input Feature Selection

In addition to the input features used to train the two DNNs for the filtered dissipation rates in the first part of this chapter ( $\tilde{Z}$ ,  $Z_v$ ,  $|\nabla\tilde{Z}|$ ,  $\tilde{\Lambda}$ ,  $\Lambda_v$ ,  $|\nabla\tilde{\Lambda}|$ ,  $\Sigma_{Z\Lambda}$ ,  $\frac{\nabla\tilde{Z}\cdot\nabla\tilde{\Lambda}}{|\nabla\tilde{Z}||\nabla\tilde{\Lambda}|}$ ,  $|\tilde{S}|$ ,  $\tilde{D}_\Lambda$ ,  $\bar{\rho}$ ,  $\bar{m}_R$ , and  $\Delta_L \equiv V_{\text{stencil}}^{1/3}$ ), the following input features were selected to predict the instantaneous normalized dissipation rate and alignment profiles: the filtered mixture fraction dissipation rate  $\tilde{\chi}_{ZZ}$ , the filtered cross-dissipation rate  $\tilde{\chi}_{Z\Lambda}$ , and the filtered generalized progress variable dissipation rate  $\tilde{\chi}_{\Lambda\Lambda}$ .

### Network Hyperparameter Selection

The instantaneous normalized dissipation rate and alignment profiles were again modeled with a fully-connected, feed-forward DNN. The same optimizer and network hyperparameters were employed using the Python library `TensorFlow` and the `Keras` API, as detailed in previous sections. The final DNN possesses 16 hidden layers with 118 fully-connected nodes per layer.

## 7.6.8 DNN Model Evaluation

The training, validation, and testing losses are given by 0.076, 0.087, and 0.083, respectively, suggesting that the DNN model does not suffer from overfitting. The final generalizability of the DNN is evaluated on the withheld testing dataset corresponding to a filter stencil size of  $\Delta_\alpha/h_\alpha = 8$ .

To assess the advantage of adopting an instantaneous, data-based modeling approach with a DNN compared to utilizing a ‘universal’ algebraic or conditional mean modeling approach, instantaneous model errors are defined according to

$$\epsilon_{\hat{f}_{\text{model}}}(Z, \Lambda) = \left| \hat{f}_{\text{model}}(Z, \Lambda) - \hat{f}_{\text{DNS}}(Z, \Lambda) \right|, \quad (7.23)$$

$$\epsilon_{\Theta_{\text{model}}}(Z, \Lambda) = \left| \Theta_{\text{model}}(Z, \Lambda) - \Theta_{\text{DNS}}(Z, \Lambda) \right|, \quad (7.24)$$

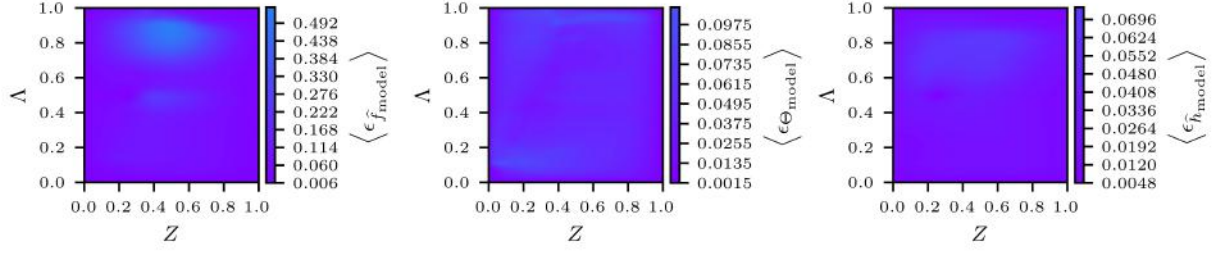
$$\epsilon_{\hat{h}_{\text{model}}}(Z, \Lambda) = \left| \hat{h}_{\text{model}}(Z, \Lambda) - \hat{h}_{\text{DNS}}(Z, \Lambda) \right|, \quad (7.25)$$

which are then conditionally averaged over the withheld testing dataset for each model. The performance of the mean DNS model from Fig. 7.7 (c) is also evaluated as a representative best-case ‘universal’ profile model.

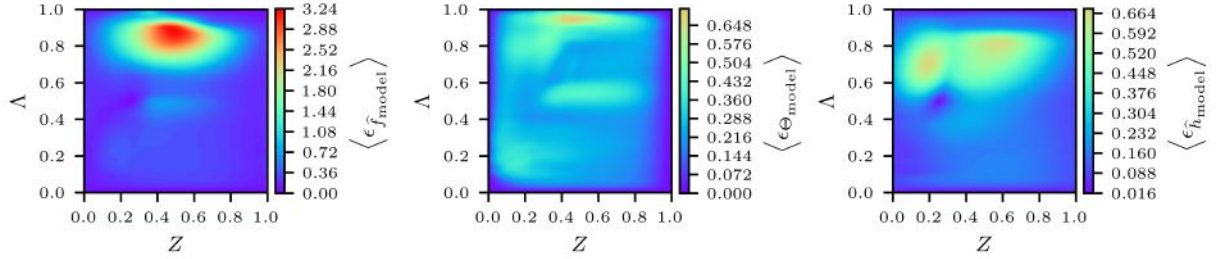
Figure 7.8 demonstrates the average instantaneous error corresponding to the instantaneous DNN model compared to the ‘universal’ mean DNS model and algebraic models. The ‘universal’ models both fail to capture locations on the DNS grid where the extracted instantaneous normalized mixture fraction dissipation rate profiles display a shift in the peak value toward larger generalized progress variable. Similarly, the ‘universal’ models both fail to capture shifts in the peak values of extracted instantaneous normalized generalized progress variable dissipation rate profiles toward lean or rich mixture fractions. By comparison, the instantaneous DNN model captures this profile shifting with a near order of magnitude improvement over the ‘universal’ models. The algebraic alignment model exhibits inaccurate predictions at lean mixture fractions, while the idealized mean DNS ‘universal’ alignment model demonstrates some improvement in this region of manifold coordinate space. The instantaneous DNN model demonstrates considerable improvement in the alignment predictions over the ‘universal’ models, again displaying up to an order of magnitude reduction in the average instantaneous error.

### 7.6.9 *A Priori* Analysis

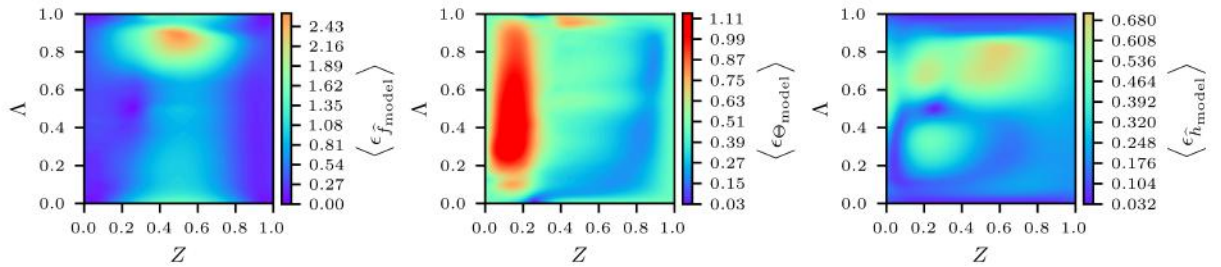
To evaluate the importance on the thermochemical state of considering the spatiotemporal variation in the instantaneous normalized dissipation rate and alignment profiles, the three dissipation rate profiles reconstructed from each modeling approach are used to solve the two-dimensional multi-modal manifold equations in Eq. 5.3 and Eq. 5.4 with the PDRs code [38, 94]. The sensitivity of the thermochemical state is assessed at a single representative



(a) DNN model errors



(b) Mean DNS model errors



(c) Algebraic model errors

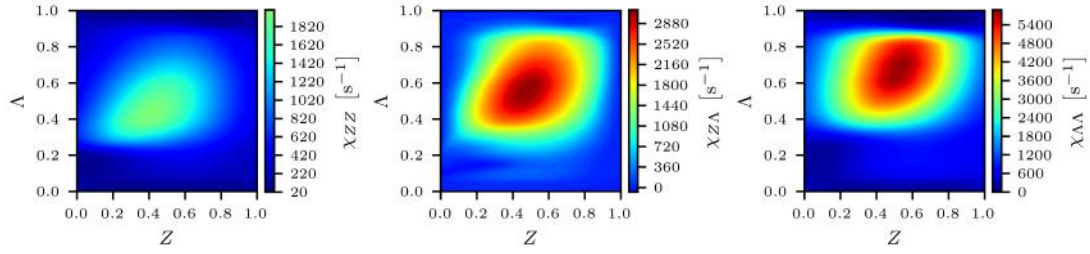
Figure 7.8: Conditionally averaged instantaneous error profiles plotted as color contour plots versus mixture fraction and generalized progress variable. (a) corresponds to the DNN model; (b) corresponds to the mean DNS model; and (c) corresponds to the algebraic models.

point on the DNS grid corresponding to the *primary* extracted profiles in Fig. 7.7 (a). Note that the conditions of the three dissipation rate profiles at this point are such that the cross-dissipation rate profile is important, corresponding to locations in physical space where combustion is inherently multi-modal in nature – that is, the maximum value of each dissipation rate is large relative to the chemical source term and the maximum values of all three dissipation rates are of similar magnitude to one another. The three dissipation rate profiles associated with this single point on the DNS grid are shown in Fig. 7.9, corresponding

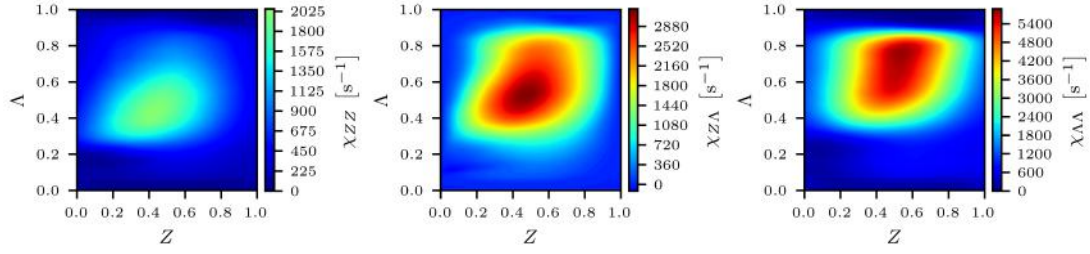
to the instantaneous profiles extracted from the DNS, the local predictions generated by the instantaneous DNN model, the ‘universal’ mean DNS model, and the ‘universal’ algebraic models.

Figure 7.10 presents the temperature profiles obtained as solutions to the multi-modal manifold equations with six different sets of dissipation rate profiles: the instantaneous dissipation rate profiles extracted from the DNS at a representative point on the DNS grid, the corresponding DNN model dissipation rate profile predictions, the mean DNS model, the algebraic models, the DNS profiles with zero cross-dissipation rate, and the algebraic models with zero cross-dissipation rate. Clearly, the temperature is not a strong function of the choice of dissipation rate profile model, remaining effectively unchanged despite considerable variation in the dissipation rate profiles. However, the temperature is only one of many thermochemical quantities of interest.

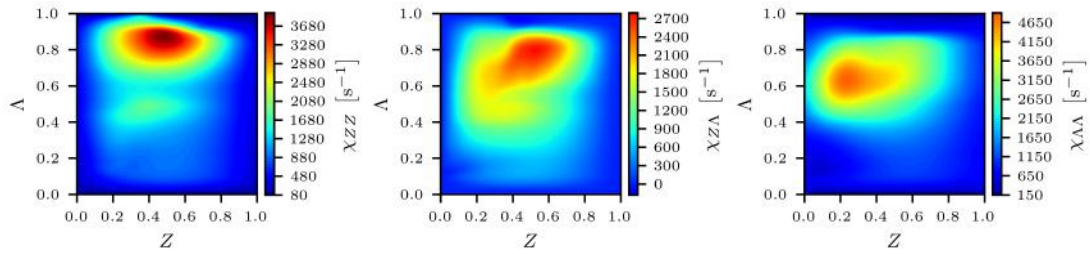
Figure 7.11 shows the carbon monoxide mass fraction solutions for the same six sets of dissipation rate profiles. Unlike the temperature, the carbon monoxide mass fraction is noticeably more sensitive to the choice of dissipation rate profile model. The ‘universal’ mean DNS and algebraic models underpredict the carbon monoxide mass fraction by 20% at moderately rich mixture fractions ( $0.4 < Z < 0.7$ ) and as much as 25% at peak values, while the DNN model predictions yield nearly identical solutions as the DNS profiles. Figure 7.11 (f) shows that neglecting the algebraic alignment model for the cross-dissipation rate entirely does not exacerbate these differences any further, implying that errors in the mixture fraction dissipation rate and generalized progress variable dissipation rate profiles are of leading-order importance. Figure 7.11 (c) demonstrates that neglecting the cross-dissipation rate profile in the DNS extracted profile results in reduced errors compared to the combined errors introduced by the algebraic models for the mixture fraction dissipation rate, cross-dissipation rate, and generalized progress variable dissipation rate. Therefore, appropriately modeling the cross-dissipation rate is less important to accurately predicting intermediate chemical species than the other dissipation rate profiles, even under the condition that all



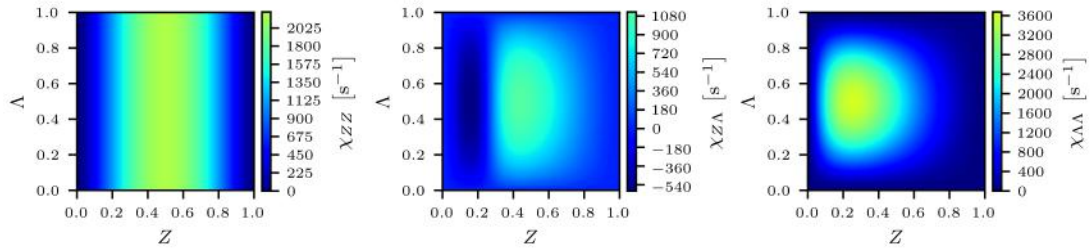
(a) DNS



(b) DNN model



(c) Mean DNS model



(d) Algebraic models

Figure 7.9: Instantaneous mixture fraction dissipation rate, cross-dissipation rate, and generalized progress variable dissipation rate profiles plotted as color contour plots versus mixture fraction and generalized progress variable. (a) corresponds to instantaneous DNS profiles; (b) corresponds to instantaneous DNN model predictions; (c) corresponds to the ‘universal’ conditional mean of the extracted DNS profiles; and (d) corresponds to the ‘universal’ algebraic models.



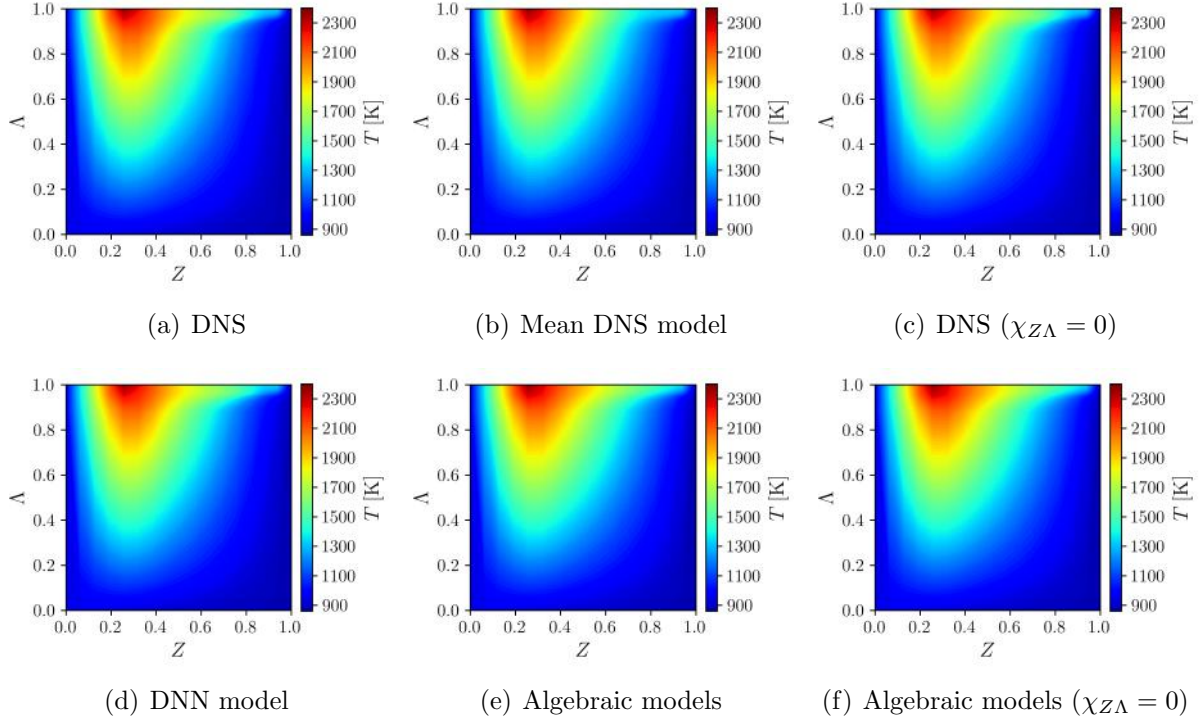


Figure 7.10: Temperature solutions plotted as color contour plots versus mixture fraction and generalized progress variable. Each subfigure corresponds to the multi-modal manifold solution for a set of dissipation rate profiles determined via a different modeling approach.

three dissipation rates are large relative to the chemical source term. However, this trend is only demonstrated here for a single representative point on the DNS grid, so the generality of this conclusion remains unconfirmed.

Figure 7.12 shows the generalized progress variable source term solutions corresponding to the six sets of dissipation rate profiles. Note that the sharp gradient discontinuity visible at  $\Lambda \approx 0.9$  is related to the omission of middle branch s-curve solutions that fail to satisfy reference species monotonicity requirements when defining the generalized progress variable according to the nonlinear reference described in Sec. 7.3. This omission is not expected to be important in late-ignition time snapshots with predominantly high-temperature chemistry, but the limitations imposed by the monotonicity constraint should be further assessed in future work that extends the present approach to earlier time snapshots. The ‘universal’ mean DNS and algebraic models underpredict the generalized progress variable source term



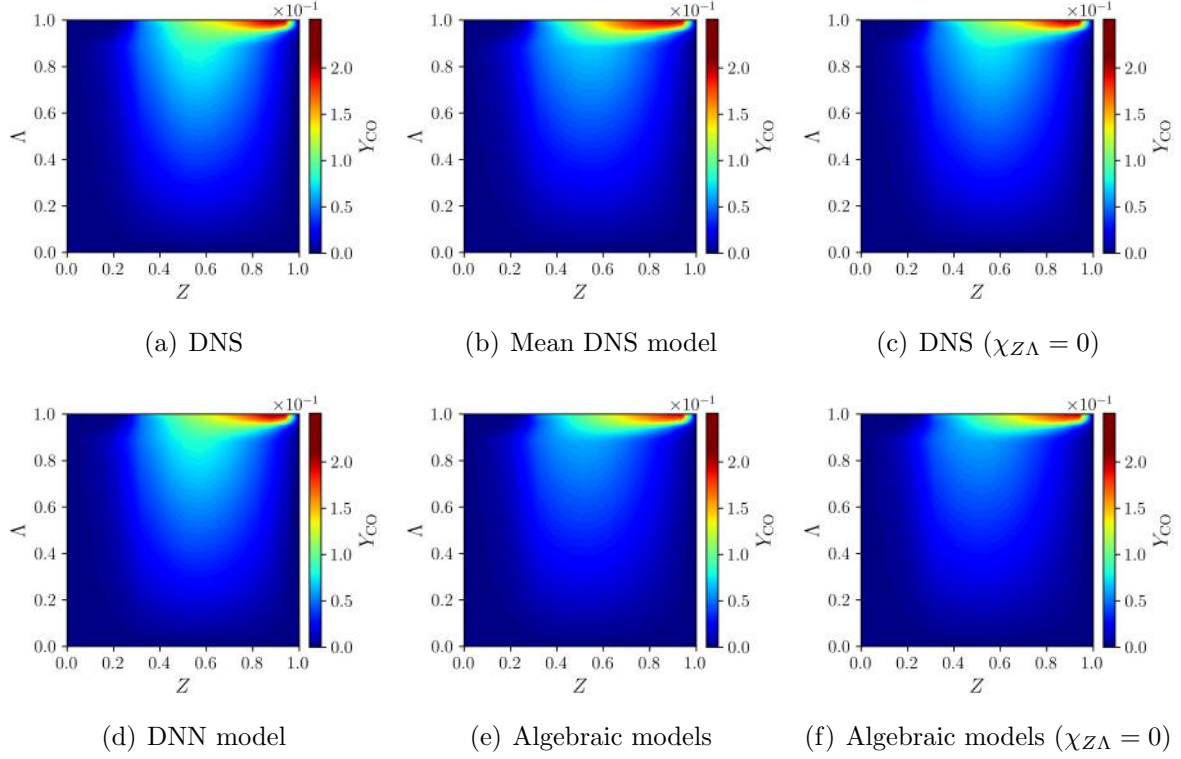


Figure 7.11: Carbon monoxide mass fraction solutions plotted as color contour plots versus mixture fraction and generalized progress variable. Each subfigure corresponds to the multi-modal manifold solution for a set of dissipation rate profiles determined via a different modeling approach.

by as much as 20% to 30% around stoichiometric mixture fraction, while the DNN model predictions again yield nearly identical solutions as the DNS profiles. Neglecting the cross-dissipation rate entirely results in similar underprediction of the generalized progress variable source term. Such an underprediction has significant implications for quantitative predictions of flame stabilization points in physical space when using the multi-modal manifold model. In fact, the underprediction associated with Fig. 7.12 (f) relative to Fig. 7.12 (a) could explain why the lift-off height observed in Sec. 5.3.2 lies on the high-end of experimentally observed lift-off heights, for an underpredicted generalized progress variable source term would lead to a larger Lagrangian ignition delay time and thus a larger lift-off height in a kinetically stabilized flame. Figure 7.12 (c) demonstrates that a considerable improvement in the generalized progress variable source term solution is obtained when using the correct

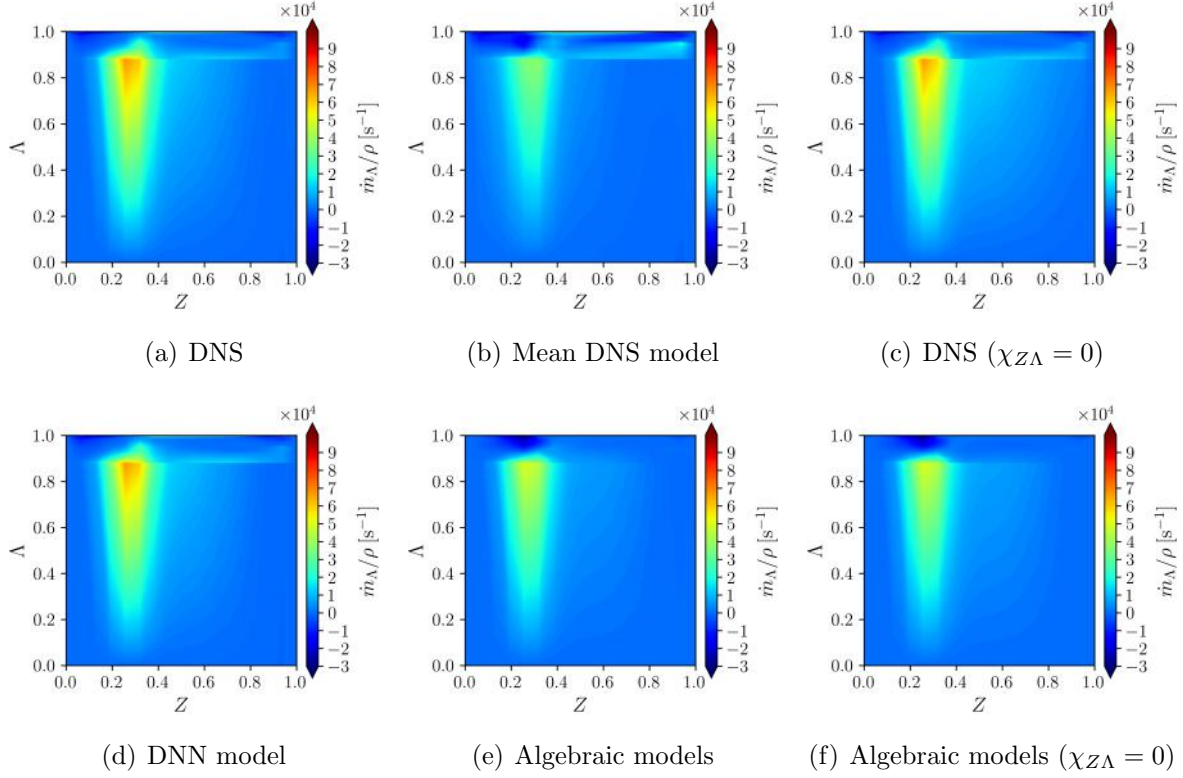


Figure 7.12: Generalized progress variable source term solutions plotted as color contour plots versus mixture fraction and generalized progress variable. Each subfigure corresponds to the multi-modal manifold solution for a set of dissipation rate profiles determined via a different modeling approach.

mixture fraction dissipation rate and generalized progress variable dissipation profiles, even when neglecting the cross-dissipation rate profile entirely. An accurate model for the cross-dissipation rate profile is therefore only of higher-order importance at this primary location on the DNS grid.

This *a priori* investigation suggests that the dissipation rate profile modeling approach is important to accurately predicting intermediate chemical species and the progress variable source term, which are in turn critical for quantitative predictions of flame stabilization using the multi-modal manifold model. However, note that the sensitivity of the filtered thermochemical state to the dissipation rate profile modeling approach and the relative importance

of accurately modeling the instantaneous alignment profile should both be assessed in detail via an *a posteriori* evaluation in LES – a task that is left for future work.

## 7.7 Outcomes: Multi-Modal Dissipation Rate Modeling

Adopting a hybrid physics- and data-based modeling approach offers a path forward to reducing reliance on training data by leveraging physics already embedded in physics-based models. In this chapter, the multi-modal model (detailed in Sec. 5.1) was augmented with DNS data from an autoigniting turbulent *n*-dodecane jet flame by providing closure for the three unclosed dissipation rates in the multi-modal manifold equations. The first part of this chapter was concerned with modeling the filtered dissipation rates, with and without enforcing physical constraints. Two DNNs for the filtered dissipation rates were trained, and evaluation of the DNNs demonstrated that enforcing physical constraints greatly improved model predictions for the filtered mixture fraction dissipation rate and filtered cross-dissipation rate. In particular, the constrained DNN yielded predictions equivalent to or better than the algebraic models for all three filtered dissipation rates. The second part of this chapter shifted focus toward modeling the instantaneous normalized dissipation rate and alignment profiles via a data-based approach, extracting training labels from DNS data. The extracted dissipation rate profiles were shown to only occupy a portion of manifold space, resulting in unstructured data and incomplete training labels. Multiple regression methods were explored to populate the unaccessed regions of manifold space including piecewise linear interpolation (PLI) and Gaussian process regression (GPR). The unfiltered and filtered thermochemical states were both found to be relatively insensitive to the regression method (up to 10%), and GPR was selected to generate structured training labels. The ‘universality’ of the instantaneous normalized dissipation rate and alignment profiles were assessed, revealing considerable spatiotemporal variation in the profile shapes. A DNN for the instantaneous

normalized dissipation rate and alignment profiles was trained to capture this observed spatiotemporal variation, demonstrating an improvement over ‘universal’ models by as much as an order of magnitude. The sensitivity of the thermochemical state to the instantaneous normalized dissipation rate and alignment profiles was evaluated, indicating that modeling these quantities appropriately can impact predictions of intermediate chemical species by up to 25% and the generalized progress variable source term by up to 30% and are therefore critically important to accurate manifold modeling of multi-modal combustion.

# Chapter 8

## Physics-Based Dimensionality Reduction (PBDR)

Future efforts directed toward *Sub-Objective 3* will likely be needed in the context of manifold modeling approaches with additional complexities. This chapter presents work useful to these future efforts – namely, a systematic approach for preprocessing and selecting a reduced-set of input training features. This approach, termed Physics-Based Dimensionality Reduction (PBDR), leverages the Buckingham Pi theorem to generate a reduced-set of dimensionless (or dimensionally-homogeneous) input features that equivalently represent the underlying functional relationship between input features and output labels. The PBDR approach is evaluated using the turbulent premixed reacting jet DNS dataset detailed in Sec. 6.2.1, comparing the performance of DNN models for the filtered progress variable dissipation rate with and without a reduced-set of PBDR input training features. PBDR is benchmarked against traditional linear PCA-based approaches based on evaluation of DNN model performance across models trained using different reduced-sets of input training features.

## 8.1 Input Feature Dimensionality Reduction

Throughout this dissertation, DNNs have been employed to provide closure for the dissipation rates and their instantaneous profiles, forming hybrid physics- and data-based models. Since the role of the dissipation rates is to parameterize the solutions to the manifold equations, the manifold solutions corresponding to these hybrid models are indirectly parameterized by the input features used to train dissipation rate DNNs. This poses a challenge for applying hybrid modeling approaches *a posteriori* in LES, for the transient cost of the ISAM approach increases as the dimensionality of the space of manifold parameters increases. From a practical standpoint, it would therefore be prudent to reduce the number of input features used when training DNNs as much as possible, minimizing the number of manifold solutions needed to populate the ISAT databases. Though this concern is specific to the present application of DNNs, reducing the number of input training features is generally desirable since a DNN with fewer input features generates model predictions more quickly, requires less memory during training, and is less prone to overfitting.

### 8.1.1 PCA-Based Dimensionality Reduction

Principal components analysis (PCA) is a linear dimensionality reduction method that seeks to identify a lower-dimensional representation of a given dataset while maximizing the captured variance [129]. Given a centered and scaled dataset  $\mathbf{X} = [\mathbf{x}_1, \dots, \mathbf{x}_m] \in \mathbb{R}^{n \times m}$  with  $m$  samples, a sample covariance matrix is defined according to  $\widehat{\mathbf{R}} = \left(\frac{1}{m-1}\right) \mathbf{X}\mathbf{X}^\top$ . The sample covariance matrix can be represented by its similarity transformation  $\widehat{\mathbf{R}} = \mathbf{V}\mathbf{L}\mathbf{V}^\top$  where the columns of  $\mathbf{V} = [\mathbf{v}_1, \dots, \mathbf{v}_n] \in \mathbb{R}^{n \times n}$  are the  $n$  orthonormal eigenvectors of  $\widehat{\mathbf{R}}$  and  $\mathbf{L} \in \mathbb{R}^{n \times n}$  is a diagonal matrix containing the  $n$  nonnegative eigenvalues  $\{\lambda_i\}_{i=1}^n$  of  $\widehat{\mathbf{R}}$  in descending order by magnitude. The  $r$ -dimensional representation of the data (where  $r < n$ ) that maximizes the captured variance comprises the space spanned by  $r$  retained eigenvectors. The variance captured by the  $r$ -dimensional representation is given by the sum of the retained

eigenvalues  $\sum_{i=1}^r \lambda_i$ , and the total variance is given by  $\sum_{i=1}^n \lambda_i$ . PCA-based dimensionality reduction is implemented via the Python library **OpenMORe** [130].

### Feature Extraction (PCA-FE)

The feature extraction approach involves selecting a reduced-set of input training features as the coordinates of the original dataset in the space of retained eigenvectors. These coordinates or ‘extracted features’  $\mathbf{C}_r = [\mathbf{c}_1, \dots, \mathbf{c}_m] \in \mathbb{R}^{r \times m}$  are computed according to

$$\mathbf{C}_r = \mathbf{V}_r^\top \mathbf{X}, \quad (8.1)$$

where the columns of  $\mathbf{V}_r = [\mathbf{v}_1, \dots, \mathbf{v}_r] \in \mathbb{R}^{n \times r}$  are the  $r$  retained orthonormal eigenvectors of  $\widehat{\mathbf{R}}$ . The coordinates in the space spanned by the retained eigenvectors are often referred to as *PCA-scores*.

### Feature Selection (PCA-FS)

The feature selection approach instead involves selecting a subset of the original  $n$  input features as the reduced-set of  $r$  input training features. This selection process follows the algorithm introduced by Krzanowski [131]. First,  $n$  reduced datasets  $\{\mathbf{X}_i\}_{i=1}^n \subset \mathbb{R}^{(n-1) \times m}$  are produced, where  $\mathbf{X}_i$  corresponds to the original dataset  $\mathbf{X}$  with the single row  $i$  omitted. PCA is applied to each of these reduced datasets, yielding the corresponding PCA coordinate matrices  $\{\mathbf{C}_{(r-1),i} = \mathbf{V}_{(r-1),i}^\top \mathbf{X}_i\}_{i=1}^n$ . A Procrustes analysis is performed to assess the similarity between each coordinate matrix  $\mathbf{C}_{(r-1),i}$  and the coordinate matrix  $\mathbf{C}_{(r-1)}$  of the original dataset  $\mathbf{X}$ . The input feature that results in the smallest deviation from  $\mathbf{C}_{(r-1)}$  is deemed the least important and dropped from the original dataset  $\mathbf{X}$  to form a new dataset  $\mathbf{X}' = \mathbf{X}_{i_P}$  (where  $i_P$  denotes the index of the row selected based on the Procrustes analysis). This process is iteratively repeated setting  $\mathbf{X} = \mathbf{X}'$  at the end of each iteration (without recomputing  $\mathbf{C}_{(r-1)}$ ) until only  $r$  input features remain in  $\mathbf{X}' \in \mathbb{R}^{r \times m}$ .

### 8.1.2 Physics-Based Dimensionality Reduction (PBDR)

An alternative approach for input feature dimensionality reduction is introduced, termed Physics-Based Dimensionality Reduction (PBDR) – an approach formulated based on the Buckingham Pi theorem [132]. Given a vector of inputs  $\mathbf{x} \in \mathbb{R}^{p_x}$  and a vector of outputs  $\mathbf{y} \in \mathbb{R}^{p_y}$  (where each element of  $\mathbf{x}$  and  $\mathbf{y}$  may possess unique physical dimensions), the underlying physical relationship between the input and output quantities can be represented by a function  $f_p$  according to  $\mathbf{y} = f_p(\mathbf{x})$ . The total number of inputs and outputs is represented by  $p = p_x + p_y$ . Simply put, the Buckingham Pi theorem states that the inputs and outputs  $\hat{\mathbf{x}} = [\mathbf{x}^\top, \mathbf{y}^\top]^\top \in \mathbb{R}^p$  can be nondimensionalized by any set of  $k'$  elements of  $\hat{\mathbf{x}}$  called repeating parameters, where  $k'$  is the number of independent physical dimensions.  $k$  is defined as the minimum of  $k'$  and the rank  $r'$  of the coefficient matrix corresponding to the power of each independent physical dimension appearing in the dimensions of each element of  $\hat{\mathbf{x}}$ . The resulting  $q = p - k$  dimensionless groups  $\hat{\boldsymbol{\pi}} = [\boldsymbol{\pi}_x^\top, \boldsymbol{\pi}_y^\top]^\top \in \mathbb{R}^q$  are referred to as pi-groups and are related according to  $\boldsymbol{\pi}_y = f_q(\boldsymbol{\pi}_x)$ . The implication of the Buckingham Pi theorem is that only  $q$  dimensionless groups are needed to describe the underlying functional relationship between  $p$  dimensional variables. The aim of the PBDR approach is to take advantage of this result, leveraging DNNs to learn the functional relationship  $f_q$  rather than the functional relationship  $f_p$  and reducing the dimensionality of the input training feature space in the process. The Buckingham Pi theorem defines the dimensionless groups according to

$$\hat{\pi}_j = \prod_{i=1}^p \hat{x}_i^{\alpha_{ij}}, \quad (8.2)$$

where  $\alpha_{ij}$  is the exponent of the original dimensional variable  $i$  in dimensionless group  $j$ . Alternatively,  $(p - k) + 1$  *dimensionally-homogeneous* groups can be defined by forming an extra grouping with the  $k'$  repeating parameters. The advantage of the dimensionally-homogeneous formulation is that situations can be avoided where  $\hat{\pi}_j$  is undefined due to quantities  $\hat{x}_i$  with negative  $\alpha_{ij}$  going to zero.



Note that the Buckingham Pi theorem does not place any restriction on the choice of repeating parameters (other than no repeating parameter should be an exact power of any others) and so the set of dimensionless – or dimensionally-homogeneous – groups is not unique. It is also worth noting that the Buckingham Pi theorem implicitly assumes that the set of original dimensional inputs  $\{x_i\}_{i=1}^{p_x}$  is sufficient for the functional dependence  $f_p$  to represent  $\mathbf{y}$ . If this is not the case, then there is no reason to expect  $f_q$  to accurately reconstruct  $\boldsymbol{\pi}_{\mathbf{y}}$ .

The PBDR approach is reminiscent of the constrained optimization approach of Bakarji et al. [133], with the distinction that the PBDR approach involves selecting a particular set of pi-groups  $\{\widehat{\pi}_i\}_{i=1}^q$  (or dimensionally-homogeneous groupings) based on the criterion outlined in Sec. 8.2.2 rather than learning a set of pi-groups from data. When the primary goal is to model  $\mathbf{y}$  without concern for the underlying dynamics, the PBDR approach offers a more straightforward path toward model reduction. Moreover, the disadvantage of learning an optimal set of pi-groups  $\{\widehat{\pi}_i\}_{i=1}^q$  from data is that it implicitly involves exploration of an *infinite-dimensional* state space spanned by all possible pi-groups from all possible pi-group sets, each raised to the power of any nonzero real number  $\beta_j$ . Though regularization terms are introduced to mitigate this issue by biasing against large  $|\beta_j|$ , the traversed state space remains infinite-dimensional. In contrast, the PBDR approach constrains the exploration of sets of pi-groups (or dimensionally-homogeneous groupings) to the finite state space of sets with fixed  $\beta_j$  that enforce a particular choice of physical dimensions for the input and output quantities of interest. The sensitivity of model fidelity to the particular set of dimensionally-homogeneous groupings is investigated in Sec. 8.3.3.

## 8.2 DNN Model Details

### 8.2.1 DNS Filtering and Training Data Generation

To benchmark the PBDR approach, fully-connected, feed-forward DNN models are trained to predict the natural logarithm of the filtered progress variable dissipation rate  $\ln(\tilde{\chi}_{\Lambda\Lambda})$  using the same turbulent premixed jet DNS datasets described in Sec. 6.2.1. The DNS data is again filtered with an inhomogeneous tensor-product Gaussian filter to emulate LES data corresponding to four filter stencil sizes  $\Delta_\alpha/h_\alpha = 2, 4, 8, 16$  for both the low Karlovitz number and high Karlovitz number configurations. 150,000 samples are randomly sampled from each dataset corresponding to each filter stencil size at each Karlovitz number. A single dataset with 900,000 samples is constructed from filter stencil sizes of  $\Delta_\alpha/h_\alpha = 2, 8, 16$ , and 15% and 20% of this dataset is divided into validation and testing data, respectively. The two remaining datasets corresponding to the low Karlovitz number and high Karlovitz number datasets with a filter stencil size of  $\Delta_\alpha/h_\alpha = 4$  are withheld for final additional testing.

### 8.2.2 Input Feature Selection

A total of six DNN models were generated to predict the natural logarithm of the filtered progress variable dissipation rate, each trained on a different set of input features summarized in Table 8.1. The first DNN model (ODI) was trained on eight original dimensionally-inhomogeneous quantities including the filtered progress variable  $\tilde{\Lambda}$ , the progress variable subfilter variance  $\Lambda_v$ , the magnitude of the filtered progress variable gradient  $|\nabla\tilde{\Lambda}|$ , the Frobenius norm of the filtered strain rate  $|\tilde{S}|$ , the filtered progress variable diffusivity  $\tilde{D}_\Lambda$ , the filtered density  $\bar{\rho}$ , the filtered progress variable source term  $\bar{m}_\Lambda$ , and the local filter size  $\Delta_L \equiv V_{\text{stencil}}^{1/3}$ .

The four fundamental physical dimensions corresponding to the original dimensional-inhomogeneous quantities include the mass of the reference species  $m_R$ , the mass of the

Table 8.1: Summary of input features used to train each DNN model.

DNN Model	Input Training Features
ODI	$\tilde{\Lambda}, \Lambda_v,  \nabla \tilde{\Lambda} ,  \tilde{S} , \Delta_L, \tilde{D}_\Lambda, \bar{m}_\Lambda, \bar{\rho}$
MC-PBDR	$\frac{\tilde{\Lambda} \bar{m}_\Lambda}{\bar{\rho}}, \frac{\Lambda_v^{1/4}  \nabla \tilde{\Lambda}  \tilde{D}_\Lambda^{1/2} \bar{m}_\Lambda^{1/2}}{\bar{\rho}^{1/2}}, \Lambda_v  \tilde{S} , \frac{\Lambda_v^{1/4} \Delta_L \bar{m}_\Lambda^{3/2}}{\tilde{D}_\Lambda^{1/2} \bar{\rho}^{3/2}}, \frac{\Lambda_v^{1/2} \bar{m}_\Lambda}{\bar{\rho}}$
LC-PBDR	$\frac{\Lambda_v  \nabla \tilde{\Lambda} ^2 \tilde{D}_\Lambda}{\tilde{\Lambda}^2}, \tilde{\Lambda}^2  \tilde{S} , \frac{ \nabla \tilde{\Lambda} ^3 \Delta_L \tilde{D}_\Lambda}{\tilde{\Lambda}}, \frac{ \nabla \tilde{\Lambda} ^4 \bar{\rho} \tilde{D}_\Lambda^2}{\tilde{\Lambda} \bar{m}_\Lambda},  \nabla \tilde{\Lambda} ^2 \tilde{D}_\Lambda$
LC-PBDR-2	$\frac{\tilde{\Lambda}  \nabla \tilde{\Lambda}  \tilde{D}_\Lambda}{\Delta_L}, \frac{\Lambda_v \tilde{D}_\Lambda}{\Delta_L^2},  \nabla \tilde{\Lambda} ^2  \tilde{S}  \Delta_L^2, \frac{ \nabla \tilde{\Lambda}  \Delta_L \bar{m}_\Lambda}{\bar{\rho}},  \nabla \tilde{\Lambda} ^2 \tilde{D}_\Lambda$
PCA-FE	$\mathbf{x} \cdot \mathbf{v}_1, \mathbf{x} \cdot \mathbf{v}_2, \mathbf{x} \cdot \mathbf{v}_3, \mathbf{x} \cdot \mathbf{v}_4, \mathbf{x} \cdot \mathbf{v}_5$
PCA-FS	$\tilde{\Lambda},  \tilde{S} , \Delta_L, \bar{m}_\Lambda, \bar{\rho}$

mixture  $m_M$ , length  $L$ , and time  $T$ . The physical dimensions of the filtered progress variable dissipation rate in terms of these fundamental physical dimensions are therefore given by  $\tilde{\chi}_{\Lambda\Lambda} [=] \frac{m_R^2}{m_M^2 T}$ . In the present work, the PBDR approach was applied while enforcing that all training input features have these same physical dimensions so that they are all dimensionally-homogeneous with each other as well as the filtered progress variable dissipation rate. Note that though the natural logarithm is applied to the filtered progress variable dissipation rate to enforce physical constraints, the PBDR approach in this context can simply be viewed as training a DNN to learn the functional relationship  $\ln(f_q)$  rather than  $f_q$  directly. As previously discussed, the Buckingham Pi theorem produces several possible combinations of dimensionally-homogeneous groupings, even after enforcing their particular physical dimensions. In turn, each of these possible combinations corresponds to a different functional relationship  $f_q$ . Though DNNs are capable of learning highly nonlinear functional relationships, it stands to reason that less complex, more linear functions will require fewer trainable network parameters and in that sense be easier to learn. The ‘optimal’ set of dimensionally-homogeneous groupings is therefore defined as the set that results in the simplest relationship  $f_q$ . To determine this ‘optimal’ set, every possible dimensionally-homogeneous grouping is formed, and a Pearson correlation coefficient is computed for each grouping from each possible set of dimensionally-homogeneous groupings. The correlation

coefficient indicates how linear the relationship is between each dimensionally-homogeneous grouping and the filtered progress variable dissipation rate according to

$$\mathcal{P}_{jk} = \frac{\langle \tilde{\chi}_{\Lambda\Lambda} \Pi_{jk} \rangle - \langle \tilde{\chi}_{\Lambda\Lambda} \rangle \langle \Pi_{jk} \rangle}{\sigma_{\tilde{\chi}_{\Lambda\Lambda}} \sigma_{\Pi_{jk}}}, \quad (8.3)$$

where  $\mathcal{P}_{jk}$  is the correlation coefficient of the dimensionally-homogeneous grouping  $j$  in the set of dimensionally-homogeneous groupings  $k$ ,  $\Pi_{jk}$  is the dimensionally-homogeneous grouping  $j$  in the set of dimensionally-homogeneous groupings  $k$ ,  $\sigma_{\tilde{\chi}_{\Lambda\Lambda}}$  is the standard deviation of the filtered progress variable dissipation rate, and  $\sigma_{\Pi_{jk}}$  is the standard deviation of  $\Pi_{jk}$ . The correlation coefficient is one when the  $\Pi_{jk}$  is exactly positively correlated with the filtered progress variable dissipation rate and negative one when  $\Pi_{jk}$  is exactly negatively correlated with the filtered progress variable dissipation rate. The ‘optimal’ set of dimensionally-homogeneous groupings  $\{\Pi_{jk^*}\}_{j=1}^r$  is therefore defined as the set with the largest  $\ell^2$ -norm of Pearson correlation coefficients for each grouping, where

$$k^* \equiv \operatorname{argmax}_k \left( \left[ \sum_{j=1}^r \mathcal{P}_{jk}^2 \right]^{1/2} \right). \quad (8.4)$$

A total of three different sets of dimensionally-homogeneous groupings were used to train three separate DNN models. The first PBDR-based DNN model (MC-PBDR) was trained on the ‘optimal,’ most correlated set according to Eq. 8.4. The second DNN model (LC-PBDR) was trained on the least correlated set, which possesses dimensionally-homogeneous groupings with the filtered progress variable in the denominator. Since the filtered progress variable goes to zero in the fuel stream, this group is undefined over a substantial portion of the training dataset. A final PBDR-based DNN model (LC-PBDR-2) was trained on the least correlated set that results after further constraining the allowable sets of dimensionally-homogeneous groupings to those that only possess quantities that go to zero in the numerator.

To select the reduced-set of input training features via PCA-based approaches, PCA was applied to the low Karlovitz number and high Karlovitz number datasets corresponding to filter stencil sizes  $\Delta_\alpha/h_\alpha = 2, 8, 16$  and eight orthonormal eigenvectors were computed. Five of these eigenvectors were retained, and the PCA-scores corresponding to these retained eigenvectors were computed according to Eq. 8.1 and used to train a DNN model (PCA-FE). Finally, five of the eight original dimensionally-inhomogeneous input training features were selected via iterative application of PCA and a Procrustes analysis. A final PCA-based DNN model (PCA-FS) was trained on these five selected quantities.

### 8.2.3 Network Hyperparameter Selection

All six network architectures were fixed with 15 hidden layers and 74 fully-connected nodes per layer. The Adam optimizer [119] with a learning rate of  $10^{-3}$  was selected along with a mean absolute error loss function and a rectified linear unit activation function with a negative slope coefficient of 0.1. Neural network training was again implemented with the Python library `TensorFlow` and the `Keras` API. Table 8.2 summarizes the resulting training, validation, and testing losses based on the datasets corresponding to filter stencil sizes  $\Delta_\alpha/h_\alpha = 2, 8, 16$ . These losses indicate that the DNN models are not overfit with respect to these datasets. The generalizability of each DNN model is further evaluated via the final retained datasets corresponding to the filter stencil size  $\Delta_\alpha/h_\alpha = 4$  at both low Karlovitz number and high Karlovitz number.

Table 8.2: Summary of training, validation, and testing losses for each DNN model (evaluated based on datasets corresponding to filter stencil sizes of  $\Delta_\alpha/h_\alpha = 2, 8, 16$ ).

DNN Model	Training Loss	Validation Loss	Testing Loss
ODI	1.53	1.40	1.41
MC-PBDR	2.47	2.25	2.27
LC-PBDR	2.58	2.29	2.29
LC-PBDR-2	2.56	2.11	2.11
PCA-FE	1.65	1.53	1.54
PCA-FS	1.81	1.77	1.77

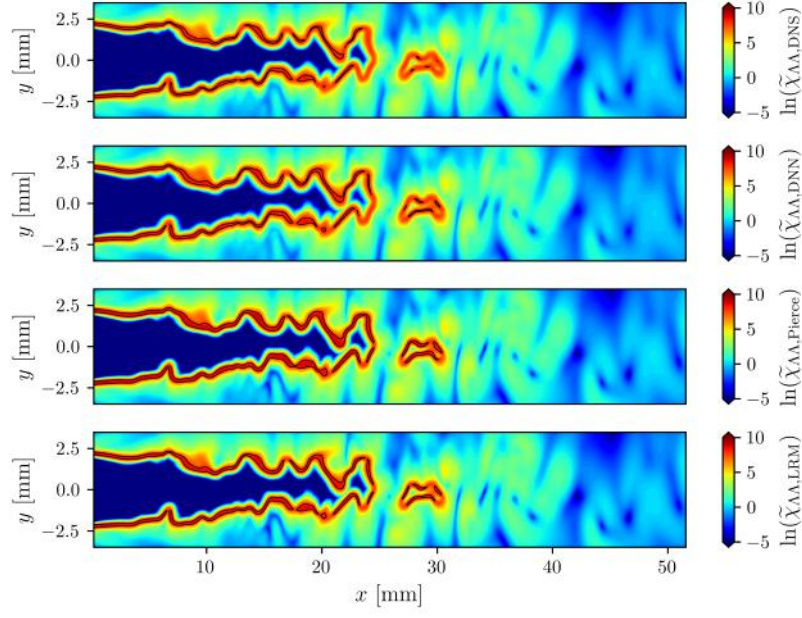
## 8.3 DNN Model Evaluation

### 8.3.1 ODI versus Algebraic Models

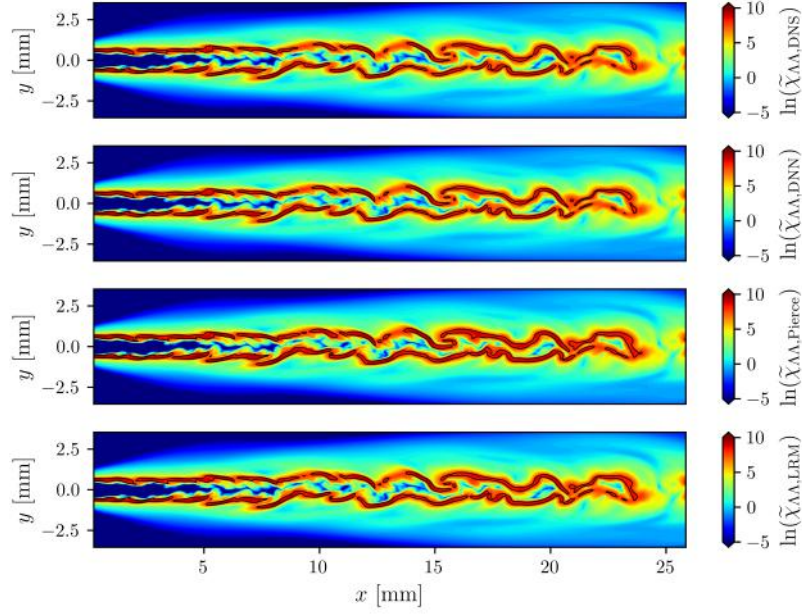
Throughout this section, the generalizability of each DNN model is evaluated on the withheld testing data at both low Karlovitz number and high Karlovitz number for a filter stencil size of  $\Delta_\alpha/h_\alpha = 4$ . Since this filter stencil size lies between those of the training datasets, the corresponding DNN model predictions amount to interpolation and are therefore expected to display good agreement with the filtered DNS data. Before assessing the PBDR approach, the advantage of using a data-based approach over the traditional algebraic models discussed in Sec. 7.5.1 is investigated. Figure 8.1 illustrates instantaneous filtered progress variable dissipation rate snapshots predicted by the (ODI) DNN trained on the eight original dimensionally-inhomogeneous input features relative to the predictions of the Pierce and LRM models as well as the filtered DNS data. At both low Karlovitz number and high Karlovitz number, the snapshots show excellent agreement between the DNS and (ODI) DNN model predictions. The Pierce and LRM models also predict qualitatively similar filtered progress variable dissipation rate fields, though with a noticeable overprediction particularly at large filtered progress variable dissipation rate – a difference made clear by the comparably larger islands formed by isocontours of  $\ln(\tilde{\chi}_{\Lambda\Lambda}) = 8$  associated with the Pierce and LRM model predictions.

### 8.3.2 ODI versus PBDR

Figure 8.2 demonstrates the conditional average of the filtered progress variable dissipation rate predictions versus the filtered progress variable for the ODI DNN model and the MC-PBDR DNN model. Despite reducing the number of input training features from eight to five, no appreciable loss in DNN model fidelity is observed in the conditional sense – both the ODI DNN model and MC-PBDR DNN model outperform the traditional algebraic models by around a factor of three or more at both Karlovitz numbers.



(a) ODI (Case K1)



(b) ODI (Case K2)

Figure 8.1: Comparison of instantaneous snapshots of the filtered progress variable dissipation rate fields from filtered DNS data, predictions of a DNN trained on the eight original dimensionally-inhomogeneous features, the Pierce model, and LRM. Isocontours of  $\ln(\tilde{\chi}_{\Lambda\Lambda}) = 8$  are denoted by solid black lines (—). Snapshots are plotted for the central span-wise plane of the withheld testing data corresponding to  $\Delta_\alpha/h_\alpha = 4$ .

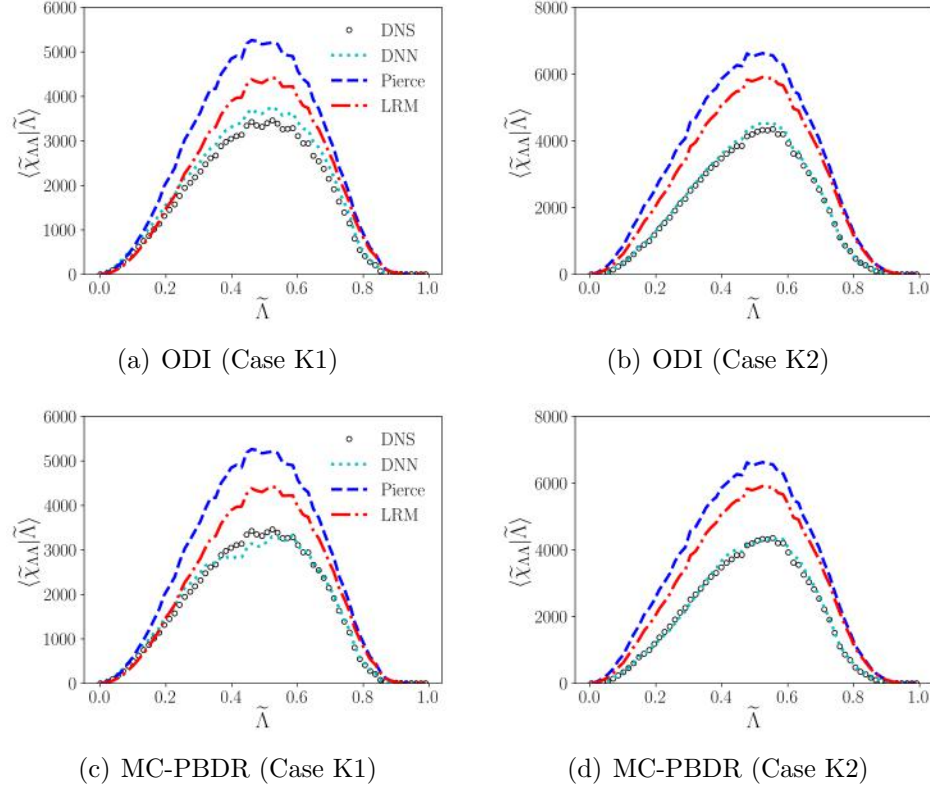


Figure 8.2: DNN predictions ( $\cdots$ ) of the filtered progress variable dissipation rate conditionally averaged on the filtered progress variable corresponding to a DNN trained on the eight original dimensionally-inhomogeneous features in (a) and (b) and corresponding to a DNN trained on the most correlated five dimensionally-homogeneous features in (c) and (d). DNN predictions are compared to conditionally averaged DNS data ( $\circ$ ), conditionally averaged Pierce model predictions ( $-\cdot-$ ), and conditionally averaged LRM predictions ( $-\cdot-$ ). Conditional averages are reported for withheld testing data with  $\Delta_\alpha/h_\alpha = 4$ .

It is also important to investigate the variance in the predictive capabilities of the ODI DNN model as compared to the MC-PBDR DNN model. Figure 8.3 shows parity plots as two-dimensional histograms of model predictions versus filtered DNS data, revealing that the MC-PBDR DNN model demonstrates some additional predictive variability as compared to the ODI DNN model. The MC-PBDR losses provided in Table 8.2 are larger than those of the ODI DNN model, suggesting that this additional predictive variability is due to underfitting resulting from enforcing the same model architecture. This trend leads to a reasonable conclusion: though  $f_q$  equivalently represents the underlying functional relationship



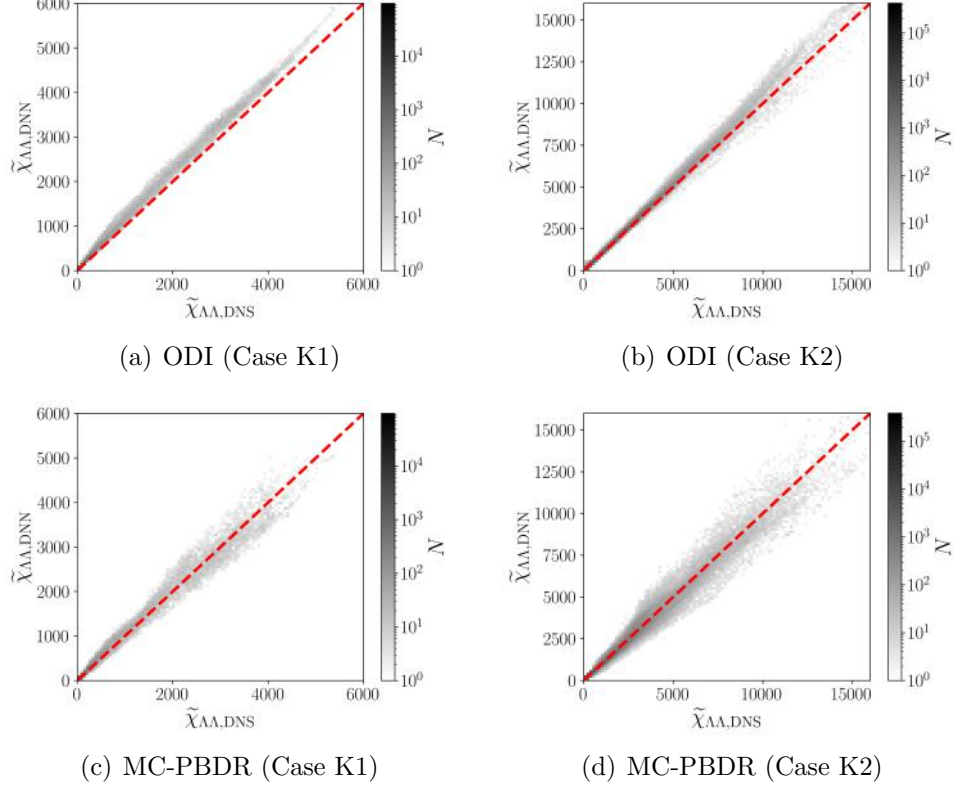


Figure 8.3: Parity plots for the filtered progress variable dissipation rate, comparing DNN predictions to corresponding filtered DNS data. (a) and (b) demonstrate the fidelity of a DNN trained on the eight original dimensionally-inhomogeneous features, and (c) and (d) demonstrate the fidelity of a DNN trained on the most correlated five dimensionally-homogeneous features, both as two-dimensional histograms shaded on a log-scale according to the number of data samples  $N$  at each point. The dashed red line (--) denotes exact agreement between DNN predictions and the filtered DNS data. Parity plots are reported for withheld testing data with  $\Delta_\alpha/h_\alpha = 4$ .

between the original dimensionally-inhomogeneous quantities of interest, it may be a more complex function than the original function  $f_p$  and require additional network complexity and trainable parameters to model appropriately. However, it is worth noting that even when constrained to the same network architecture as the ODI DNN model, the MC-PBDR DNN model demonstrates good agreement with the filtered DNS model.

### 8.3.3 Sensitivity to the Dimensionally-Homogeneous Set

As previously discussed, the Buckingham Pi theorem produces nonunique sets of dimensionally-homogeneous groupings. The least correlated of these groupings represents the set of input training features corresponding to the most nonlinear functional relationship  $f_q$  – expected to be the most difficult to model. Figure 8.4 displays the predictive capabilities of the LC-PBDR DNN model as well as the LC-PBDR-2 DNN model, each evaluated in the conditionally averaged sense. The LC-PBDR-2 DNN model performs similarly well as the MC-PBDR DNN model in the conditionally averaged sense, but the LC-PBDR DNN model performs considerably worse, now on par with the traditional algebraic models. This relative decrease in predictive performance reveals that dividing by quantities that go to zero in the domain of the training dataset should be avoided as it introduces additional nonphysical noise during training. One of the distinct advantages of training on dimensionally-homogeneous groupings via the PBDR approach over directly using nondimensional pi-groups is that one is able to avoid these situations entirely by carefully selecting the physical dimensions of the dimensionally-homogeneous input and output groupings. For instance, the particular case at hand only involves three variables that do not go to zero anywhere in the domain:  $\Delta_L$ ,  $\widetilde{D}_\Lambda$ , and  $\bar{\rho}$ . Since none of these variables possess the mass of the reference species  $m_R$  as a part of their physical dimensions (and the remaining variables only possess physical dimensions with positive powers of  $m_R$ ), it would be *impossible* to construct nondimensional pi-groups free of at least one pi-group that is somewhere undefined within the domain of the training dataset.

Figure 8.5 shows the variance in the predictive capabilities of the two DNN models trained on the least correlated sets of dimensionally-homogeneous groupings. The LC-PBDR DNN model systematically overpredicts the filtered progress variable dissipation rate, particularly at low Karlovitz number – a trend that is consistent with the behavior observed in the conditionally averaged predictions. When further omitting dimensionally-homogeneous groupings with undefined groupings, the performance of the LC-PBDR-2 DNN model demonstrates

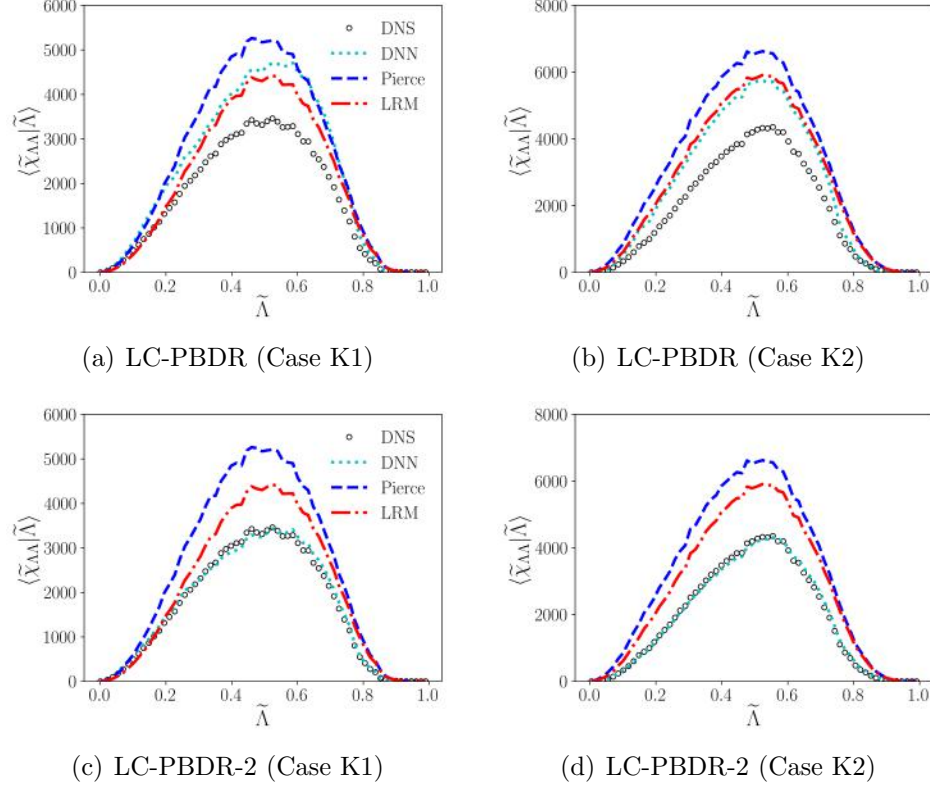


Figure 8.4: DNN predictions ( $\cdots$ ) of the filtered progress variable dissipation rate conditionally averaged on the filtered progress variable corresponding to a DNN trained on the least correlated five dimensionally-homogeneous features (with division by zero) in (a) and (b) and corresponding to a DNN trained on the least correlated five dimensionally-homogeneous features (without division by zero) in (c) and (d). DNN predictions are compared to conditionally averaged DNS data ( $\circ$ ), conditionally averaged Pierce model predictions ( $-\cdot-$ ), and conditionally averaged LRM predictions ( $-\cdot-$ ). Conditional averages are reported for withheld testing data with  $\Delta_\alpha/h_\alpha = 4$ .

that model fidelity increases. The variance in the predictive capability of the LC-PBDR-2 DNN model remains slightly larger than the ODI DNN model for the same reason as before. The losses provided in Table 8.2 suggest that both the LC-PBDR DNN model and LC-PBDR-2 DNN model are underfit relative to the ODI DNN model and would benefit from additional model complexity. The LC-PBDR-2 DNN model demonstrates a similar but slightly reduced predictive capability compared to the MC-PBDR DNN model at high Karlovitz number and a reduced predictive variance at low Karlovitz number. This trend

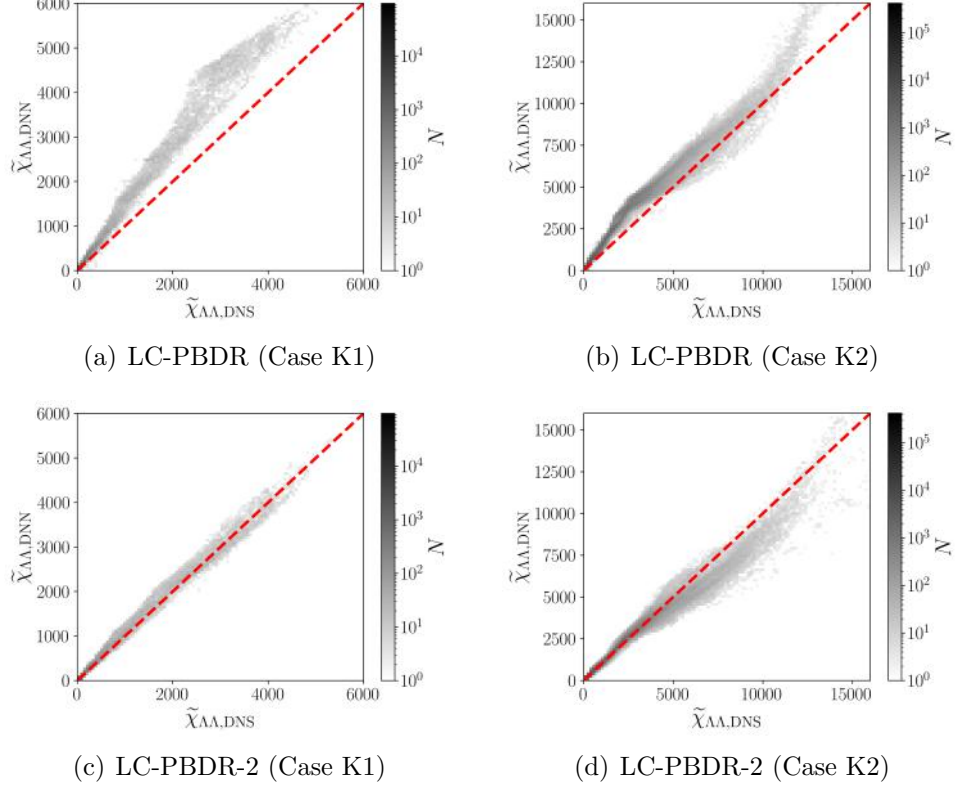


Figure 8.5: Parity plots for the filtered progress variable dissipation rate, comparing DNN predictions to corresponding filtered DNS data. (a) and (b) demonstrate the fidelity of a DNN trained on the least correlated five dimensionally-homogeneous features (with division by zero), and (c) and (d) demonstrate the fidelity of a DNN trained on the least correlated five dimensionally-homogeneous features (without division by zero), both as two-dimensional histograms shaded on a log-scale according to the number of data samples  $N$  at each point. The dashed red line (---) denotes exact agreement between DNN predictions and the filtered DNS data. Parity plots are reported for withheld testing data with  $\Delta_\alpha/h_\alpha = 4$ .

indicates that Eq. 8.3 and Eq. 8.4 constitute an imperfect but still useful selection criterion across both Karlovitz numbers.

### 8.3.4 PBDR versus PCA-FE and PCA-FS

The PCA-based dimensionality reduction approaches are evaluated via parity plots corresponding to the withheld low Karlovitz number and high Karlovitz number datasets. Figure 8.6 clearly demonstrates a significant increase in the variance in the predictive capabilities of both the PCA-FE DNN model as well as the PCA-FS DNN model as compared to the ODI

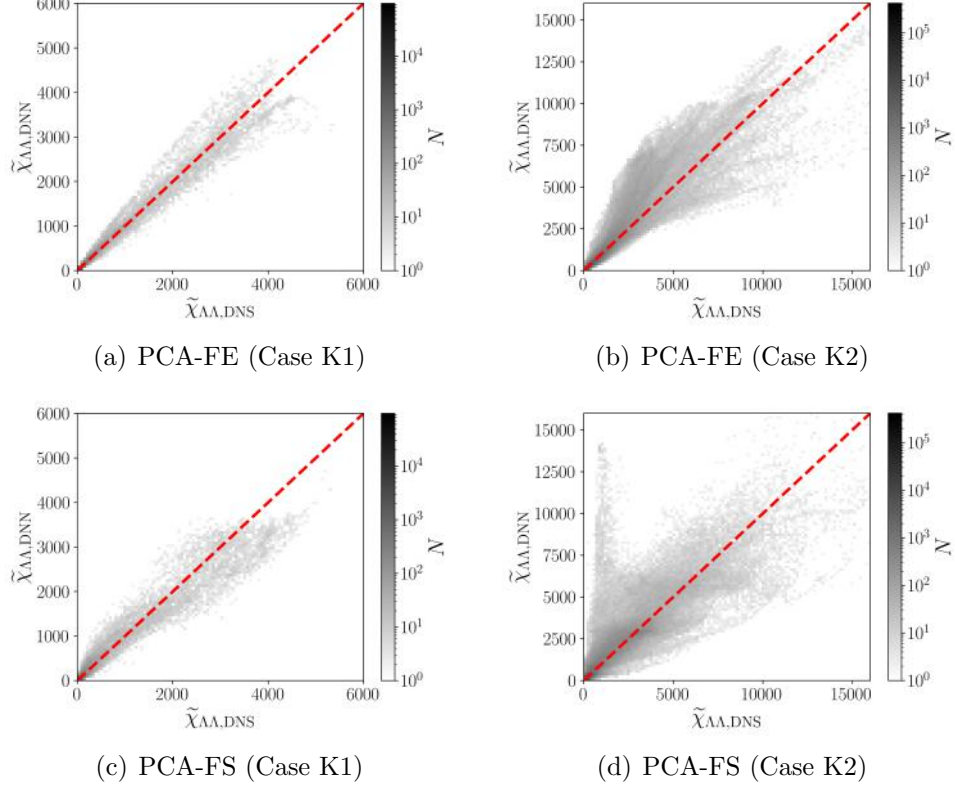


Figure 8.6: Parity plots for the filtered progress variable dissipation rate, comparing DNN predictions to corresponding filtered DNS data. (a) and (b) demonstrate the fidelity of a DNN trained on the five extracted PCA-scores, and (c) and (d) demonstrate the fidelity of a DNN trained on the five features selected via the algorithm of Krzanowski [131], both as two-dimensional histograms shaded on a log-scale according to the number of data samples  $N$  at each point. The dashed red line (--) denotes exact agreement between DNN predictions and the filtered DNS data. Parity plots are reported for withheld testing data with  $\Delta_\alpha/h_\alpha = 4$ .

DNN model and the PBDR-based DNN models. This reduction in model fidelity is most pronounced at high Karlovitz number but is observed at low Karlovitz number as well. The losses corresponding to the PCA-based DNN models in Table 8.2 imply that the PCA-based DNN models are not overfit to the datasets corresponding to filter stencil sizes  $\Delta_\alpha/h_\alpha = 2, 8, 16$  – yet, the predictive capability of the PCA-FE DNN model and PCA-FS DNN model drop appreciably when applied to the datasets corresponding to a filter stencil size of  $\Delta_\alpha/h_\alpha = 4$ . This trend suggests that the poor PCA-based DNN model performance is attributed not to underfitting, but an indirect form of overfitting inherent to the reliance on PCA.

PCA was only applied to the  $\Delta_\alpha/h_\alpha = 2, 8, 16$  datasets, so the  $\Delta_\alpha/h_\alpha = 4$  dataset can be expected to contain variance in the data that is not well explained by the identified PCs. As a result, the PCA-FE DNN model implicitly learns correlations between PC-scores that do not hold in the withheld testing data. Similarly, the PCA-FS DNN model was trained on input features selected based on PCs that are no longer representative of the withheld testing data. The PCA-based DNN models therefore fail to generalize to the  $\Delta_\alpha/h_\alpha = 4$  dataset despite the additional testing dataset occupying regions *interior* to the training dataset. In contrast, the PBDR-based DNN models simply rely on dimensional analysis (which is always valid), so they are able to offer dimensionality reduction of the input feature space without restricting the generalizability of the resulting DNN model.

## 8.4 Outcomes: Physics-Based Dimensionality Reduction

This chapter presented a Physics-Based Dimensionality Reduction (PBDR) approach for DNN model training based on the Buckingham Pi theorem. It has been demonstrated that DNN models may be trained on a reduced set of dimensionally-homogeneous input training features, resulting in comparable model fidelity as compared to DNN models trained on an increased number of dimensionally-inhomogeneous input training features. Three PBDR-based DNN models were trained corresponding to the most correlated, least correlated, and least correlated set without any undefined dimensionally-homogeneous groupings, illustrating that the particular choice of set of dimensionally-homogeneous groupings is of lesser importance relative to excluding groupings that are undefined in regions of the training dataset. One of the marked advantages of the PBDR approach with dimensionally-homogeneous groupings is that it offers the flexibility to restrict sets of dimensionally-homogeneous groupings to those that do not contain quantities that go to zero in the denominator. The PBDR-based DNN models were benchmarked against DNN models trained on reduced sets of input train-

ing features obtained via linear PCA-based dimensionality reduction approaches, revealing that PBDR-based DNN models offer a considerable improvement in model generalizability compared to PCA-based DNN models.

# Chapter 9

## Conclusions

Simulations of turbulent reacting flows possess the potential to unlock more efficient, less polluting power generation technology at a point in human history when such advancements are especially important. Until now, the turbulent combustion modeling state-of-the-art have been constrained by a fundamental trade-off between model generality and computational efficiency. Brute-force modeling approaches offer model generality but come at a computational cost that renders their application to engineering scale problems infeasible. Manifold modeling approaches presume a reduced-order dependence of the thermochemical state on a small subset of manifold variables, providing considerable reduction in computational cost, though traditionally at the expense of model generality. More general manifold models exist in theory, but practical considerations have precluded their implementation in LES – namely, computational cost and memory limitations as well as the existence of outstanding unclosed model parameters that appear in the manifold equations. The work of this dissertation comprises efforts toward breaking the trade-off between model generality and computational efficiency in turbulent combustion modeling, dividing the problem into manageable sub-objectives before systematically overcoming each obstacle.

First, *Sub-Objective 1* required that the practical computational cost and memory limitations associated with implementing existing general, high-dimensional manifold models be



addressed. A new computational implementation of manifold modeling called In-Situ Adaptive Manifolds (ISAM) was developed to overcome these limitations by computing manifold solutions online in an LES and storing them for later reuse with In-Situ Adaptive Tabulation (ISAT). The performance of the newly-developed ISAM approach was benchmarked via LES of turbulent nonpremixed jet flames with both hydrogen and methane fuels, using the nonpremixed manifold model as a vehicle to compare to pretabulation approaches. Constructing the ISAT databases during the first few time steps was shown to be the dominant source of computational cost in ISAM, though this transient cost still proves to be less than that of traditional pretabulation approaches. The computational cost of ISAM plateaued to a steady-state value comparable to that of the pretabulation approaches once the ISAT databases were saturated with manifold solutions, demonstrating that the overhead associated with traversing the binary trees in ISAT is on par with a simple lookup from a pretabulated database. This trend was observed for both hydrogen and methane fuels, suggesting the ISAM approach is applicable to combustion problems with complex fuels. Most notably, the memory requirement of ISAM was shown to be several orders of magnitude less than that of pretabulation – only a small portion of manifold parameter space is accessed over the course of a simulation, and precomputing solutions spanning the entire state space is wasted effort. Introducing a numerical ISAT Jacobian demonstrated an increase in algorithm robustness without a net increase in computational cost. ISAM refinements including synchronization of ISAT tables across MPI processes, manifold solver vectorization, and hybrid MPI/OpenMP parallelization further reduced the principal transient cost of the ISAM approaches by as much as an additional order of magnitude over the initial ISAM implementation.

*Sub-Objective 2* involved extending the ISAM approach to more general manifold models capable of characterizing more complex combustion processes. ISAM was extended to configurations with multiple and/or inhomogeneous stream mixing by modifying the fuel-side boundary conditions in the nonpremixed manifold model and introducing an additional

parameter in the manifold equations – the fuel premixing fraction. LES of a turbulent partially premixed jet flame was performed while constraining the reference mixture fraction dissipation to a single value, isolating the impact that the sensitivity of the thermochemical state to the ISAT parameter in question has on the performance of ISAM. The transient cost proved larger for the more sensitive fuel premixing fraction, though more frequent MPI synchronization during the first time step aided in mitigating additional cost with and without constraining the reference mixture fraction dissipation rate. The computational cost and memory requirement associated with generating thermochemical databases with ISAM both demonstrated a two order of magnitude reduction relative to pretabulation for the multiple and/or inhomogeneous stream mixing case.

The ISAM approach was then applied to a higher-dimensional manifold model applicable to multi-modal combustion, possessing both multiple ISAT parameters and higher-dimensional manifold equations. LES of a turbulent lifted hydrogen jet flame was performed to assess the feasibility and interpretability of the multi-modal manifold model *a posteriori*. The first time step was shown to only cost around one hour, and this computational cost quickly dropped off to the same level as that of the simple single-mode models, indicating that the ISAM approach is feasible for multi-modal combustion and beyond. Even without MPI synchronization, manifold solver vectorization, or hybrid MPI/OpenMP parallelization, generating thermochemical databases in ISAM involved a two order of magnitude reduction in computational cost relative to pretabulation as well as up to a seven order of magnitude reduction in required memory. Moreover, the multi-modal manifold model demonstrated promising predictive capability, producing the combustion mode as a model output rather than a model input for the first time ever in a manifold model. The highly interpretable nature of the multi-modal manifold model provided insight into the qualitative flame behavior of the Cabra flame (autoignition stabilized with a trailing nonpremixed flame) that exactly aligns with prior consensus.

Though ISAM was successfully extended to the multi-modal model, the mixture fraction dissipation rate and generalized progress variable dissipation rate were closed with ad hoc algebraic models, and the cross-dissipation rate was neglected entirely. Approaching *Sub-Objective 3* demanded pivoting from developing and extending the ISAM approach to providing data-based closure models for the manifold parameters – specifically, the three scalar dissipation rates that parameterize the solutions to the multi-modal manifold equations. As a first step, data-based closure was sought for the instantaneous normalized dissipation rates in turbulent premixed combustion via DNS datasets of turbulent premixed jet flames at multiple Karlovitz numbers. Significant spatiotemporal variation in the instantaneous profiles was observed in profiles extracted from the DNS dataset, particularly at high Karlovitz number. A deep neural network (DNN) was trained to capture this observed variation in the profile shape, demonstrating considerable improvement over algebraic models that presume the shape is ‘universal’ (invariant in space and time). An *a priori* evaluation of the sensitivity of the instantaneous thermochemical state to the shape of the dissipation rate profile was conducted via comparison of solutions to the one-dimensional premixed manifold equations. Predictions of intermediate chemical species and the progress variable source term were shown to improve when using the DNN predictions compared to the ‘universal’ algebraic models, implying that an instantaneous modeling approach for the normalized dissipation rate profiles may be necessary at high Karlovitz number in order to accurately characterize ignition and flame propagation. Data-based and physics-based variable importance studies revealed that the spatiotemporal variation in the dissipation rate profile shape is an inherent function of the conditional velocity gradient aligned with the progress variable gradient. As this quantity is challenging and computationally expensive to model directly, learning correlations with the conditional velocity gradient aligned with the progress variable gradient to provide closure offers a distinct advantage to data-based approaches.

A data-based approach was then employed to close the three dissipation rates associated with the multi-modal manifold model. LES closure was attained by dividing each of the

mixture fraction dissipation rate, cross-dissipation rate, and generalized progress variable dissipation rate into a respective magnitude and profile shape (now in mixture fraction and generalized progress variable) before proceeding to model the magnitudes and profile shapes separately. Training data was obtained from a DNS dataset of an autoigniting turbulent  $n$ -dodecane jet flame, representing an ideal configuration for multi-modal turbulent combustion. DNN models for the dissipation rate magnitudes were obtained by predicting the filtered mixture fraction dissipation rate, filtered generalized progress variable dissipation rate, and pseudo-filtered alignment. DNN model predictions for these quantities demonstrated an improvement in all three filtered dissipation rates compared to traditional algebraic models with a marked improvement when enforcing physical constraints on the DNN outputs. The instantaneous dissipation rate and alignment profiles were extracted from the DNS dataset, and Gaussian process regression (GPR) was employed to generate structured training labels from unstructured data. Considerable spatiotemporal variation of the instantaneous normalized dissipation rate and alignment profiles was observed and accounted for via DNN models. These DNN models were assessed *a priori*, again demonstrating an improvement over existing algebraic models. Comparison of solutions to the two-dimensional multi-modal manifold equations further revealed enhancement in the prediction of intermediate species and the progress variable source term when using a DNN model versus ‘universal’ models, highlighting the importance of using an appropriate instantaneous dissipation rate and alignment model when closing the multi-modal manifold equations.

Finally, a systematic approach called Physics-Based Dimensionality Reduction (PBDR) was presented to aid in the selection of a reduced-set of input features for DNN training. PBDR leverages the Buckingham Pi theorem to select fewer dimensionless or dimensionally-homogeneous variables that theoretically characterize the relationship between an original set of dimensionally-inconsistent input and output variables. The PBDR approach was assessed via performance evaluations of DNN models for the filtered progress variable dissipation rate trained on the original dimensionally-inconsistent input features, the most and least corre-

lated sets of dimensionally-homogeneous groupings, and an equivalent number of extracted and selected features determined via PCA-based approaches. This analysis indicated that the PBDR approach reduces the number of input training features with a minimal change in model fidelity, particularly when compared to linear PCA-based approaches.

## 9.1 Opportunities for Future Work

The present body of work has undoubtedly redefined the limitations associated with simulating turbulent reacting flows by enabling a new generation of simultaneously general *and* computationally efficient manifold models. However, not all questions have been answered, and several opportunities for future development remain. Suggestions for potentially valuable avenues to explore moving forward are summarized in the following:

- **ISAM Algorithm Refinement:** Though the current iteration of ISAM has already enabled a considerable reduction in computational cost relative to pre-tabulation approaches, when applied to even higher-dimensional manifold models, the transient cost of ISAM may still benefit greatly from additional refinement. For instance, the MPI implementation of ISAT currently allocates a separate ISAT database for each MPI process. ISAM would benefit from a dynamic load-balancing approach – the number of manifold calculations needed in each physical space subdomain is not known *a priori*, constraining the transient cost associated with initial ISAM time steps by the rate-limiting MPI process with the greatest number of required manifold calculations. Rather than immediately performing a direct evaluation when deemed necessary in ISAT, ISAM could be modified to first perform an initial pass over the physical space grid with ISAT (without direct evaluations) to determine the locations in manifold state space where there are no previously tabulated manifold solutions. Since the ellipsoids of accuracy corresponding to many of these locations will overlap in manifold state space, only a small subset of these manifold calculations are truly necessary.

Downsampling to a smaller subset of necessary manifold calculations may be accomplished by iteratively applying a clustering algorithm in manifold state space, varying the number of clusters until all points in the largest cluster lie within an estimated ellipsoid of accuracy associated with the central point of the largest cluster. The central points corresponding to each final identified cluster represent the downsampled locations in manifold state space where manifold calculations are necessary and may be divided evenly among available MPI processes. Finally, the manifold solver should be initialized with manifold solutions that are nearby in manifold state space, resulting in faster solution convergence and reduced transient computational cost.

- **Large Eddy Simulation of Multiple and/or Inhomogeneous Stream Mixing:**

When simulating the Sydney flame in Chapter 4 with a manifold approach in LES, the pilot stream has so far only been modeled with constant inlet boundary conditions corresponding to each of two transported mixture fractions. However, this approach implicitly assumes that only mixing with the inhomogeneous central stream is of fundamental importance to the combustion process. To investigate this assumption in more detail, a third mixture fraction may be transported to discern between mixing with the additional pilot stream, resulting in modifications to the manifold equations and additional inputs to ISAT.

- **Large Eddy Simulation of Multi-Modal Combustion:** Though Chapter 5 successfully demonstrated the interpretability and feasibility of the multi-modal manifold model, it did so without considering the cross-dissipation rate. Revisiting the Cabra flame LES accounting for this cross-dissipation rate would provide greater insight into its effect on combustion processes. The form of the presumed subfilter PDF used in the multi-modal manifold model implementations of this work have been limited to the beta-beta distribution, neglecting the covariance of the mixture fraction and generalized progress variable. However, the particular form of the subfilter PDF is important

for reconstructing the filtered thermochemical state from the manifold solutions in LES, so the impact of alternative algebraic or data-based subfilter PDF closure should be investigated in more detail. Finally, the definition of the generalized progress variable fundamentally depends on the choice of reference species – a general, systematic approach for appropriately determining the reference species (subject to a constraint on the monotonicity with respect to the generalized progress variable) should therefore be developed. The impact of the choice of reference species should further be explored in the context of the low-temperature chemistry regimes dominant in early-stage ignition.

- ***A Posteriori* DNN Validation:** The data-based models in this work have thus far only been evaluated *a priori*. A more accurate assessment of the DNN models trained in Chapter 6, Chapter 7, and Chapter 8 should involve incorporating data-based models into LES. Such an *a posteriori* evaluation would elucidate how errors in the DNN models propagate over the course of a simulation as well as interact with other errors associated with turbulence models and numerical discretization. When implementing DNN models for the dissipation rates into LES with ISAM, the dimensionality of the ISAT parameter space will be determined by the number of input features used to train the DNNs. Practically speaking, as the dimensionality of the ISAT parameter space increases, the transient cost of ISAM increases. It is therefore likely worth applying the PBDR approach discussed in Chapter 8 to the instantaneous dissipation rate profile models in Chapter 6 and Chapter 7. Application of PCA-based approaches to the space spanned by the selected dimensionally-homogeneous groupings may offer additional input feature reduction, if necessary. Furthermore, the DNN models of Chapter 7 have thus far been trained on a single time snapshot of data and should be extended to additional snapshots to ensure the DNN models generalize to regimes where different combinations of combustion modes and low- and high-temperature ignition dominate.

- **Higher-Dimensional Manifold Models:** The work in this dissertation has already demonstrated considerable success leveraging the ISAM approach to simulate non-premixed combustion, multiple and/or inhomogeneous stream mixing, and multi-modal combustion. However, additional complexity and generality may be introduced into manifold models to account for pressure variation and heat losses. ISAM should be separately implemented for and applied to these yet unexplored applications. A single unified manifold model may then be formed, capable of accounting for every possible complexity simultaneously – a ‘turnkey’ modeling approach [134] that enables accurate simulations of novel power generation technology at low computational cost.



# Appendix A

## Conditional Progress Variable

## Dissipation Rate Transport Equation

## Derivation

The conditional generalized progress variable dissipation rate transport equation is obtained by beginning with the generalized progress variable dissipation rate transport equation [135] given by

$$\begin{aligned} \frac{\partial}{\partial t} (\rho \chi_{\Lambda\Lambda}) + \frac{\partial}{\partial x_j} (\rho u_j \chi_{\Lambda\Lambda}) &= \frac{\partial}{\partial x_j} \left( \rho D \frac{\partial \chi_{\Lambda\Lambda}}{\partial x_j} \right) - 4\rho D^2 \left[ \frac{\partial}{\partial x_j} \left( \frac{\partial \Lambda}{\partial x_j} \right) \right]^2 - 4\rho D \frac{\partial \Lambda}{\partial x_i} S_{ij} \frac{\partial \Lambda}{\partial x_j} \\ &\quad + 2\rho \chi_{\Lambda\Lambda} \frac{\partial u_j}{\partial x_j} + 4D \frac{\partial \Lambda}{\partial x_j} \frac{\partial \dot{m}_\Lambda}{\partial x_j}, \end{aligned} \quad (\text{A.1})$$

and the transport equation for the fine-grained subfilter PDF [59] given by

$$\frac{\partial}{\partial t} (\rho \psi) + \frac{\partial}{\partial x_j} (\rho u_j \psi) + \frac{\partial}{\partial \lambda} (\dot{m}_\Lambda \psi) = -\frac{\partial^2}{\partial x_j \partial \lambda} \left( \rho D \psi \frac{\partial \Lambda}{\partial x_j} \right) - \frac{\partial^2}{\partial \lambda^2} \left( \frac{1}{2} \rho \chi_{\Lambda\Lambda} \psi \right). \quad (\text{A.2})$$

Equation A.2 is multiplied by  $\chi_{\Lambda\Lambda}$  and the result is added to the product of Eq. A.1 and  $\psi$  to yield the transport equation for  $\psi\chi_{\Lambda\Lambda}$ :

$$\begin{aligned}
\frac{\partial}{\partial t}(\rho\psi\chi_{\Lambda\Lambda}) + \frac{\partial}{\partial x_j}(\rho u_j\psi\chi_{\Lambda\Lambda}) + \underbrace{\chi_{\Lambda\Lambda}\frac{\partial}{\partial\lambda}(\dot{m}_\Lambda\psi)}_{\text{I}} &= \psi\frac{\partial}{\partial x_j}\left(\rho D\frac{\partial\chi_{\Lambda\Lambda}}{\partial x_j}\right) - 4\psi\rho D^2\left[\frac{\partial}{\partial x_j}\left(\frac{\partial\Lambda}{\partial x_j}\right)\right]^2 \\
&\quad - 4\psi\rho D\frac{\partial\Lambda}{\partial x_i}S_{ij}\frac{\partial\Lambda}{\partial x_j} + 2\psi\rho\chi_{\Lambda\Lambda}\frac{\partial u_j}{\partial x_j} + 4\psi D\frac{\partial\Lambda}{\partial x_j}\frac{\partial\dot{m}_\Lambda}{\partial x_j} \\
&\quad - \underbrace{\chi_{\Lambda\Lambda}\frac{\partial^2}{\partial x_j\partial\lambda}\left(\rho D\psi\frac{\partial\Lambda}{\partial x_j}\right)}_{\text{II}} - \underbrace{\chi_{\Lambda\Lambda}\frac{\partial^2}{\partial\lambda^2}\left(\frac{1}{2}\rho\chi_{\Lambda\Lambda}\psi\right)}_{\text{III}}.
\end{aligned} \tag{A.3}$$

Leveraging the product rule and the fact that derivatives of any unconditioned quantity (not multiplied by  $\psi$ ) with respect to the phase space generalized progress variable are zero, the terms labeled with Roman numerals can be manipulated to yield the following equivalent expressions:

$$\text{I} : \chi_{\Lambda\Lambda}\frac{\partial}{\partial\lambda}(\dot{m}_\Lambda\psi) = \frac{\partial}{\partial\lambda}(\dot{m}_\Lambda\chi_{\Lambda\Lambda}\psi), \tag{A.4}$$

$$\text{II} : \chi_{\Lambda\Lambda}\frac{\partial^2}{\partial x_j\partial\lambda}\left(\rho D\psi\frac{\partial\Lambda}{\partial x_j}\right) = \frac{\partial^2}{\partial x_j\partial\lambda}\left(\chi_{\Lambda\Lambda}\rho D\psi\frac{\partial\Lambda}{\partial x_j}\right) - \frac{\partial}{\partial\lambda}\left(\frac{\partial\chi_{\Lambda\Lambda}}{\partial x_j}\rho D\psi\frac{\partial\Lambda}{\partial x_j}\right), \tag{A.5}$$

$$\text{III} : \chi_{\Lambda\Lambda}\frac{\partial^2}{\partial\lambda^2}\left(\frac{1}{2}\rho\chi_{\Lambda\Lambda}\psi\right) = \frac{\partial^2}{\partial\lambda^2}\left(\frac{1}{2}\rho\chi_{\Lambda\Lambda}\chi_{\Lambda\Lambda}\psi\right). \tag{A.6}$$

Substituting Eq. A.4 - A.6 into Eq. A.3 yields an alternative form of the  $\psi\chi_{\Lambda\Lambda}$  transport equation given by

$$\begin{aligned}
\frac{\partial}{\partial t}(\rho\psi\chi_{\Lambda\Lambda}) + \frac{\partial}{\partial x_j}(\rho u_j\psi\chi_{\Lambda\Lambda}) + \frac{\partial}{\partial \lambda}(\dot{m}_\Lambda\chi_{\Lambda\Lambda}\psi) = & \psi \frac{\partial}{\partial x_j} \left( \rho D \frac{\partial \chi_{\Lambda\Lambda}}{\partial x_j} \right) - 4\psi \rho D^2 \left[ \frac{\partial}{\partial x_j} \left( \frac{\partial \Lambda}{\partial x_j} \right) \right]^2 \\
& - 4\psi \rho D \frac{\partial \Lambda}{\partial x_i} S_{ij} \frac{\partial \Lambda}{\partial x_j} + 2\psi \rho \chi_{\Lambda\Lambda} \frac{\partial u_j}{\partial x_j} \\
& + 4\psi D \frac{\partial \Lambda}{\partial x_j} \frac{\partial \dot{m}_\Lambda}{\partial x_j} - \frac{\partial^2}{\partial x_j \partial \lambda} \left( \chi_{\Lambda\Lambda} \rho D \psi \frac{\partial \Lambda}{\partial x_j} \right) \\
& + \frac{\partial}{\partial \lambda} \left( \frac{\partial \chi_{\Lambda\Lambda}}{\partial x_j} \rho D \psi \frac{\partial \Lambda}{\partial x_j} \right) - \frac{\partial^2}{\partial \lambda^2} \left( \frac{1}{2} \rho \chi_{\Lambda\Lambda} \chi_{\Lambda\Lambda} \psi \right).
\end{aligned} \tag{A.7}$$

Finally, filtering Eq. A.7 and applying the identities  $\overline{\rho\psi\phi} = \bar{\rho} \tilde{P} \tilde{\phi}_{,\lambda}$  and  $\overline{\psi\phi} = \bar{P} \bar{\phi}_{,\lambda}$  for a general quantity  $\phi$  (where  $P$  is the filter density function defined according to  $P(\lambda) = \int \delta[\Lambda(\mathbf{x} - \mathbf{r}, t) - \lambda] G(\mathbf{r}, \mathbf{x}; \Delta) d\mathbf{r}$ ,  $G$  is the LES filter, and  $\Delta$  is the filter size) yields the conditional generalized progress variable dissipation rate transport equation in Eq. 6.15.

# Bibliography

- [1] R. K. Pachauri, M. R. Allen, V. R. Barros, J. Broome, W. Cramer, R. Christ, J. A. Church, L. Clarke, Q. Dahe, P. Dasgupta, et al., Climate change 2014: synthesis report. Contribution of Working Groups I, II and III to the fifth assessment report of the Intergovernmental Panel on Climate Change, Tech. rep., IPCC (2014).
- [2] The National Aeronautics and Space Administration, `climate.nasa.gov`.
- [3] M. C. Turner, Z. J. Andersen, A. Baccarelli, W. R. Diver, S. M. Gapstur, C. A. Pope III, D. Prada, J. Samet, G. Thurston, A. Cohen, Outdoor air pollution and cancer: An overview of the current evidence and public health recommendations, *CA-Cancer J. Clin.* 70 (6) (2020) 460–479.
- [4] K. Victorin, Review of the genotoxicity of nitrogen oxides, *Mutat. Res.-Rev. Genet.* 317 (1) (1994) 43–55.
- [5] A. García-Olivares, J. Solí, O. Osychenko, Transportation in a 100% renewable energy system, *Energy Convers. Manage.* 158 (2018) 266–285.
- [6] B. Heard, B. Brook, T. Wigley, C. Bradshaw, Burden of proof: A comprehensive review of the feasibility of 100% renewable-electricity systems, *Renew. Sust. Energy Rev.* 76 (2017) 1122–1133.
- [7] U. S. Energy Information Administration, Annual energy outlook 2022, Tech. rep. (2022).
- [8] F. Nicoud, K. Wiecek, About the zero Mach number assumption in the calculation of thermoacoustic instabilities, *Int. J. Spray Combust.* 1 (2009) 67–111.
- [9] N. Peters, *Turbulent Combustion*, Cambridge University Press, 2000.
- [10] C. K. Law, *Combustion Physics*, Cambridge University Press, 2006.
- [11] H. Wei, T. Zhu, G. Shu, L. Tan, Y. Wang, Gasoline engine exhaust gas recirculation – a review, *Appl. Energy* 99 (2012) 534–544.
- [12] S. K. Dhanuka, J. E. Temme, J. F. Driscoll, H. C. Mongia, Vortex-shedding and mixing layer effects on periodic flashback in a lean premixed prevaporized gas turbine combustor, *Proc. Combust. Inst.* 32 (2) (2009) 2901–2908.

- [13] K. Poorghasemi, F. Ommi, H. Yaghmaei, A. Namaki, An investigation on effect of high pressure post injection on soot and NO emissions in a DI diesel engine, *J. Mech. Sci. Technol.* 26.
- [14] T. Lu, C. K. Law, Toward accommodating realistic fuel chemistry in large-scale computations, *Prog. Energy Combust. Sci.* 35 (2) (2009) 192–215.
- [15] T. Lu, Y. Ju, C. K. Law, Complex CSP for chemistry reduction and analysis, *Combust. Flame* 126 (1) (2001) 1445 – 1455.
- [16] T. Lu, C. K. Law, A directed relation graph method for mechanism reduction, *Proc. Combust. Inst.* 30 (1) (2005) 1333 – 1341.
- [17] P. Pepiot-Desjardins, H. Pitsch, An efficient error-propagation-based reduction method for large chemical kinetic mechanisms, *Combust. Flame* 154 (1) (2008) 67 – 81.
- [18] S. Yang, R. Ranjan, V. Yang, S. Menon, W. Sun, Parallel on-the-fly adaptive kinetics in direct numerical simulation of turbulent premixed flame, *Proc. Combust. Inst.* 36 (2) (2017) 2025–2032.
- [19] R. Van de Vijver, N. M. Vandewiele, P. L. Bhoorasingh, B. L. Slakman, F. Seyedzadeh Khanshan, H.-H. Carstensen, M.-F. Reyniers, G. B. Marin, R. H. West, K. M. Van Geem, Automatic mechanism and kinetic model generation for gas- and solution-phase processes: A perspective on best practices, recent advances, and future challenges, *Int. J. Chem. Kinet.* 47 (4) (2015) 199–231.
- [20] J. C. Sutherland, A. Parente, Combustion modeling using principal component analysis, *Proc. Combust. Inst.* 32 (1) (2009) 1563–1570.
- [21] B. J. Isaac, J. N. Thornock, J. Sutherland, P. J. Smith, A. Parente, Advanced regression methods for combustion modelling using principal components, *Combust. Flame* 162 (6) (2015) 2592–2601.
- [22] M. R. Malik, P. Obando Vega, A. Coussement, A. Parente, Combustion modeling using Principal Component Analysis: A posteriori validation on Sandia flames D, E and F, *Proc. Combust. Inst.* 38 (2) (2021) 2635–2643.
- [23] M. R. Malik, A. Coussement, T. Echekki, A. Parente, Principal component analysis based combustion model in the context of a lifted methane/air flame: Sensitivity to the manifold parameters and subgrid closure, *Combust. Flame* 244 (2022) 112134.
- [24] A. C. Nunno, B. A. Perry, J. F. Macart, M. E. Mueller, Data-driven dimension reduction in turbulent combustion: Utility and limitations, in: *AIAA SciTech* 2019, 2019.
- [25] Y. Yang, S. B. Pope, J. H. Chen, Empirical low-dimensional manifolds in composition space, *Combust. Flame* 160 (10) (2013) 1967–1980.

- [26] N. Peters, Laminar diffusion flamelet models in non-premixed turbulent combustion, *Prog. Energy Combust. Sci.* 10 (3) (1984) 319–339.
- [27] H. Pitsch, M. Chen, N. Peters, Unsteady flamelet modeling of turbulent hydrogen-air diffusion flames, *Symp. (Int.) Combust.* 27 (1) (1998) 1057–1064.
- [28] C. D. Pierce, P. Moin, Progress-variable approach for large-eddy simulation of non-premixed turbulent combustion, *J. Fluid Mech.* 504 (2004) 73–97.
- [29] J. A. Oijen, van, L. P. H. Goey, de, Modelling of premixed laminar flames using flamelet-generated manifolds, *Combust. Sci. Technol.* 161 (1) (2000) 113–137.
- [30] O. Gicquel, N. Darabiha, D. Thévenin, Laminar premixed hydrogen/air counterflow flame simulations using flame prolongation of ILDM with differential diffusion, *Proc. Combust. Inst.* 28 (2) (2000) 1901–1908.
- [31] M. Ihme, Y. C. See, LES flamelet modeling of a three-stream MILD combustor: Analysis of flame sensitivity to scalar inflow conditions, *Proc. Combust. Inst.* 33 (1) (2011) 1309–1317.
- [32] L. Gomet, V. Robin, A. Mura, A multiple-inlet mixture fraction model for nonpremixed combustion, *Combust. Flame* 162 (3) (2015) 668–687.
- [33] B. A. Perry, M. E. Mueller, A. R. Masri, A two mixture fraction flamelet model for large eddy simulation of turbulent flames with inhomogeneous inlets, *Proc. Combust. Inst.* 36 (2) (2017) 1767–1775.
- [34] C. Bekdemir, L. M. T. Somers, L. P. H. Goey, de, Modeling diesel engine combustion using pressure dependent flamelet generated manifolds, *Proc. Combust. Inst.* 33 (2) (2011) 2887–2894.
- [35] J. A. Oijen, van, F. A. Lammers, L. P. H. Goey, de, Modeling of complex premixed burner systems by using flamelet-generated manifolds, *Combust. Flame* 127 (3) (2001) 2124–2134.
- [36] B. Marracino, D. Lentini, Radiation modelling in non-luminous nonpremixed turbulent flames, *Combust. Sci. Technol.* 128 (1-6) (1997) 23–48.
- [37] P.-D. Nguyen, L. Vervisch, V. Subramanian, P. Domingo, Multidimensional flamelet-generated manifolds for partially premixed combustion, *Combust. Flame* 157 (1) (2010) 43–61.
- [38] M. E. Mueller, Physically-derived reduced-order manifold-based modeling for multi-modal turbulent combustion, *Combust. Flame* 214 (2020) 287–305.
- [39] M. E. Mueller, H. Pitsch, LES model for sooting turbulent nonpremixed flames, *Combust. Flame* 159 (6) (2012) 2166–2180.
- [40] S. Weise, C. Hasse, Reducing the memory footprint in Large Eddy Simulations of reactive flows, *Parallel Comput.* 49 (C) (2015) 50–65.

- [41] K. A. Kemenov, S. B. Pope, Molecular diffusion effects in LES of a piloted methane–air flame, *Combust. Flame* 158 (2) (2011) 240–254.
- [42] L. Shunn, Large-eddy simulation of combustion systems with convective heat-loss, Ph.D. thesis, Stanford University (2009).
- [43] C. E. Lacey, A. G. Novoselov, M. E. Mueller, In-Situ Adaptive Manifolds: Enabling computationally efficient simulations of complex turbulent reacting flows, *Proc. Combust. Inst.* 38 (2) (2021) 2673–2680.
- [44] S. B. Pope, Computationally efficient implementation of combustion chemistry using in situ adaptive tabulation, *Combust. Theory Model.* 1 (1) (1997) 41–63.
- [45] B. Fiorina, O. Gicquel, L. Vervisch, S. Carpentier, N. Darabiha, Approximating the chemical structure of partially premixed and diffusion counterflow flames using FPI flamelet tabulation, *Combust. Flame* 140 (3) (2005) 147–160.
- [46] E. Knudsen, H. Pitsch, A general flamelet transformation useful for distinguishing between premixed and non-premixed modes of combustion, *Combust. Flame* 156 (3) (2009) 678–696.
- [47] M. P. Sitte, E. Mastorakos, Large Eddy Simulation of a spray jet flame using Doubly Conditional Moment Closure, *Combust. Flame* 199 (2019) 309–323.
- [48] A. Kronenburg, M. Cleary, Multiple mapping conditioning for flames with partial premixing, *Combust. Flame* 155 (1) (2008) 215–231.
- [49] G. R. Hendra, W. Bushe, The uniform conditional state model for turbulent reacting flows, *Combust. Flame* 205 (2019) 484–505.
- [50] J. H. Chen, Petascale direct numerical simulation of turbulent combustion—fundamental insights towards predictive models, *Proc. Combust. Inst.* 33 (1) (2011) 99–123.
- [51] P. Domingo, L. Vervisch, Recent developments in DNS of turbulent combustion, *Proc. Combust. Inst.*
- [52] L. Gicquel, G. Staffelbach, T. Poinso, Large Eddy Simulations of gaseous flames in gas turbine combustion chambers, *Prog. Energy Combust. Sci.* 38 (6) (2012) 782–817.
- [53] D. C. Wilcox, *Turbulence Modeling for CFD*, DCW Indust., 2006.
- [54] K. S. Klemmer, M. E. Mueller, Implied models approach for turbulence model form physics-based uncertainty quantification, *Phys. Rev. Fluids* 6 (2021) 044606.
- [55] S. B. Pope, PDF methods for turbulent reactive flows, *Prog. Energy Combust. Sci.* 11 (2) (1985) 119–192.
- [56] D. Haworth, Progress in probability density function methods for turbulent reacting flows, *Prog. Energy Combust. Sci.* 36 (2) (2010) 168–259.

- [57] S. S. Girimaji, Assumed beta-PDF model for turbulent mixing: Validation and extension to multiple scalar mixing, *Combust. Sci. Technol.* 78 (4-6) (1991) 177–196.
- [58] A. W. Cook, J. J. Riley, A subgrid model for equilibrium chemistry in turbulent flows, *Phys. Fluids* 6 (8) (1994) 2868–2870.
- [59] A. Klimenko, R. Bilger, Conditional moment closure for turbulent combustion, *Prog. Energy Combust. Sci.* 25 (6) (1999) 595–687.
- [60] N. Swaminathan, R. W. Bilger, Analyses of conditional moment closure for turbulent premixed flames, *Combust. Theory Model.* 5 (2) (2001) 241–260.
- [61] A. Y. Klimenko, S. B. Pope, The modeling of turbulent reactive flows based on multiple mapping conditioning, *Phys. Fluids* 15 (7) (2003) 1907–1925.
- [62] M. J. Cleary, A. Y. Klimenko, A generalised multiple mapping conditioning approach for turbulent combustion, *Flow Turbul. Combust.* 82 (2009) 477–491.
- [63] P. A. McMurthy, S. Menon, A. R. Kerstein, A linear eddy sub-grid model for turbulent reacting flows: Application to hydrogen-air combustion, *Proc. Combust. Inst.* 24 (1) (1992) 271–278.
- [64] B. Magnussen, On the structure of turbulence and a generalized eddy dissipation concept for chemical reaction in turbulent flow, no. 42, 1981.
- [65] A. Péquin, S. Iavarone, R. Malpica Galassi, A. Parente, The partially stirred reactor model for combustion closure in large eddy simulations: Physical principles, sub-models for the cell reacting fraction, and open challenges, *Phys. Fluids* 34 (5) (2022) 055122.
- [66] L. Valiño, A field Monte Carlo formulation for calculating the probability density function of a single scalar in a turbulent flow, *Flow Turbul. Combust.* 60 (1998) 157–172.
- [67] O. Colin, F. Ducros, D. Veynante, T. Poinso, A thickened flame model for large eddy simulations of turbulent premixed combustion, *Phys. Fluids* 12 (7) (2000) 1843–1863.
- [68] N. Peters, Local quenching due to flame stretch and non-premixed turbulent combustion, *Combust. Sci. Technol.* 30 (1-6) (1983) 1–17.
- [69] A. G. Novoselov, B. A. Perry, M. E. Mueller, Two-dimensional manifold equations for multi-modal turbulent combustion: Nonpremixed combustion limit and scalar dissipation rates, *Combust. Flame* 231 (2021) 111475.
- [70] A. G. Novoselov, C. E. Lacey, B. A. Perry, M. E. Mueller, Large Eddy Simulation of a turbulent lifted flame using multi-modal manifold-based models: Feasibility and interpretability, *Proc. Combust. Inst.* 38 (2) (2021) 2581–2588.
- [71] C. E. Lacey, S. Sundaresan, M. E. Mueller, Data-based instantaneous conditional progress variable dissipation rate modeling for turbulent premixed combustion, *Combust. Flame* (2023) submitted.



- [72] T. Poinso, D. Veynante, Theoretical and Numerical Combustion, Edwards, 2005.
- [73] R. S. Barlow, J. H. Frank, A. N. Karpetis, J.-Y. Chen, Piloted methane/air jet flames: Transport effects and aspects of scalar structure, *Combust. Flame* 143 (4) (2005) 433–449.
- [74] N. Burali, S. Lapointe, B. Bobbitt, G. Blanquart, Y. Xuan, Assessment of the constant non-unity Lewis number assumption in chemically-reacting flows, *Combust. Theory Model.* 20 (4) (2016) 632–657.
- [75] A. J. Aspden, M. S. Day, J. B. Bell, Towards the distributed burning regime in turbulent premixed flames, *J. Fluid Mech.* 871 (2019) 1–21.
- [76] B. Savard, B. Bobbitt, G. Blanquart, Structure of a high Karlovitz n-C7H16 premixed turbulent flame, *Proc. Combust. Inst.* 35 (2) (2015) 1377–1384.
- [77] M. V. Papalexandris, On the applicability of Stokes’ hypothesis to low-Mach-number flows, *Continuum Mech. Therm.* 32 (4) (2019) 1245–1249.
- [78] L. Prandtl, Bericht über die entstehung der turbulenz, *Z. Angew. Math. Mech.* 5 (1925) 136–139.
- [79] J. Smagorinsky, General circulation experiments with the primitive equations, *Mon. Weather Rev.* 91 (3) (1963) 99–164.
- [80] S. B. Pope, *Turbulent Flows*, Cambridge University Press, 2000.
- [81] M. Germano, U. Piomelli, P. Moin, W. H. Cabot, A dynamic subgrid-scale eddy viscosity model, *Phys. Fluids A-Fluid* 3 (7) (1991) 1760–1765.
- [82] D. K. Lilly, A proposed modification of the Germano subgrid-scale closure method, *Phys. Fluids A-Fluid* 4 (3) (1992) 633–635.
- [83] G. V. Cybenko, Approximation by superpositions of a sigmoidal function, *Math. Control Signal.* 2 (1989) 303–314.
- [84] Izaak Neutelings, [tikz.net/neural\\_networks/](https://tikz.net/neural_networks/).
- [85] D. Masters, C. Luschi, Revisiting small batch training for deep neural networks, *ArXiv abs/1804.07612*.
- [86] T. Elsken, J. H. Metzen, F. Hutter, Neural architecture search: A survey, *J. Mach. Learn. Res.* 20 (1) (2019) 1997–2017.
- [87] P. Ren, Y. Xiao, X. Chang, P.-y. Huang, Z. Li, X. Chen, X. Wang, A comprehensive survey of neural architecture search: Challenges and solutions, *ACM Comput. Surv.* 54 (4).
- [88] H. Pitsch, N. Peters, A consistent flamelet formulation for non-premixed combustion considering differential diffusion effects, *Combust. Flame* 114 (1) (1998) 26–40.

- [89] V. Raman, H. Pitsch, A consistent LES/filtered-density function formulation for the simulation of turbulent flames with detailed chemistry, *Proc. Combust. Inst.* 31 (2) (2007) 1711–1719.
- [90] B. A. Perry, M. E. Mueller, Effect of multiscalar subfilter PDF models in LES of turbulent flames with inhomogeneous inlets, *Proc. Combust. Inst.* 37 (2) (2019) 2287–2295.
- [91] G. Lodier, L. Vervisch, V. Moureau, P. Domingo, Composition-space premixed flamelet solution with differential diffusion for in situ flamelet-generated manifolds, *Combust. Flame* 158 (10) (2011) 2009–2016.
- [92] O. Desjardins, G. Blanquart, G. Balarac, H. Pitsch, High order conservative finite difference scheme for variable density low Mach number turbulent flows, *J. Comput. Phys.* 227 (15) (2008) 7125–7159.
- [93] J. F. MacArt, M. E. Mueller, Semi-implicit iterative methods for low Mach number turbulent reacting flows: Operator splitting versus approximate factorization, *J. Comput. Phys.* 326 (2016) 569–595.
- [94] M. E. Mueller, PDRs, <https://ctrfl.princeton.edu/software/>.
- [95] R. S. Barlow, Sandia H<sub>2</sub>/He Flame Data - Release 2.0, <http://www.ca.sandia.gov/TNF> (2003).
- [96] R. S. Barlow, C. D. Carter, Raman/Rayleigh/LIF measurements of nitric oxide formation in turbulent hydrogen jet flames, *Combust. Flame* 97 (3) (1994) 261–280.
- [97] R. S. Barlow, C. D. Carter, Relationships among nitric oxide, temperature, and mixture fraction in hydrogen jet flames, *Combust. Flame* 104 (3) (1996) 288–299.
- [98] S. G. Davis, A. V. Joshi, H. Wang, F. Egolfopoulos, An optimized kinetic model of H<sub>2</sub>/CO combustion, *Proc. Combust. Inst.* 30 (1) (2005) 1283–1292.
- [99] R. S. Barlow, J. H. Frank, Effects of turbulence on species mass fractions in methane/air jet flames, *Proc. Combust. Inst.* 27 (1) (1998) 1087–1095.
- [100] G. P. Smith, D. M. Golden, M. Frenklach, GRI-Mech 3.0, [http://www.me.berkeley.edu/gri\\_mech/](http://www.me.berkeley.edu/gri_mech/).
- [101] H. Pitsch, Improved pollutant predictions in large-eddy simulations of turbulent non-premixed combustion by considering scalar dissipation rate fluctuations, *Proc. Combust. Inst.* 29 (2) (2002) 1971–1978.
- [102] W. Han, V. Raman, M. E. Mueller, Z. Chen, Effects of combustion models on soot formation and evolution in turbulent nonpremixed flames, *Proc. Combust. Inst.* 37 (1) (2019) 985–992.

- [103] I. J. Bonilla, C. E. Lacey, M. E. Mueller, Performance considerations for In-Situ Adaptive Manifolds for turbulent combustion modeling, in: APS Division of Fluid Dynamics Meeting Abstracts, 2022, p. T25.00006.
- [104] S. Meares, A. R. Masri, A modified piloted burner for stabilizing turbulent flames of inhomogeneous mixtures, *Combust. Flame* 161 (2) (2014) 484–495.
- [105] S. Meares, V. Prasad, G. Magnotti, R. Barlow, A. Masri, Stabilization of piloted turbulent flames with inhomogeneous inlets, *Proc. Combust. Inst* 35 (2) (2015) 1477–1484.
- [106] R. Barlow, S. Meares, G. Magnotti, H. Cutcher, A. Masri, Local extinction and near-field structure in piloted turbulent CH<sub>4</sub>/air jet flames with inhomogeneous inlets, *Combust. Flame* 162 (10) (2015) 3516–3540.
- [107] R. Cabra, T. Myhrvold, J. Chen, R. Dibble, A. Karpetis, R. Barlow, Simultaneous laser Raman-Rayleigh-LIF measurements and numerical modeling results of a lifted turbulent H<sub>2</sub>/N<sub>2</sub> jet flame in a vitiated coflow, *Proc. Combust. Inst.* 29 (2) (2002) 1881–1888.
- [108] R. Cabra, J.-Y. Chen, R. Dibble, A. Karpetis, R. Barlow, Lifted methane–air jet flames in a vitiated coflow, *Combust. Flame* 143 (4) (2005) 491–506.
- [109] R. L. Gordon, A. R. Masri, S. B. Pope, G. M. Goldin, A numerical study of auto-ignition in turbulent lifted flames issuing into a vitiated co-flow, *Combust. Theory Model.* 11 (3) (2007) 351–376.
- [110] G.-S. Jiang, C.-W. Shu, Efficient implementation of weighted ENO schemes, *J. Comput. Phys.* 126 (1) (1996) 202–228.
- [111] S. Yao, B. Wang, A. Kronenburg, O. Stein, Conditional scalar dissipation rate modeling for turbulent spray flames using artificial neural networks, *Proc. Combust. Inst.* 38 (2) (2021) 3371–3378.
- [112] J. Lee, J. F. MacArt, M. E. Mueller, Heat release effects on the reynolds stress budgets in turbulent premixed jet flames at low and high Karlovitz numbers, *Combust. Flame* 216 (2020) 1–8.
- [113] J. F. MacArt, T. Grenga, M. E. Mueller, Effects of combustion heat release on velocity and scalar statistics in turbulent premixed jet flames at low and high Karlovitz numbers, *Combust. Flame* 191 (2018) 468–485.
- [114] W. L. Chan, H. Kolla, J. H. Chen, M. Ihme, Assessment of model assumptions and budget terms of the unsteady flamelet equations for a turbulent reacting jet-in-cross-flow, *Combust. Flame* 161 (4) (2014) 2601–2613.
- [115] J. F. MacArt, T. Grenga, M. E. Mueller, Evolution of flame-conditioned velocity statistics in turbulent premixed jet flames at low and high Karlovitz numbers, *Proc. Combust. Inst.* 37 (2) (2019) 2503–2510.

- [116] J. W. Rogerson, N. Swaminathan, M. Tanahashi, N. Shiwaku, Analysis of progress variable variance equations using DNS data, *Proceedings of the European Combustion Meeting*.
- [117] J. Lee, M. E. Mueller, Closure modeling for the conditional Reynolds stresses in turbulent premixed combustion, *Proc. Combust. Inst.* 38 (2) (2021) 3031–3038.
- [118] S. Yellapantula, B. A. Perry, R. W. Grout, Deep learning-based model for progress variable dissipation rate in turbulent premixed flames, *Proc. Combust. Inst.* 38 (2) (2021) 2929–2938.
- [119] D. P. Kingma, J. Ba, Adam: A method for stochastic optimization (2017). [arXiv: 1412.6980](https://arxiv.org/abs/1412.6980).
- [120] B. Savard, G. Blanquart, An a priori model for the effective species Lewis numbers in premixed turbulent flames, *Combust. Flame* 161 (6) (2014) 1547–1557.
- [121] M. Sundararajan, A. Taly, Q. Yan, Axiomatic attribution for deep networks, *Proceedings of the 34th International Conference on Machine Learning* 70 (2017) 3319–3328.
- [122] G. Borghesi, A. Krisman, T. Lu, J. H. Chen, Direct numerical simulation of a temporally evolving air/n-dodecane jet at low-temperature diesel-relevant conditions, *Combust. Flame* 195 (2018) 183–202.
- [123] S. Treichler, M. Bauer, A. Bhagatwala, G. Borghesi, R. Sankaran, H. Kolla, P. McCormick, E. Slaughter, W. Lee, A. Aiken, J. H. Chen, S3D-Legion: An Exascale Software for Direct Numerical Simulation of Turbulent Combustion with Complex Multi-component Chemistry, *CNC Press*, 2017, Ch. 12, pp. 257–277.
- [124] C. D. Pierce, P. Moin, A dynamic model for subgrid-scale variance and dissipation rate of a conserved scalar, *Phys. Fluids* 10 (12) (1998) 3041–3044.
- [125] M. Ihme, H. Pitsch, Prediction of extinction and reignition in nonpremixed turbulent flames using a flamelet/progress variable model: 1. a priori study and presumed PDF closure, *Combust. Flame* 155 (1) (2008) 70–89.
- [126] W. H. Press, S. A. Teukolsky, W. T. Vetterling, B. P. Flannery, *Numerical Recipes*, 3rd Edition, Cambridge University Press, 2007.
- [127] C. E. Rasmussen, C. K. I. Williams, *Gaussian Processes for Machine Learning*, The MIT Press, 2005.
- [128] F. Pedregosa, G. Varoquaux, A. Gramfort, V. Michel, B. Thirion, O. Grisel, M. Blondel, P. Prettenhofer, R. Weiss, V. Dubourg, J. Vanderplas, A. Passos, D. Cournapeau, M. Brucher, M. Perrot, E. Duchesnay, Scikit-learn: Machine learning in Python, *J. Mach. Learn. Res.* 12 (2011) 2825–2830.
- [129] I. T. Jolliffe, *Principal Component Analysis*, Springer New York, NY, 1986.

- [130] G. D'Alessio, A. Attili, A. Cuoci, H. Pitsch, A. Parente, Analysis of Turbulent Reacting Jets via Principal Component Analysis, Springer International Publishing, Cham, 2020, pp. 233–251.
- [131] W. J. Krzanowski, Selection of variables to preserve multivariate data structure, using principal components, *J. Roy. Stat. Soc. C-App.* 36 (1) (1987) 22–33.
- [132] E. Buckingham, On physically similar systems; illustrations of the use of dimensional equations, *Phys. Rev.* 4 (1914) 345–376.
- [133] J. Bakarji, J. Callaham, S. L. Brunton, Dimensionally consistent learning with Buckingham Pi, *Nat. Comput. Sci.* 2 (2022) 834–844.
- [134] M. E. Mueller, A computationally efficient turnkey approach to turbulent combustion modeling: From elusive fantasy to impending reality, in: *AIAA SciTech 2019*, 2019.
- [135] N. Swaminathan, K. Bray, Effect of dilatation on scalar dissipation in turbulent premixed flames, *Combust. Flame* 143 (4) (2005) 549–565.